Nuclear-matter modification of decay widths in the $\phi \to e^+e^-$ and $\phi \to K^+K^-$ channels studied in 12 GeV $p + A$ reactions

Fuminori Sakuma

Abstract

The experiment KEK-PS E325 has measured the ϕ meson production via the e^+e^- and K^+K^- decay channels in 12 GeV $p + \mathrm{C}$ and $p + \mathrm{Cu}$ reactions in order to search for in-medium modification of ϕ mesons, which was theoretically predicted as a consequence of partially-restored chiral-symmetry at the normal nuclear-matter density. Using the nuclear mass-number dependences of the $\phi \to e^+e^-$ and $\phi \to K^+K^-$ yields, we have searched for a possible change of the branching ratio $\Gamma_{\phi\to K^+K^-}/\Gamma_{\phi\to e^+e^-}$, since the partial decay width $\Gamma_{\phi\to K^+K^-}$ is sensitive even to a small change in the spectral function of the ϕ meson and/or kaon because of the small Q value in $\phi \to K^+K^-$ decays. The observed K^+K^- spectra are well reproduced by the relativistic Breit-Wigner function with a combinatorial background shape in three $\beta\gamma$ regions between 1.0 and 3.5. The nuclear mass-number dependence of the yields of the K^+K^- decay channel is compared to those of the e^+e^- decay channel. We parameterize the production yields as $\sigma(A) = \sigma_0 \times A^\alpha$ and obtain $\alpha_{\phi\to K^+K^-} - \alpha_{\phi\to e^+e^-}$ to be 0.14 ± 0.12. Although we have concluded that $\alpha_{\phi\to e^+e^-}$ and $\alpha_{\phi\to K^+K^-}$ are consistent with each other within an error in the measured kinematical region, upper limits are obtained for the partial decay widths of ϕ mesons in nuclear matter.

Contents

Chapter 1

Introduction

The properties of hadrons, such as mass, decay width, and branching ratio, have been extensively studied and well established in the history of particle physics. Recent interests have been extended to understand how these properties are modified in hot or dense matter. This issue is of fundamental importance since such modifications can be related to the basic nature of the quantum chromodynamics (QCD), spontaneous chiral symmetry breaking, i.e., the mechanism that creates most of the hadron masses.

1.1 Chiral Symmetry Breaking and its Restoration

It is well established that most of the masses of leptons, weak bosons, and heavy quarks are given by the Higgs mechanism, while light quarks obtain their constituent masses mainly due to spontaneous chiral-symmetry breaking in QCD [1, 2]. The former mechanism has been studied by searching for Higgs boson(s) in the LEP at CERN and the Tevatron at Fermilab, and the searches will continue later at the LHC at CERN. On the other hand, the experimental approach to the latter mechanism is not well established yet, because the QCD vacuum has a non-trivial structure which has non-vanishing quark condensate $\langle\bar{q}q\rangle$, the order parameter of the symmetry breaking. Figure 1.1 shows a theoretical calculation of $|\langle\bar{q}q\rangle|$ as a function of density ρ and temperature T of a medium [3]. In the figure, the broken symmetry is expected to be restored as T or ρ increases. In extreme circumstances, the quark gluon plasma (QGP) phase at very high T or the color superconducting (CSC) phase at very high ρ, the chiral symmetry is expected to be restored completely; therefore, u and d quarks may have only masses from 3 to 10 MeV/c^2 resulting from the Higgs mechanism. Further, Fig. 1.1 suggests that the quark masses at the normal nuclear density may be significantly smaller than that at normal vacuum.

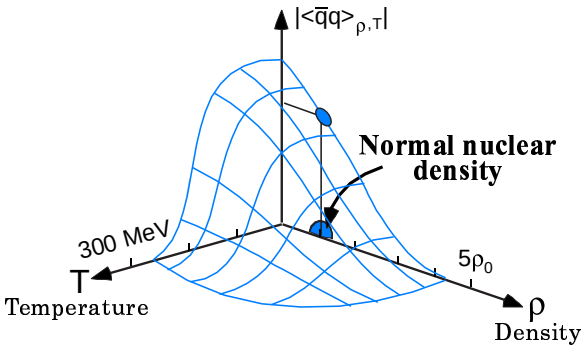

Figure 1.1: A chiral condensation $|\langle\bar{q}q\rangle|$ as a function of temperature T and density ρ. The density is given in units of the nuclear matter density $\rho_0 \simeq 0.17\text{fm}^{-3}$.

1.2 Theoretical Predictions for Meson Modifications

Many theoretical models predict modifications of meson spectral functions in terms of chiral symmetry restoration in hot/dense matter.

The present experiment is largely motivated by the following pioneering works. Using an effective chiral Lagrangian, Brown and Rho proposed an in-medium scaling law, "Brown-Rho scaling", which predicted a decrease in the meson mass of 20% at the normal nuclear density ρ_0 [4]. Based on a QCD sum rule, Hatsuda and Lee predicted that the vector-meson masses decrease in a medium as shown in Fig. 1.2; the mass decreases of ρ and ω are about 16% ($\simeq$130 MeV) and ϕ in the range of 1 to 4% ($\simeq$10 to 40 MeV) at the normal nuclear density [5, 6]. They also pointed out that the mass of vector meson (1^{--}) has a relatively simple connection to the constituent quark mass and consequently to the quark condensate.

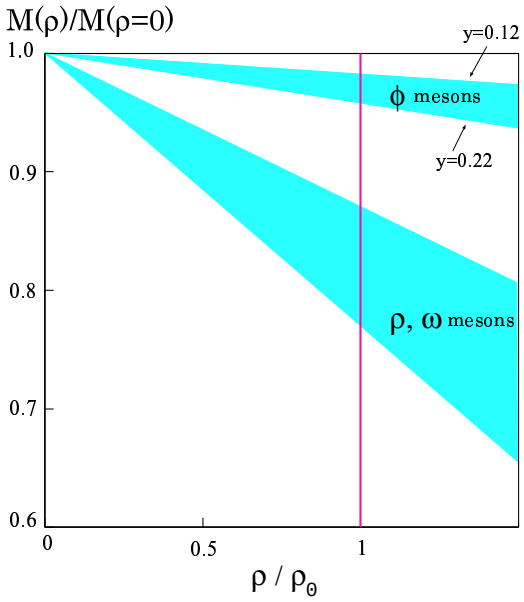

Figure 1.2: Masses of ρ, ω, and ϕ mesons as functions of density, which is normalized by the normal nuclear density ρ_0, predicted by Hatsuda and Lee [6]. The hatched regions represent the theoretical uncertainty which is caused in estimating quark condensates from limited experimental information. The uncertainty for ρ and ω mesons is from $\langle\bar{u}u + \bar{d}d\rangle_N$, the u and d quark contents in the nucleon. For ϕ meson, there is an extra error from the strange contents in the nucleon, $y = 2\langle\bar{s}s\rangle_N/(\langle\bar{u}u\rangle_N + \langle\bar{d}d\rangle_N)$.

Especially, the ϕ meson, which is a vector meson of an almost pure $s\bar{s}$ state, has very attractive features as a probe to detect possible changes in its properties. Its natural width is narrow (Γ_ϕ = 4.26 MeV/c^2) [7] without any resonance nearby; therefore, we may be able to detect the possible mass modification clearly. There are theoretical predictions not only for the mass shift of the ϕ meson as described above, but also for the width broadening. The calculation taking kaon-nucleon interactions into account predicted the ϕ-meson spectrum to be modified in a nuclear medium, since the spectrum of the ϕ meson is dominantly characterized by its decay into $K\bar{K}$ [8, 9, 10, 11]. Klingl *et al.* calculated the significant broadening of the decay width as large as 45 MeV/c^2 for the ϕ at rest, 10 times larger than in free space as shown in Fig 1.3 [8], for example. Table 1.1 lists theoretical predictions for the ϕ meson modification in a medium. According to these predictions, the decrease in mass at the normal nuclear density is up to 40 MeV/c^2 and the width broadening is up to 45 MeV/c^2.

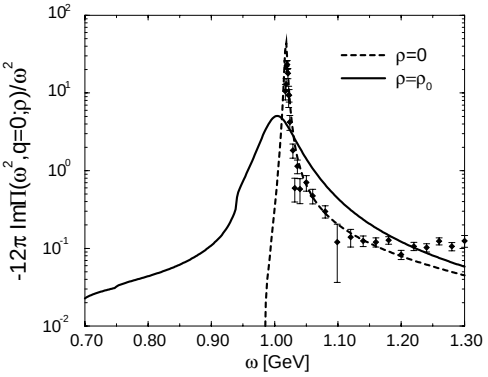

Figure 1.3: The spectrum of the ϕ meson in vacuum (dashed) and in nuclear matter at $\rho = \rho_0$ (solid curve) predicted in Ref. [8]. The data are from the reaction $e^+e^- \to K^+K^-$ [12].

authors	model	matter	predictions	
			mass change	total width
T. Hatsuda and S. H. Lee [5, 6]	QCD sum rule	**cold**	$-10 \sim -40\text{MeV}/c^2@\rho = \rho_0$	–
F. Klingl, T. Waas, and W. Weise [8]	chiral effective Lagrangian	**cold**	$-10\text{MeV}/c^2@\rho = \rho_0$	$45\text{MeV}/c^2@\rho = \rho_0$
E. Oset and A. Ramos [9]	kaon mass renormalization	**cold**	unchanged	$22\text{MeV}/c^2@\rho = \rho_0$
D. Cabrera and M. J. Vicente Vacas [10]	chiral SU(3)	**cold**	$-8\text{MeV}/c^2@\rho = \rho_0$	$30\text{MeV}/c^2@\rho = \rho_0$
S. Pal, C. M. Ko, and Z.-w. Lin [11]	AMPT model, chiral effective Lagrangian	**cold**	$-26\text{MeV}/c^2@\rho = \rho_0$	$45\text{MeV}/c^2@\rho = 2\rho_0$
P.-Z. Bi and J. Rafelski [13]	Bag model, chiral invariance	**hot**	$+5\text{MeV}/c^2@T \sim T_c$	$10\text{MeV}/c^2@T \sim T_c$
J. P. Blaizot and R. Mendez Galain [14]	NJL model	**hot**	$-(m_\phi - 2m_K)@T = T_c$	$0.7\text{MeV}/c^2@T = T_c$
W. Smith and K. L. Haglin [15]	one-boson-exchange model	**hot**	unchanged	$14 \sim 24\text{MeV}/c^2@T = T_c$

Table 1.1: Theoretical predictions for the ϕ meson modification in a medium. Where T_c is the critical temperature ($\sim$ 170 MeV).

Moreover, since m_ϕ is only 32 (24) MeV/c^2 greater than $2m_{K^\pm}$ ($2m_{K^0}$), the partial decay width $\Gamma_{\phi\to K\bar{K}}$ is sensitive even to a small change in the spectral functions of the ϕ and/or K mesons. Several theoretical models pointed out the possible change of the branching ratio $\Gamma_{\phi\to K\bar{K}}/\Gamma_{\phi\to l^+l^-}$ in a nuclear medium [13, 14, 16] like;

- the ϕ-meson mass is unchanged in a nuclear medium but the kaon mass decreases, then $\Gamma_{\phi\to K\bar{K}}$ increases because of an increase in $\Delta m \equiv m_\phi - 2m_K$, or
- the ϕ-meson mass decreases in a nuclear medium while the kaon mass is unchanged, then $\Gamma_{\phi\to K\bar{K}}$ decreases because of a decrease in Δm.

1.3 Experimental Searches for Meson Modifications

As for the modification of vector mesons in "cold" matter, several experiments including ours have been performed so far. The TAGX collaboration at the INS-ES studied in-medium modification of the invariant mass distribution of ρ meson in ^{2}H, ^{3}He, ^{12}C$(\gamma, \pi^+\pi^-)$X reactions [17, 18, 19, 20]. They have concluded that the observed ρ-meson spectra show a decrease of its mass by about 100 MeV/c^2 [20]. The GSI-SIS S236 collaboration reported changes in the pion-nucleus potential in deeply bound pionic ^{115}Sn, ^{119}Sn, ^{123}Sn nuclei as a possible signature of chiral symmetry restoration [21]. They argued the 36% reduction of the pion decay constant $f_\pi^*(\rho)^2/f_\pi^2$, which can be connected with the mass of ρ/ω meson in a nuclear medium by the Brown-Rho scaling $m_V^*/m_V \simeq f_\pi^*/f_\pi (V = \rho, \omega)$. The CBELSA/TAPS collaboration at the ELSA has reported the mass modification of the ω meson by measuring the $\omega \to \pi^0\gamma$ channel as shown in Fig. 1.4(a) [22]. They concluded that the mass of ω meson decreases by 8% with respect to the vacuum value at an estimated average nuclear density of $0.6\rho_0$, being consistent with a scaling of the ω mass by $m = m_0(1 - 0.14\rho/\rho_0)$.

For the modification of vector mesons in "hot" matter, there are several measurements at the CERN-SPS and BNL-RHIC. The experiment CERES/NA45 at the CERN-SPS measured the low-mass electron-pairs in $p + A$ and $A + A$ collisions as shown in Fig. 1.4(b) [23]. They observed a large enhancement at the lower side of the ρ/ω-meson mass in $A+A$ not in $p+A$, but their poor mass resolution is not enough to discuss an origin of the enhancement. The STAR experiment at BNL-RHIC measured the $\pi^+\pi^-$ spectra in $p+p$ and peripheral Au+Au collisions at $\sqrt{s_{NN}} = 200$ GeV [24]. The measured ρ peak in the invariant mass distribution is shifted by 40 MeV/c^2 in minimum bias $p+p$ interactions and 70 MeV/c^2 in peripheral Au+Au collisions. The NA60 experiment at the CERN-SPS measured the dimuon spectra in 158 A GeV In+In collisions as shown in Fig. 1.4(c) [25]. The observed spectrum shows the modification of the ρ meson, not the peak shift but the width broadening.

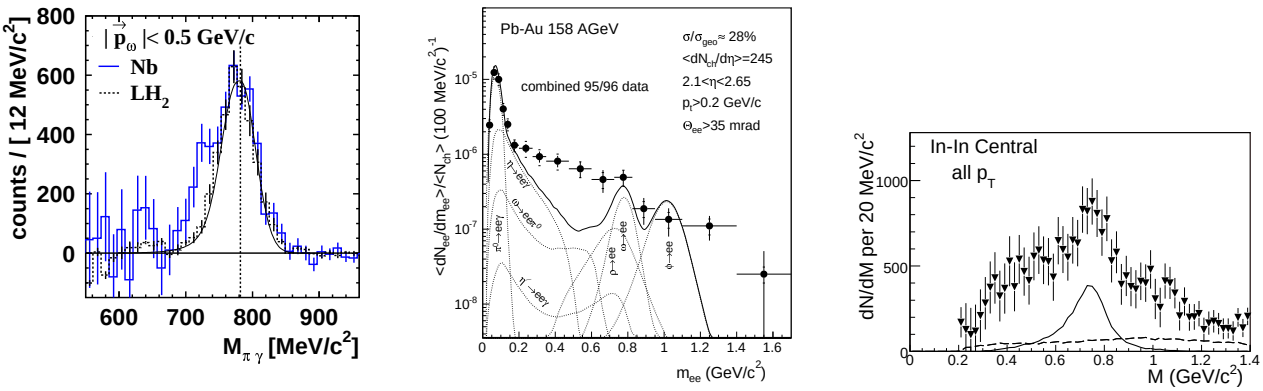

(a) $\omega \to \pi^0\gamma$ @ CBELSA/TAPS (b) e^+e^- @ CERES (c) $\rho \to \mu^+\mu^-$ @ NA60

Figure 1.4: (c) The $\omega \to \pi^0\gamma$ spectrum at CBELSA/TAPS [22]. (b) The low-mass e^+e^- spectrum in Pb+Au at CERES [26]. (c) The $\rho \to \mu^+\mu^-$ spectrum at NA60 [25].

Compared to ρ and ω mesons, there are a limited number of experimental reports on the search for the in-medium modification of the ϕ meson. With regard to the partial decay width $\Gamma_{\phi\to K\bar{K}}/\Gamma_{\phi\to l^+l^-}$, the experiments NA49 and NA50 in Pb-Pb collisions at 158 A·GeV/c at the CERN-SPS reported ϕ-meson yields in the K^+K^- and $\mu^+\mu^-$ channels, respectively [27, 28, 29]. There are discrepancies by factors ranging from 2 to 4 between these two measurements as shown in Fig. 1.5. These discrepancies have been denied recently by the CERES experiment with their new results of $\phi \to e^+e^-$ and $\phi \to K^+K^-$ measurements [30]. The results in the

K^+K^- channels are in agreement with those of NA49 and with those in the e^+e^- channel as shown in Fig. 1.5. However, the $\phi \to e^+e^-$ data of the CERES is not clear enough, so that it can not conclude evidently the in-medium modification of the branching ratio $\Gamma_{\phi\to K\bar{K}}/\Gamma_{\phi\to l^+l^-}$ does not exist. For the spectral modification of the ϕ meson, the present experiment E325 recently reported the modification in nuclear matter measured in the e^+e^- decay channel for the first time [31].

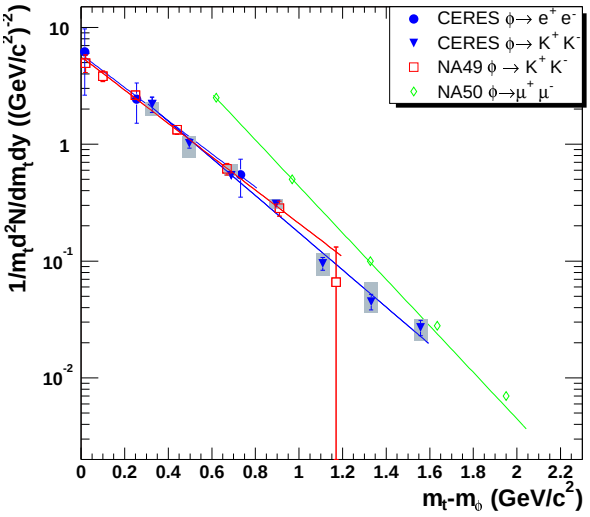

Figure 1.5: Transverse mass distribution of ϕ mesons measured in K^+K^- at NA49 (squares), $\mu^+\mu^-$ at NA50 (diamonds), K^+K^- at CERES (triangles), and e^+e^- at CERES (circles) [30].

1.4 KEK-PS E325 Experiment

The experiment KEK-PS E325 has measured the invariant mass spectra of e^+e^- and K^+K^- pairs in 12 GeV $p + A$ reactions at High Energy Accelerator Research Organization (KEK) 12 GeV Proton-Synchrotron. The goal of the experiment is to detect a signature of the partially-restored chiral-symmetry at the normal nuclear density appearing by a modification of the spectral shape of vector mesons, and a possible change of the branching ratio $\Gamma_{\phi\to K\bar{K}}/\Gamma_{\phi\to e^+e^-}$ using the nuclear mass-number dependences of $\phi \to e^+e^-$ and $\phi \to K^+K^-$.

The spectrometer was newly constructed at the high-intensity primary beam-line in KEK to detect slowly moving vector mesons in $\rho \to e^+e^-$, $\omega \to e^+e^-$, $\phi \to e^+e^-$, and $\phi \to K^+K^-$ modes simultaneously. It should be noted that high quality primary beam on thin targets is needed to suppress the background from γ-conversions in the e^+e^- channel.

The experiment E325 was proposed in the year 1993, and the construction of the spectrometer started on June 1996. The engineering run was performed on November 1996, and the first physics run was executed in June 1997 for the K^+K^- channel. All the electron-arm counters were completed on February 1998, and the first measurement of the e^+e^- channel was done in 1998. In July 1999, June 2000, December 2000, and from November to December in 2001, simultaneous data takings both for the e^+e^- and K^+K^- channels were performed. From February to March in 2002, the data taking dedicated to the e^+e^- channel was performed, and the experiment was completed.

The E325 experiment used 440 shifts of beam time (= 3520 hours) in total, and is the longest nuclear-physics experiment in the 35 years of the history of KEK 12 GeV PS. From the earlier data, we reported the signature of ρ/ω modification measured in the e^+e^- channel in Ref. [32, 33]. This discovery was reconfirmed later with use of 100 times more statistics in Ref. [34, 35].

For the ϕ meson, we recently reported the evidence of ϕ meson mass modification in Ref.[31, 36]. From these results, we conclude that the modification of vector mesons in dense nuclear matter is experimentally confirmed. We also reported the production cross sections and the rapidity and transverse momentum (p_T) distributions of ω and ϕ mesons in Ref. [37, 38], where we confirmed that our measurements on those yields are consistent with other experiments.

In this manuscript, we report the final results on the $\phi \to K^+K^-$ channel. Based on much improved analysis procedures, and more importantly with improved statistics compared to our earlier reports [39, 40], we examine the $\phi \to K^+K^-$ invariant mass spectra in terms of the spectral-function modification. We also examine the relative yields of $\phi \to K^+K^-$ decays and $\phi \to e^+e^-$ decays for carbon and copper targets, in order to find a modification on the partial decay widths. Finally, we set upper limits on those decay widths in nuclear media with use of a simple theoretical model.

The e^+e^- data presented in this manuscript was taken from the run in 2001 and 2002, and the K^+K^- data was from the run in 2001. In Chap. 2, the experimental procedure is presented. The detail of the analysis is described in Chap. 3. The invariant mass spectra of ϕ meson both in the e^+e^- and K^+K^- decay channels and the nuclear mass-number dependence of the ϕ-meson production cross section are presented and discussed in Chap. 4. Finally, the conclusion is given in Chap. 5.

Chapter 2

Experimental procedure

2.1 Overview of Apparatus

The spectrometer for studying vector mesons produced in nuclei was constructed at the primary beam-line EP1-B in 12 GeV Proton Synchrotron (PS) at KEK. The beam line EP1-B was newly constructed for experiments requiring a high-intensity primary beam [41]. The spectrometer was designed to measure the invariant mass spectra both in the e^+e^- channel for the $\rho/\omega/\phi$ meson decays and in the K^+K^- channel for the ϕ meson decays within the same apparatus.

There are two key points in this spectrometer. First is to optimize the acceptance for slowly moving vector mesons, which have a larger probability to decay inside a nucleus. The typical acceptance for $\phi \to e^+e^-$ is $0 < p_T < 1$ GeV/c and $0.5 < y < 2.0$ where the beam rapidity is $y_{\rm beam} = 3.3$ ($y_{\rm c.m.} = 1.66$). This coverage corresponds to $0.5 < \beta\gamma_\phi < 4$. Second is to use high quality primary beam on thin targets. The combination of the high intensity beam with thin targets was essential to keep the γ-conversion rate in the target material below the Dalitz decay rate. The typical interaction rate was as high as 1.2 MHz in the year 2002. Detailed descriptions of the E325 spectrometer can be found in [42]. The detector elements relevant to this manuscript are discussed below.

The layout of the detectors is shown in Fig. 2.1 and 2.2 [1], and photographs of the spectrometer are shown in Fig. 2.3. The spectrometer had two electron arms and two kaon arms, which shared the dipole magnet and the tracking devices. The electron arms covered from $\pm$12 degrees to $\pm$90 degrees horizontally and $\pm$22 degrees vertically. The kaon arms covered from $\pm$12 degrees to $\pm$54 degrees horizontally and $\pm$6 degrees vertically.

In this manuscript, results of the analysis with the e^+e^--triggered data collected in 2001 and 2002, and the K^+K^--triggered data collected in 2001 are presented. Primary protons with a typical intensity of 8.7×10^8 protons per spill in 2001 and 6.4×10^8 protons in 2002 were delivered to the targets at the center of the dipole magnet. In 2001, one carbon and two copper targets were used simultaneously, while in 2002 one carbon and four copper targets were used simultaneously. The interaction length of each copper target was 0.054% and that of the carbon target was 0.11% in 2001 and 0.21% in 2002.

Tracking was performed with the cylindrical drift chamber (CDC) and the barrel-shaped drift chambers (BDC's). The vertex drift chamber (VTC) was installed at the center of CDC to improve the vertex reconstruction resolution. However, we do not use the VTC information in the present analysis because the mass acceptances of VTC are significantly different between the five targets. The dipole magnet which had circular pole pieces of 880 mm in radius, provided the field integral of 0.81 T·m from the center to 1680 mm in radius where the BDC's were located.

[1] In this manuscript, we adopt the right-handed coordinate system of which the origin is at the center of the spectrometer magnet, the x-axis is parallel to the beam direction, and the z-axis is vertical pointing upward.

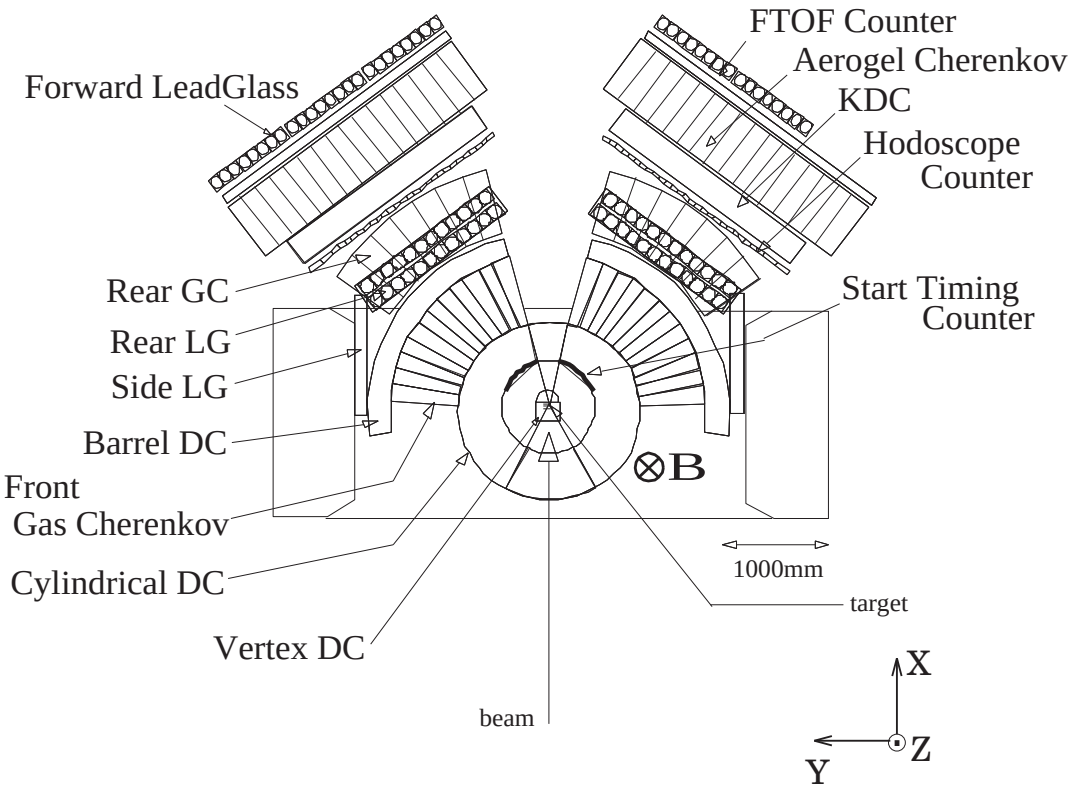

Figure 2.1: Schematic view of the E325 spectrometer, the top view.

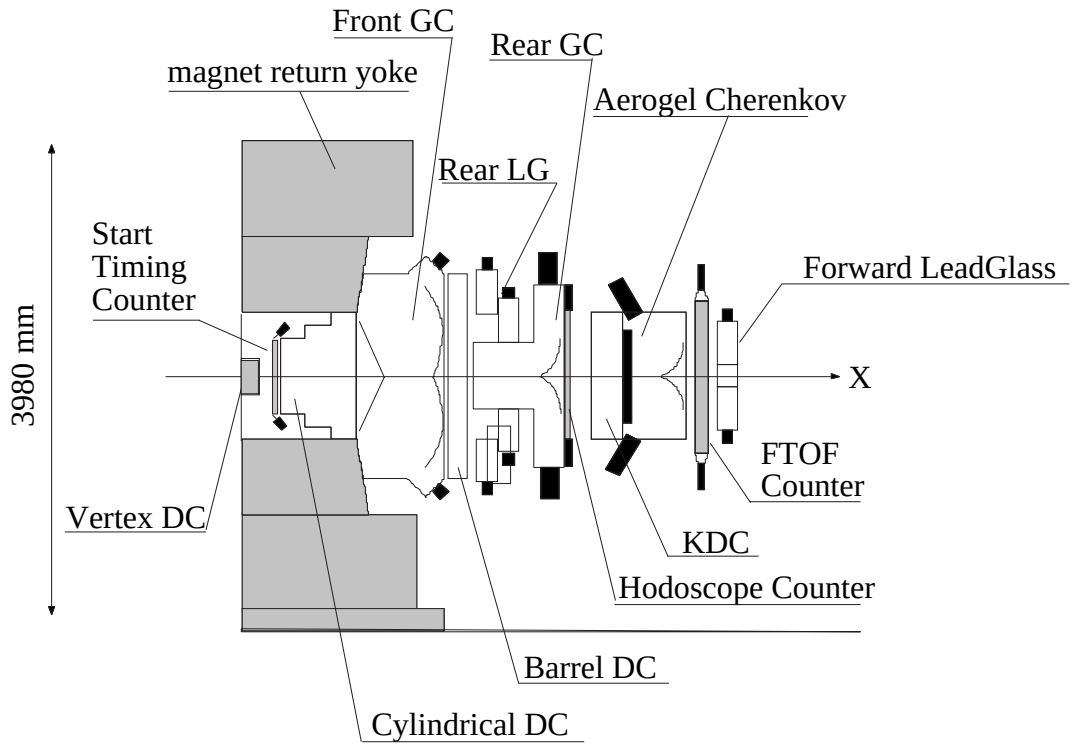

Figure 2.2: Schematic view of the E325 spectrometer, the cross section along the center of the kaon arm, 33 degrees from the beam line, is shown.

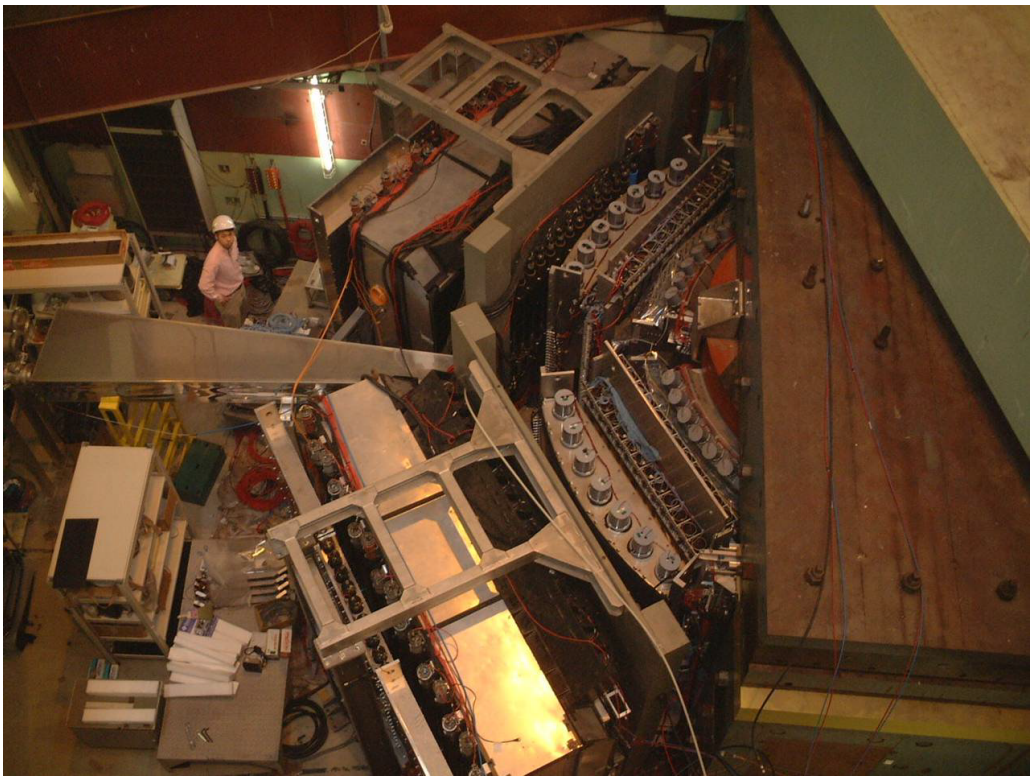

(a) the top view

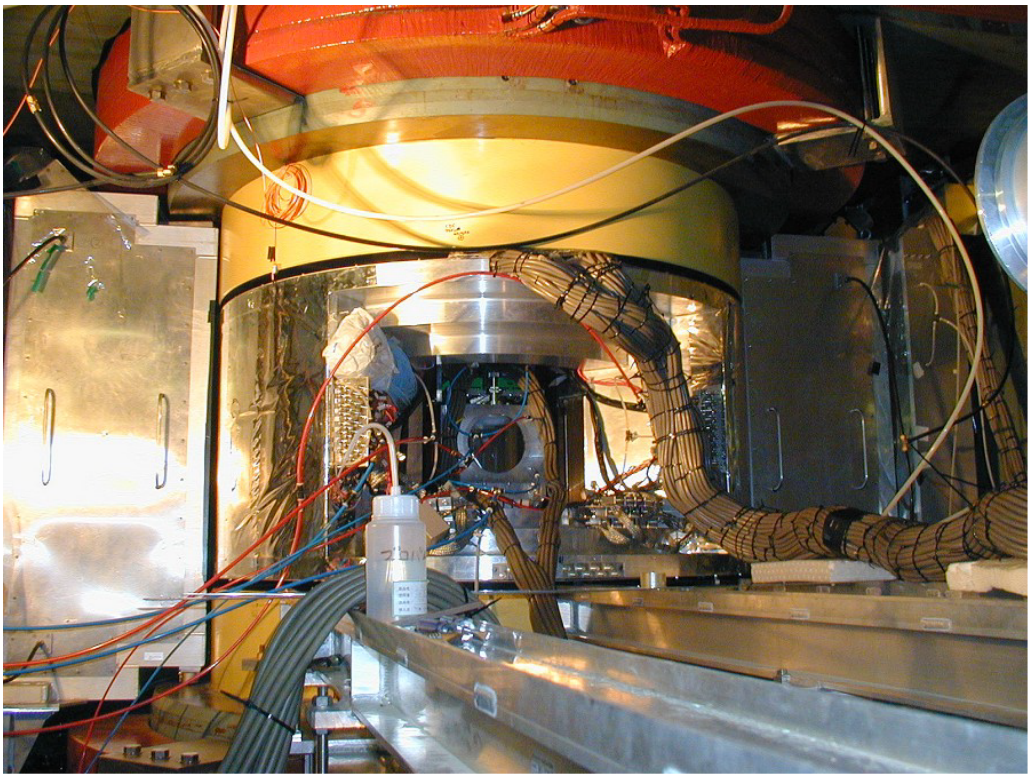

(b) the front view

Figure 2.3: Photographs of the E325 spectrometer for (a) the top view and (b) the front view.

For the electron identification the whole region of the electron arm was covered by two or three stages of electron identification counters. The first stage of the electron identification was done by the front gas-Čerenkov counters (FGC's) which covered from ±12 degrees to ±90 degrees horizontally and ±23 degrees vertically. The second stage consisted of three types of electron-identification counters. The rear gas-Čerenkov counters (RGC's) covered from ±12 degrees to ±54 degrees horizontally and ±6 degrees vertically. These regions corresponded to the kaon-arm acceptance. The rear lead-glass EM calorimeters (RLG's) covered the same horizontal angle as RGC's, but vertically covered outside the kaon-arm acceptance, from ±9 degrees to ±23 degrees. In the backward region where the horizontal angle was larger than 57 degrees, the second-stage electron identification was done by the side lead-glass EM calorimeters (SLG's) which covered from ±57 degrees to ±90 degrees horizontally and ±23 degrees vertically. As the third-stage electron identification counter in the kaon-arm acceptance, the forward lead-glass EM calorimeters (FLG's) vertically covered ± 7 degrees, and horizontally from 12 to 54 degrees in the left arm, from –40 to –12 degrees in the right arm.

For the kaon identification, the segmented aerogel Čerenkov counters and time of flight counters were used. The aerogel Čerenkov counters (AC's) were threshold-type Čerenkov detectors using aerogel whose refractive index was 1.034, to separate kaons from pions in the momentum region of 0.53 to 1.88 GeV/c [43, 44]. Since we could not count beam protons particle by particle due to the high intensity, the event time-zero was given by the start timing counters (STC's) placed at 380 mm from the targets. The forward time of flight counters (FTOF's) were used to measure the time of flight of particles in the kaon acceptance. They were also used in combination with the hodoscope counters (HC's) to determine the charge and the crude momentum of the particles, and to make the kaon selection possible with the β (=v/c) measurements in the trigger.

In the following section, details of the experimental components are described.

2.2 Accelerator Facility and Beam Line

The proton synchrotron facility at KEK consists of four stages of accelerators, the 750 kV Cockroft-Walton, the 40 MeV LINAC, the 500 MeV Booster Synchrotron and the 12 GeV Proton Synchrotron (PS).

The typical beam intensity was 3×10^{12} in PS. During our experiment these protons were delivered to two primary beam lines simultaneously, about 1% to the EP1 beam line and 99% to EP2. The beam in EP1 can be switched either to EP1-A or to EP1-B. The beam line EP1-A is used for experiment using low energy kaons in the slow extraction mode and for the neutrino oscillation experiment in the fast extraction mode. The present experiment is performed at EP1-B which is a special beam line for primary proton usage. The schematic view of the beam line EP1-B is shown in Fig. 2.4.

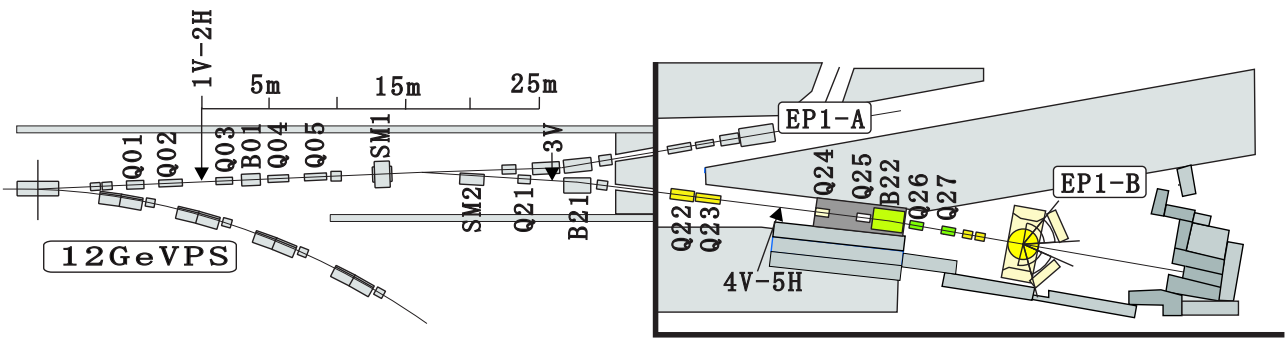

Figure 2.4: Schematic view of Beam Line (EP1B).

When EP1-B is in operation, protons extracted to the EP1 beam line were focused with a set of quadrupole magnets, Q01 and Q02 to the first vertical collimator 1V where the intensity was typically reduced to one-fifteenth. Here the initial image of the beam was defined by 1V together with the horizontal collimator 2H. At this point, the beam spot from PS is vertically long so that the beam intensity was controlled by changing the aperture of the collimator 1V. Typical aperture of the collimators 1V and 2H were set as 8.0 mm and 2.2 mm respectively. Then the beam was bent by six degrees with the steering magnets SM1 and SM2, and was vertically focused with a set of quadrupole magnets (Q03, Q04, Q05, Q21) to the point where the vertical collimator 3V was placed. The vertical collimator 3V was used to remove beam halo. Then the beam was transferred by the 'DQQ' (B21, Q22, Q23) complex to the first focusing point where the collimators 4V and 5H were located and again the rejection of beam halo was performed. After passing through the other beam-focusing complex 'QQDQQ' (Q24, Q25, B22, Q26, Q27), the beam was delivered to the final focusing point at the center of the spectrometer. At the target, we obtained the size of the beam spot of 1∼2 mm in FWHM. At the end of the EP1-B beam line, the intensity of beam protons was monitored with 10% accuracy using an ionization chamber [45]. The repetition period was four seconds, and the flat top of the spill was about 1.8 seconds.

In prior to the experimental data accumulation, the aperture of the collimators were tuned to reduce the beam halo. It was turned out that the adjustment of the collimators was effective to reduce the random trigger rate, so that the adjustment was done to minimize the interaction trigger rate of the spectrometer with keeping the transmission of beam particles constant. The scanning of the magnetic field strengths of B21 and B22 was also effective to reduce the beam halo, by controlling the beam trajectory and minimize the interference of the beam halo with the beam pipe. We chose the setting where the least trigger rate was realized. The collimator settings in the present data-taking period are listed in Table 2.1. The collimator 4V (and 3V in 2002) was full opened, because these were not effective to reduce the halo.

year	1V	2H	3V	4V	5H
2001	8.0mm	4.0mm	50mm	*full*	15.0mm
2002		2.7mm	*full*		

Table 2.1: The collimator width setting.

2.3 Spectrometer Magnet

The spectrometer magnet was a dipole type with the overall weight of 300 ton. The dimension was 5655 mm in width, 3980 mm in height and 2120 mm in depth. To ensure the maximum vertical acceptance for electrons (±23 degrees), the pole piece was made of two layers of cylinder with the diameters of 1760 mm and 2120 mm as shown in Fig. 2.5. The gap between the poles was 907 mm. Other dimensions can be seen in Fig. 2.5.

The magnetic field at the center of the pole piece was adjusted at 0.71 T to supply the integrated magnetic-field $\int \boldsymbol{B} \cdot d\boldsymbol{l}$ of 0.81 T·m from the targets to the radius of 1680 mm where the barrel drift chambers (BDC's) were located. The materials through the flight path of particles from the target to BDC are summarized in Table 2.2. As described later in Sec. 3.5, by taking into account Coulomb scattering and energy losses in the materials and the chamber resolutions, we estimated the mass resolution for $\phi \to e^+e^-(\phi \to K^+K^-)$ decays to be 10.7(2.3) MeV/c^2 using a detailed detector simulation.

Since the amplitude of the $\int \boldsymbol{B} \cdot d\boldsymbol{l}$ is proportional to the rigidity of tracks, it is important to know the precise magnetic field-strength everywhere in the acceptance. The magnetic field

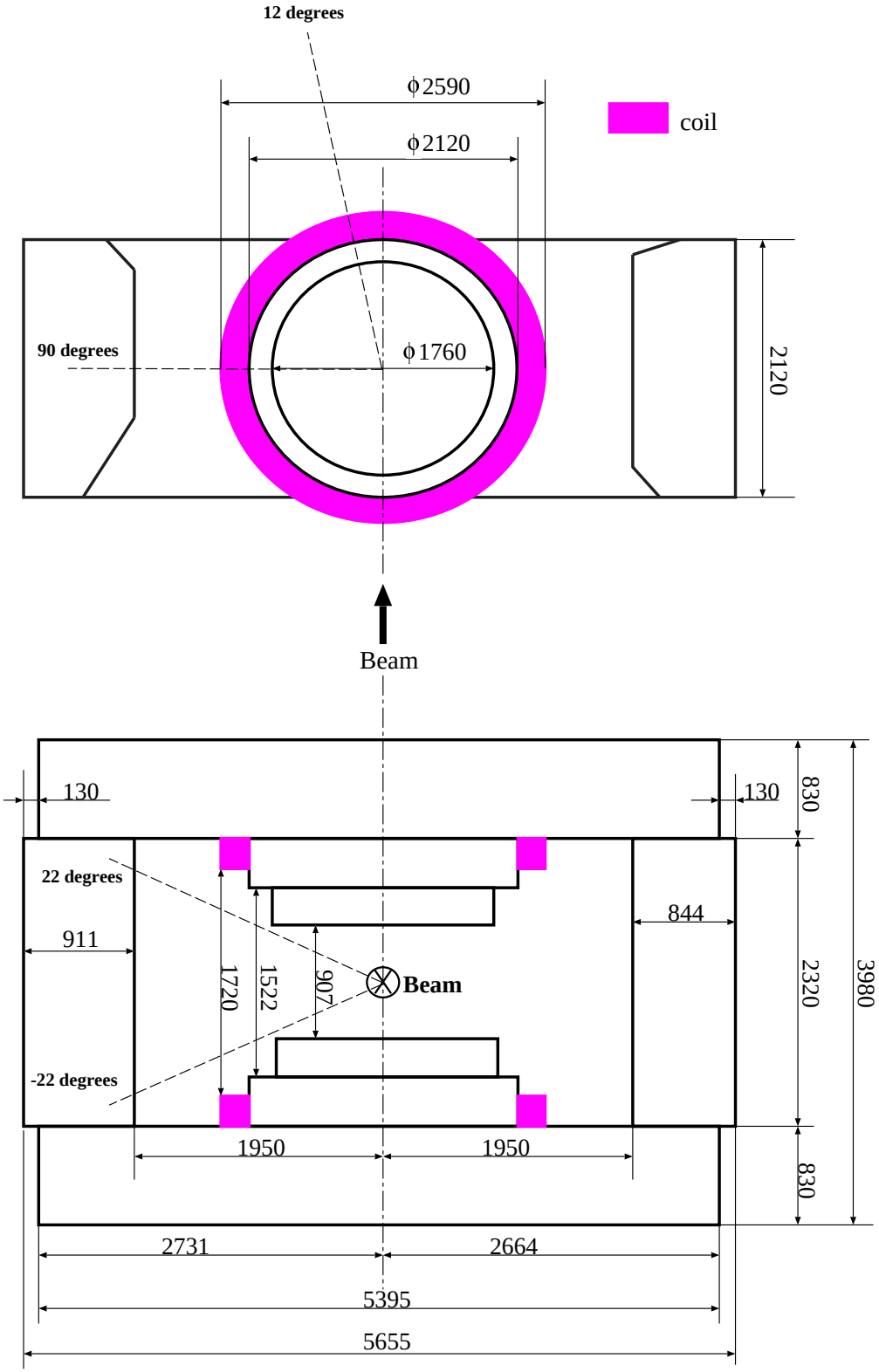

Figure 2.5: Schematic view of spectrometer magnet. The dashed lines indicate the electron acceptance.

Counter	material	radius [mm]	thickness X [mm]	λ_{rad} [mm]	X/λ_{rad} [%]
VTC	Ar-C_2H_6(50:50)	0.00	245.00	340350.0	0.072
	Wire(Cu-Be)	-	0.0173	14.3	0.121
	Wire(W)	-	0.0004	3.5	0.011
	Mylar	245.00	0.05	287.0	0.017
	air	245.05	134.95	304200.0	0.044
STC	scintillator	380.00	5.00	425.0	1.176
	lapping	385.00	0.20	287.0	0.070
	air	385.20	14.80	304200.0	0.005
CDC	Mylar	400.00	0.05	287.0	0.017
	Ar-C_2H_6(50:50)	400.05	479.95	340350.0	0.141
	Wire (Cu-Be)	-	0.031	14.3	0.217
	Wire (W)	-	0.0005	3.5	0.014
	Mylar	880.00	0.05	287.0	0.017
	air	880.05	19.90	304200.0	0.007
FGC	Mylar	899.95	0.05	287.0	0.017
	isobutane	900.00	660.00	169300.0	0.390
	acrylic mirror	1560.00	3.00	344.0	0.872
	aluminum cover	1563.00	1.00	89.0	1.124
	air	1564.00	5.95	304200.0	0.002
BDC	Mylar	1569.95	0.05	287.0	0.017
	Ar-C_2H_6(50:50)	1570.00	110.00	340350.0	0.032
	Wire (Cu-Be)	-	0.010	14.3	0.070
	Wire (W)	-	0.0001	3.5	0.003
SUM					4.458

Table 2.2: List of the materials and their radiation lengths from the center of CDC to the radius of 1680 mm where BDC's were located.

map were obtained by the calculation and compared to the hall-probe measurements. The magnet itself is symmetrically build from left to right and upstream to downstream, and top to down. The actual field, however, was distorted due to other magnetic materials which were the iron plate on the floor to support the magnet weight and the magnetic shield placed just front of the photomultiplier tubes of the aerogel Čerenkov counter. We calculated the magnetic field map using TOSCA [46], which performs finite-element-method analysis. All the magnetic materials were taken into account in the calculation. Since the preliminary calculations and the measurements proved the left-right symmetry of the field, we performed a full calculation assuming the left-right symmetry to reduce the calculation time. The strength of magnetic field on the x-y plane (the horizontal plane 400 mm below the beam line) is shown in Fig. 2.6.

We measured the magnetic field (B_x, B_y, B_z) with a set of hall probes which were placed orthogonal to each other. The measured region was limited within the reach of the measurement device. We covered the region shown in Fig. 2.7 with 3-dimensional lattice points of 50 mm pitch. The three components of the magnetic field on the horizontal plane 363 mm below the nominal beam height is shown in Fig. 2.8.

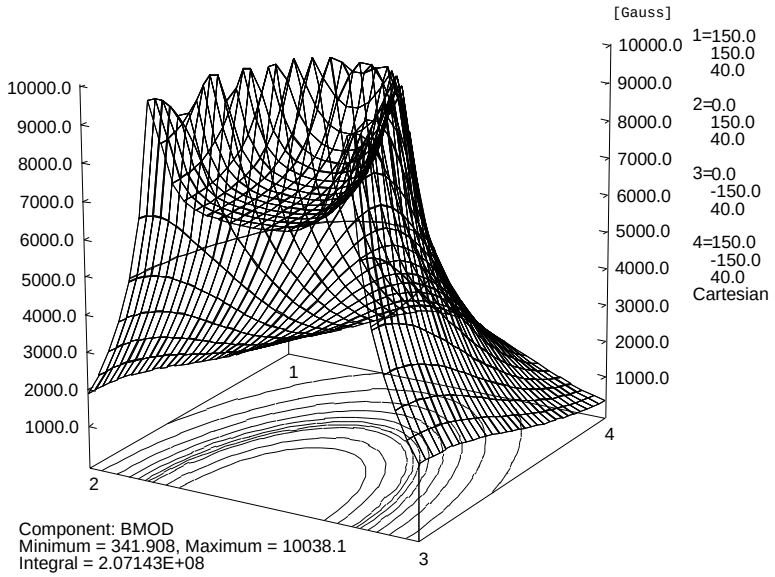

Figure 2.6: The calculated magnetic field map (z = -400 mm).

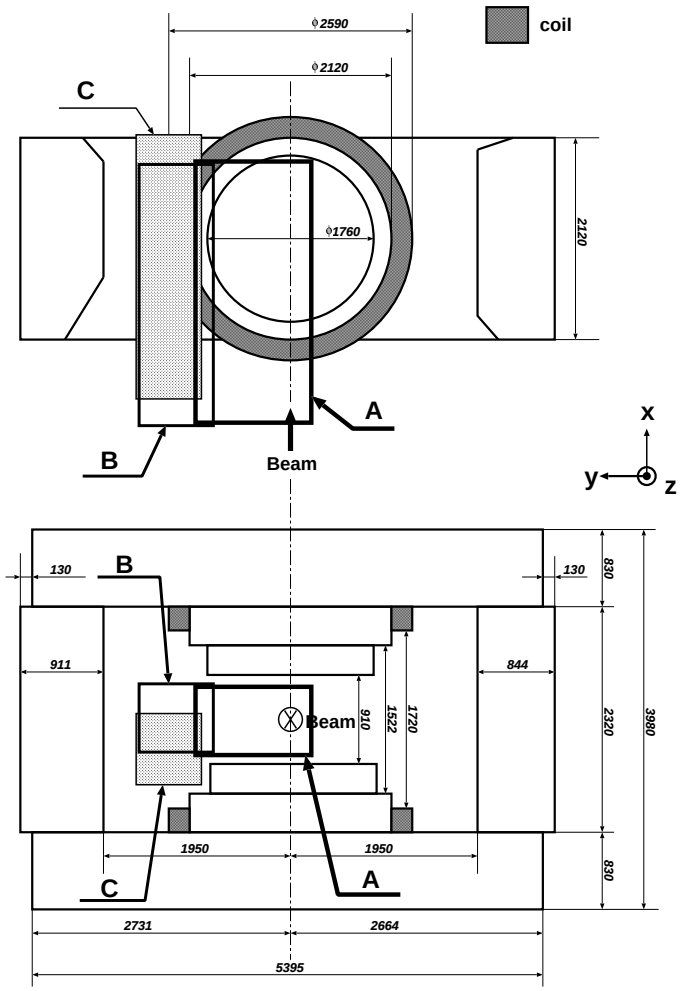

Figure 2.7: The region of the magnetic field measurements. The three areas, A, B, and C are with different settings of the measuring device.

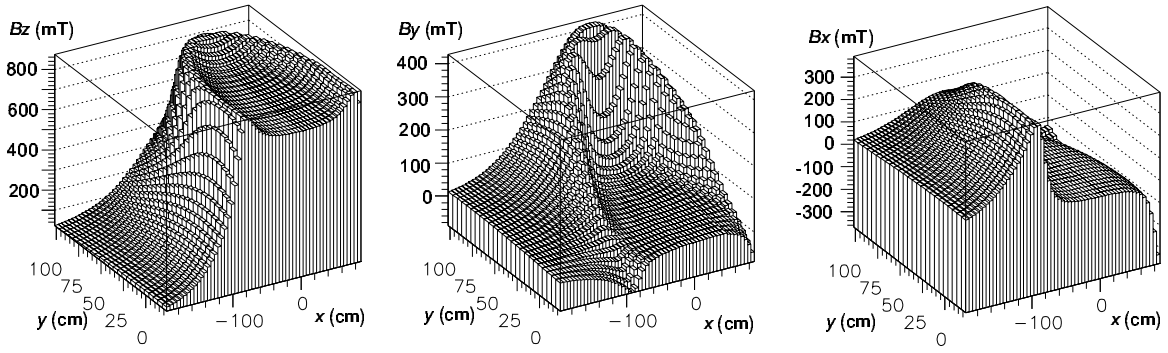

Figure 2.8: The measured magnetic field map (z = -363 mm).

The measured map was compared to the calculated one, and we observed a good agreement on $\int \boldsymbol{B} \cdot d\boldsymbol{l}$. However the magnitude in average was 0.2% larger than the TOSCA calculation; it probably comes from the incomplete knowledges for the magnetic permeability of the iron of the spectrometer around 0.71T, which was an input parameter of TOSCA. We increased the field strength of the calculated map by 0.2% and used it for the track fitting.

We evaluated the systematic uncertainty of the momentum determination caused from the inaccuracy of the magnetic field map as follows. We generated the drift chamber hits points for the charged particle trajectories which were generated with the measurement map, and we fitted them using the Runge-Kutta method with the calculated map. By comparing the original momenta with the fitted results, we found that the discrepancy was within 0.3% in the momentum region from 0.5 to 2.0 GeV/c, as shown in Fig. 2.9. The systematics is small enough compared with the present momentum resolution. Since the measured region was limited, the calculated magnetic field was used to find a track of particles.

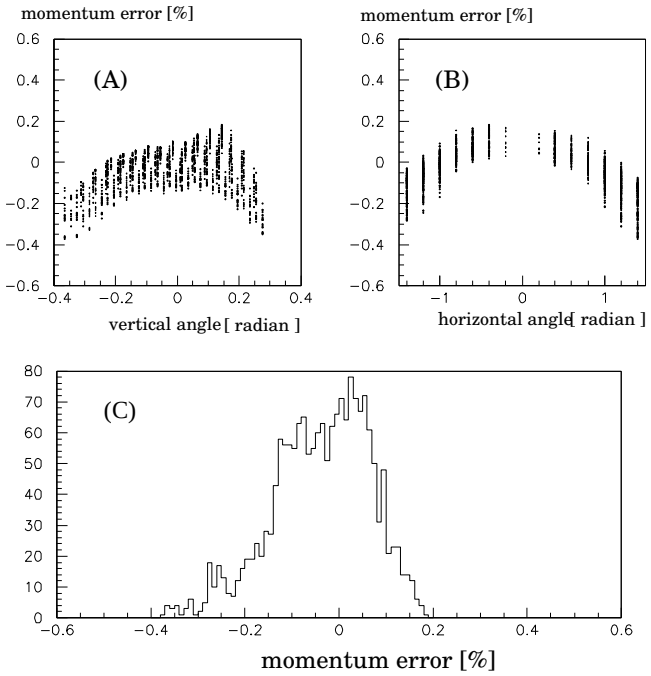

Figure 2.9: Possible uncertainty of the momentum determination due to the magnetic field map. Test tracks were generated with the measured map and reconstructed with the calculated map. The differences of the reconstructed momenta from the generated momenta were plotted as a function of the vertical angle in (A), and the horizontal angle in (B). The histogram (C) gives the projection of all the differences.

In 2001, we had a trouble in isolation in the coils of the dipole magnet. We had 14 independent coils for the magnet, seven coils for each pole piece. Because of the trouble, we had to give up the three coils for the upper pole piece. To keep the field integral as before, we had to operate the magnet with 14/11 times larger current than before. Since the available 11 coils are four in the upper side and seven in the lower side, the magnetic field became asymmetric from top to down. Under this condition, the magnetic field map was calculated again with TOSCA. The systematic uncertainty was estimated through the measurement of the magnetic field with a NMR probe for several sample heights at the center of the magnet. The measured values are listed in Table 2.3. The absolute values of the calculated magnetic field were 0.48±0.03% larger than the measured values, as shown in Fig. 2.10. We scaled the absolute value of the calculated magnetic field to the measured value. A systematic error on the momentum determination due to this discrepancy is then expected to be within 0.03% and is negligible.

z[mm]	measured[mT]	calculated[mT]
446.5	698.367	701.910
225.5	699.225	702.792
1.5	706.540	710.069
-222.5	721.317	724.732
-446.5	730.180	733.540

Table 2.3: The measured and calculated magnetic fields for five values of z. The voltage was set to 1985.45A.

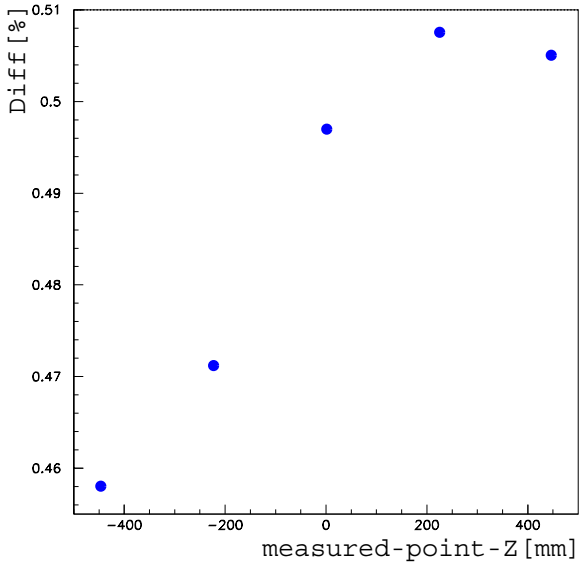

Figure 2.10: Differences between the measured magnetic field strength and the calculation with TOSCA. Definition of the vertical axis is the ratio of the differences to the measured values. The horizontal axis is the z position of the measured points.

The magnetic field strength was monitored with a MNR probe placed at the center of the bottom pole peace, at the beginning and the end of each run of about 2 hour long, and the averaged value for each run was used for a run-by-run correction for the scale of the field map strength. An actual drift was as small as 0.07%, as shown in Fig. 2.11.

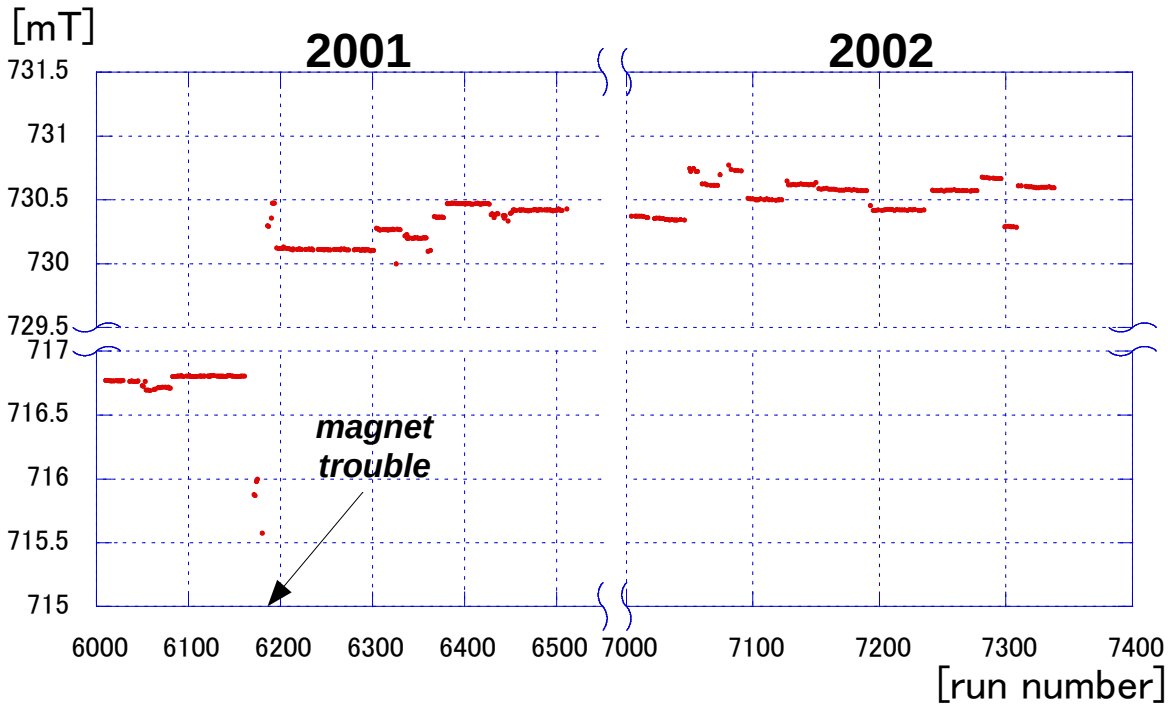

Figure 2.11: The magnetic field strength for each run measured with a NMR probe. The jumps were caused by switching on and off the power supply.

2.4 Targets and Beam Profile

2.4.1 Targets

We used two copper targets and one carbon target in 2001, and four copper targets and one carbon target in 2002, which were aligned in-line along the beam axis. We call them Cu-1, C, and Cu-2 in 2001, and Cu-1, Cu-2, C, Cu-4, and Cu-5 in 2002, from upstream to downstream target. The interaction length and radiation length of the targets are summarized in Table 2.4.

year	material		mass number	number of targets	width [mm]	hight [mm]	thickness [g/cm^2]	interaction length [%]	radiation length [%]
2001	carbon	C	12.011	1	25	25	0.092	0.106	0.215
	copper	Cu	63.546	2	25	25	0.073	0.054	0.564
2002	carbon	C	12.011	1	10	25	0.184	0.213	0.431
	copper	Cu	63.546	4	10	25	0.073	0.054	0.565

Table 2.4: The target dimensions, interaction lengths, and radiation lengths used in the experiment.

These targets were placed at the center of CDC by 46 mm apart from each other in 2001, and 23 mm in 2002. The schematic view of the target holder in 2002 is shown in Fig. 2.12. The targets were attached on the polyethylene stays with a thickness of 1 mm. In 2001, the target x-positions with respect to the center of CDC were –47 mm, 0 mm and 45 mm for the Cu-1, C and Cu-2 targets, respectively. In 2002, those were –43 mm, –23 mm, 0 mm, 24 mm and 48 mm for the Cu-1, Cu-2, C, Cu-4 and Cu-5 targets, respectively. The width of each target was determined that no target was in the acceptance of any other targets.

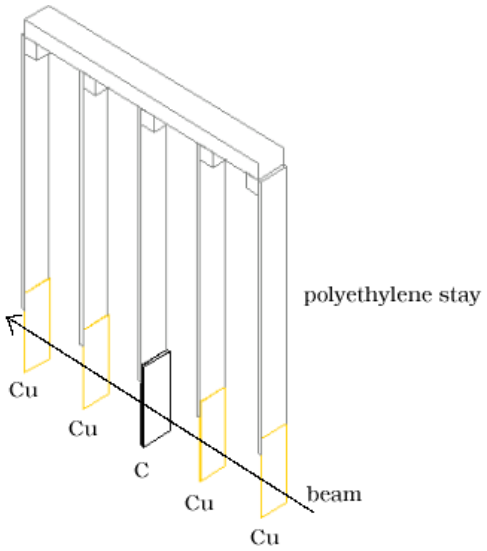

Figure 2.12: Schematic view of Target in 2002.

To reduce the interaction of beam protons with air, the entire beam line was kept as vacuum from the extraction point to a front of VTC. The region of vacuum was terminated with a 200-μm-thick Mylar sheet at the front of VTC. Behind the exit of VTC, the beam line was followed by a helium-filled beam pipe, as shown as "He Bag" in Fig. 2.13. A helium gas was flowed at

a rate of 1000 cc per minute. The ion chambers (IC's) were located at the end of the He Bag to measure the beam intensity. Between the IC and the beam dump, a vacuum beam pipe of 2.5 m long was placed.

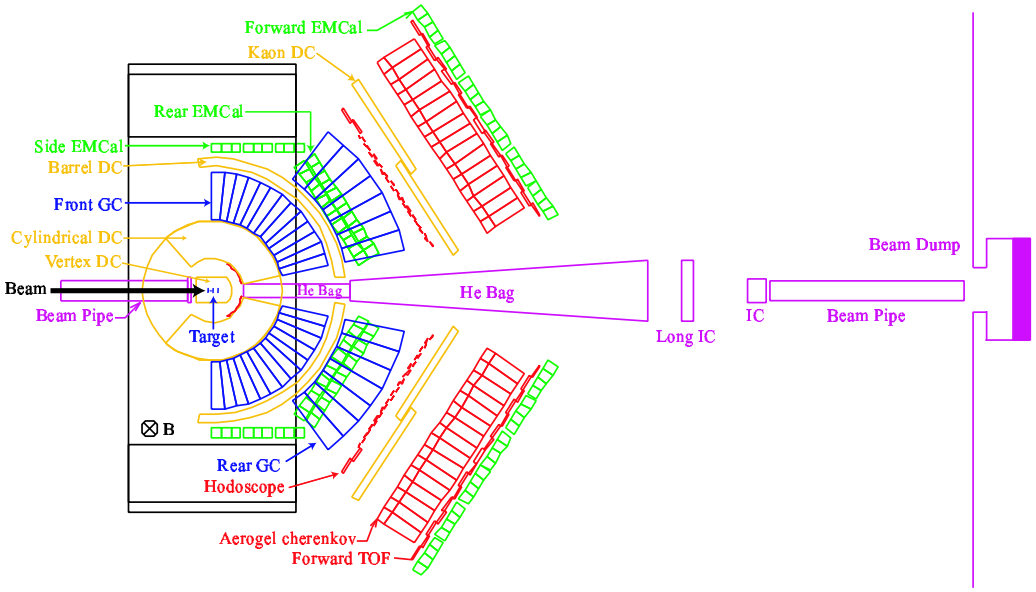

Figure 2.13: Schematic view of Target and Beam Pipe.

2.4.2 Beam Profile

Figure 2.14 shows the beam profile at the target position which was measured as follows. The center target, which was carbon of 0.5(1) mm thick in 2001(2002), worked as the 0.5(1) mm-wide probe for the beam profile measurement when the target holder was rotated by 90 degrees around the z axis.

The horizontal beam position was moved with the bending magnet B22 located most downstream of EP1-B beam line (see Fig. 2.4). The beam profile in the horizontal direction can be measured by counting the interaction rate by changing the beam position. The interaction rate as a function of the beam position is plotted in Fig. 2.14. Here, the beam position y [mm] is obtained as

$$y = 0.109 \times (V - V_0)\,, \tag{2.1}$$

where V [V] is the reference voltage of the B22 power supply, and V_0 is the nominal value to shoot the target center. The one standard deviation of the beam spot size in the horizontal direction was estimated to be 1.59 mm in 2001 and 0.83 mm in 2002 by subtracting the effective thickness of the carbon target.

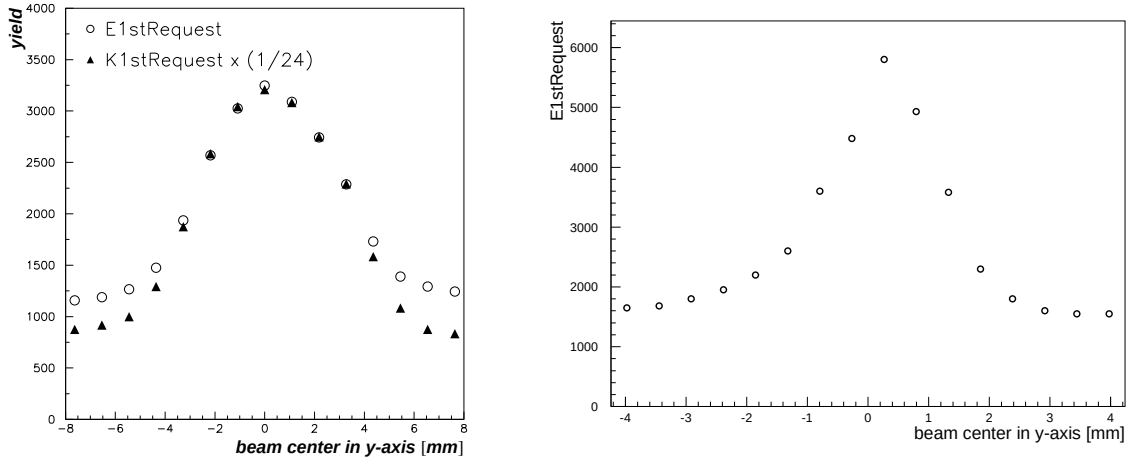

(a) 2001 (b) 2002

Figure 2.14: Interaction rate as a function of the beam position.

2.5 Tracking Chambers

2.5.1 Cylindrical Drift Chamber

The schematic view of Cylindrical Drift Chamber (CDC) is shown in Fig. 2.15. The outer diameter of CDC is 1760 mm, the inner diameter is 800 mm and the height is 840 mm. We located CDC on the pole piece of the spectrometer magnet. The acceptance of CDC was from ± 12 degrees to ± 132 degrees horizontally and ± 22 degrees vertically.

The CDC consists of ten radial layers of the drift cells, and they were grouped into three super-layers. The first super-layer was in the radial region from 445.0 to 475.0 mm having three layers of drift cells (X, X′, U), the next was from 602.5 to 642.5 mm having four layers (V, V′, X, X′), and the last was from 800.0 to 830.0 mm having three layers (U, X, X′). In the X and X′ layers the direction of wires was vertical and in the U and V layers the wires were tilted by about $\pm$ 0.1 radian. Argon-ethane mixed gas of 50% and 50% was used at 1 atm.

The structures of the drift cells are shown in Fig. 2.16. The sense wires were gold-plated tungsten of 30 μmϕ and the potential wires were Be-Cu of 100 μmϕ. The position of the wire was determined by the bush inserted at the end of the feed through pipes. We used the bush with an 80 μmϕ hole for the sense wires, so that the precision of the wire positioning was about 25 μm. All the drift cells of CDC had the same horizontal angular coverage of 1.5 degrees with respect to the center. Details of the wire arrangements were shown in Table 2.5.

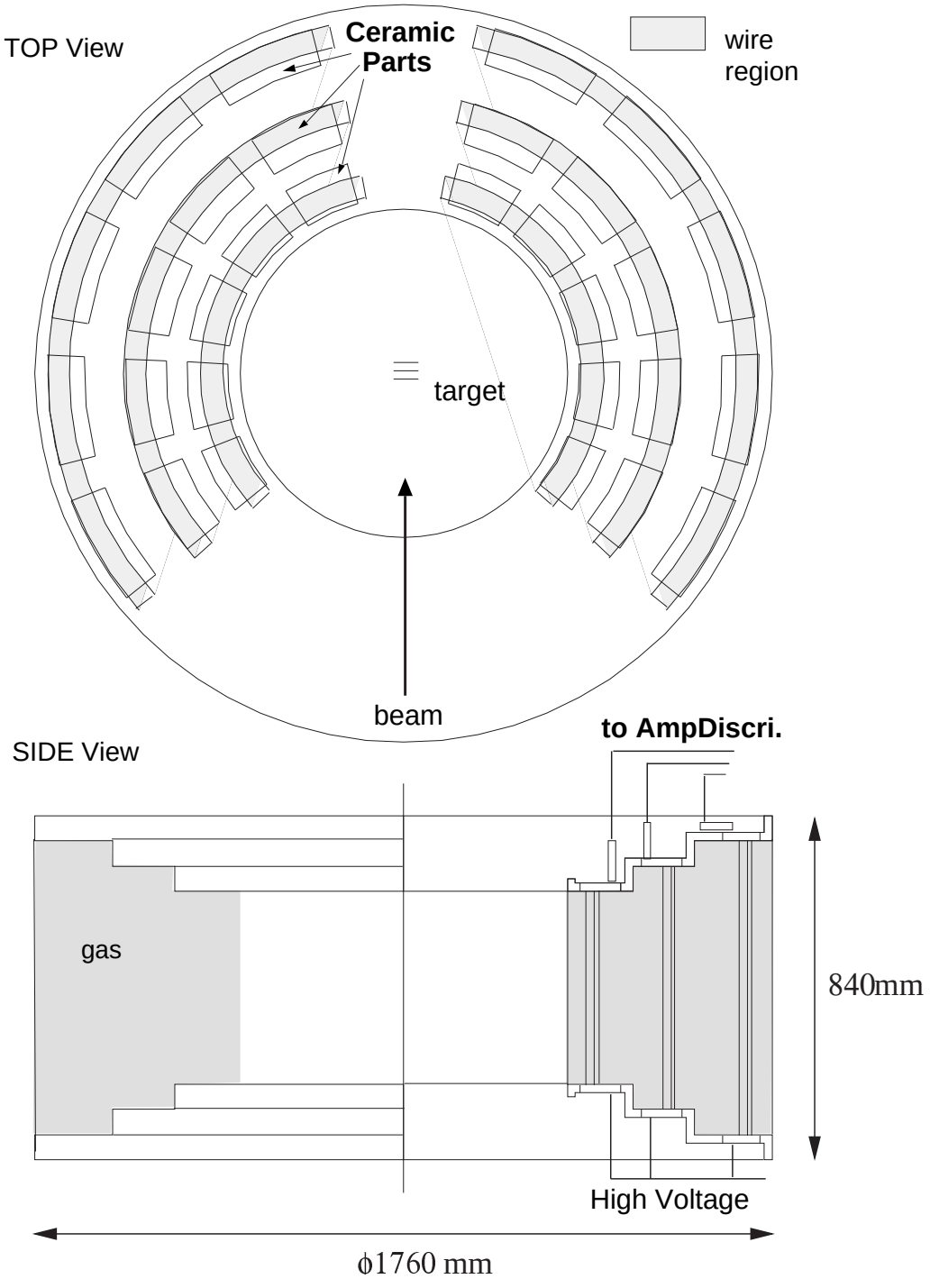

Figure 2.15: Schematic view of CDC.

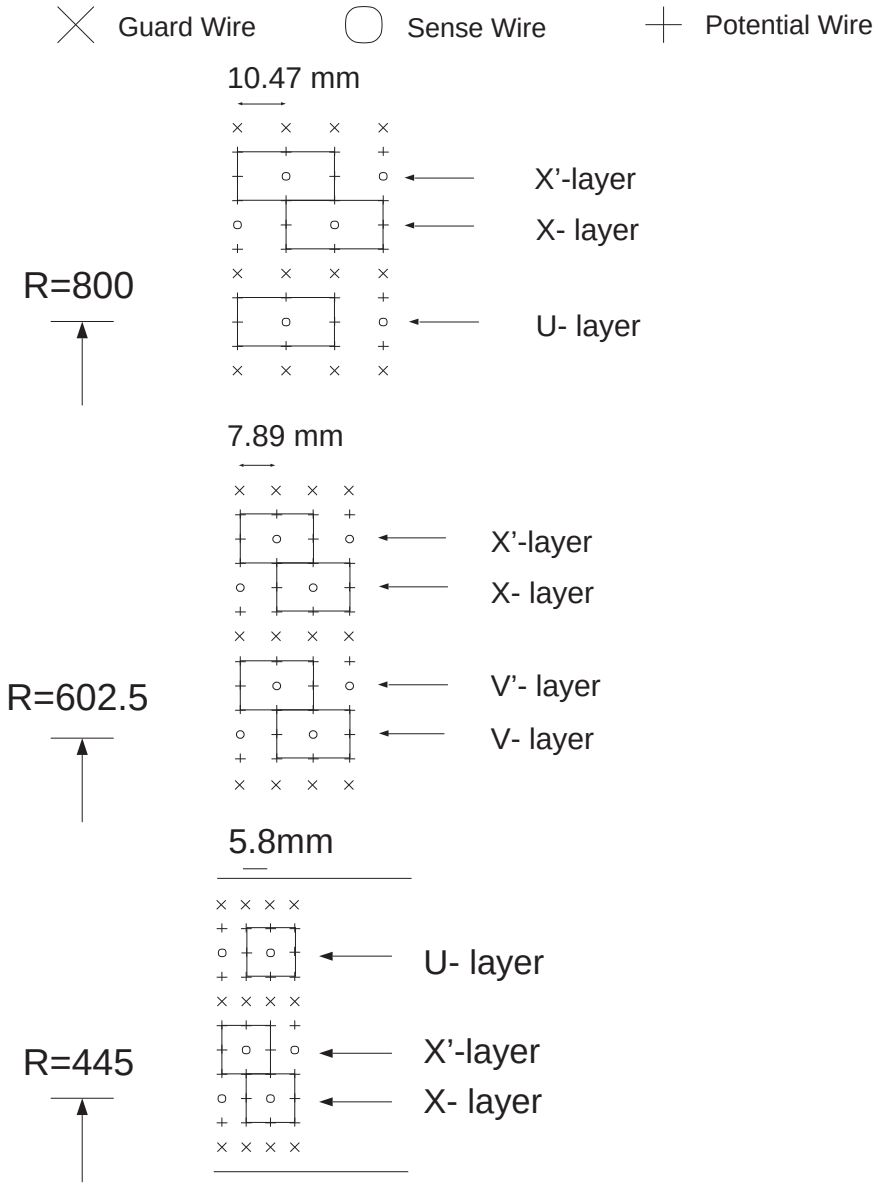

Figure 2.16: The cell structures of CDC.

layer number	1	2	3	4	5	6	7	8	9	10
wire direction	X	X′	U	V	V′	X	X′	U	X	X′
radial location of sense wire [mm]	445	455	475	602.5	612.5	632.5	642.5	800	820	830
cell width [degree]	1.5	1.5	1.5	1.5	1.5	1.5	1.5	1.5	1.5	1.5
cell width [mm]	11.65	11.91	12.43	15.77	16.04	16.55	16.82	20.94	21.47	21.73
tilt angle [radian]	0	0	0.1127	0.1116	0.1135	0	0	0.1174	0	0
wire length [mm]	441	441	443.8	568.5	568.7	565	565	717.9	713	713
number of sense wires	81	81	77	76/77 (*)	77/76 (*)	81	81	77	82	82

(*) left-arm and right-arm

Table 2.5: CDC wire configuration.

We calculated the electrical field shape in the chamber cell and the relation between the drift length and the drift time with use of the drift chamber simulation code Garfield [47]. The simulated drift line in the outer super-layer is shown in Fig. 2.17(a), and the relation between the drift length and the drift time (x-t relation) is shown in Fig. 2.17(b). The obtained x-t relation was used to determine hit positions after the adjusting the drift velocity and the time zero to the real data.

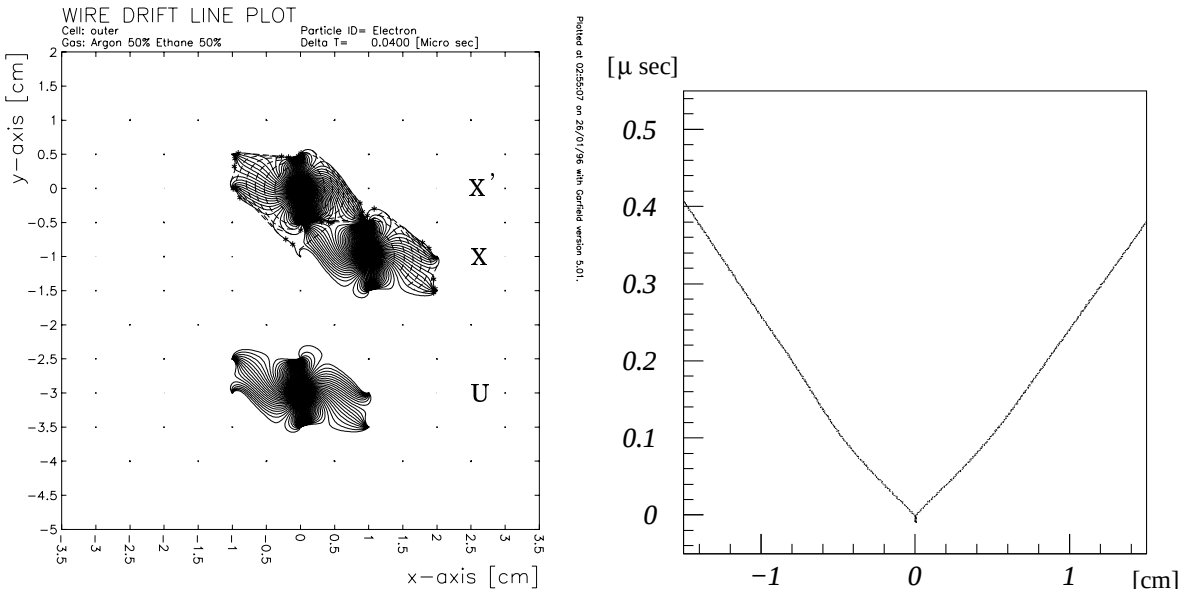

(a) simulated drift line (b) calculated x-t relation

Figure 2.17: (a)The simulated drift line in the outer super-layer (3 layers) in the magnetic field of 0.61T, which is the magnetic field strength at this location when the spectrometer magnet is fully excited. (b)The calculated relation between the drift time and the drift length of the X layer.

The structure of CDC was designed to restrict its active region only to the spectrometer acceptance. The top and bottom end plates were semi-curved with 3 stages as shown in Fig. 2.15. This structure was effective to gain the mechanical strength of the chamber frame and consequently to minimize the support structure within the spectrometer acceptance.

The end plates and the support structure of CDC were made of aluminum. Thirty ceramic plates were mounted on each aluminum end plate as shown in Fig. 2.15 and Fig. 2.18. The ceramic plates had a print-circuit pattern which provided electrical connections to the feedthrough pins as shown in Fig. 2.19(a). The feedthroughs were made of gold plated brass of a 1.6 mm diameter pipe. To secure the electrical connection, a cut-ring spring was inserted between the feedthrough and the through hole. The ceramic board on the top provided the signal connections to the sense wires and these on the bottom provided the high voltage connections. The ceramic boards were 100 mm in width, 200 mm in length and 20 mm in thickness and located precisely on the end plates by the knock pins with the machining precision of about 10 μm. In-between the ceramic boards, there were the ribs of the aluminum end plate, where the feedthroughs made of Delrin as shown in Fig. 2.19(b) were used.

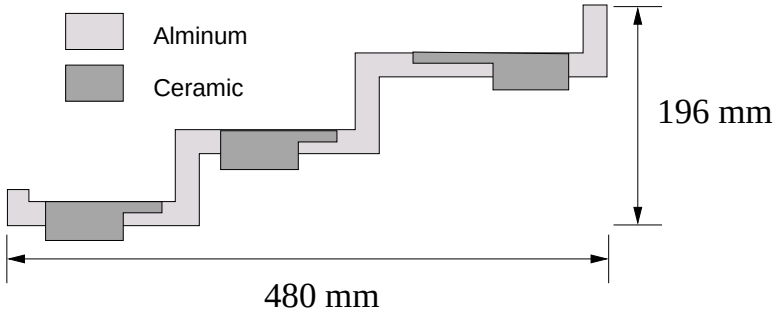

Figure 2.18: The cross section of the aluminum end plate and the ceramic plate.

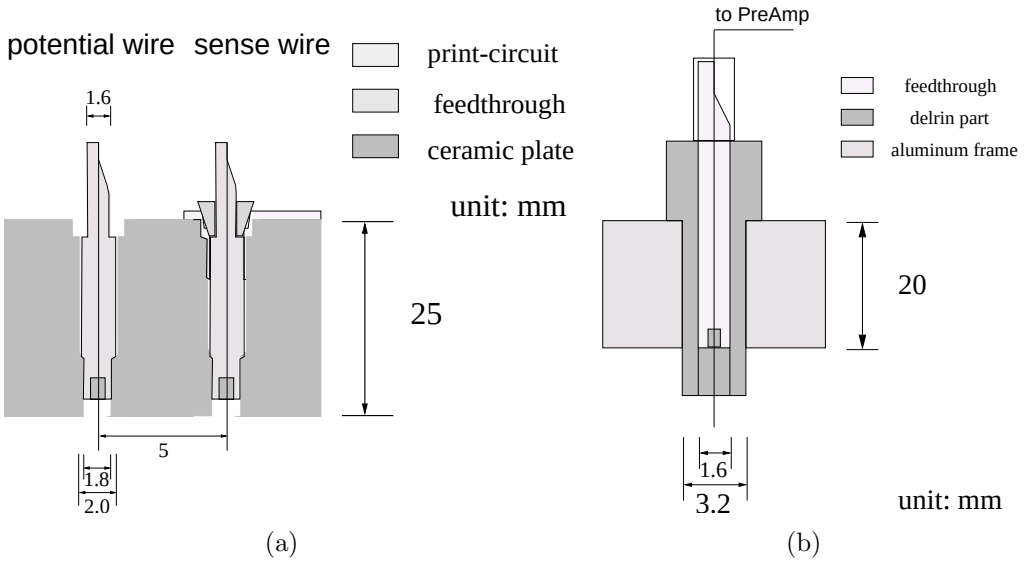

Figure 2.19: (a) Schematic view of the feedthrough structure for the ceramic plate of CDC. (b) Schematic view (not to the scale) of the feedthrough structure for the one on the aluminum ribs of CDC.

The read-out electronics of CDC consisted of Amplifier-Shaper-Discriminator (ASD) IC's on a print circuit board mounted on CDC (ASD board, Fig. 2.20(a)), a LVDS-ECL converter (Fig. 2.20(b)) and a time to digital converter (TDC). The ASD IC was developed for the Thin Gap Chambers in the forward muon trigger system of the LHC ATLAS experiment [48]. The block diagram of the ASD chip and the pin assignment of the ASD IC are shown in Fig. 2.21. The observed gain of the pre-amplifier of the ASD is 360 mV/pC, and the observed gain of the main-amplifier is 4, while the specification values are 800 mV/pC and 7 for the pre-amplifier and the main-amplifier, respectively. The output signal of the ASD board was sent to LVDS-ECL converter board via 10 m-long twisted-pair cables. From the LVDS-ECL converter, the signal was transferred to the counting house with 35 m-long twisted-pair cables.

When a minimum ionizing particle passed through one drift cell of CDC, it generated about a hundred ionizing electrons. The electric field around the wire amplified these electrons by 1.6×10^4. Through the ASD, the pulse height of the signals before the discriminator was typically 240 mV for minimum ionizing particles (observed value). The threshold voltage of the discriminator was set at from 5 to 18 mV [2].

[2]The threshold voltage is magnified by 20 times compared to the pulse height before the discriminator. The actual set up values were from 100 to 350 mV.

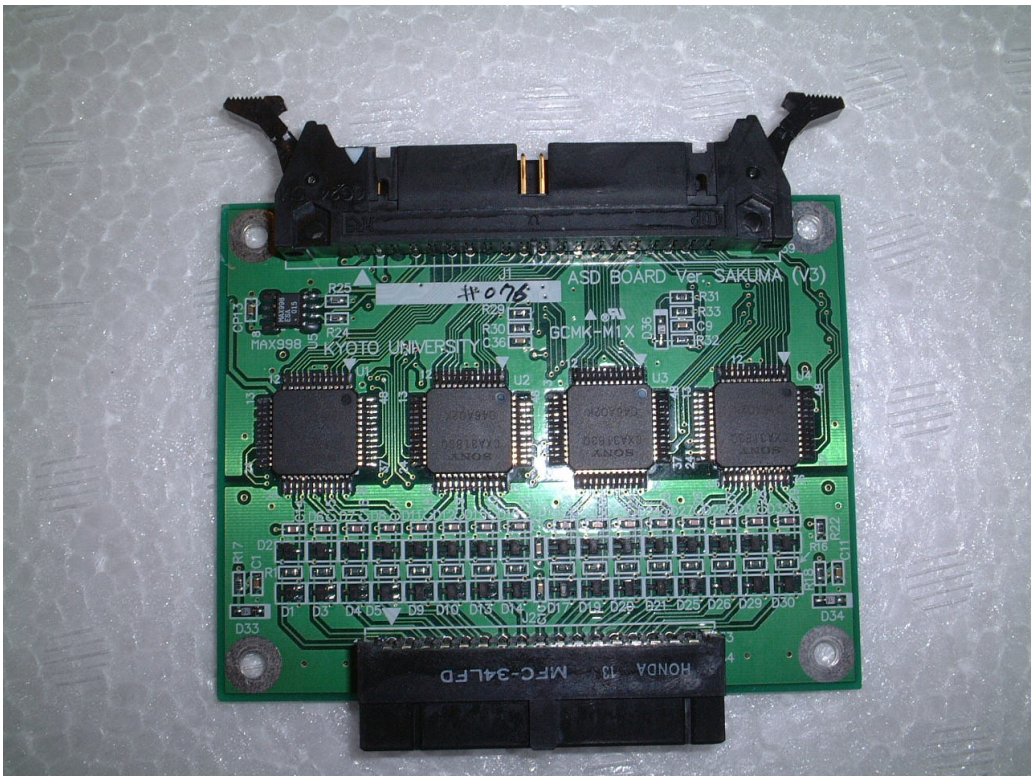

(a) ASD board

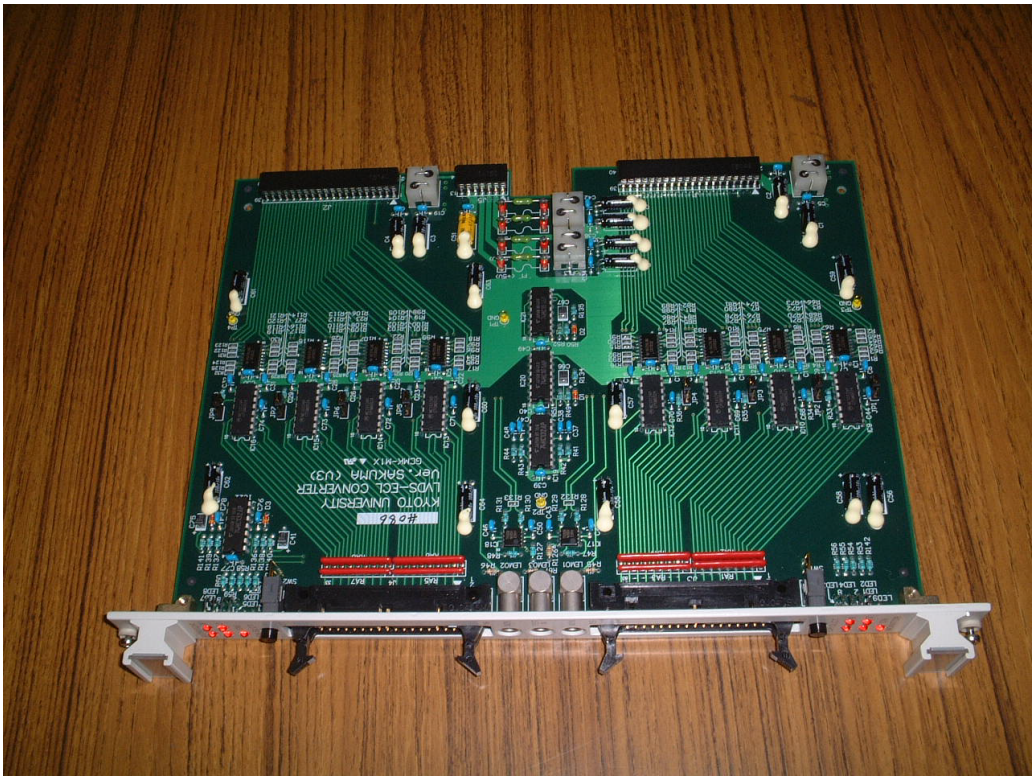

(b) LVDS-ECL converter

Figure 2.20: Photographs of (a) ASD board and (b) LVDS-ECL converter.

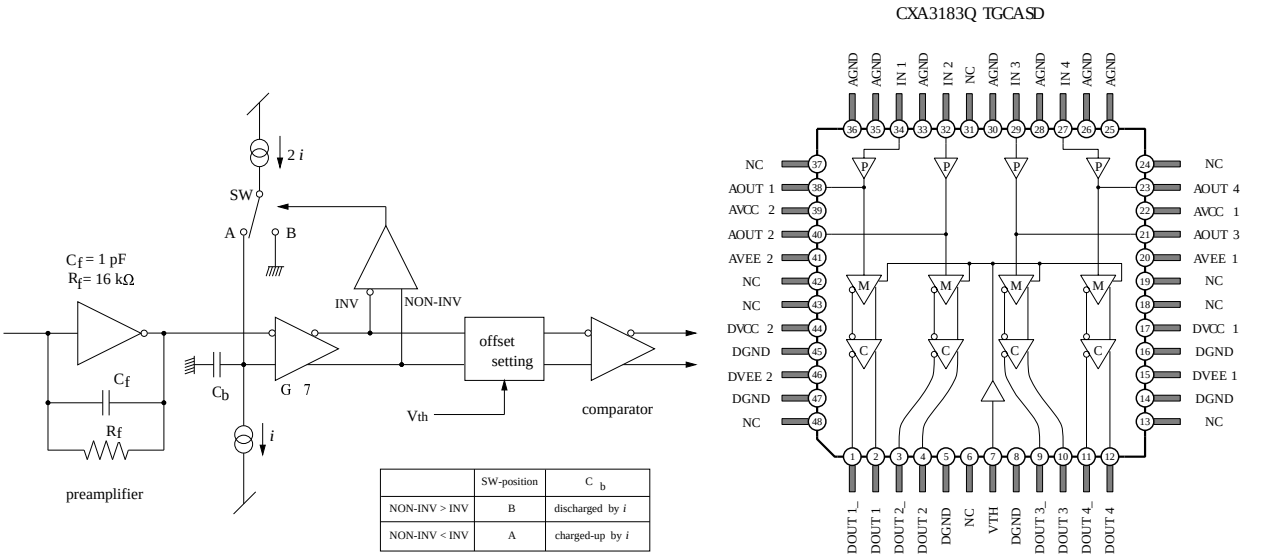

(a) Block diagram (b) Pin assignment

Figure 2.21: (a)Block diagram of the ASD chip. (b)Pin assignment of the ASD IC.

2.5.2 Barrel-shaped Drift Chambers

The mechanical structure of Barrel-shaped Drift Chambers (BDC's) consisted of 90-degrees arc-shaped end plates at the top and the bottom which were supported by three aluminum bars as shown in Fig. 2.22. The inner radius was 1570 mm, the outer radius was 1680 mm and the height was 1420 mm. The acceptance of BDC's was the same as CDC in the vertical coverage, but with a smaller horizontal coverage from ±7.5 degrees to ±94.5 degrees. The BDC's have 4 layers of drift cells with an X-X′-U-V configuration, located at r=1600 to 1650 mm. In the X and X′ layers the direction of wires was vertical and in the U and V layers the wires were tilted by about ± 0.1 radian. As CDC argon-ethane mixed gas of 50% and 50% was used at 1 atm.

The structure of the drift cells is shown in Fig. 2.23. All the drift cells of BDC had the same horizontal angular coverage of 0.75 degrees with respect to the target position. The size of the drift cells of BDC was the same as that of the outer super layer of CDC. Details of the wire arrangements are shown in Table 2.6.

The read-out electronics of BDC were the same as that of CDC and the threshold voltage of the discriminator was set at from 13 to 15 mV.

layer number	1	2	3	4
wire direction	X	X′	U	V
location of sense wire	1600	1610	1630	1650
from the center of the arc [mm]				
cell width [degree]	0.75	0.75	0.75	0.75
cell width [mm]	20.81	20.94	21.21	21.47
tilt angle [radian]	0	0	0.1058	0.1071
wire length [mm]	1403	1403	1410.9	1411.1
number of sense wires	116	116	109	109

Table 2.6: BDC wire configuration.

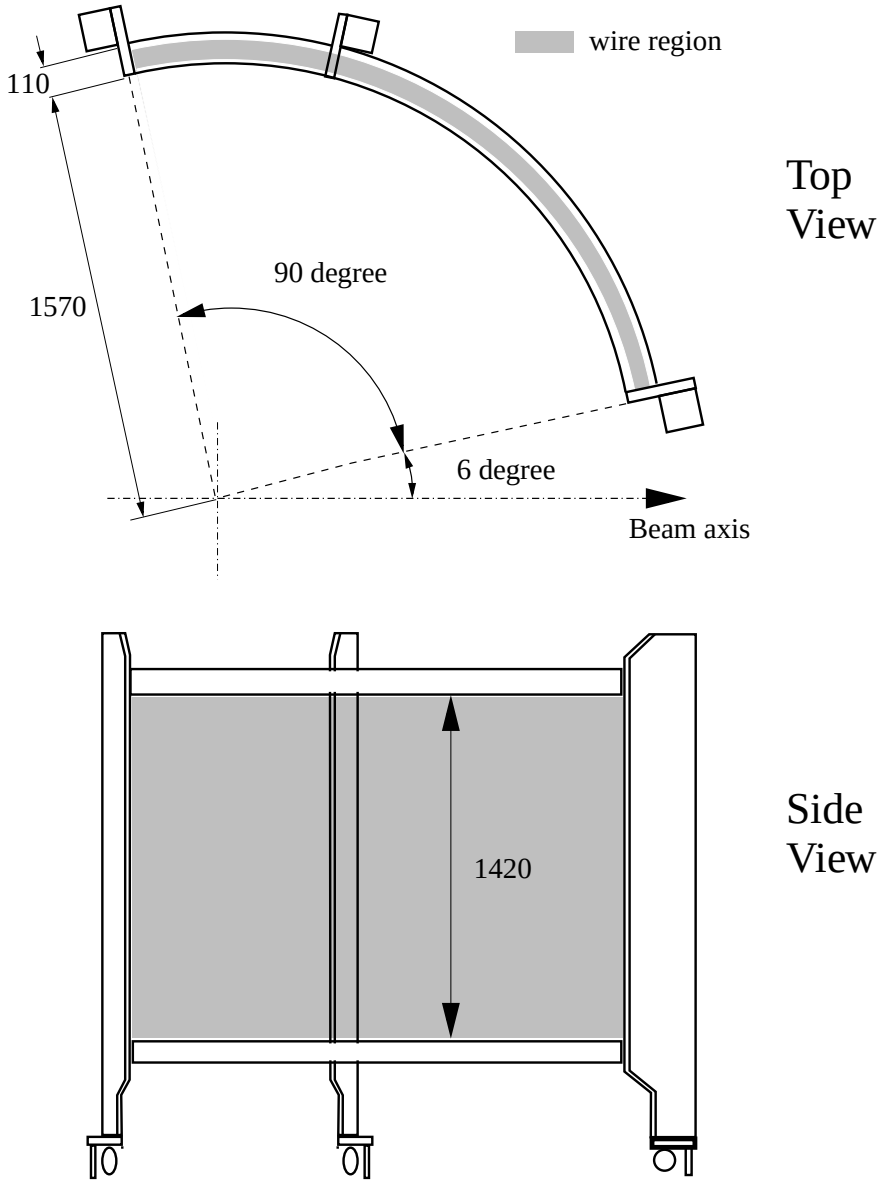

Figure 2.22: Schematic view of BDC.

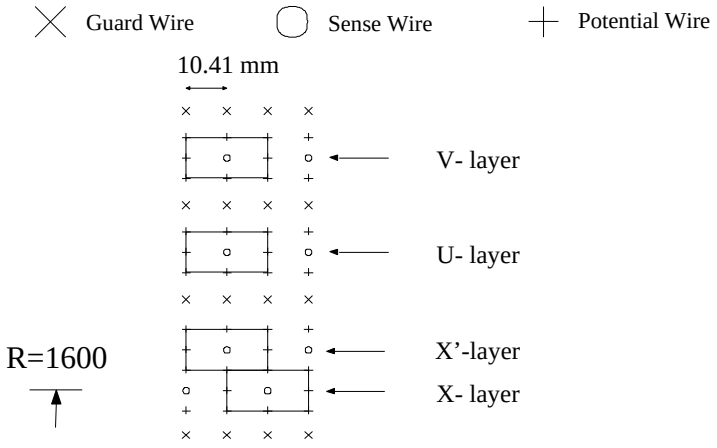

Figure 2.23: The cell structure of BDC

2.5.3 Vertex Drift Chamber

The Vertex Drift Chamber (VTC) was newly installed in 2000 to give tracking information in the vicinity of the beam and the targets. A significant beam halo of about 100 kHz was observed at 20 mm away from the beam with a 120 mm long and 1 mm wide scintillator. To make the chamber operational under such a circumstance, special cell arrangements as shown in Fig. 2.24, were chosen. The VTC was located in the center of CDC, and the frame of VTC was made of aluminum with dimension of 445 mm long, 320 mm wide and 220 mm high. To minimize the material in the spectrometer acceptance, the top and bottom end-plates were supported only at the upstream side. The acceptance of VTC was from ±6 degrees to ±141 degrees horizontally, and the same as CDC vertically.

The VTC consisted of six radial layers of the drift cells, and they were grouped into two; the backward and the forward layers. The backward 3 layers covered from ±18 to ±141 degrees at r = 100 mm, and the forward three layers covered the horizontal region from ±6 to ±24 degrees at r = 200 mm. All of the layers had a hexagonal cell structure, as shown in Fig. 2.25. In the backward layers, the drift length was 2.62 mm, and in the forward layer it was 1.75 mm.

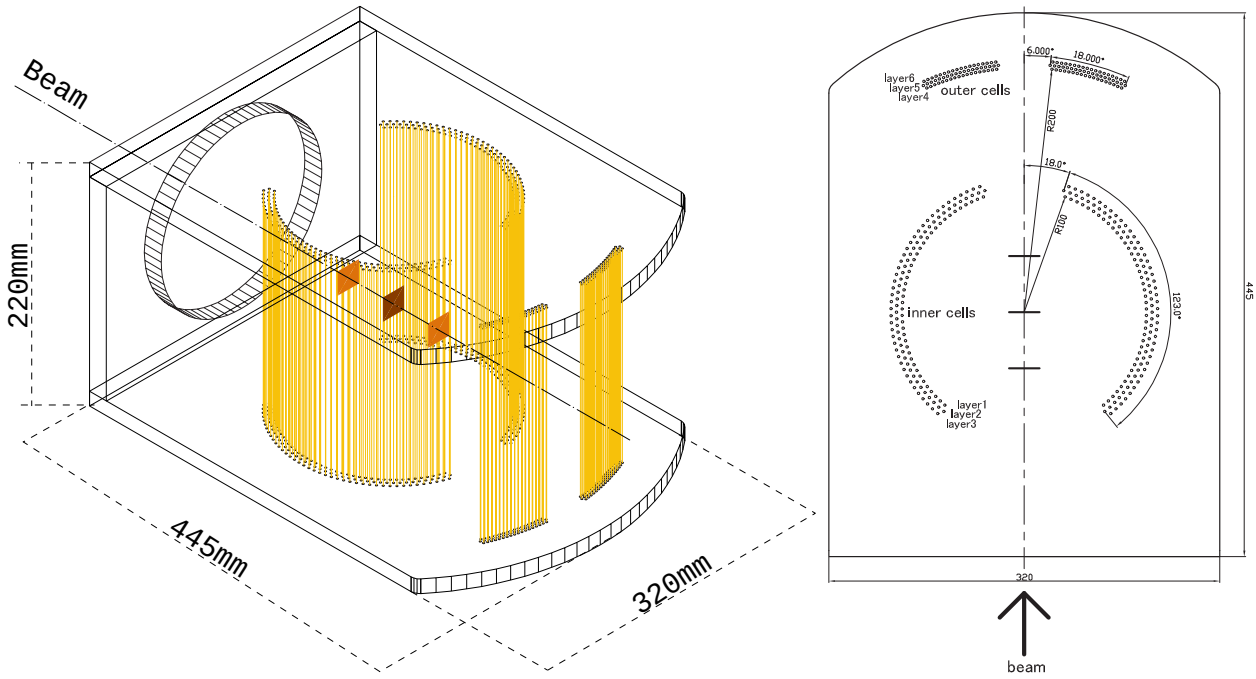

Figure 2.24: Schematic view of VTC. The target arrangement in 2001 is also shown.

layer number	1	2	3	4	5	6
wire direction	X	X′	X	X	X′	X
radial location of sense wire [mm]	100.00	104.53	109.06	200.00	203.03	206.06
cell width [degree]	3.0	3.0	3.0	1.0	1.0	1.0
cell width [mm]	5.24	5.47	5.71	3.49	3.54	3.60
wire length [mm]	184	184	184	184	184	184
number of sense wires	41	42	41	18	19	18
global angle of wire ID=1 [degree]	19.5	18.0	19.5	6.5	6.0	6.5

Table 2.7: VTC wire configuration.

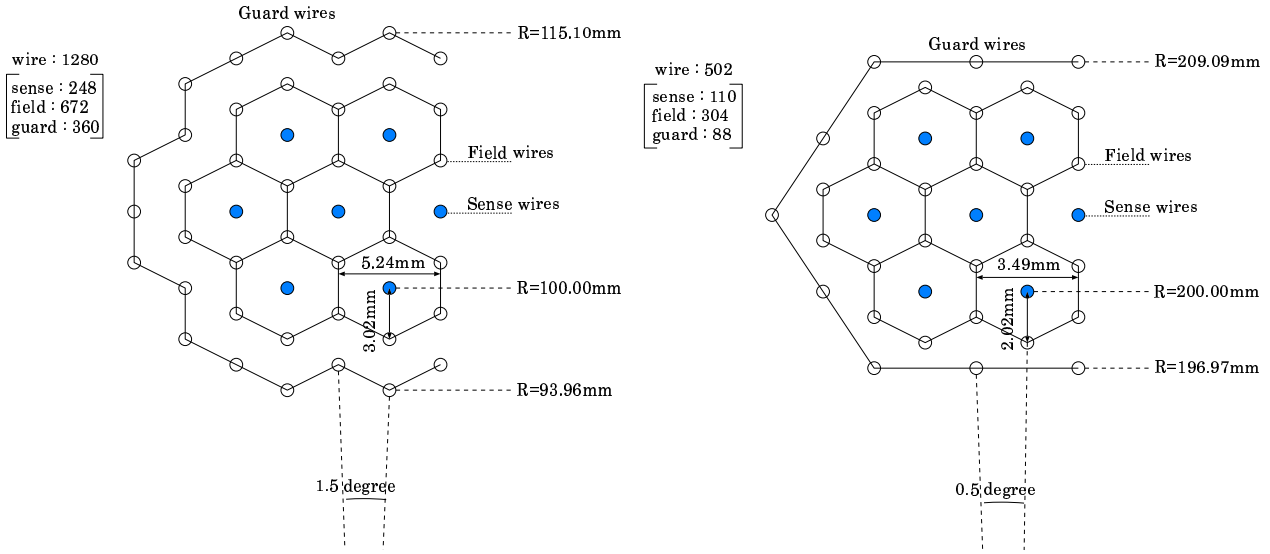

(a) backward cells (b) forward cells

Figure 2.25: The cell structures of VTC (a) for the backward cells and (b) for the forward cells.

The sense wires were gold-plated tungsten of 30 μmϕ and the potential wires were Be-Cu of 100 μmϕ as same as CDC. In the backward cells, 2.9 mmϕ NORYL (degeneration PPE resin) feedthroughs are used with a pitch of 3.02 mm (Fig. 2.26(a)). The sense wires were kept at the ground level, and the signals are read out through DC coupling (Fig. 2.27(a)). In the forward cells, all of the cathode wires are grounded through metallic feedthroughs which are directly mounted on the end-plate (Fig. 2.26(b)). For the anodes, NORYL feedthroughs as the backward cells are used. A positive high voltage is applied on the sense wires, and the signals are read out through AC coupling (Fig. 2.27(b)). Details of the wire arrangements were shown in Table 2.7. Figure. 2.28 shows a photograph of the VTC with the targets in 2000 [3], and concentration of the wires can be seen.

In the typical data-taking condition, the maximum hit rates per wire were 100 kHz in the backward cells and 300 kHz in the forward cells. As the chamber gas, an argon(50%)-ethane(50%) mixture was used through an ethanol bubbler at room temperature and 1 atm. Without ethanol, the chamber could not work at such high rates. H_2O and ethanol are known to be effective in a wire ageing [49].

As CDC and BDC we calculated the electrical field shape in the chamber cell and the relation between the drift length and the drift time with the drift chamber simulation code Garfield. The simulated drift line in the forward layer is shown in Fig. 2.29(a), and the relation between the drift length and the drift time (x-t relation) is shown in Fig. 2.29(b).

The read-out electronics of VTC were the same as that of CDC, and the threshold voltage of the discriminator was typically set at 5 mV in the forward layers and 30 mV in the backward.

[3] in 2000, polyethylene, copper, and carbon targets were used

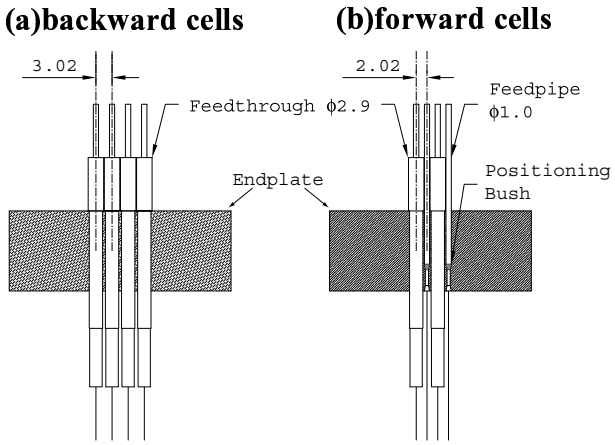

Figure 2.26: Feedthrough structures (a) for the backward cells and (b) for the forward cells.

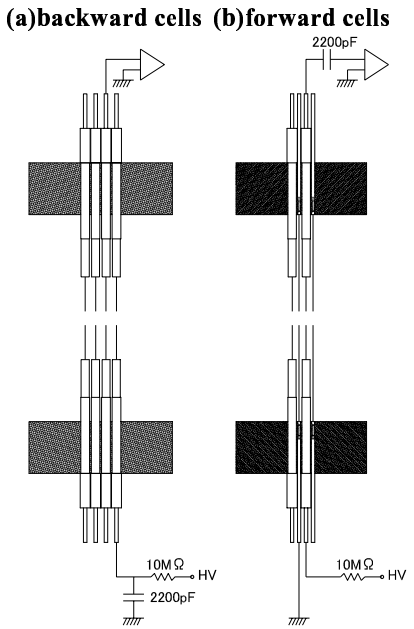

Figure 2.27: The read-out and high-voltage circuit (a) for the backward cells and (b) for the froward cells.

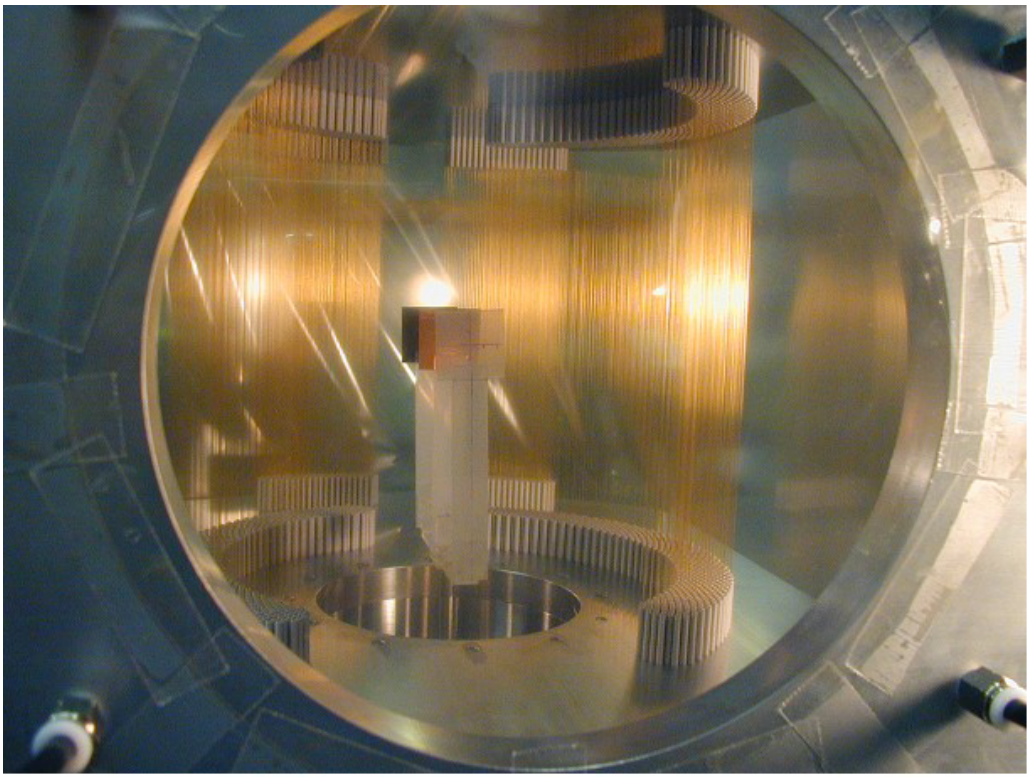

Figure 2.28: Photograph of the VTC and the targets in 2000.

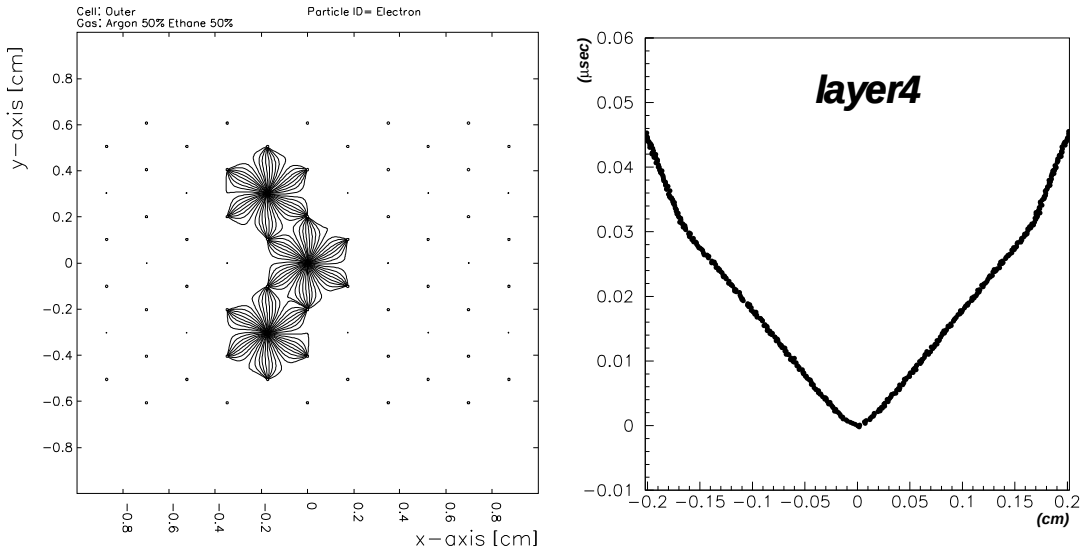

(a) simulated drift line (b) calculated x-t relation

Figure 2.29: (a) The simulated drift line in the forward layer in the magnetic field of 0.71T, which is the magnetic field strength at this location when the spectrometer magnet is fully excited. (b) The calculated relation between the drift time and the drift length of the layer-4 under the magnetic field of 0.71T.

2.6 Electron Identification Counters

2.6.1 Start Timing Counter

The time zero of an event was defined by the start timing counters (STC's), since we could not count the beam protons one by one because of their high rate ($\sim 9 \times 10^8$ protons per spill). We located STC at 380 mm from the center of the spectrometer, covering from ± 12 to ± 60 degrees in the horizontal angle and ± 23 degrees in the vertical angle. In each arm STC was segmented into 8 units horizontally.

The scintillators of STC were made of Bicron BC404. The dimension of the scintillator segment was 400 mm in height, 40 mm in width and 5 mm in thickness. The scintillation light was transferred through light guides to a pair of photomultipliers attached at the top and bottom ends. The photomultipliers were H6154 of Hamamatsu Photonics, whose diameter of the photo-cathode was 2 inches and the dynode structure was a fine-mesh type. They could be operated under the magnetic field of 0.71 T. The number of dynodes was 19 with the typical gain of 1×10^6 at the present field strength. Since the coincidence rate of the top and bottom photomultipliers reached 1M counts per spill in the forward segments close to the beam, the high voltage breeder was modified to supply enough current to the last three dynodes. The breeder circuit is shown in Fig. 2.30. Typical breeder current was 0.4 mA which was increased to 4 mA at the last three dynodes. Discriminated signals from the top and bottom photomultipliers were fed into the mean timers and provided the timing of each segment. The timings of all the STC segments were adjusted within 1 nsec. These signals were OR-ed and used as the event time-zero signal.

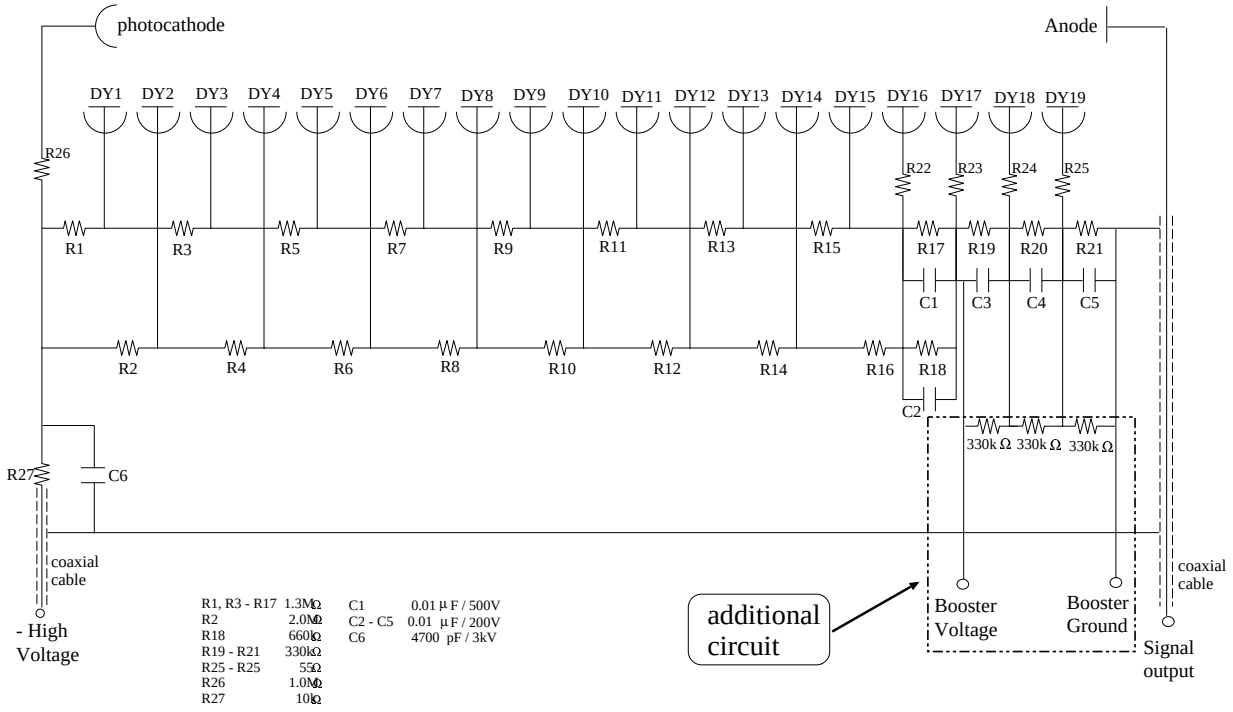

Figure 2.30: The breeder circuit of the photomultiplier used for STC (Hamamatsu H6154).

2.6.2 Front Gas-Čerenkov Counter

The front gas-Čerenkov counters (FGC's) covered from ±12 degrees to ±90 degrees horizontally and ±23 degrees vertically. They were horizontally segmented into 13 units in each arm so that one segment covered 6 degrees. The cross section of FGC is schematically shown in Fig. 2.31, together with the light collection scheme. Iso-butane gas with the refractive index of 1.00127 at room temperature (1.0019 at STP) was used as the Čerenkov photon radiator . The threshold momentum for pions is 2.7 GeV/c. Since the path length of particles in the counter was rather short, we used the gas having high refractive index. Another merit of iso-butane was its transparency for ultra-violet lights down to the wave length of 220 nm. It is important for the detection of the Čerenkov light because the intensity of Čerenkov light is higher at a short wavelength with a $1/\lambda^2$ dependence.

A radiated Čerenkov photons were reflected twice on the flat and the arc mirrors. To suppress multiple scattering, it was required to use thin mirrors. For the flat mirror we used 0.05 mm-thick aluminized Mylar supported with a honeycomb backplane made of paper. The arc mirrors were made by a 3 mm-thick Acrylic plastic on which aluminum and SiO were successively evaporated. Čerenkov photons were reflected also at the side walls which separated the 13 segments. We used MgF_2-coated aluminized Mylar which has 88% reflectance for the wave length down to 200 nm.

The Čerenkov photons were focused with a Winston funnel [50] attached on the photomultipliers. Since the photomultipliers of FGC's were operated under the magnetic field of about 0.2 T, we used R5542 of Hamamatsu Photonics which had 19 stages of fine-mesh dynodes. For the detection of Čerenkov photons, their window was made of UV-transparent glass with a diameter of 3 inches.

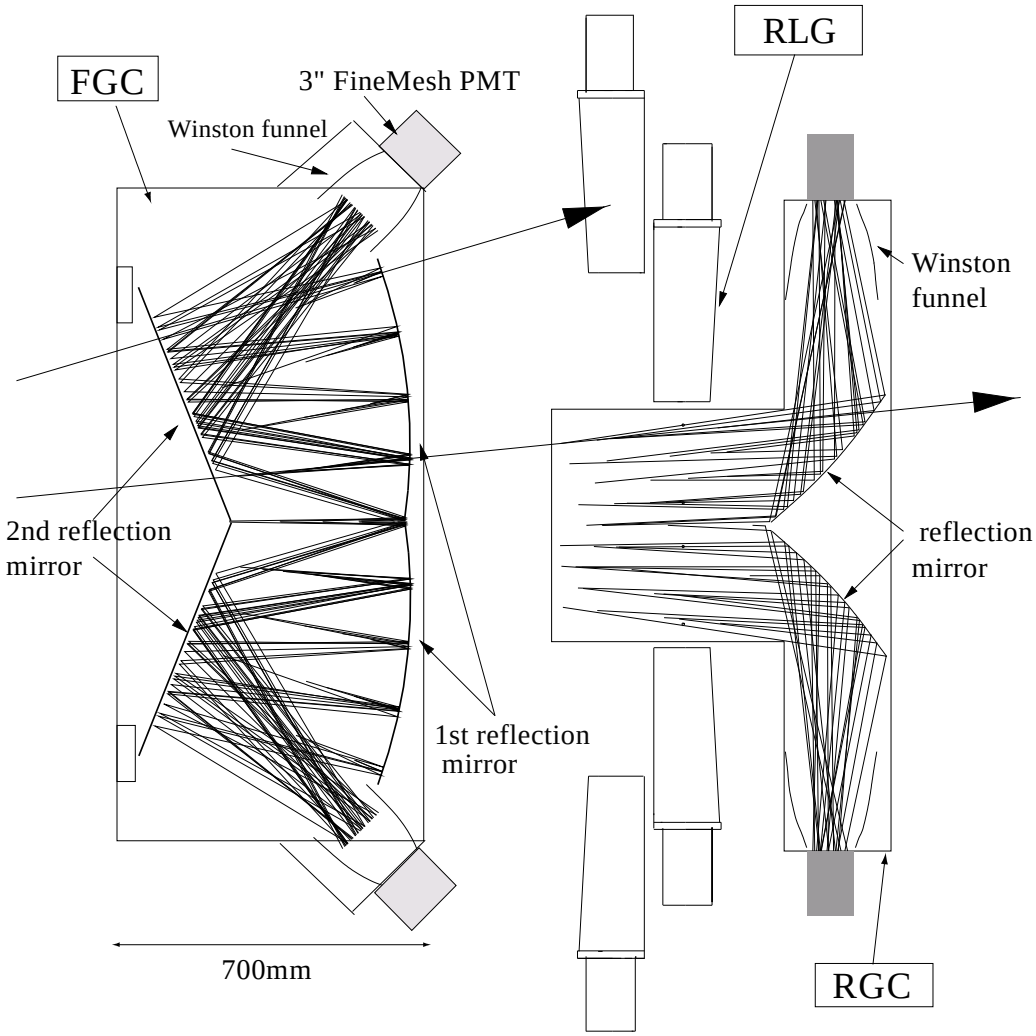

Figure 2.31: Schematic view of FGC,RGC and RLG.

We tested a 1/2 sector model with no magnetic field. The vertical and horizontal incident-angle dependence of the efficiency and the number of mean photo-electron were obtained using 500 MeV/c electrons. The results are summarized in Fig. 2.32 and 2.33. We obtained more than five photo-electrons in all the angular region required for the spectrometer. With the horizontal angle more than 0.15 radians electrons pass more than one segment so that the pulse from the neighbor segment must be added. The horizontal incident angle of 0.2 radian corresponds to the momentum of 400 MeV/c. Figure 2.34 shows the ADC spectrum for 1 GeV/c pions. The pion rejection is 0.8×10^{-2} when the threshold is set to one photo-electron.

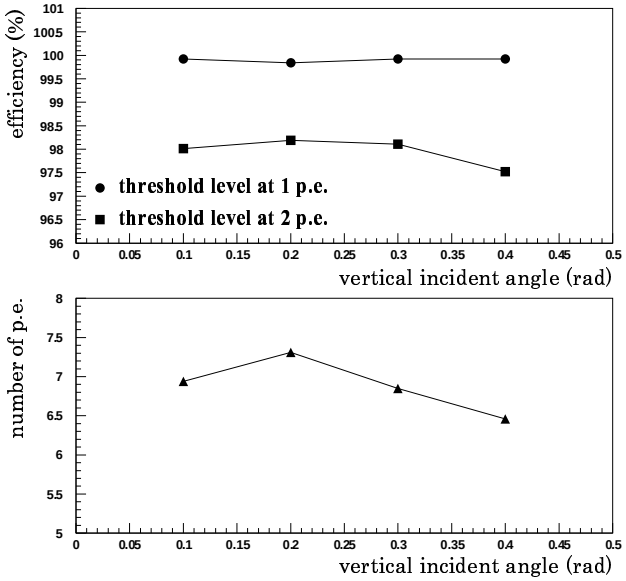

Figure 2.32: The efficiencies (upper figure) and the averaged number of photo-electrons (lower figure) of the FGC test module for 0.5 GeV/c electrons as a function of the vertical incident angle. The circles and the squares show efficiencies with threshold at one and two photo-electron levels, respectively.

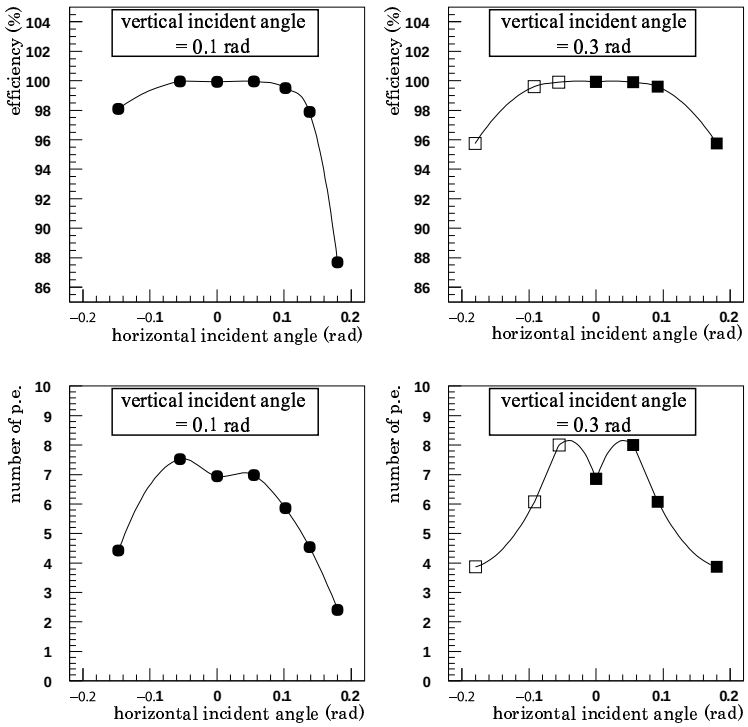

Figure 2.33: The efficiencies (upper figures) and the averaged number of photo-electrons (lower figures) of the FGC test module for 0.5 GeV/c electrons as functions of the horizontal incident angle. The left figures were measured when the vertical incident angle was 0.1 rad, and the right figures were when that was 0.3 rad. The open marks are mirror image of the closed marks.

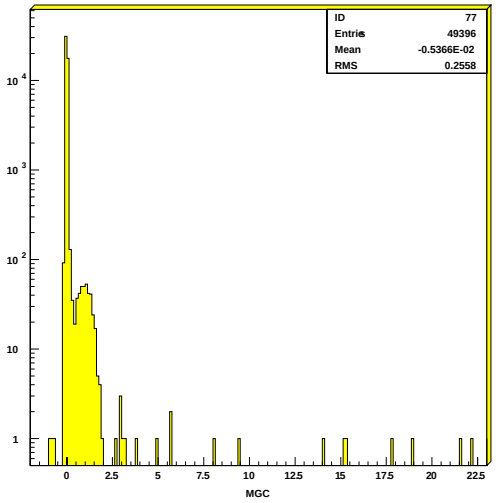

Figure 2.34: FGC response for 1 GeV/c pions. The horizontal axis is normalized to the number of photo-electrons.

2.6.3 Rear Gas-Čerenkov Counter

The rear gas-Čerenkov counters (RGC's) covered from ±12 degrees to ±54 degrees horizontally and ±6 degrees vertically with 7 horizontal segments in each arm. These regions corresponded to the kaon-arm acceptance. The cross section of RGC is schematically shown also in Fig. 2.31, together with the light collection scheme.

Iso-butane gas was used for the radiator as FGC. A radiated Čerenkov photons were reflected once on the arc mirror which was made by the 3 mm thick Acrylic plastic on which aluminum and SiO were evaporated. Čerenkov photons were reflected also at the side walls for the segmentation. The photons were focused with a Winston funnel [50] attached on the photomultipliers. We used R1652 of Hamamatsu Photonics with a diameter of 3 inches.

The test results for a 1/2 sector model with no magnetic field are shown in Fig. 2.35(a) and (b). The vertical and horizontal incident-angle dependence of the efficiency and the number of mean photo-electron were obtained using 1.0 GeV/c electron. We obtained the number of photo-electrons of more than three in the acceptance required for the spectrometer. The lower number of photo-electrons at 0.0125 radian (Fig. 2.35(a)) is due to the acceptance of the test module. The pion rejection is also demonstrated in Fig. 2.36, which shows the ADC spectrum of 1 GeV/c pions. When the threshold is set to 10 ADC channel above the pedestal, which realize the 99% efficiency for electrons, the pion rejection power is estimated to be 3×10^{-3}.

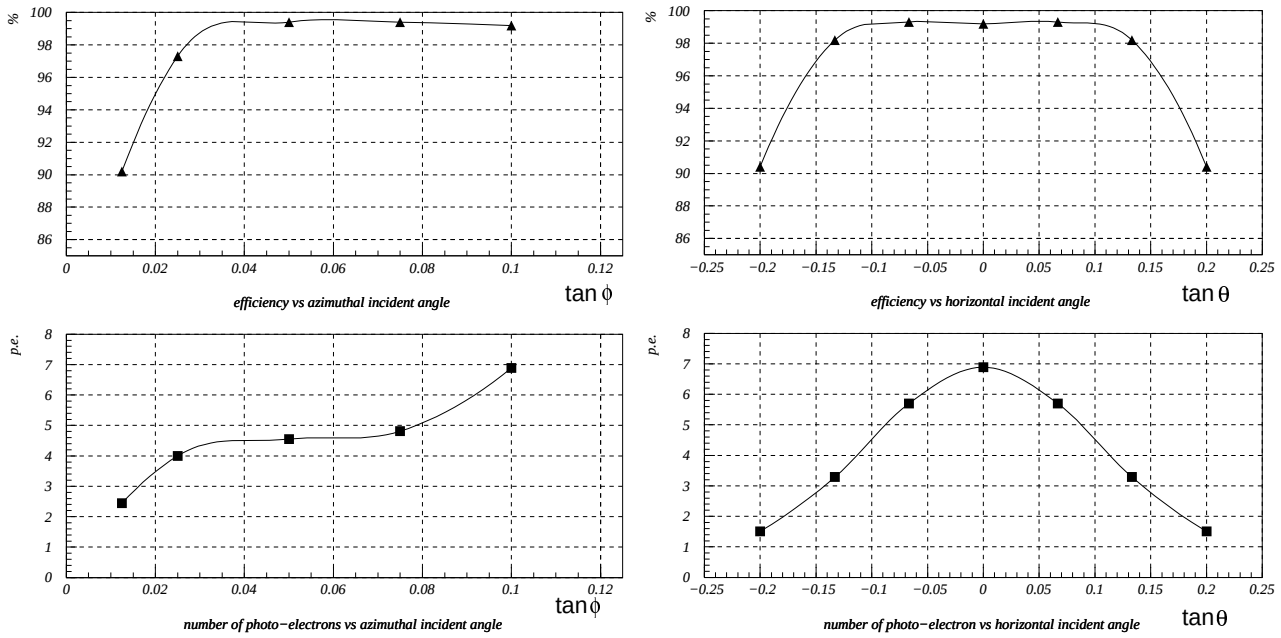

(a) vertical angle (b) horizontal angle

Figure 2.35: The efficiency (top panels) and the number of photo electron (bottom panels) of the RGC test module as functions of (a) the vertical angle of incident electrons and (b) the horizontal angle of incident electrons.

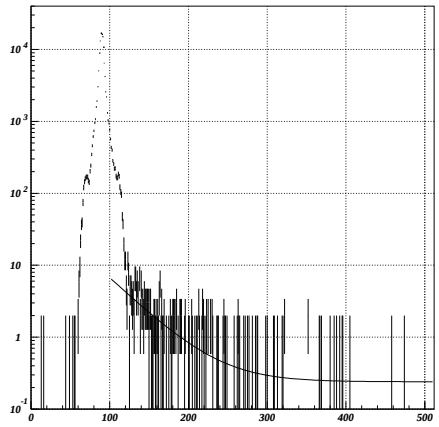

Figure 2.36: RGC response for 1 GeV/c pions.

Radiation length	1.69cm
Refractive index	1.805
Critical energy	12.6MeV
Moliere radius	2.8cm
Density	5.20g/cm^3

Table 2.8: Characteristics of SF6W [51].

2.6.4 Rear Lead-Glass EM Calorimeter

The rear lead-glass EM calorimeters (RLG's) covered the same horizontal angle as RGC's with 12 segments in each arm, but vertically covered outside the kaon-arm acceptance, from ±9 degrees to ±23 degrees.

The one unit of RLG consisted of SF6W lead-glass block, which had the size of 340 mm height, 124 mm width and 114 mm thickness, and a PMT 1652 of Hamamatsu Photonics with a diameter of 3 inches was attached. The characteristics of SF6W are listed in Table 2.8. These units were recycled from the EM calorimeter of the TOPAZ experiment at KEK TRISTAN.

These units were arranged as particles come into the side of each block, as shown in Fig. 2.31. So that typical effective thickness as a Čerenkov radiator was 6.7 radiation lengths. To cover

a large region with the small number of segments, such unusual arrangements were adapted. Čerenkov photons from an EM shower were transported vertically by the total reflection to the photomultipliers at the end of the block.

2.6.5 Side Lead-Glass EM Calorimeter

In the backward region where the horizontal angle was larger than 57 degrees, the second-stage electron identification was done by the side lead-glass EM calorimeters (SLG's) which covered from ±57 degrees to ±90 degrees horizontally and ±23 degrees vertically with 9 horizontal segments in each arm. The cross section of SLG is schematically shown in Fig. 2.37 with FGC.

We reuse the TRISTAN/TOPAZ lead glass calorimeter blocks same as RLG. For SLG, we reshaped and re-polished the blocks in Tochigi Nikon Corporation into a rectangular shape from the original tapered shape, and 5 units of the lead-glass blocks were stacked vertically and glued epoxy resin to form one segment of the calorimeter. The one segment of SLG had the size of 165 cm height, 12 cm width and 11 cm thickness. We placed SLG along the return yoke of the magnet like a hodoscope behind BDC. Čerenkov photons from an EM shower were transported vertically by the total reflection to the photomultipliers at the top and bottom ends. We used R1911 of Hamamatsu Photonics with a diameter of 3 inches.

We tested a one-segment model. The light yield was measured as a function of the vertical position using a 500 MeV/c electron beam. Although the light yield decreased by 75% at each block, the sum of the both end was almost flat as shown in Fig. 2.38(a). Typical response for pions and electrons was obtained as shown in Fig. 2.38(b). Although the effective thickness for the electron shower-development was only 6.5 radiation lengths, typical energy resolution of $15\%/\sqrt{E}$ was obtained. By keeping 95% efficiency for electrons, the pion rejection of 2×10^{-2} was achieved.

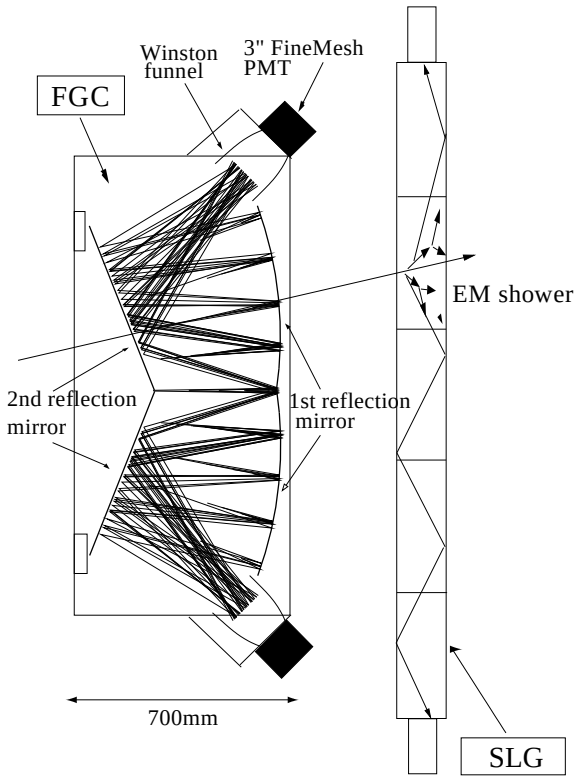

Figure 2.37: Schematic view of FGC and SLG.

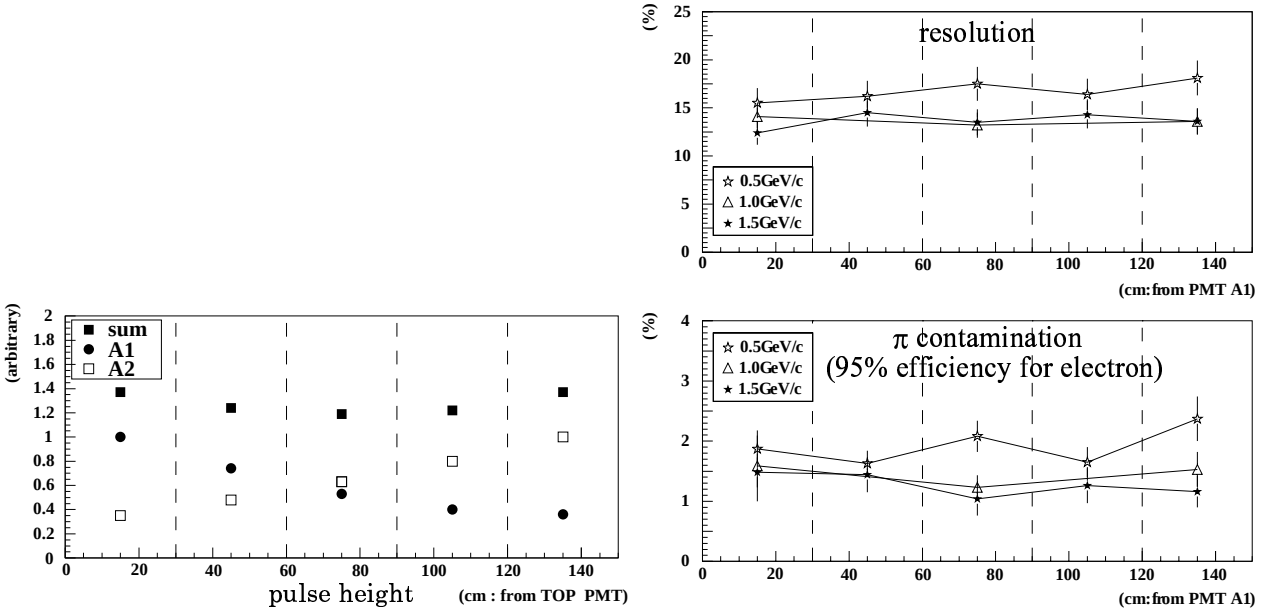

(a) (b)

Figure 2.38: (a)Vertical position dependence of the light yield for SLG. The open rectangles and closed circles are the light yields from the top and the bottom PMT's. The closed rectangles are for the sum. (b)The vertical position dependence of the energy resolution for electrons (top) and the pion rejection power (bottom) of SLG, measured with 0.5, 1.0, and 1.5 GeV/c electrons and pions.

2.6.6 Forward Lead-Glass EM Calorimeter

The forward lead-glass EM calorimeters (FLG's) were installed in 2000 to improve the electron identification capability in the kaon arm acceptance. The FLG's were located at just behind the FTOF wall covering the same acceptance as RGC's. The FLG's had 24 segments in the left arm and 16 segments in the right arm. The 8 segments to cover the most right end of the right arm were omitted due to the space limitation of the experimental area.

We reused the TRISTAN/TOPAZ lead-glass calorimeter blocks also for FLG. One segment of FLG consisted of three lead-glass blocks. Only the center block was reshaped and re-polished at Tochigi Nikon Corporation into a rectangular shape from the original tapered shape. Top and bottom blocks just reused the TOPAZ modules as they were. The three blocks of the lead-glass blocks were stacked vertically and glued with epoxy resin, as shown in Fig. 2.39. The one segment of FLG had the size of 950 mm height, 124 mm width and 110 mm thickness. Čerenkov photons from an EM shower were transported vertically by the total reflection to the photomultipliers at the top and bottom ends. We used R1652 of Hamamatsu Photonics with a diameter of 3 inches.

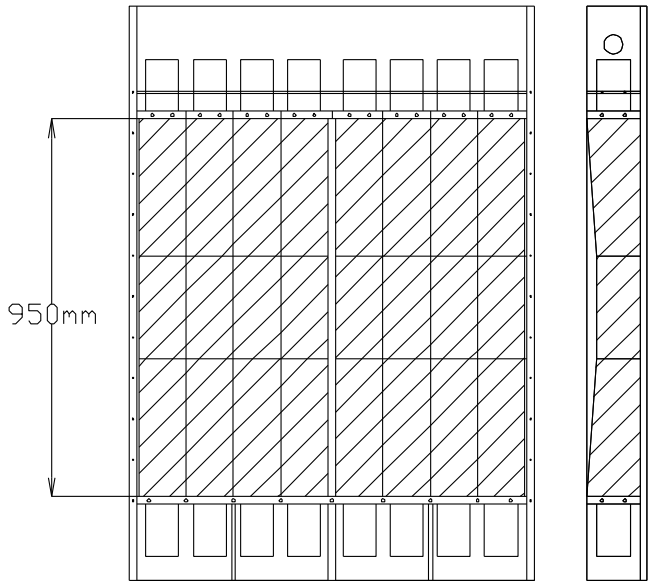

Figure 2.39: Schematic view of FLG. The hatched areas are lead-glass radiators.

2.7 Kaon Identification Counters

2.7.1 Hodoscope Counter

Hodoscope Counters (HC's) were used to determine the sign of a charged particle and its rough momentum in the trigger in combination with the FTOF counters. Signals from HC were used in the on-line first-level and the second-level kaon-triggers, as described in Sec. 2.8.2.

The HC's covered from ±12 degrees to ±54 degrees in the horizontal angle, and ±6 degrees in the vertical angle, and were placed 2632.5 mm from the center of the magnet. They consisted of 28 segments in each arm. The dimension of the scintillator was 660 mm in height, 70 mm in width, and 5 mm in thickness. The two segments located most backward had a different width of 200 mm. They were arrayed with an horizontal overlap of 5 mm. Each segment was read by a pair of photomultipliers from the top and bottom ends through light guides. The photomultipliers were H1161 of Hamamatsu Photonics with the photocathode diameter of 2 inches. The number of dynodes was 12 of linear focusing type with the typical operation gain of 1.1×10^6.

2.7.2 Forward Time Of Flight Counter

Forward Time Of Flight Counters (FTOF's) were used to measure the flight time of charged particles together with STC's. Particle identification was performed with the flight time information together with a flight length and a momentum given by the track fitting.

The FTOF's were located behind the Aerogel Čerenkov counters (AC's), and they covered from ±12 degrees to ±54 degrees in the horizontal angle, and ±6 degrees in the vertical angle. The distance from the center of the spectrometer to the center of the FTOF array was 3951 mm. The FTOF's consisted of 16 segments in each arm. Two types of scintillator slabs were used, one was 800 mm in height, 200 mm in width and 30 mm in thickness, and the other was 800 mm in height, 170 mm in width and 20 mm in thickness. They were arrayed alternatively with an horizontal overlap of 2 mm. The scintillation light was read out with a pair of photomultipliers through light guides mounted on the both ends of the slabs. The photomultipliers were H1949 of Hamamatsu Photonics with a photocathode diameter of 2 inches. This photomultiplier was

specialized for the time of flight measurements with a high gain of 2.0×10^7 and the typical signal rise-time of 1.3 nsec.

2.7.3 Aerogel Čerenkov Counter

To trigger kaons, we used the threshold-type Aerogel Čerenkov counters (AC's). Since the refractive index of the Čerenkov radiator was 1.034, we can separate kaons from pions in the momentum region from 0.53GeV/c to 1.88GeV/c . The AC's were located just in front of the FTOF counters, and both of them had geometrically-matched 16 segments in each arm. The cross section of the AC is schematically shown in Fig. 2.40 together with the light collection scheme. When a hit in a FTOF segment was associated with a hit in either of 3 AC segments in the front, it was considered as a pion having a momentum above 0.53GeV/c, and the FTOF hit was vetoed in the first-level kaon trigger as described in Sec. 2.8.2.

The AC's covered from ±12 to ±54 degrees in the horizontal angle and ±6 degrees in the vertical angle. The AC's had an effective area of 2640 mm in width, 706 mm in height, and 125 mm in thickness. The dimension of each AC segment was 160 mm in width and 706 mm in height. Radiated Čerenkov photons were read out by a pair of photomultipliers through the optical system made with cylindrical concave mirrors and Winston funnels [50] attached on each photomultiplier. The equipped photomultipliers were single-photoelectron sensitive H6527 of Hamamatsu Photonics with a photocathode diameter of 5 inches. It had 14 dynodes of linear-focusing type. They were operated with a typical gain of 1.4×10^7.

In Fig. 2.41, the pulse height distributions of AC are shown for 1.4 GeV/c positive pions and protons delivered at the center of the segment. We obtained 5.4 photoelectrons for pions. The photoelectrons observed for protons are attributed to δ rays or scintillation lights. Setting the threshold level at 1.1 photoelectron, we have achieved the pion rejection efficiency of 99.0% and an over-killing rate for protons of 0.3%.

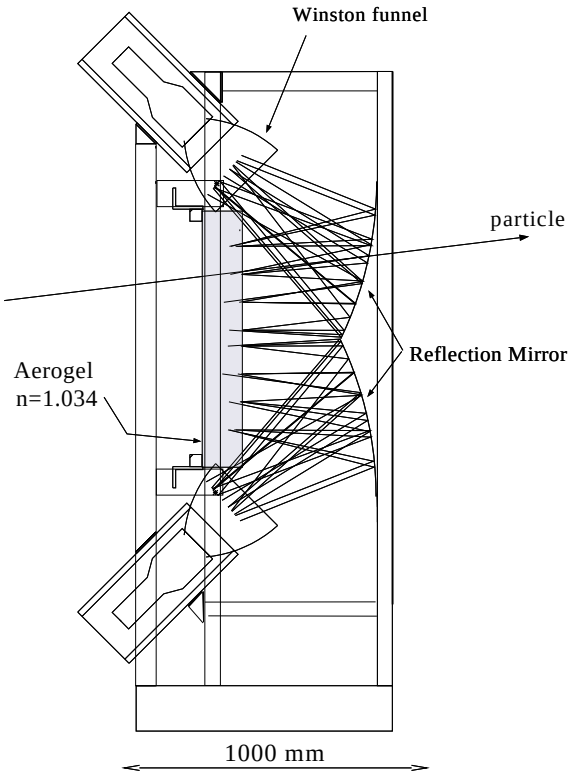

Figure 2.40: Schematic view of AC and the light collection scheme.

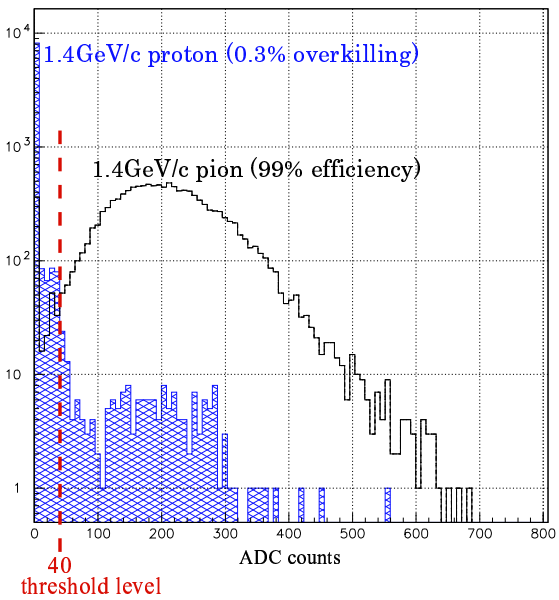

Figure 2.41: Pulse height distributions of AC for 1.4 GeV/c positive pions and protons.

2.8 Trigger

The schematic diagram of the trigger control system is shown in Fig. 2.42. We applied the three-level trigger logic for e^+e^- events and the two-level for K^+K^- events. The both modes worked simultaneously. If the condition of the electron or the kaon first-level trigger logic was satisfied, the event latch was set as "busy", the gates for ADC's were opened and the common start (or stop) timing signals for TDC were generated. The "busy" state of the event latch was kept until the clear signal was generated by the higher-level triggers.

If the latched events satisfied all the levels of the electron or kaon trigger requirements, the "event accept" signal was issued and the digitized data in the ADC and the TDC modules were transferred to the memory modules. When the data transfer was completed, the event latch was cleared and the trigger logic became ready for a next event. If the latched event did not satisfy the higher-level trigger logic, the clear signal was sent to the ADC's and TDC's and the event latch was also cleared. Typically the duration of the "busy" state was 600 μsec for the recorded events and 50 μsec for the cleared events.

In order to estimate the trigger efficiencies and to monitor the trigger logic operation, we recorded events which satisfied the lower-level trigger logics regardless of the result of the higher-level triggers. Such sampled events were about 5% of all the recorded events.

We required the second and third level trigger for e^+e^- events until the year 2000. After the year 2000, we decided to collect only "double-arm events" which mean either positron in the left arm and electron in the right arm ("LR event") or vice versa ("RL event"), to suppress the background trigger from Dalitz decays and conversions. This change reduced the rate of the electron first-level trigger significantly so that higher-level triggers were not used. The typical trigger rates in 2001 and 2002 are shown in Table 2.8.

Below we explain the electron first-level trigger and the kaon first and second-level triggers.

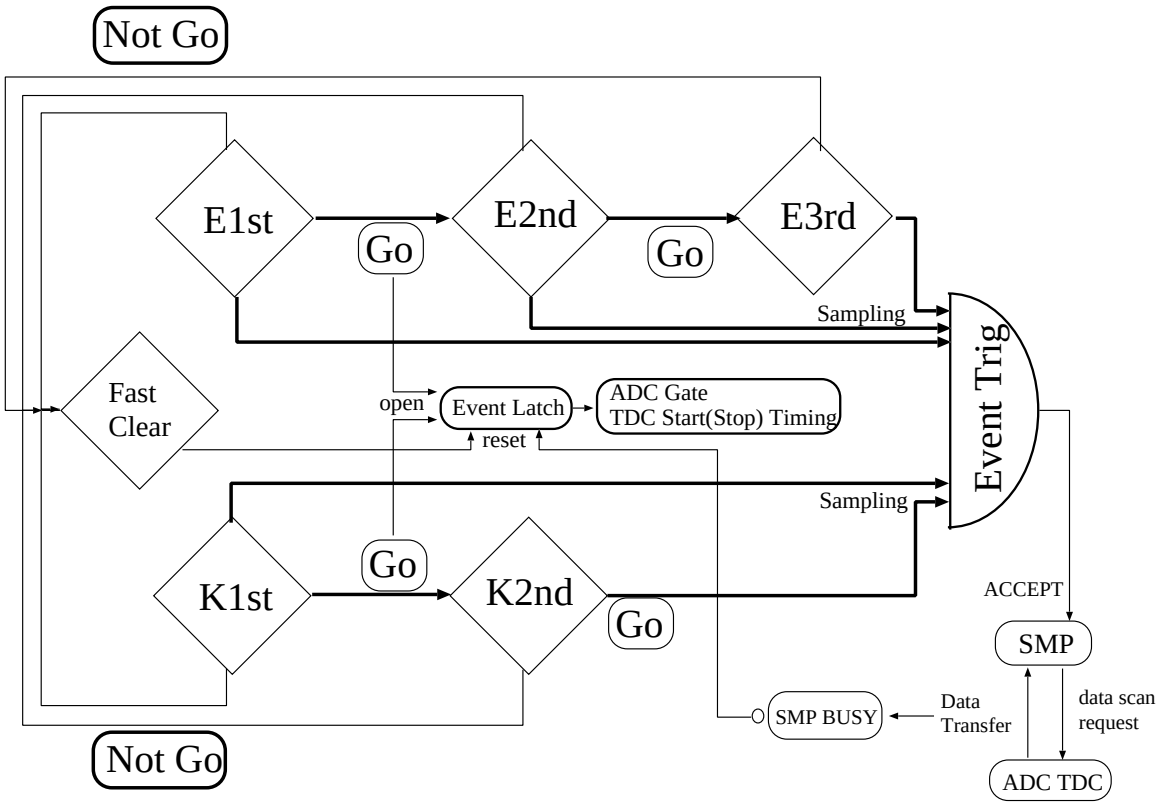

Figure 2.42: A diagram of the trigger control system.

Level		2001		2002
		Kaon trigger	Electron trigger	Electron trigger
1st	Request	57.8k	1.2k	1.6k
	Preset Scale	1/50	1/1	1/1
	Accept	0.8k	0.7k	1.0k
2nd	Accept	0.5k	–	–

Table 2.9: Trigger rates in a typical spill of 1.8 sec-long in the year 2001 and 2002.

2.8.1 Electron Trigger

The electron first-level trigger worked as follows. We selected electron-pair candidates using the coincidence signal of the front-stage (FGC) and the rear-stage detectors (RGC, RLG, SLG), by requiring the horizontal position matching as shown in Table 2.10. The hit signals of each segment were defined as an ORed signal of the top and the bottom PMT's and strobed by the STC or-signal in the corresponding arm. The size of the matching windows corresponds to the momentum range greater than 400 MeV. To suppress electron pairs with a small opening angle, such as from Dalitz decays and γ-conversions, we required the electron candidates to be present in both arms during the data taking periods used in the present analysis.

		FGC ID												
		1	2	3	4	5	6	7	8	9	10	11	12	13
RGC ID	1		○											
	2		○	○										
	3		○	○	○									
	4			○	○	○								
	5				○	○	○							
	6					○	○	○						
	7						○	○	○					
RLG ID	1		○											
	2		○	○										
	3		○	○										
	4		○	○	○									
	5		○	○	○									
	6		○	○	○	○								
	7			○	○	○	○							
	8				○	○	○							
	9				○	○	○	○						
	10					○	○	○						
	11					○	○	○	○					
	12						○	○	○					
SLG ID	1						○	○	○	○	○			
	2							○	○	○	○	○		
	3							○	○	○	○	○		
	4								○	○	○	○	○	
	5									○	○	○	○	
	6									○	○	○	○	○
	7										○	○	○	○
	8											○	○	○
	9											○	○	○

Table 2.10: The pattern of the matrix coincidence for the FGC segments and the RGC, RLG, and SLG segments in the electron first-level logic. The counters were numbered from forward to backward in each arm.

2.8.2 Kaon Trigger

The kaon first-level trigger selected events with two kaon candidates by using the information from the kaon-arm counters. To eliminate pions whose momentum was larger than 0.53 GeV/c, at least two FTOF hits which were not associated with geometrically-matched AC hits were required. To select tracks whose momentum was larger than 0.4 GeV/c, these AC-vetoed FTOF signals were fed into matrix-coincidence logic together with the HC signals. The matrix pattern was set as shown in Table 2.11. To invoke an event trigger, at least one STC hit both in the left and right arms was also required. The rate of the kaon first-level trigger requests was typically 58k per spill and it was down-scaled to 1/50 to keep the live time at the level of 60% for the electron trigger.

	FTOF ID																
Hodoscope ID		1	2	3	4	5	6	7	8	9	10	11	12	13	14	15	16
	1	○	○	○													
	2	○	○	○													
	3	○	○	○	○												
	4	○	○	○	○												
	5		○	○	○	○											
	6		○	○	○	○											
	7			○	○	○	○										
	8			○	○	○	○										
	9				○	○	○	○									
	10				○	○	○	○									
	11					○	○	○	○								
	12					○	○	○	○								
	13						○	○	○	○							
	14						○	○	○	○							
	15							○	○	○	○						
	16							○	○	○	○						
	17								○	○	○	○					
	18								○	○	○	○					
	19									○	○	○	○				
	20									○	○	○	○				
	21										○	○	○	○			
	22										○	○	○	○			
	23											○	○	○	○		
	24											○	○	○	○		
	25												○	○	○	○	
	26												○	○	○	○	
	27														○	○	○
	28														○	○	○

Table 2.11: The pattern of the matrix coincidence for the FTOF segments and the HC segments in the kaon first-level trigger logic. The counters were numbered from forward to backward in each arm.

The kaon second-level trigger used the flight time information from the FTOF counters and the hit information of HC counters. Since average momentum of charged particles is different in each hit combination of FTOF and HC, a timing window for kaons was determined for each FTOF-HC pair. Before starting the every run of about 90 minutes long, the peak positions of TDC counts for pions in all the FTOF segments were monitored, and the timing windows for kaons with a momentum larger than 0.5 GeV/c were determined for each FTOF-HC hit pair. We required at least two FTOF-HC hit pairs whose flight time was inside the kaon window and the charges were at least one positive and one negative. The kaon second-level logic reduced the trigger rate to about 60% and the decision time was less than 100 μsec including the conversion time of the fast encoding TDC's.

2.9 Data Acquisition System

The on-line data-acquisition system (DAQ) was constructed with the VME [52], TKO [53] and CAMAC [54] based front-end electronics. Schematic diagram of the DAQ is shown in Fig. 2.43.

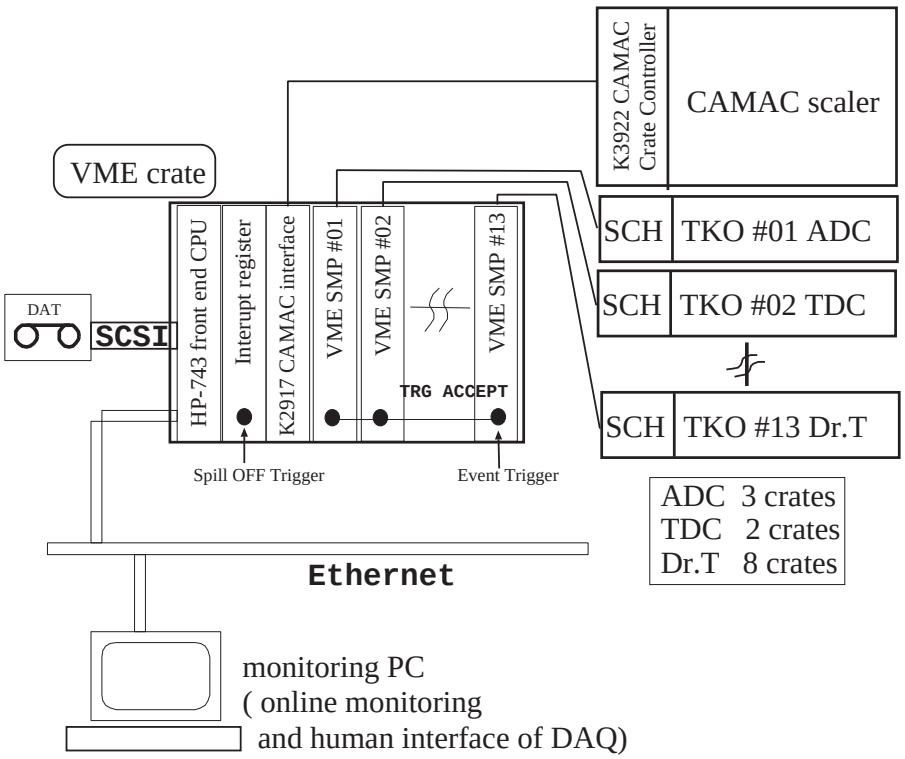

Figure 2.43: The schematic view of Data Acquisition System.

The Hewlett-Packard Model 743 (HP-743), VME on-board workstation, played a main role in the front-end data-acquisition system. There were 13 Super Memory Partner (SMP) modules and a Kinetic K2917 VME-CAMAC interface-board in the VME crate. There were also 13 TKO crates, 2 of them contain high resolution TDC's, 3 of them ADCs, and 8 of them TDC's for drift chambers (Dr.T). The SMP's work as an interface module between the VME bus and the TKO bus via the Super Controller Head (SCH) module which was installed in each TKO crate.

Once the trigger signal was supplied to the ACCEPT input in the front panel of SMP, data scanning for all the channels of ADC's and TDC's in the TKO boxes was performed by SCH's, and the scanned data were stored in the local memories in SMP's. A busy signal was issued by SMP's during the scanning of the data, and further triggers were prohibited by the trigger control system. The process was repeated during the spill on, and at the spill end, these stored data were read out by HP-743 via VME bus and written in the digital data storage (DDS-4) tape, as well as the scaler data via the VME-CAMAC interface boards connected to the Kinetic K3922 CAMAC crate controller.

Software for the data collection, recording, transfer and monitoring was written in programming language C/C++. The data collection process (collector), the recording process (recorder) and transfer process (sender) were also running on HP-743, on which HP-RT v2.0 was operated.

The "collector" read the accumulated data on SMP's and CAMAC scalers through the VME bus at the timing of the spill-end notified by the VME interrupt register. Device drivers for TKO and CAMAC on HP-RT, used in "collector", were developed by KEK on-line group. The data were written to the buffer area on the UNIX shared memory region in the format which has some additional informations like as run number, date and time, event-number and

headers/footers for decoding. The data buffering system is NOVA [55], which is implemented using UNIX shared memory for a local host environment, and TCP/IP (socket) for the network distributed machines. The buffer size for one event was 4 Mbyte and six buffers were kept.

The "recorder" read the data from NOVA and wrote to the DDS-4 drive connected to HP-743 via SCSI. The "sender" also read the data from NOVA and sent them to a PC for data monitoring via Ethernet by the subroutine in the NOVA system, which was implemented using UNIX socket.

For the data monitoring, IBM PC was used, on which Linux (kernel 2.2) was operated. All the data monitoring processes, "analyzer", "scaleranalyzer" and "visualscaler" are read the data from NOVA operated in the PC. The "visualscaler" displayed the scaler data tabularly spill by spill. The "analyzer" and "scaleranalyzer" read the event and the scaler data respectively, analyzed them and filled the HBOOK histograms, which were displayed by PAW [56] via "global memory" function in HBOOK [57] which is also implemented using UNIX shared memory.

The Graphical User Interface process to control and to monitor these many processes named "Z2" was written in the script language ruby/Tk. Typical view of the GUI environment on X window system [58] running on Linux on the monitoring PC is shown in Fig. 2.44.

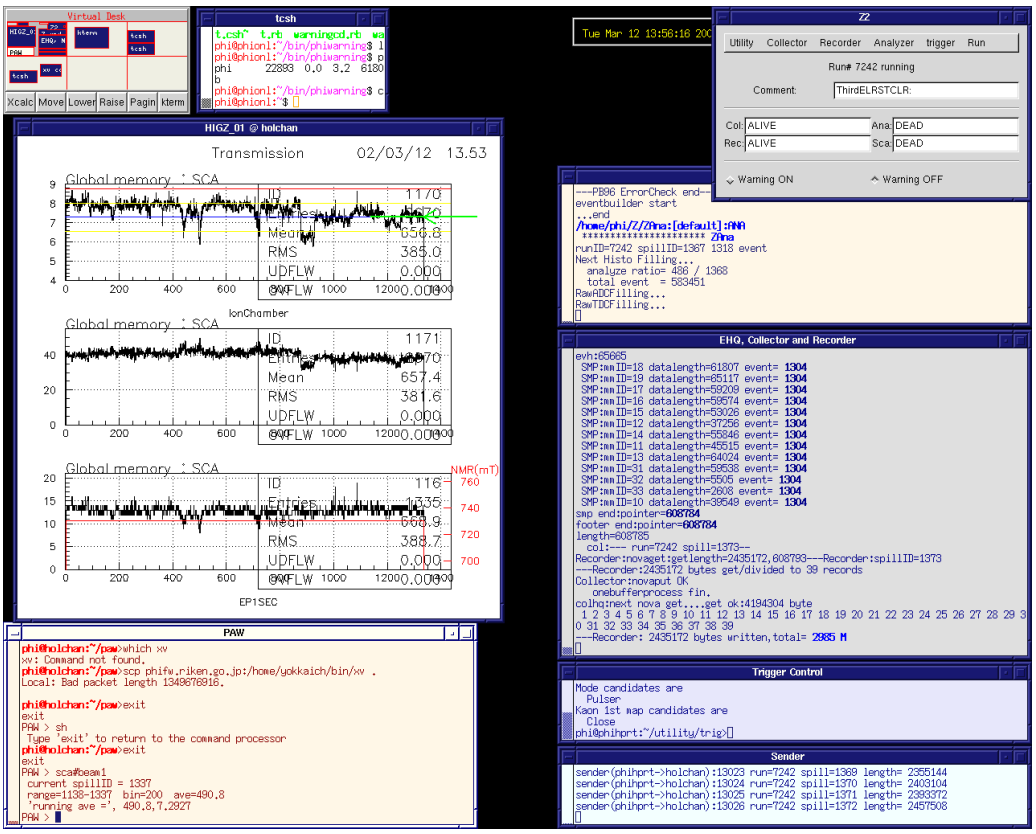

Figure 2.44: Screen shot of the GUI environment on X window system.

The typical data taking rate was 3 Mbyte/spill in a 1.8 sec-long spill, corresponding to about 1k event per spill, and the live time of the data acquisition system was about 56%.

The data are also transferred to Mass Storage system in a semi-realtime way. The recorded data on the DDS-4 tape are read out by another IBM PC (Linux) in the counting house, transferred to RIKEN-CCJ [59] via Internet using the command bbcp [60] and archived in HPSS [61] in CCJ. The typical transfer rate between KEK and RIKEN was about 2 Mbyte/sec. The amount of the data taken in 2001 was about 1.2 Tbyte, and in 2002 was about 1.1 Tbyte.

Chapter 3

Data Analysis

3.1 Outline of Data Analysis

The data described in this manuscript were taken for 34 days from November to December in 2001 and 32 days from February to March in 2002. The electron events were acquired in the year 2001 and 2002, and the kaon events were acquired in 2001. The number of beam protons on target and the number of triggered events in this period are summarized in Table 3.1.

year	number of beam protons	number of spills	averaged proton intensity	number of electron triggered events	number of kaon triggered events
2001	3.8×10^{14}	435k	8.7×10^{8}	3.1×10^{8}	2.1×10^{8}
2002	3.2×10^{14}	508k	6.4×10^{8}	5.1×10^{8}	-

Table 3.1: The number of beam protons and triggered events.

The calibration of the detectors is described in Sec. 3.2. We explain the calibration of the chambers, i.e., the iterative determination of the x-t relation, the position alignment of the tracking chambers, the energy gain calibration of the EM calorimeters, and the calibration of the kaon identification counters.

The track reconstruction using hits in CDC and BDC is described in Sec. 3.3.1. In the first step of the track finding, a track was approximated by a quadratic function in the horizontal plane which was perpendicular to the magnetic field and a straight line in the vertical plane. For the electron-triggered events, the events were required to have oppositely-charged tracks in different arm. For the kaon triggered events, the events were required to have more than two tracks in the kaon acceptance. In the next step, track candidates were fitted by the Runge-Kutta method over the magnetic-field map to determine the precise momenta and the trajectories of the charged particles. And then vertex position for each event was determined as described in Sec. 3.3.4.

Particle identification was performed as follows. For electrons, tracks were required to have position-matched hits in both the first and the second stage electron counters, certain pulse heights in associated FGC and RGC, and energy/momentum matching in the EM calorimeters as described in Sec. 3.3.5. We required at least one positron candidate and one electron candidate in each arm. For kaons, tracks were required to have position-matched hits in the scintillation counters without associated hits in AC. With the Time-of-Flight measurements, we identified kaons as described in Sec. 3.3.6, and a pair of positive and negative kaon was required. Because of small Q value in $\phi \to K^+K^-$ decay, such pairs were normally in a same arm. For the final electron or kaon pair tracks, we repeated the Runge-Kutta fit by requiring that both tracks from the pairs were originated from the same point on the target disks.

As described in Sec. 3.5, the event simulation was performed using Geant4.5.1.p01 [62] to evaluate all the detector effects, such as energy loss of particles, multiple scattering, and the tracking performance with the chamber resolution. An event generator is made by hand. The nuclear cascade code JAM (1.011.00) [63] was used mainly to generate the momentum distribution of mesons in the event generator. The mass shapes of the mesons used in the generator are discussed in the Sec. 3.5.

3.2 Calibration

3.2.1 Chamber TDC Calibration

For the drift time measurement, we used TKO 32CH DRIFT CHAMBER TDC(Dr.TII) modules produced by REPIC (RinEi Precision Instruments Corporation [64]). The full scale of this module is 1000 ns and typical time resolution is 350 ps. The time gain was calibrated using CAMAC TDC TESTER which is also produced by REPIC. The obtained time gain was typically 0.7 ns/channel.

We determined the relative time offset of all the CDC, BDC and VTC signals using drift time spectra. The time spectrum of each wire had an edge structure close to the wire as shown in the upper panel of Fig. 3.1. The peak position of the differentiated time spectrum (the lower panel of Fig. 3.1) provided the relative time offset in each signal.

This calibration was done run by run to cope with the temperature-dependent drift of delay in the signal cables and the common stop logic. The run dependence of time offset was shown in Fig. 3.2. The typical drift was within 3 ns.

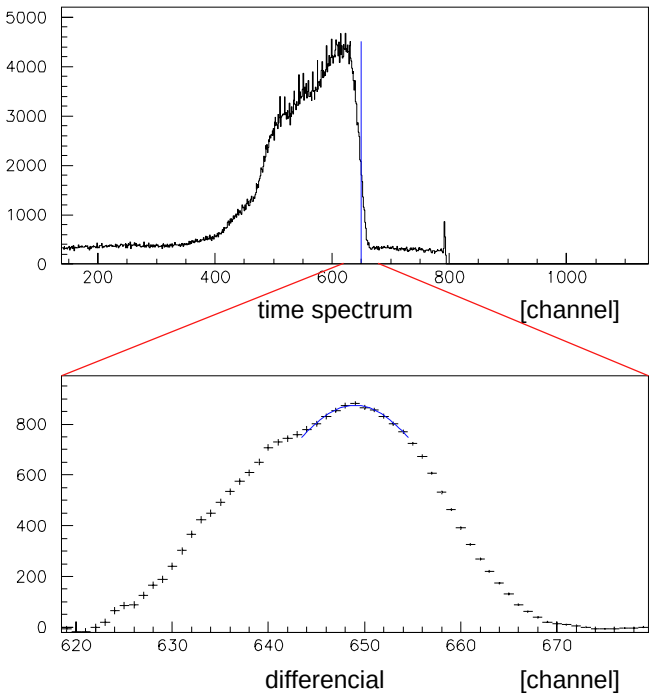

Figure 3.1: Typical TDC spectrum and its differential.

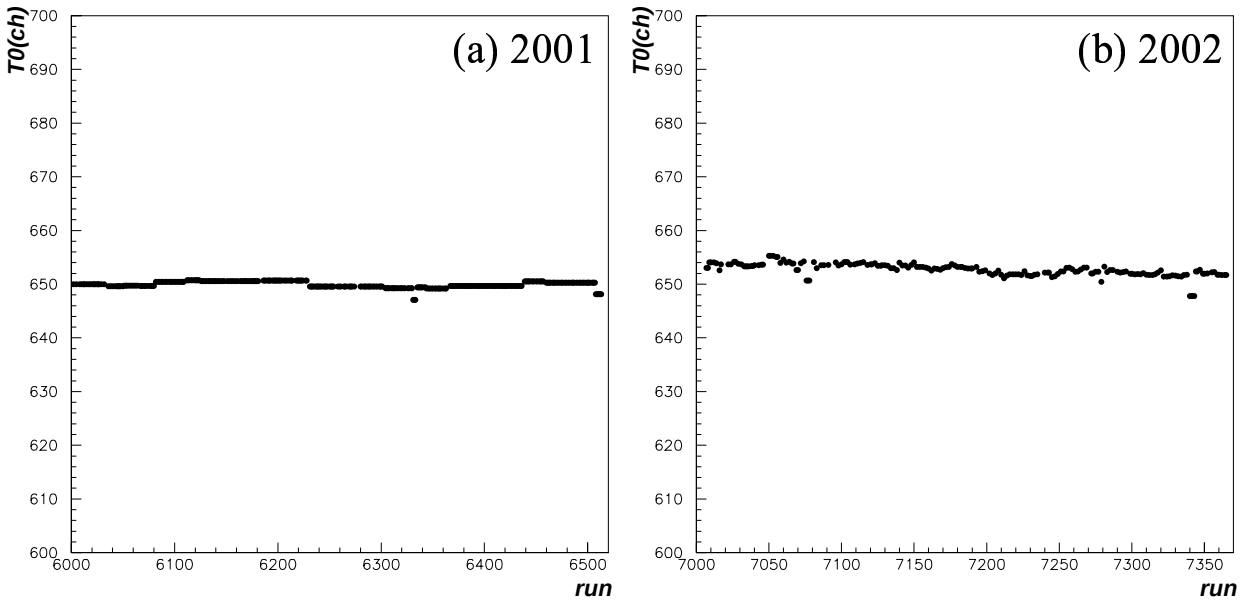

(a) the year 2001 (b) the year 2002

Figure 3.2: Run dependence of typical time-offset adjustment, (a) in the year 2001 and (b) in the year 2002.

3.2.2 Determination of Drift Length from Drift Time

To convert the measured drift time to the hit position in the cell, the relation of drift length (X) and drift time (T) was determined by the procedure described below. The initial parameterization of this relation was obtained with the drift chamber simulation code Garfield [47]. We iteratively adjusted the common time-zero offset and the scaling factors of drift velocity, by minimizing systematic shifts in the residuals as a function of the drift length between the hit points and the track positions obtained by the Runge-Kutta fitting. The incident angle dependence was small and neglected. After the calibration, we obtained the position resolution of 350 μm typically as shown in Fig. 3.3. Noted that the resolution in the Fig. 3.3(c) includes the precision of the Runge-Kutta fit and their intrinsic resolution.

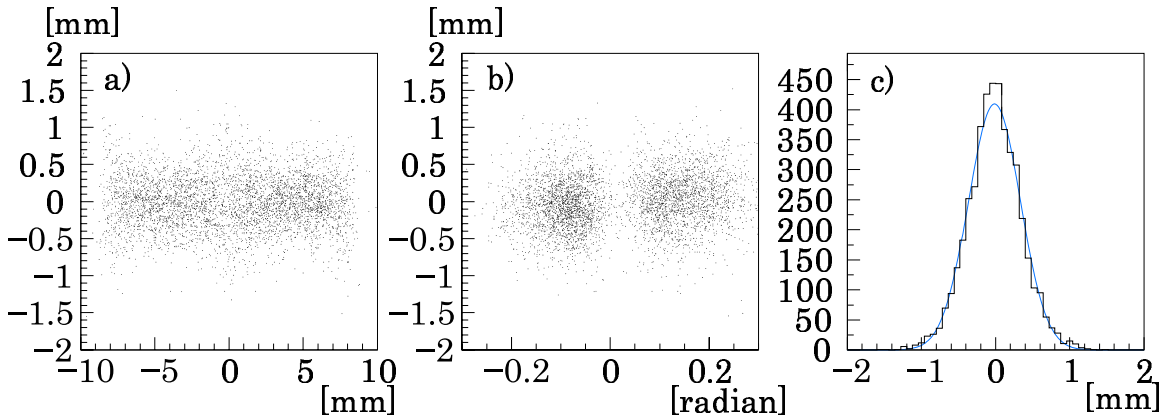

Figure 3.3: The correlations between the CDC residual as a function of the drift length (a) and of the incident angle of tracks (b). (c) shows the over all resolution.

3.2.3 Global Position Alignment

In the present analysis, the origin of the coordinate was set at the center of CDC. All the other chambers and counters were aligned to the CDC coordinate. The magnet position with respect to CDC was obtained by the survey performed before and after the beam time. The alignment of the BDC position with respect to CDC was also surveyed and refined using the data taken without the magnetic field. Since the trajectories of all the particles were straight, a linear equation was adopted as a track-fitting function.

In the alignment procedure, the residuals in BDC with respect to the straight track obtained with the CDC hits were systematically analyzed to determine 6 parameters which determines the three dimensional positions and rotations of BDC (see Appendix A in Ref. [35]). Hit associations to the tracks were required to be at least 5 out of 6 X-X′ layers and 3 out of 4 stereo layers in CDC and all the layers in BDC. The active area in BDC was divided into 30, 6 in horizontal and 5 in vertical. We obtained 6 parameters of the transfer matrix by minimizing the systematic shifts appeared in the horizontal matchings between CDC track and BDC hit in the 30 BDC regions. The residual distributions of the BDC hits to the CDC tracks after the alignment are shown in Fig. 3.4. The values of the shifts (dx, dy, dz) and the rotations (τ_x, τ_y, τ_z) for the run 2001 and 2002 are summarized in Table 3.2. Here rotation angles are defined around the 3 axes which cross the origin of the global coordinate (the center of CDC).

period	arm	dx [mm]	dy [mm]	dz [mm]	τ_x [$\times 10^{-3}$ rad]	τ_y [$\times 10^{-3}$ rad]	τ_z [$\times 10^{-3}$ rad]
I	L	$+2.40 \pm 0.90$	-0.85 ± 0.65	$+2.54 \pm 0.33$	-0.33 ± 0.55	$+1.59 \pm 0.59$	$+2.30 \pm 0.39$
	R	$+2.35 \pm 0.99$	$+0.47 \pm 0.70$	-0.35 ± 0.44	-0.19 ± 0.58	$+0.02 \pm 0.61$	-1.69 ± 0.37
II	L	$+2.30 \pm 0.92$	-0.62 ± 0.67	$+2.15 \pm 0.14$	-0.13 ± 0.37	$+1.33 \pm 0.35$	$+2.12 \pm 0.29$
	R	$+1.94 \pm 0.79$	$+0.47 \pm 0.58$	-1.06 ± 0.13	-0.24 ± 0.16	-0.22 ± 0.17	-1.49 ± 0.25
III	L	$+2.44 \pm 0.54$	-1.11 ± 0.42	$+2.60 \pm 0.15$	-0.20 ± 0.43	$+1.42 \pm 0.37$	$+1.08 \pm 0.20$
	R	$+2.20 \pm 0.73$	-0.05 ± 0.52	-0.39 ± 0.21	-0.38 ± 0.46	-0.24 ± 0.45	-2.79 ± 0.24

Table 3.2: The shifts and rotations parameters of BDC with respect to the nominal position. The unit of dx, dy and dz are [mm], and τ_x, τ_y and τ_z are [$\times 10^{-3}$ radian]. The period I corresponds to from run 6000 to 6292 in 2001, the period II from run 6293 to 6999 in 2001, and the period III from run 7000 to 7999 in 2002.

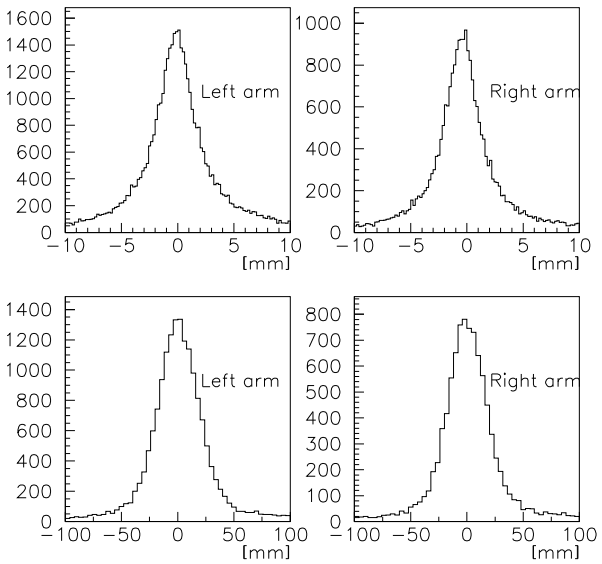

Figure 3.4: The residual distributions between BDC hit positions and the CDC extrapolated tracks. The upper figures show the residuals in the horizontal position at the BDC location, the lower are in the vertical position.

3.2.4 Gain Calibration of EM Calorimeter

The energy gain of each EM calorimeter was calibrated using the electron data sample. Since the energy deposit in calorimeters is linear to the momentum of the reconstructed track for electrons, we adjusted the gain of each segments so that the energy deposit divided by the track momentum (E/p) became unity. After the track reconstruction, segments of the calorimeters were associated to the track. Since a distribution of the energy deposit on the calorimeter spreads over a few segments, the pulse heights of the associated segments were summed up if the difference between the segment ID and a cross point of the associated track at the segment location was within $\pm$ 2.2, 2.0 and 2.5 segments for RLG, SLG and FLG, respectively. We calibrated the E/p ratio for the energy sums to be unity iteratively, thus the gain of any single segment should also be unity. Figure 3.5 shows the scatter plot of the energy deposit versus the track momentum. The peak positions of the Gaussian fit on the E/p distributions were adjusted to unity within 4% as shown in the Fig. 3.6.

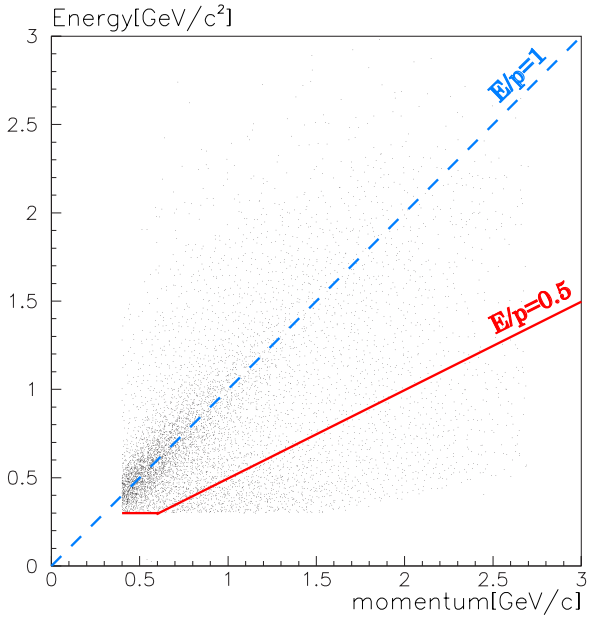

Figure 3.5: The correlation between RLG energy and momentum. The region $E/p > 0.5$ is chosen for the electron selection.

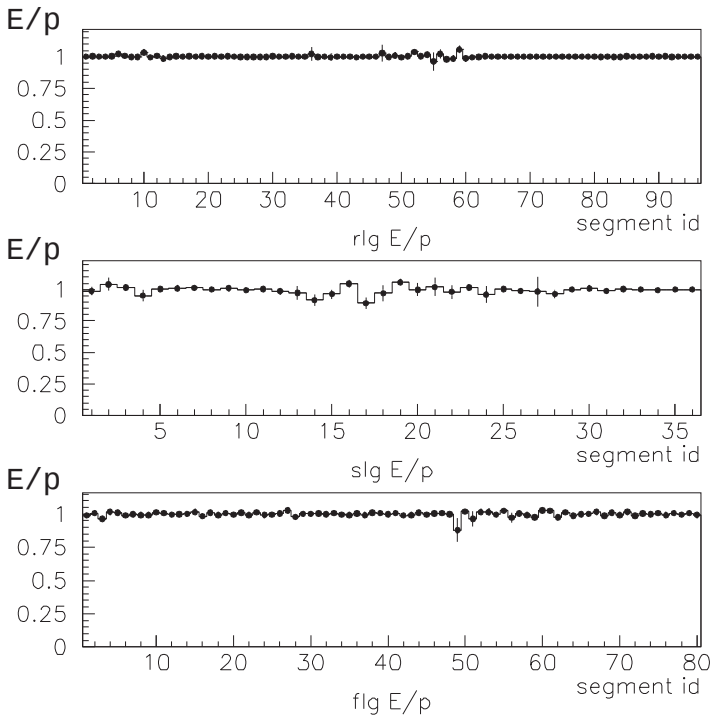

Figure 3.6: The E/p ratios in all the segments of RLG/SLG/FLG. The segment id is numbered from top to bottom PMT, from forward to backward, and from left to right arm. The error bars only show the statistical errors.

3.2.5 Slew Correction and Time Zero Calibration of Scintillation Counters

Since the transmission delays of the signals from the photomultipliers were different channels by channels and they could have some drift during the data taking period, we have chased the stability of the time zeros of all the TDC channels over the runs. We used negative pion to adjust the time zero of all the STC, FTOF and HC counters.

The negative tracks which had geometrically-matched hits in all the scintillation counters were selected to obtain negative pion tracks. We calculated the hit time of the FTOF counter ($T_{\rm FTOF}$) from the measured time ($T_{\rm measure}$) by

$$T_{\rm FTOF} = (T_{\rm measure} - T0) \times G_{\rm time} \tag{3.1}$$

where time zero ($T0$) was given temporarily and the time gain ($G_{\rm time}$) of TDC was measured for all the channels in advance. We also evaluated the hit time of STC and HC similarly, and we got the measured flight time between STC and FTOF as $T_{\rm FTOF} - T_{\rm STC}$.

We calculated the expected flight time $T_{\rm exp}$ from the momentum p and the flight length L assuming all the tracks were pion;

$$T_{\rm exp} = \frac{L}{(c \times \beta)}, \quad \beta = \sqrt{p^2/(p^2 + M_\pi^2)}\ , \tag{3.2}$$

where p and L were obtained by the Runge-Kutta fitting. We adjusted the center of the distribution of $T_{\rm exp} - (T_{\rm FTOF} - T_{\rm STC})$ within ± 50 psec for all the possible hit combinations by iteratively changing the time zeros (T_0) of STC and FTOF.

Another important correction for the flight-time measurements was time slewing which was caused because the timing of crossing the discriminator level is pulse-height dependent due to the signal rise-time. We corrected the time slewing with $1/\sqrt{A}$, where A is the ADC counts. The hit time of the STC counter $T_{\rm STC}$, for example, were thus obtained by

$$T_{\rm STC} = (T_{\rm measure} - T0) \times G_{\rm time} + \alpha/\sqrt{A_{\rm STC}}\ , \tag{3.3}$$

where α is the slewing-correction parameter. The correlation plot between $T_{\rm exp} - (T_{\rm FTOF} - T_{\rm STC})$ and $A_{\rm STC}$ before the slewing correction on STC is shown in Fig. 3.7(a) (the slewing correction on FTOF was already done.). The bottom figure shows averaged $T_{\rm exp} - (T_{\rm FTOF} - T_{\rm STC})$ as a function of $A_{\rm STC}$ with the best fit function of $\alpha/\sqrt{A_{\rm STC}} + T0$. We can see the correlation is well described with this function. After the slewing correction on STC, the distribution of $T_{\rm exp} - (T_{\rm FTOF} - T_{\rm STC})$ was improved as shown in Fig. 3.7(b). The pulse height dependence of the timing was diminished. The slewing correction was done for all the STC and FTOF segments, and we have achieved the time resolution of 400 psec as shown in Fig. 3.8 for any combination of the STC and FTOF counters. This value was used in the detector simulation as the resolution of time of the flight measurements.

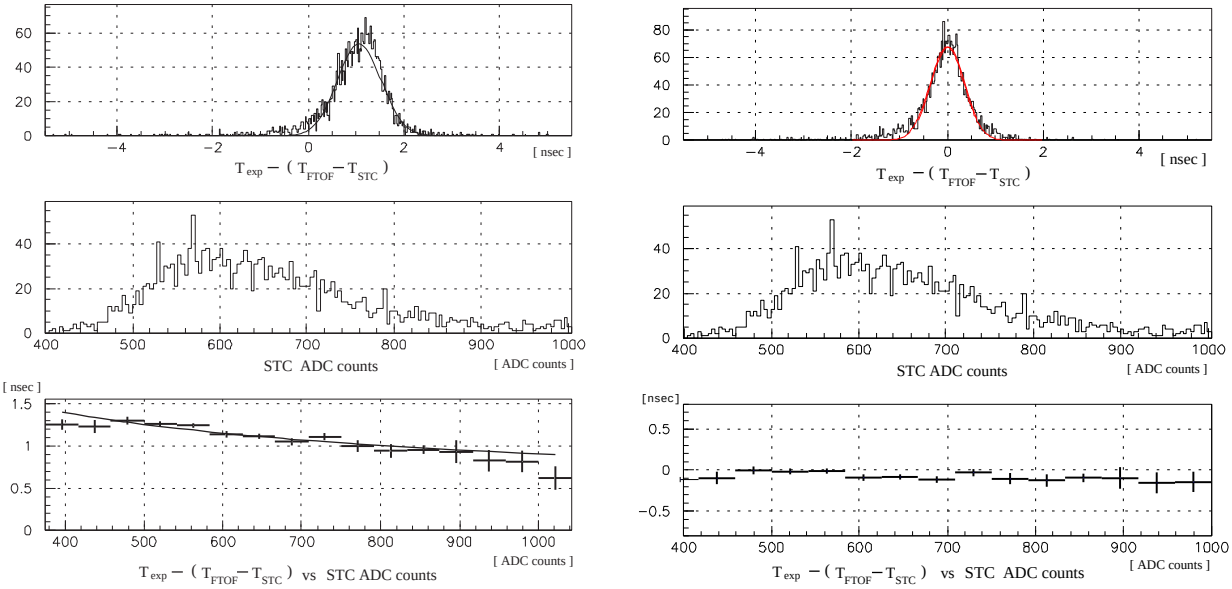

(a) before slewing correction

(b) after slewing correction

Figure 3.7: (a)Before the STC slewing correction, the distribution of the time difference between the measured time and the expected time is shown at top. The ADC distributions at middle, and the slewing effect at bottom. (b)As same as (a) but after the STC slewing correction.

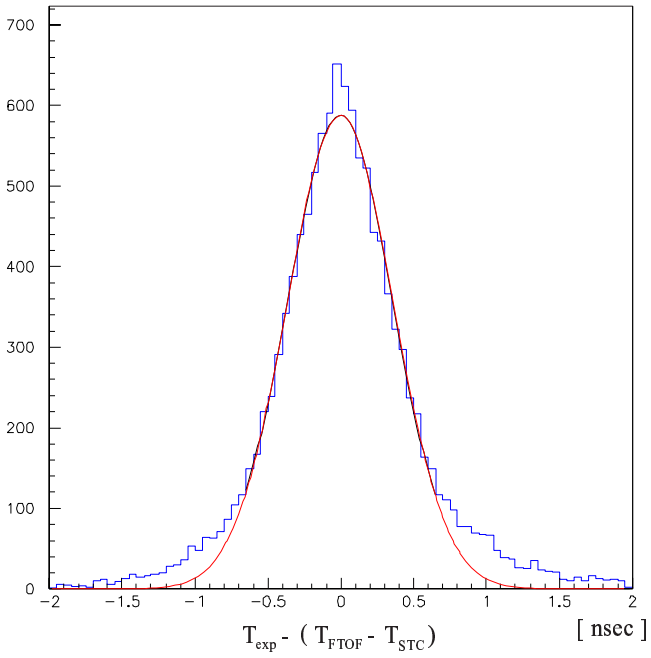

Figure 3.8: The resolution of the flight time measurements of any combinations between the STC and FTOF counters after the slewing correction.

3.3 Event Reconstruction

3.3.1 Track Reconstruction

As described in Chap. 2, CDC had 10 layers of drift cells which were grouped into 3 super-layers. Track candidates were searched using the X and X′ layers in each super-layer. Since we cannot determine whether the drift direction is left or right without track fitting, each hit was treated as 2 independent hits in both sides of the sense wire. To reduce CPU time for the track finding, a hit combination in the X and X′ layers was regarded as a hit pair with the position at the center of the 2 hits. A hit without an associated hit in the adjacent layer was also kept as a hit-pair candidate.

All the possible combination of 3 hit-pair candidates over the 3 super-layers was regarded as a track candidate if the following conditions were satisfied:

(a) The track candidate included 5 or more hits in the X-X′ layers.

(b) Since the magnetic field was almost constant at the location of CDC, a trajectory of a charged particle was approximately a circle in the x-y plane and a straight line in the r-z plane. The circle which passes over the 3 hit-pair combinations gives the simple track momentum on the x-y plain. This momentum should be greater than 0.35 GeV/c.

(c) The circle should cross the target region within a distance of 50 mm from either of the center, the most upstream or the most downstream target.

(d) The local vector which is determined by the 2 hits in a pair should be consistent with the tangent of this circle within 0.4 radians.

Next, associated hits in the tilt layers were searched for each track candidate. Since there was a pair of the V-V′ layers in the middle super-layer, hit pairs were made similarly to the X-X′ layers. The search region of hit points in the tilt layers was limited within the neighboring 5 cells which were determined by the tilt angle of 0.11 radian. The three-dimensional track candidate required 3 or more hits from the 4 tilt layers. In the X-X′ layers, 5 hits were required out of 6 layers. Now the track candidates were fit with a quadratic function in the horizontal plane and a straight line in the vertical plane.

Track candidates in BDC were searched independently. As least 3 hits out of 4 in the BDC layers (X, X′, U, V) were required to form a track segment in BDC. The combination of X and X′ was only made if they were apart less than a quarter of a cell, otherwise they were treated as 2 independent hits. Associated U and V hits were required to be in the neighboring 9 cells from the hit position in the X-X′ plains, which was determined by the tilt angle of 0.11 radian. If a track segment in BDC has both U and V hits, the vertical heights determined from X-X′-U and X-X′-V combinations were required to be within ± 290 mm.

Then the CDC track was extrapolated to BDC, where we required the horizontal position matching of ± 1.2 BDC cells and the height (z) matching of 100 mm. The track segments in BDC were fitted with a linear function with the constraint of the vertical angle given by the CDC track, and we required the residual of each hit of BDC did not exceed 0.2 BDC cells.

At this point, there were so many track candidates which could not be fitted with the Runge-Kutta method in limited CPU time. So we selected tracks with the best χ^2 of the fitting among those who shared the same combinations of hits in CDC and BDC cells but with different drift directions.

All the track candidates obtained in CDC with a connection to a BDC track segment were fit with the Runge-Kutta method to determine the refined momentum and the precise trajectory. The particle trajectories were traced in a 50 mm step through the magnetic field map described in Sec. 2.3. The Runge-Kutta track tracing started from the surface of a virtual cylinder with

a diameter of 100 mm located at the center of the magnet. The initial starting point and the initial momentum vector for the minimization were given by the track finding process. In each trace by the Runge-Kutta method, a reduced χ^2 was calculated for all the hit along the track. The χ^2 value was minimized with a help of the minimization code MINUIT [65].

Finally, if there were 2 or more track candidates sharing more than 2 common hits in CDC and BDC, we selected the track candidate with the best χ^2 in the Runge-Kutta fitting and discarded others. The reduced χ^2 distribution of the final sample is plotted in Fig. 3.9. We used the tracks whose reduced χ^2 was less than 5 for the later analysis.

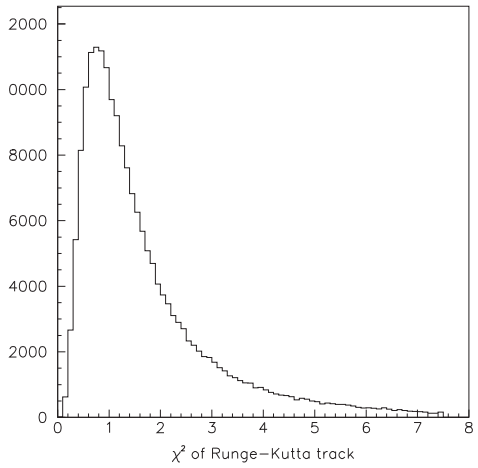

Figure 3.9: Reduced χ^2 distribution in the Runge-Kutta fitting.

3.3.2 Chamber Efficiency and Resolution

Chamber Efficiency

We evaluated the each layer efficiency, $\mathcal{E}(layer)$, defined as

$$\mathcal{E}(layer) = N_{\rm all}/(N_{\rm all} + N_{\rm off}(layer)). \tag{3.4}$$

Here, $N_{\rm all}$ denotes the number of tracks having hits in all the layers of the chambers (VTC-forward+CDC+BDC or VTC-backward+CDC+BDC) [1]. And $N_{\rm off}(layer)$ denotes the number of track missing only one hit in the relevant *layer*. The results are summarized in Table 3.3.

Chamber Resolution

We evaluated the resolution of each chamber layer as follows.

1. We obtained the chamber residual and the track χ^2/N distribution in the final e^+e^- sample (shown as DATA in Fig. 3.10).

2. The e^+e^- pairs from the ϕ mesons which were generated by JAM were traced in the detector simulation using Geant4 as described in Sec. 3.5.

[1] The VTC hit candidates were searched from the CDC-BDC tracks, which were obtained from the Runge-Kutta fit using the CDC and BDC hits as described above. The tracks were extrapolated to VTC, and we required the horizontal position matching in VTC within ± 1.5 VTC cells. The associated hits, which were required 1 or more hits from the 3 layers either in the forward layers or the backward layers, were fitted with the Runge-Kutta method together with the CDC and BDC hits.

super layer	layer	efficiency [%]
VTC backward	(X,X′,X)	(73.5, 64.7, 52.4)
VTC forward	(X,X′,X)	(92.4, 100.0, 93.3)
CDC inner	(X,X′,U)	(96.1, 96.8, 90.2)
CDC middle	(X,X′,V,V′)	(94.6, 95.7, 94.6, 93.1)
CDC outer	(U,X,X′)	(97.2, 95.7, 94.2)
BDC	(X,X′,U,V)	(99.0, 99.1, 99.0, 96.8)

Table 3.3: Estimated efficiency of each chamber layer.

3. The chamber hits obtained from the simulation were smeared with a double Gaussian distribution to reproduce the chamber residual and the track χ^2/N distribution in the data. For the main component of the double Gaussian, we applied an independent width (σ_1) to each layer. For the second component, which was wider than the main component, we applied a common width (σ_2) and a common second/main ratio within a super layer.

4. The simulated hits were reconstructed as same as the real-data analysis, and the hit residual and the track χ^2/N distribution were obtained (shown as MC in Fig. 3.10).

5. The chamber residual and the track χ^2/N distribution were compared between DATA and MC, and we iteratively adjusted the chamber resolution until MC reproduced DATA.

The typical chamber residual and track χ^2/N distribution for DATA and MC are shown in Fig. 3.10, and the results are summarized in Table 3.4. Similar procedure was repeated for the K^+K^- pairs using Table 3.4, and the results are shown in Fig. 3.11.

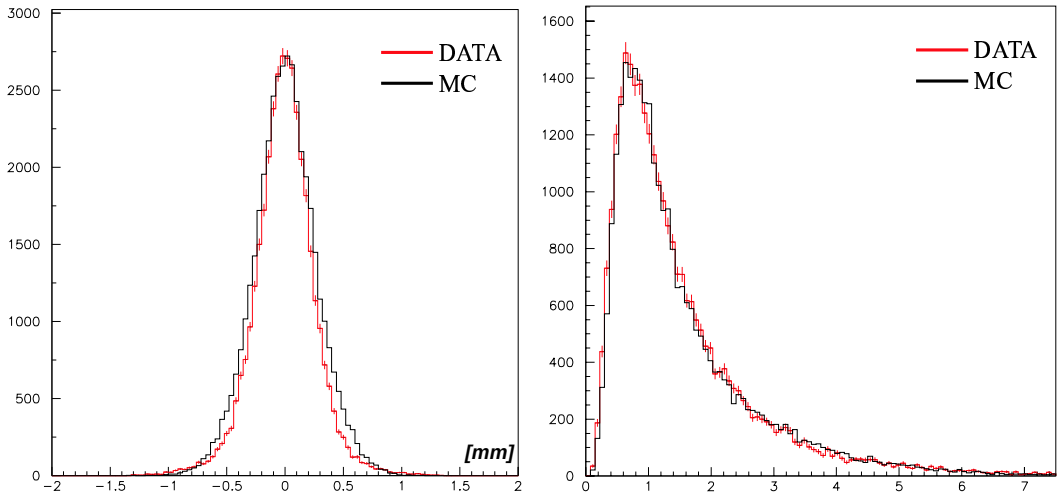

(a) chamber residual (b) track χ^2/N

Figure 3.10: The typical chamber residual and track χ^2/N distribution for the data (DATA) and the tuned detector simulation (MC) in the final e^+e^- sample.

super layer	layer	σ_1 [mm]	σ_2 [mm]	ratio
VTC backward	(X,X′,X)	(0.389, 0.394, 0.429)	0.75	0.37
VTC forward	(X,X′,X)	(0.174, 0.212, 0.183)	0.75	0.37
CDC inner	(X,X′,U)	(0.197, 0.203, 0.286)	0.595	0.436
CDC middle	(X,X′,V,V′)	(0.238, 0.217, 0.183, 0.181)	0.644	0.367
CDC outer	(U,X,X′)	(0.285, 0.212, 0.261)	0.718	0.395
BDC	(X,X′,U,V)	(0.292, 0.289, 0.340, 0.261)	0.661	0.488

Table 3.4: Estimated resolution of the chamber layers. The values σ_1 are the widths for the main component of the double Gaussian distribution, σ_2 are those for the second component, and "ratio" are the second/main ratios.

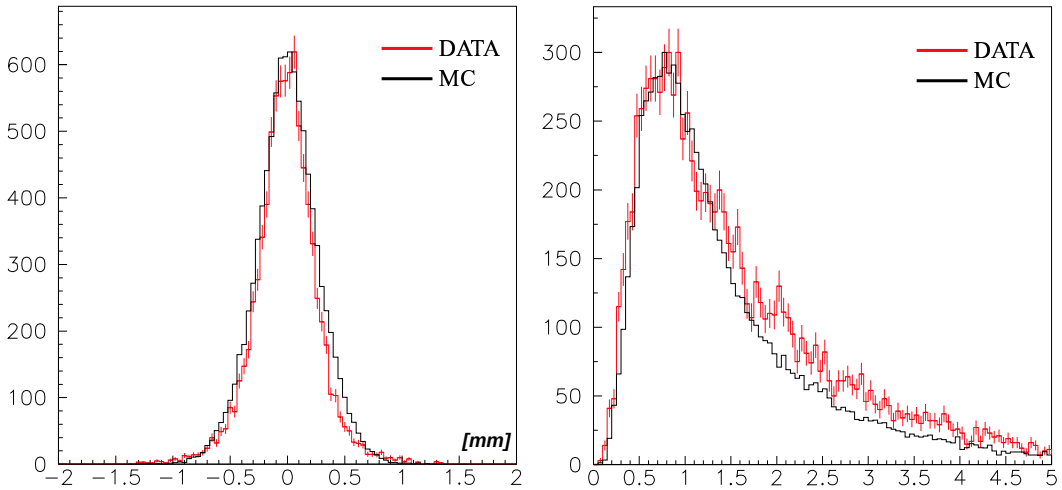

(a) chamber residual (b) track χ^2/N

Figure 3.11: The typical chamber residual and track χ^2/N distribution for the data (DATA) and the tuned detector simulation (MC) in the final K^+K^- sample.

3.3.3 Mass Scale and Resolution

To evaluate the performance of the spectrometer, the mass resolution was examined for the observed peaks of $\Lambda \to p\pi^-$ and $K^0_s \to \pi^+\pi^-$ decays as shown in Fig. 3.12. The observed peak widths and centroids of the mass spectra were compared with the expectations from a detailed detector simulation described in Sec. 3.5. In the simulation, the three-momentum distributions of daughter particles were tuned to reproduce the data. The effects on the invariant mass spectrum caused by multiple scattering and energy loss of particles, the tracking performance with the chamber resolution, and a miss-alignment of the tracking devices were minutely inspected. The expected peak position and resolution of K^0_s are 496.9 MeV/c^2 and 3.5 MeV/c^2, whereas the measured peak position was 496.8 $\pm$ 0.2 MeV/c^2, with the Gaussian σ of 3.9 $\pm$ 0.4 MeV/c^2. The simulated spectrum reproduces the data almost perfectly as shown in Fig. 3.12. Note that the non-Gaussian shape of the Λ peak is well reproduced with the simulated shape [2].

[2]When we fit the shape by a Gaussian only around the peak, the expected peak position and Gaussian σ are 1115.52 MeV/c^2 and 1.63 MeV/c^2, whereas the obtained values were 1115.62 $\pm$ 0.02 MeV/c^2 and 1.78 $\pm$ 0.04 MeV/c^2.

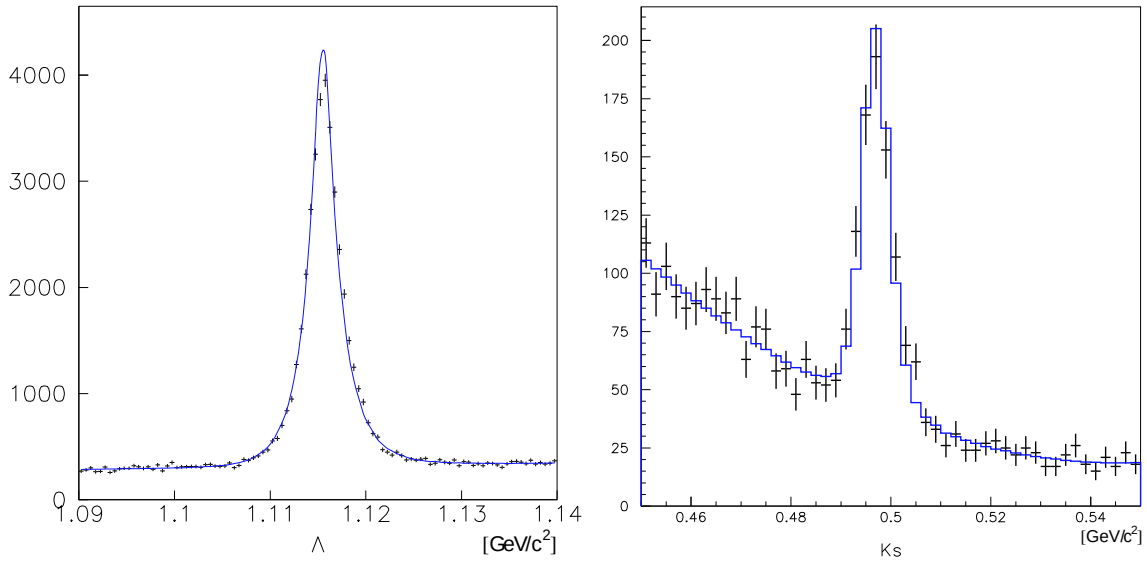

(a) $\Lambda \to p\pi^-$ (b) $K^0_s \to \pi^+\pi^-$

Figure 3.12: (a) Invariant Mass spectrum of p π^- showing the Λ peak. The curve is the fit result with the simulated mass shape over a linear background. (b) Invariant Mass spectrum of $\pi^+\pi^-$ showing the K^0_s peak. The curve is the fit result with the simulated shape over a quadratic background.

3.3.4 Vertex Reconstruction

The vertex point of the interaction in each event was determined by minimizing S, the weighted quadratic sum of the distances from the vertex to each track, which was defined as;

$$S = (\sum_{j=1}^{N_t}[(d^j_x/\sigma_x)^2 + (d^j_y/\sigma_y)^2 + (d^j_z/\sigma_z)^2])/(3N_t - 4), \tag{3.5}$$

where N_t is the number of the tracks, d^i_j(i=x, y, z) is the distance between the vertex point and the nearest point of the j-th track in each axis, and the weight σ_i represents the error in the track-vertex determination in each axis. The weights σ_i were determined as $\sigma_x = 1.14$ mm, $\sigma_y = 1.80$ mm, and $\sigma_z = 7.15$ mm. We examined the quality of the determined vertex by requiring the equation below to be satisfied to each track-j.

$$(d^j_x/3\sigma_x)^2 + (d^j_y/3\sigma_y)^2 + (d^j_z/3\sigma_z)^2 < 1.0. \tag{3.6}$$

We discarded tracks which did not satisfy this requirement, and re-determined the vertex from the remained tracks by repeating the same procedure. We determined the spatial points with the minimum S with use of MINUIT [65].

The reconstructed vertex distributions for double-arm e^+e^- events are shown in Fig. 3.13. The obtained target positions and the vertex resolution are listed in Table 3.5. We required the vertex to be inside the rectangles shown in Fig. 3.13 in the x-y plane which corresponded to 3 σ cuts, and in the vertical (z) axis within 3 σ_z. The reconstructed vertex distributions for single-arm K^+K^- events are also shown in Fig. 3.14. When the two tracks were in the same arm, the accuracy of the vertex point determinations got worse due to a narrow opening angle between the two tracks. So we used the target-image distribution viewed from the direction of the kaon arm as shown in Fig. 3.14(b). We required the vertex to be inside the rectangles shown in Fig. 3.14(b) in the x-y plane, and in the vertical (z) axis within $\pm$ 10 mm.

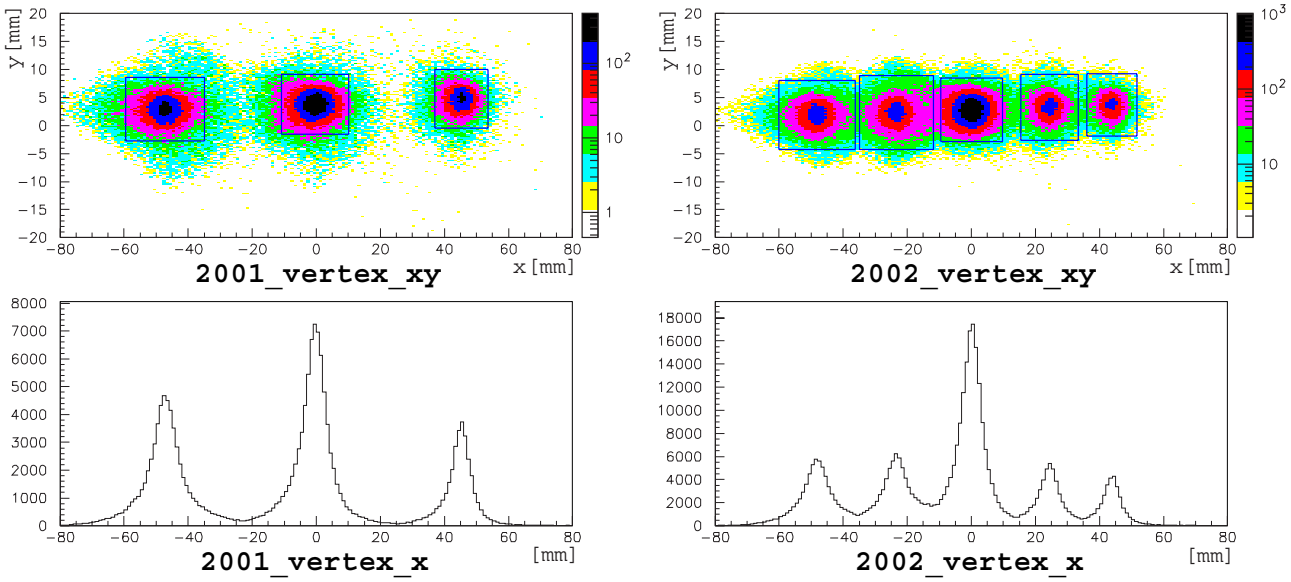

Figure 3.13: Vertex distribution for double-arm e^+e^- events in 2001 (left) and 2002 (right). Vertex distribution in the xy-plane (upper) and the projection in the x-axis (lower). The indicated rectangles in the upper figure are the cut regions for the vertex position in the x-y plane.

year	2001			2002				
target	Cu1	C	Cu2	Cu1	Cu2	C	Cu3	Cu4
x [mm]	−47.04	−0.14	45.46	−48.03	−23.41	0.17	24.6	44.21
y [mm]	3.18	4.03	4.91	0.89	1.31	1.72	2.22	2.57
z [mm]	0.61	0.62	0.67	0.55	0.54	0.52	0.54	0.57
σ_x [mm]	3.73	3.48	2.71	3.21	3.35	3.20	1.98	2.01
σ_y [mm]	3.24	3.74	2.41	1.93	2.27	1.97	2.94	2.61
σ_z [mm]	3.68	3.70	3.14	4.33	4.54	3.85	3.98	3.74

Table 3.5: The mean values (target position) and precisions of the vertex determination for double-arm e^+e^- events.

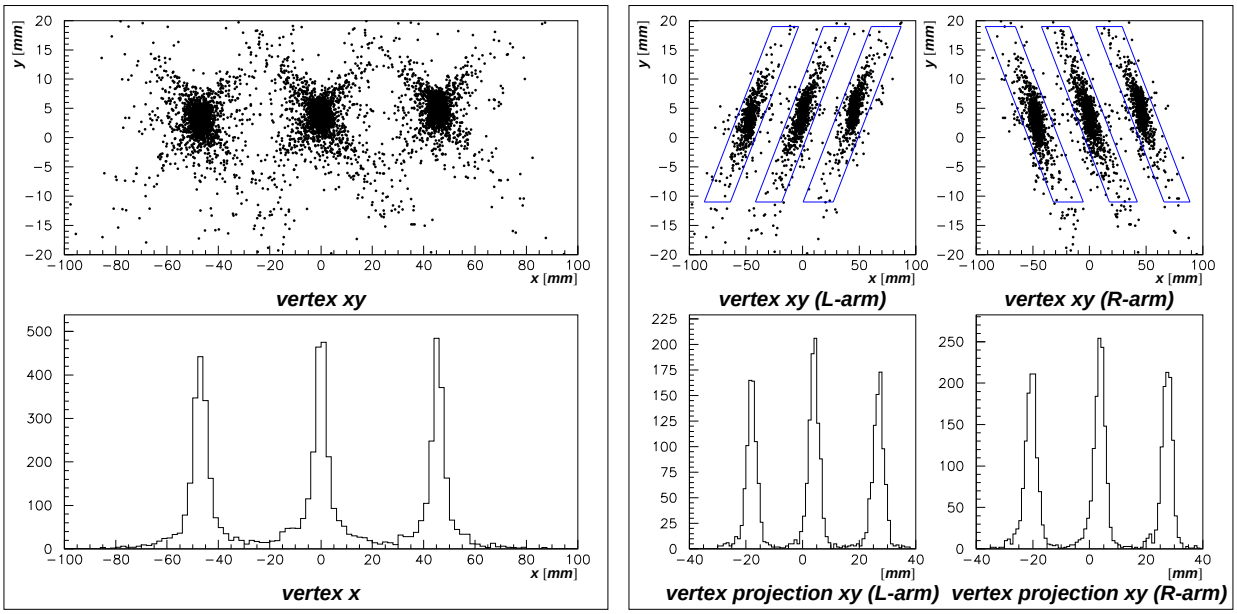

(a) (b)

Figure 3.14: Vertex distribution for single-arm K^+K^- events in 2001. (a)Vertex distribution in the xy-plane (upper) and the projection in the x-axis (lower). (b)Vertex distribution in the xy-plane (upper) and the projection in the direction of the corresponding arm (lower). The left figure is for left arm events, the right figure is for right arm events. The indicated rectangles in the upper figure are the cut regions for the vertex position in the x-y plane.

For the final e^+e^- and K^+K^- pair tracks, we repeated the Runge-Kutta fit procedure, which was named as "Common Vertex Track Fitting", by requiring that both tracks were originated from the same point of particular target plate determined as described above. The x positions (beam direction) of the targets were fixed to the measured values on Table 3.5. In this fit, we minimized the quadratic sum of residuals at all the hit layers of the chambers and residuals at the vertex point from the nominal beam position in the y and z directions. The weights for the vertex position in the y and z directions were set to be the one standard deviation of the beam size, 1.59 mm in 2001 and 0.83 mm in 2002, which was described in Sec. 2.4.2. Since the beam size was measured only in the y direction, we assumed that the size in the z direction was same as that in the y direction. This procedure improved the mass resolution for e^+e^- events 1.5 times, and for K^+K^- events 1.2 times.

3.3.5 Electron Identification

The electron identification was performed with 2 or 3 stages of the iso-butane-filled gas-Čerenkov counters and the lead-glass EM calorimeters in the momentum range from 0.4 to 2.7 GeV/c. The lower limit is determined by the trigger condition in which a geometrical matching of 2 stages of the electron ID counters was required. The upper limit is the momentum where pions started to produce Čerenkov light in iso-butane. The observed momentum distributions of electrons and positrons are shown in Fig. 3.15.

The horizontal position matching between the Runge-Kutta tracks and the electron identification counters is shown in Fig. 3.16. We defined the matching window to be within ± 1.0 counter size for all the counters.

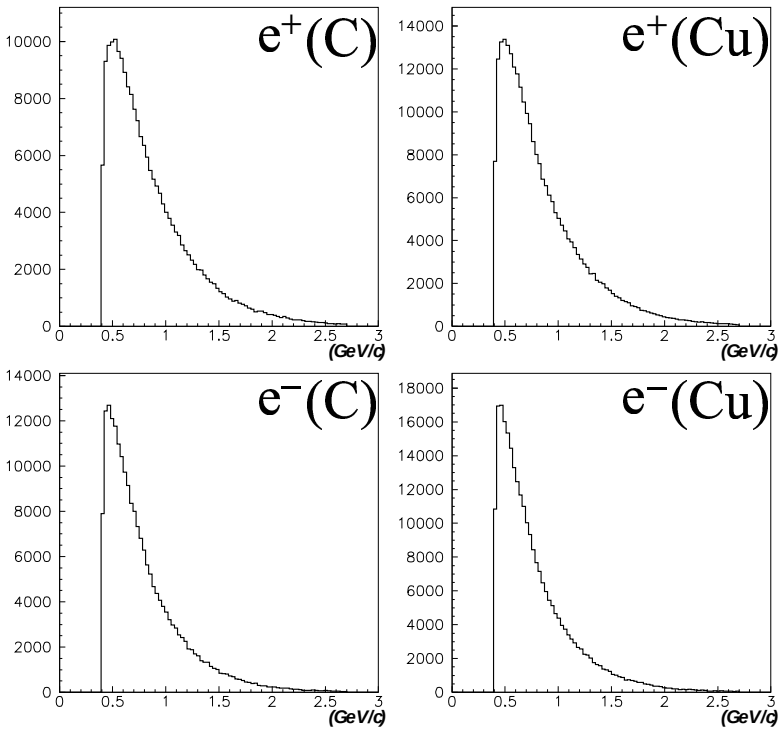

Figure 3.15: The momentum distributions of electrons in the final sample. The upper figures are for e^+ and the lower figures are for e^-. The left figure is for the C targets and the right figure is for the Cu targets.

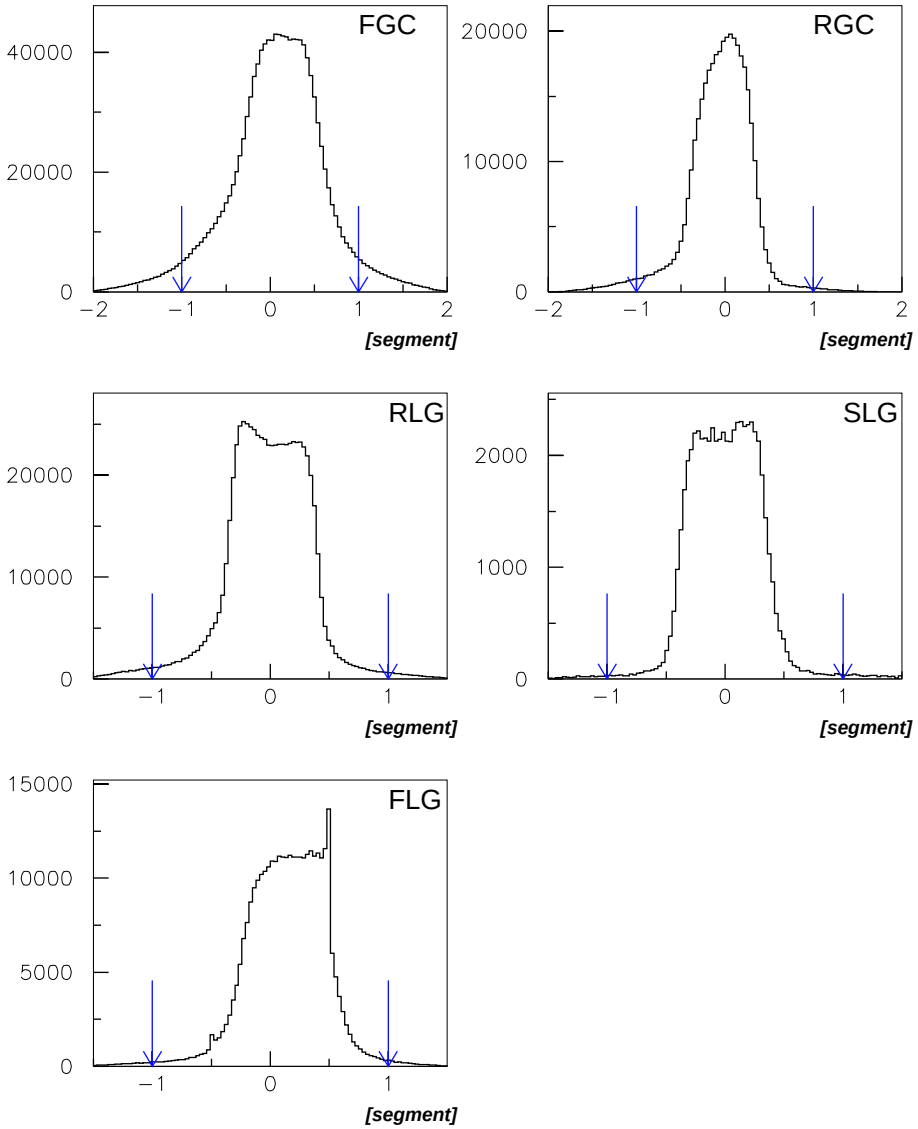

Figure 3.16: Horizontal matching between electron tracks and electron-counter hits in the final e^+e^- sample. The arrows indicate the region for the electron selection, and the x coordinate is in a unit of the counter size.

Electron Identification with Gas Čerenkov Counters

For FGC, the horizontal matching was examined at r = 1200 mm. We required that ADC sums from the top and the bottom photomultipliers to exceed 200 channels. The gain of FGC was calibrated using the ADC distribution. We required the time difference between the measured TOF value ($T_{\rm FGC} - T_{\rm STC}$) and the expected TOF value ($T_{\rm exp}$) to be within ± 10 ns, as shown in Fig. 3.17. Since the vertical acceptance of FGC is ±0.4 radian, we required the dip angle of the track to be within ±0.45 radian.

For RGC, the horizontal position matching was examined at r = 2105 mm as shown in Fig. 3.16. The RGC hit was defined when the ADC sum from the top and the bottom photomultipliers of the associated segments exceeded 50 channels, which corresponds to about one photo-electron. The time difference was required to be within ± 10 ns, as FGC. Since the vertical acceptance of RGC is ±0.1 radian, we required the dip angle of the track to be within ±0.15 radian.

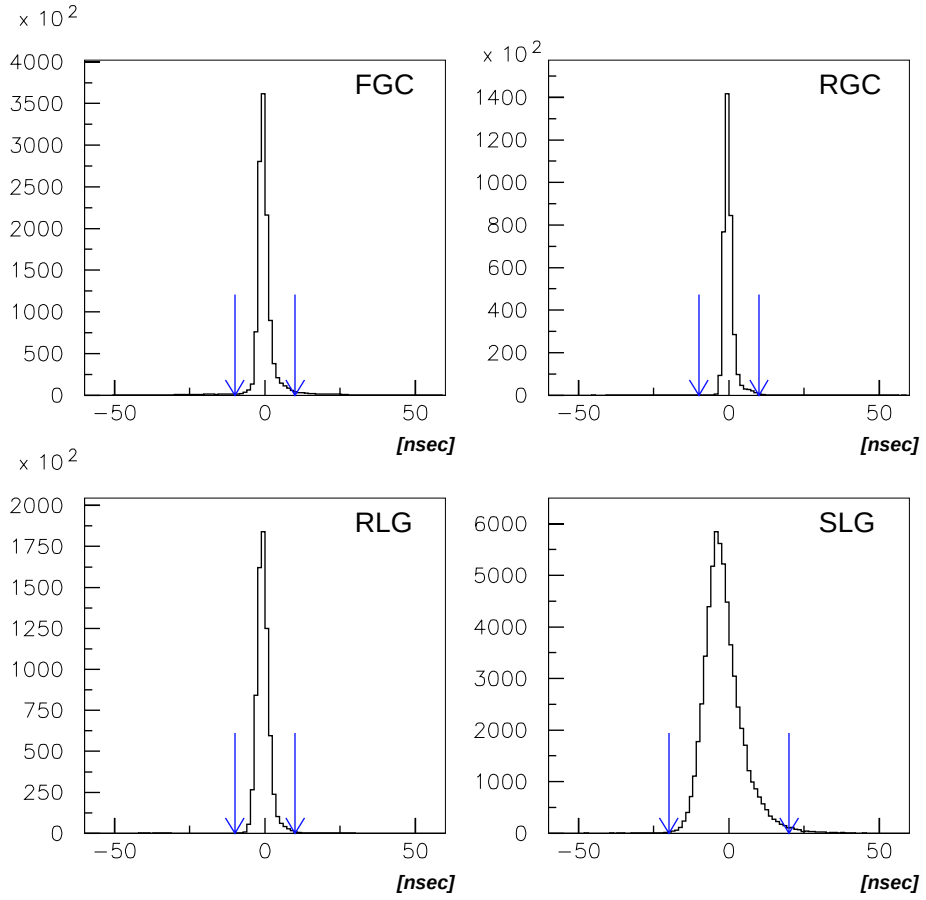

Figure 3.17: The time difference between the measured TOF value ($T_{\rm counter} - T_{\rm STC}$) and the expected TOF value ($T_{\rm exp}$). The arrows indicate the region for the electron selection.

Electron Identification with Lead Glass Calorimeters

The tracks were selected as an electron in RLG, SLG or FLG when the sum of the energies from the horizontally-associated three segments exceeded 0.3 GeV and the energy over the momentum (E/p) was greater than 0.5, as shown Fig. 3.18.

The time difference between the measured TOF value ($T_{\rm RLG} - T_{\rm STC}$) and the expected TOF value ($T_{\rm exp}$) to be within ± 10 ns. For SLG, the time difference was required to be within ± 20 ns. Since the vertical acceptance of RLG is 270 mm < z < 880 mm and –880 mm < z < –270 mm from the beam line as shown in Fig. 2.2, we required the vertical position of the track at RLG, at r = 1730 mm, to be in the range from ±170 mm to ±980 mm, including 100 mm as a margin. Similarly, the vertical position of the track was required to be in the range from –575 mm to +575 mm for FLG, since the vertical acceptance of FLG is from –475 mm to +475 mm. The dip angle of the track which was associated to SLG was required to be within ± 0.45 radian.

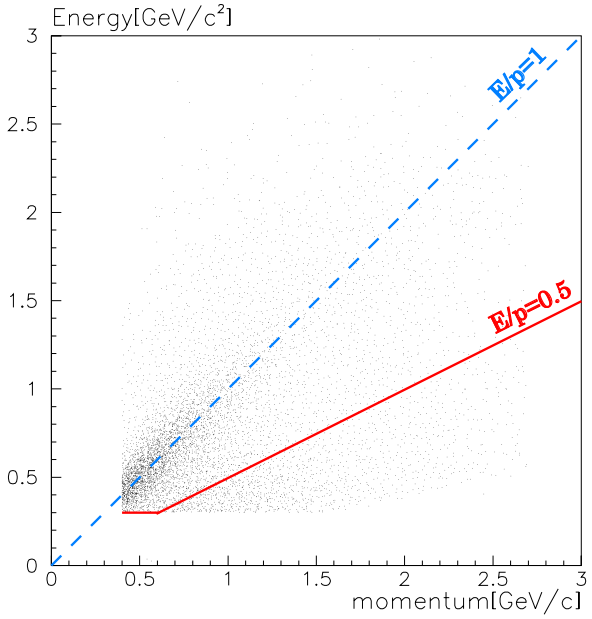

Figure 3.18: The correlation between RLG energy and momentum. The region $E/p > 0.5$ is chosen for the electron selection.

Efficiency of Electron Identification

To evaluate the efficiency of the electron identification, we used a pure electron sample extracted γ-conversion and Dalitz decay electrons in the data. To eliminate the trigger-bias, the following procedure was taken. At first, one e^+ track and one e^- track which satisfied the triggered condition were excluded. If there were two or more e^+ or e^- tracks which satisfied the trigger condition in the same event, one of them was randomly selected and excluded as the trigger particle. For the remaining tracks, we required that they had a partner track with which the opening angle was less than 0.01 radian and the invariant mass was less than 0.01 GeV/c^2, to ensure that they were originated from Dalitz decays or γ-conversions. The opening angle and the invariant mass distributions of those no-bias electrons are shown in Fig. 3.19(a) and (b), respectively. Electrons from γ-conversions and Dalitz decays appear as a clear peak at a zero mass. Using these no-bias electrons, the electron identification efficiencies were obtained. Figure 3.20 shows energy-momentum correlation of the pure electron sample.

The electron identification efficiency as a function of the momentum of pure electrons is shown in Fig. 3.21. The efficiency curves were fitted with a phenomenological function;

$$f = a - b/p^c, \tag{3.7}$$

where a, b, c are the fit parameters, and p is the momentum of electrons. The obtained parameters are listed in Table 3.6(a) and the curves are plotted in Fig. 3.21. These efficiency functions were used in the detector simulation to take into account an effect of the electron identification efficiency. For single electron tracks in the final e^+e^- sample, the averaged efficiencies including the off-line cuts were summarized in Table 3.6(b). Using the detector simulation (see Sec. 3.5), the efficiency for $\phi \to e^+e^-$ decays was estimated to be 33%.

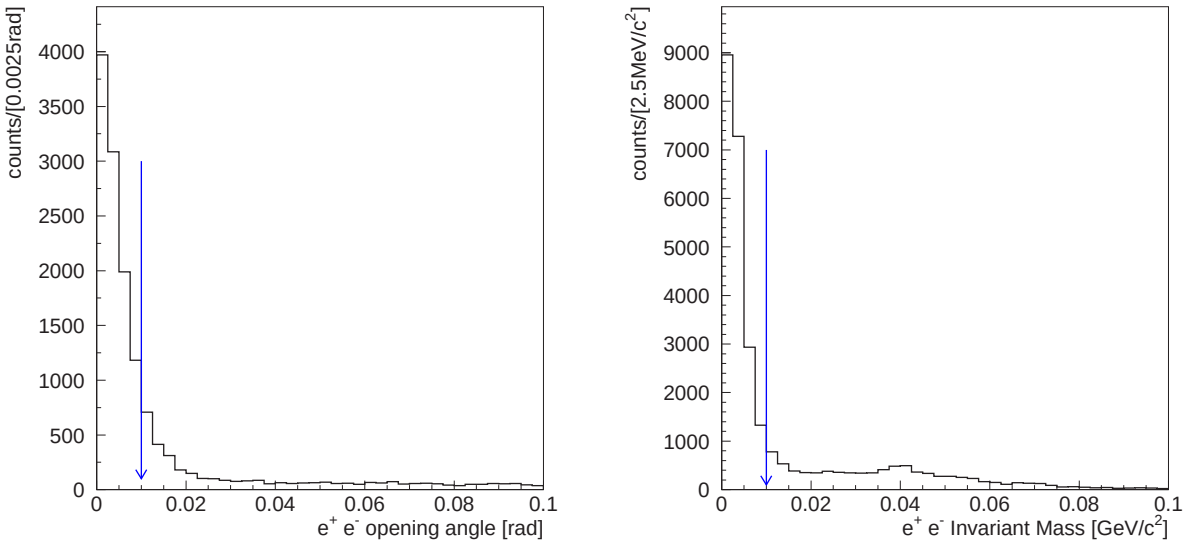

(a) opening angle distribution (b) invariant mass distribution

Figure 3.19: (a)The opening angle distribution of the pure electron candidates. The region lower than the arrow was used to select pure electrons. (b)Invariant mass distribution of electron pair in the low mass region. The region lower than the arrow was used to select pure electrons.

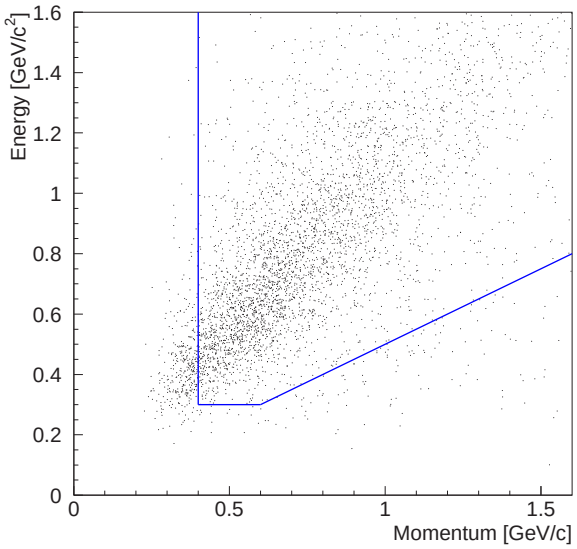

Figure 3.20: The correlation between RLG energy and momentum for the pure electron sample. The solid lines show the region for the electron identification.

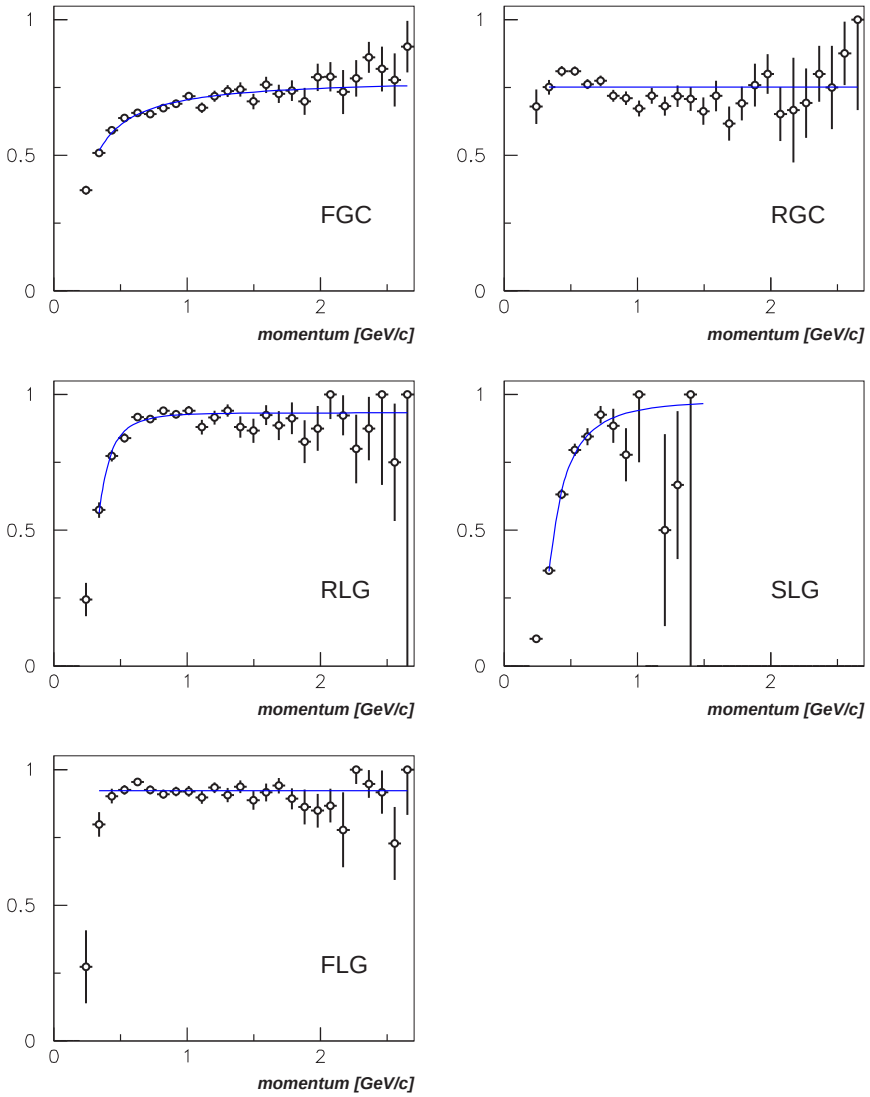

Figure 3.21: The electron identification efficiency as a function of track momentum.

(a) Parameters of the efficiency curve

counter	a	b	c
FGC	0.782	0.078	1.129
RGC	0.752	0	0
RLG	0.933	0.006	3.770
SLG	0.982	0.041	2.527
FLG	0.922	0	0

(b) Averaged efficiencies

counter	efficiency(%)
FGC	66±1
RGC	75±1
RLG	88±1
SLG	74±2
FLG	92±1

Table 3.6: (a)The parameters of the efficiency curves for the electron identification counters. The parameter b and c were fixed to zero for RGC and FLG. (b)The averaged efficiencies including the off-line cuts for single electron tracks in the final e^+e^- sample.

Other Cut for e^+e^- Pairs

If there were three or more electron tracks in an event, such an event was excluded from the final e^+e^- sample. This selection effectively works as Dalitz decay and γ-conversion rejection. The amount of the eliminated events was 7% of the final e^+e^- sample.

3.3.6 Kaon Identification

Kaon identification was performed using the particle mass calculated from the flight time measurements and the momentum analysis, helped by the pion veto with the aerogel Čerenkov counters. To determine the flight time, tracks were required to have an associated hit in STC, HC and FTOF. The horizontal and vertical position matching of counter hits to the Runge-Kutta tracks were shown in Fig. 3.22 and 3.23, respectively. The vertical position of the counter hit was obtained by the timing difference between the top and bottom TDC's. Since the refractive index of the aerogel was 1.034, the threshold for pions was 0.53GeV/c and for kaons was 1.88GeV/c. In the following analysis, a cut for the highest momentum was set at 1.9 GeV/c. The observed momentum distributions of kaon are shown in Fig. 3.24.

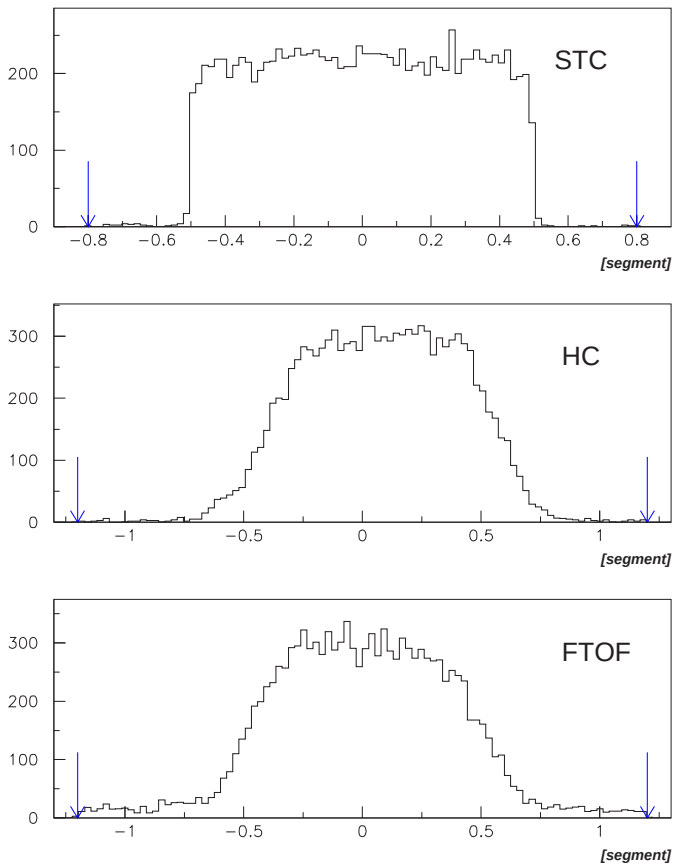

Figure 3.22: Horizontal matching between kaon tracks and the kaon identification counters in the final K^+K^- sample. The arrows indicate the region for the kaon selection, and the x coordinate is in a unit of the counter size. (The figures are shown after the matching cuts were applied.)

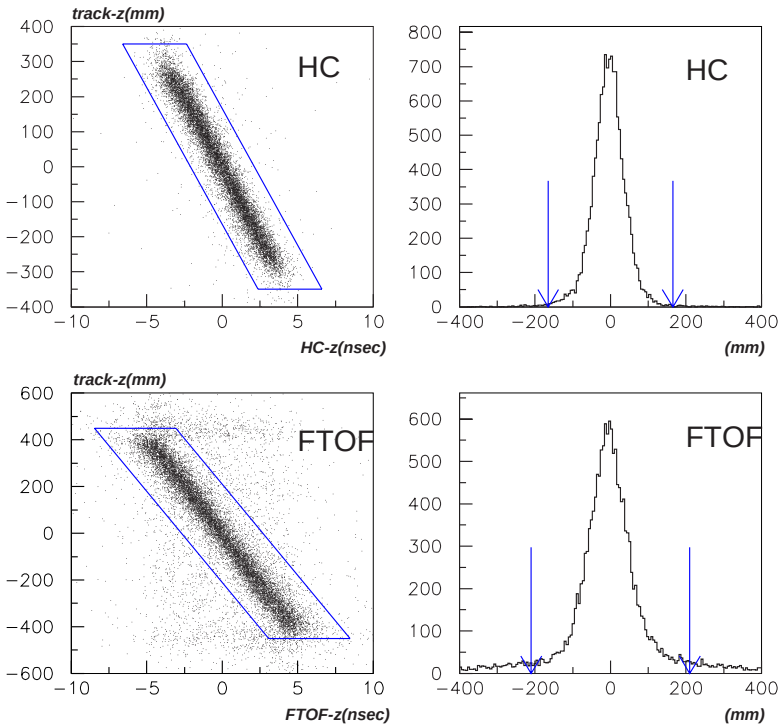

Figure 3.23: Vertical matching between kaon tracks and differential timings of two PMT's in the kaon identification counters in the final K^+K^- sample. The right figures show projection along the correlation line of the left figures. The indicated rectangles in the left figures and the arrows in the right figures are the cut regions for the matching.

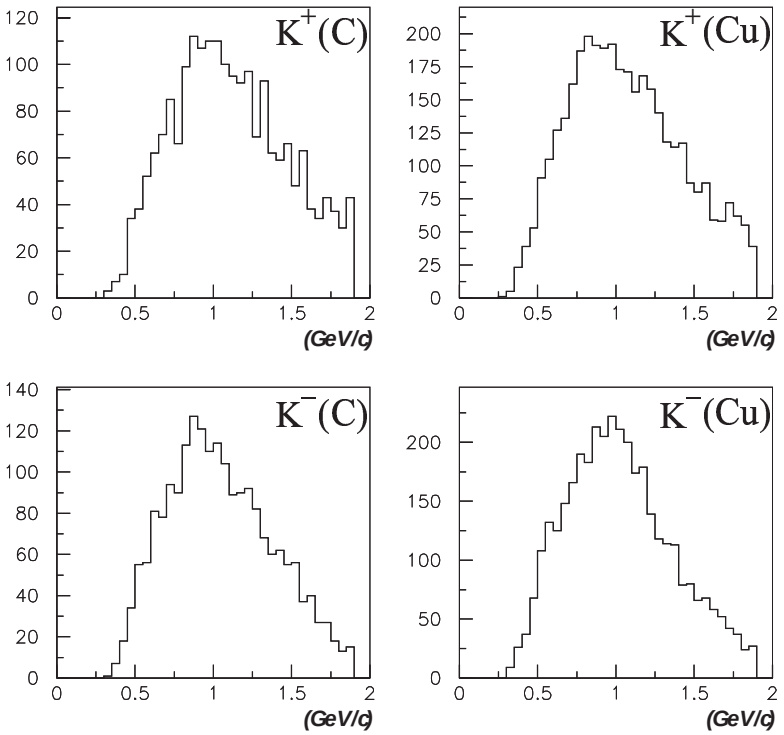

Figure 3.24: The momentum distributions of kaons in the final sample. The upper figures are for K^+ and the lower figures are for K^-. The left figures are for the C target and the right figures are for the Cu targets.

Particle Identification with Particle Mass

The mass square (M^2) of a particle is obtained as

$$M^2 = p^2 \times \frac{(1-\beta^2)}{\beta^2}, \tag{3.8}$$

with

$$\beta = \frac{L}{T \times c}\ , \tag{3.9}$$

where p is a momentum of the particle, T and L are the flight time and the flight length between STC and FTOF respectively, and c is the light velocity. The resolution of the squared mass (σ_{M^2}) is represented as

$$\sigma^2_{M^2} = 4M^4(\frac{\sigma_p}{p})^2 + 4c^2p^2(p^2+M^2)(\frac{\sigma_{\rm TOF}}{L})^2, \tag{3.10}$$

where σ_p is the resolution of the momentum, and $\sigma_{\rm TOF}$ is the resolution of the time of the flight measurements. For kaons with 1GeV/c of momentum, the error contribution from the second term is fifty times larger than that from the first term, so the error for the mass measurements is almost described with $\sigma_{\rm TOF}$. The distributions of the momentum versus squared-mass are shown in Fig. 3.25.

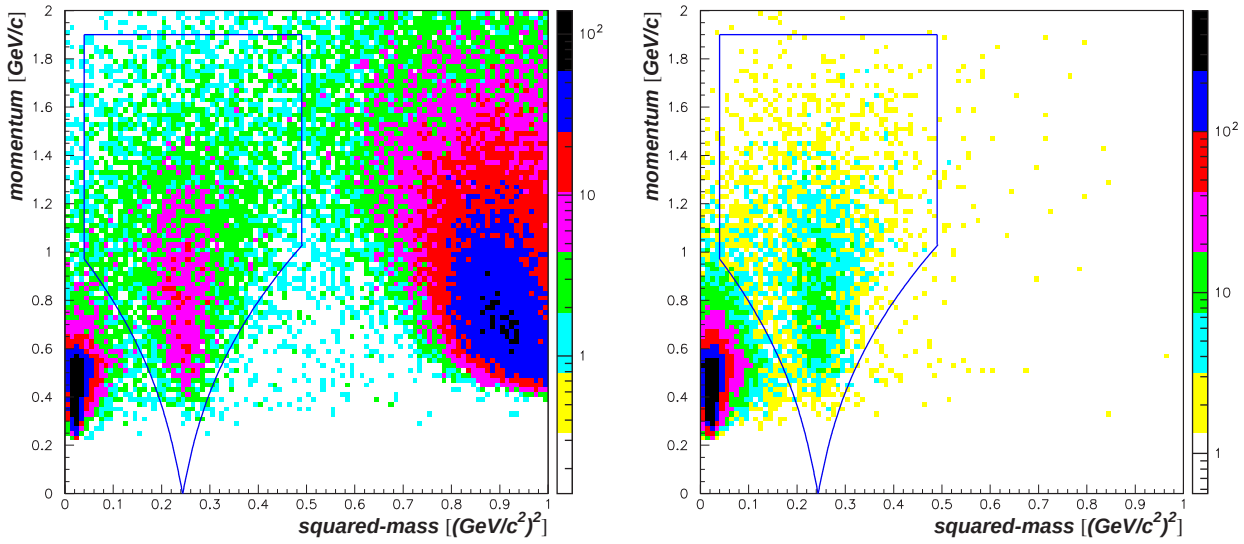

(a) + charge (b) − charge

Figure 3.25: The distributions of the momentum versus squared-mass for (a) positive and (b) negative particles, after the AC veto is applied. The indicated regions are the selected regions for the kaon identification.

To select kaons we assumed that all the particles had the kaon mass, and the expected flight time was calculated from the momentum and the flight length between STC and FTOF. We required the time difference between the expected time and the measured time to be less than 1.2 nsec which corresponds to $\pm 3\sigma_{\rm TOF}$. Additionally, the cut was set on the squared mass from 0.04 to 0.49 (GeV/c^2)^2, and the momentum was required to be less than 1.9 GeV/c. The kaon identification regions are shown in Fig. 3.25.

The purity of the kaon candidates in the final sample was obtained as described below. Since σ_{M^2} is a function of momentum, we obtained the momentum-sliced M^2 distributions from Fig. 3.25, and each M^2 distribution was fitted by three peaks, pion, kaon and proton using a

double Gaussian distribution. We fixed the centroid of pion mass to the value which determined in counter calibration, and fixed the main component of σ_{M^2} of kaon to the evaluated values from Eq. 3.10 using the obtained $\sigma_{\rm TOF}$ and the simulated σ_p as described in Sec. 3.5.3 for each M^2 distribution. Thus for the fit, free parameters were the centroids of kaon and proton, and the two widths of double Gaussian for pion and proton, and the second component width for kaon. Examples of the sliced M^2 distributions and the fit results are shown in Fig. 3.26 (the others are shown in Appendix A). By summing the background over the sliced M^2 distributions, the purity of the kaon candidates is obtained as Table 3.7.

In the detector simulation for $\phi \to K^+K^-$ (see Sec. 3.5), the flight time is smeared with $\sigma_{\rm TOF}$ and the above cuts were applied. We found that the efficiency for the squared-mass cut was estimated to be 87% for $\phi \to K^+K^-$ decays.

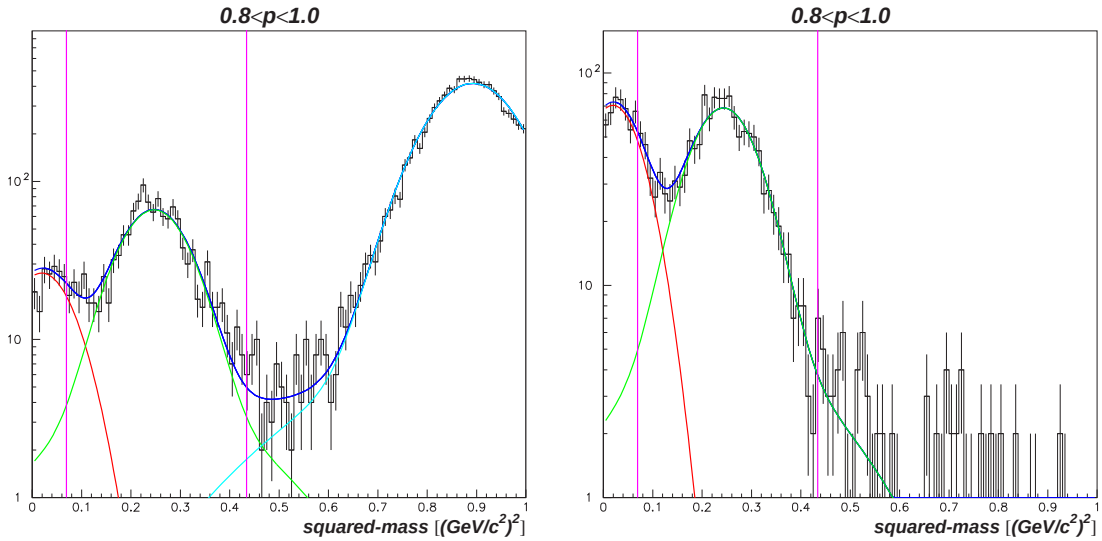

(a) + charge (b) – charge

Figure 3.26: The distributions of the squared-mass, when the momentum from 0.8 to 1.0 GeV/c is selected. The distributions were fitted with a sum of double-Gaussian distributions. The lines indicate the approximate region for the kaon selection.

	purity(%)
K^+	93.4 ± 3.4(stat) ± 0.6(syst)
K^-	91.7 ± 3.7(stat) ± 0.5(syst)
K^+K^-	85.6 ± 4.7(stat) ± 0.7(syst)

Table 3.7: The kaon purity of the final sample.

Particle Identification with Aerogel Čerenkov Counters

We have examined the performance of the aerogel Čerenkov counters (AC) using the data triggered by requiring any two charged particles.

The horizontal position matching of AC to the Runge-Kutta tracks is shown in Fig. 3.27(a). Since a cross talk over the aerogel segments occurred due to the segmentation, the cut region for the matching became broader than the scintillation counters. The AC was considered to have a hit when the ADC sum from the top and bottom photomultipliers of the track-associated segments exceeded 0.5-photoelectron level and the discriminator signal gave a good timing as

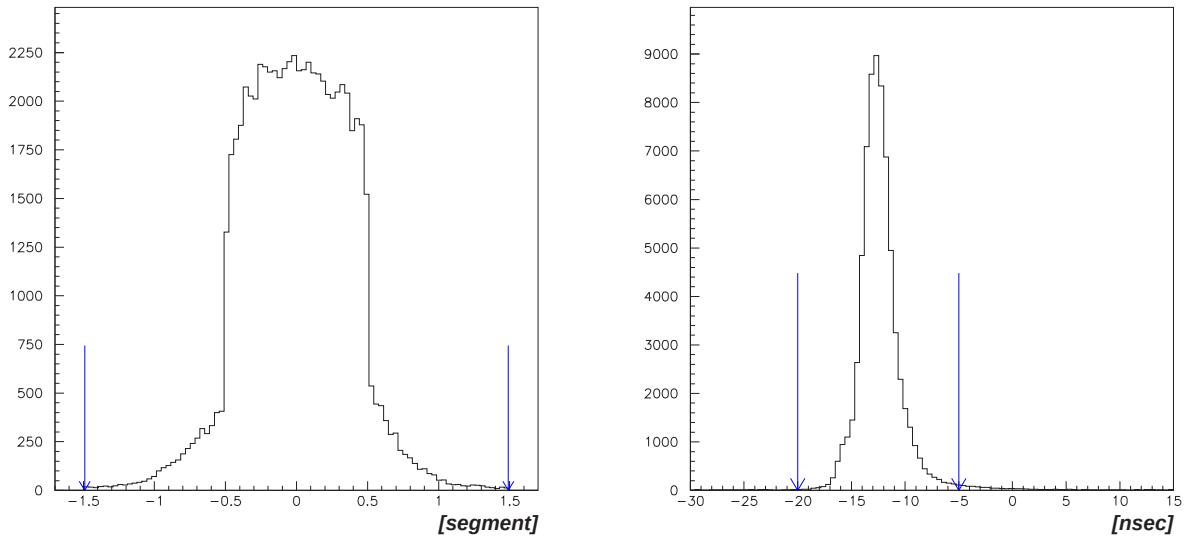

(a) Horizontal matching

(b) Hit-timing difference

Figure 3.27: (a) Horizontal matching between pion tracks and AC hits in the pion sample. (The figures are shown after the matching cuts were applied.) (b) Hit-timing difference between AC and associated FTOF counters. The arrows indicate the cut regions for the AC hit.

shown in Fig. 3.27(b). It should be noted that the input signals to the discriminators for the on-line trigger was also a linear sum of the top and bottom photomultiplier-outputs. The summed signal was discriminated at also 0.5-photoelectron level.

The correlations between the vertical positions of the Runge-Kutta tracks and the asymmetries of the ADC counts of the top and bottom photomultipliers are shown in Fig. 3.28. The asymmetry $\mathcal{A}$ was defined as

$$\mathcal{A} = \frac{\Sigma A^{\rm top} - \Sigma A^{\rm bottom}}{\Sigma A^{\rm top} + \Sigma A^{\rm bottom}} \ , \tag{3.11}$$

where $A^{\rm top}(A^{\rm bottom})$ is the ADC counts of the top (bottom) photomultiplier and the summation was made over the phototubes which satisfied the position matching criteria and the timing requirement. The region indicated in Fig. 3.28(a) corresponds to particles which radiate Čerenkov photons. Since Čerenkov angle for β=1 particles is 0.257 radian, the tracks whose vertical position was within $\pm$120 mm from the center made hits in both top and bottom photomultipliers. The same plot for protons does not show such correlation as can be seen in Fig. 3.28(b).

When we apply the regions in Fig 3.28 as the definition of track associated AC hits, the AC efficiency for pions and protons as a function of the momentum can be obtained as shown in Fig. 3.29. For particles with a momentum greater than 1.0 GeV/c, the vertical position dependence of the AC efficiency is plotted in Fig. 3.30, (a) for pions and (b) for protons.

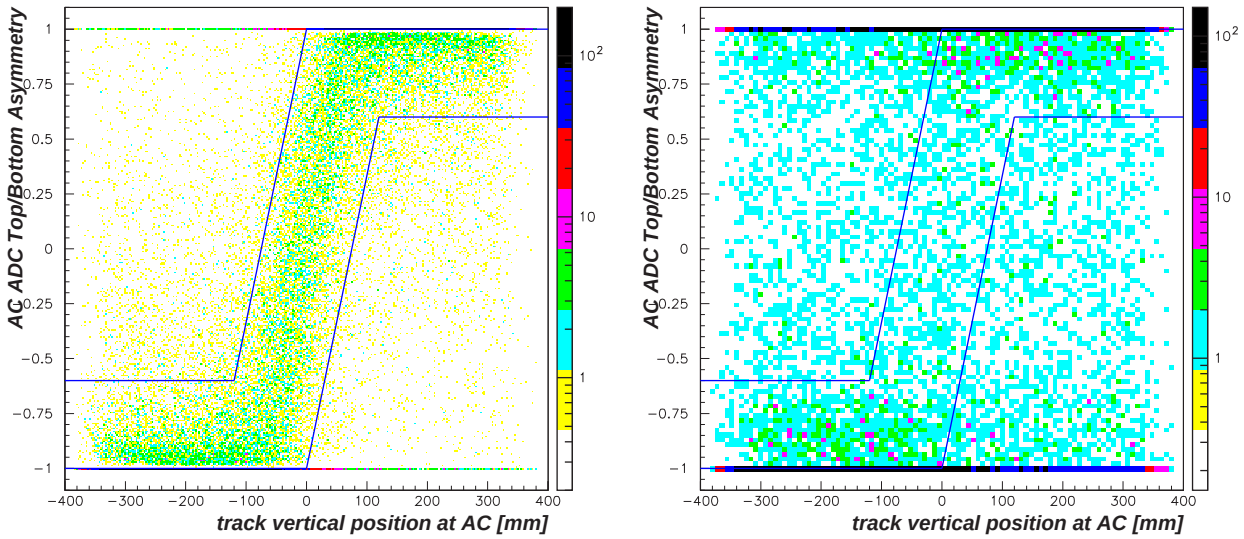

(a) pion (b) proton

Figure 3.28: Correlation between the track vertical position and the asymmetry of the top and bottom photomultipliers of AC.

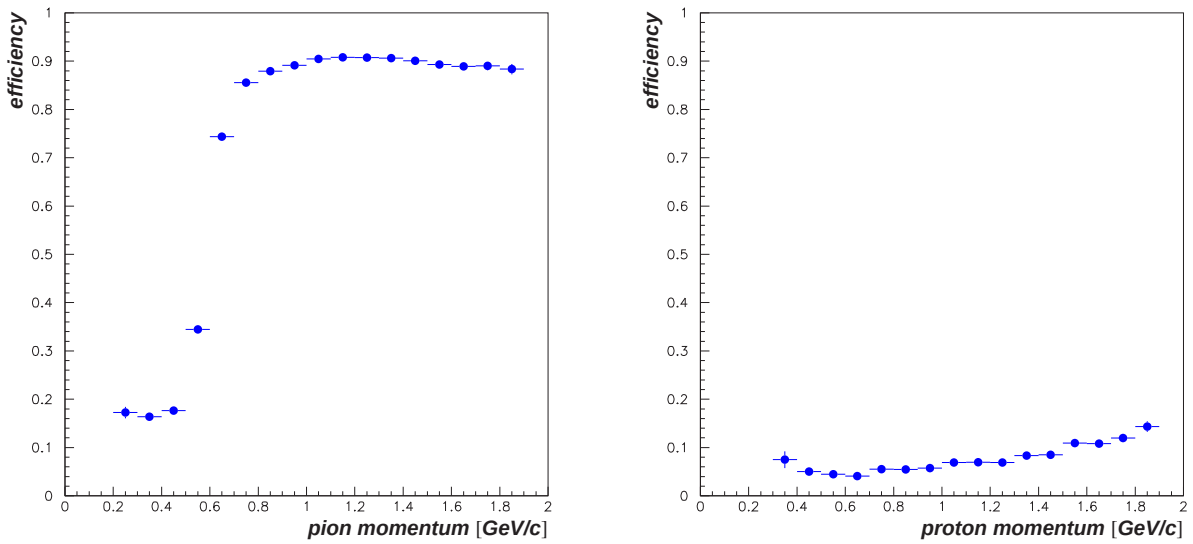

(a) pion (b) proton

Figure 3.29: The momentum dependence of the AC efficiencies, (a) for pions and (b) for protons.

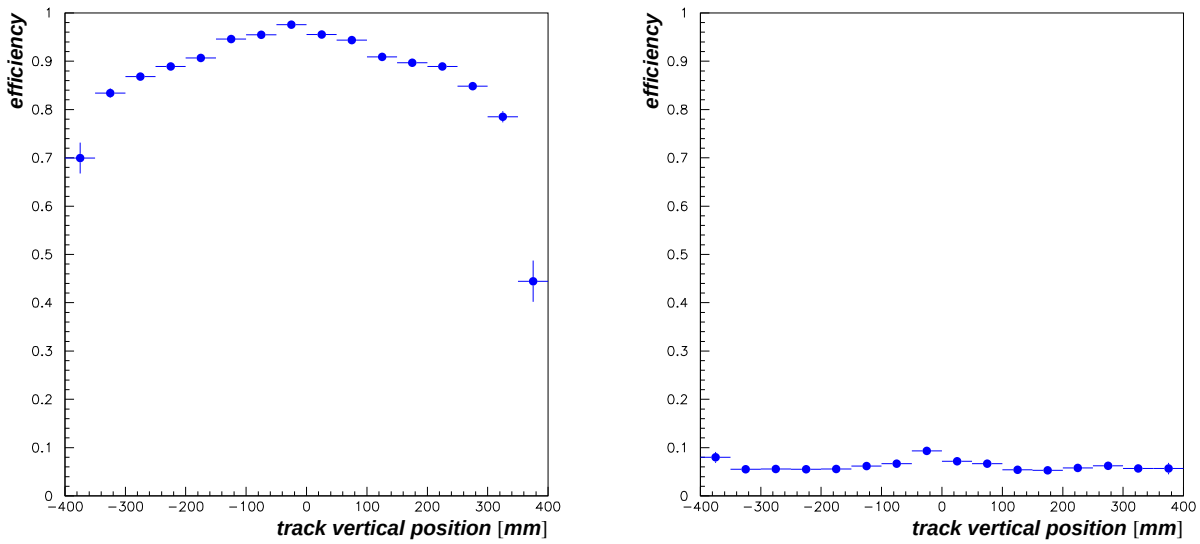

(a) pion (b) proton

Figure 3.30: The vertical position dependence of the AC efficiencies, (a) for pions whose momentum was larger than 1.0 GeV/c and (b) for protons

Other Cut for K^+K^- Pairs

We required the K^+K^- track pairs not to share the common hit in a FTOF segment and in HC, because these tracks possibly had a wrong hit timing and a wrong vertical position. We also eliminated events which contained three or more kaon tracks in a same event, and the amount of the eliminated events was 5%.

3.4 Reconstructed Invariant Mass Spectra

3.4.1 e^+e^- Invariant Mass Spectra

We defined e^+e^-pairs with a positron coming into the left arm and a electron coming into the right arm as LR events, and pairs with the opposite pattern as RL events, as shown in Fig. 3.31.

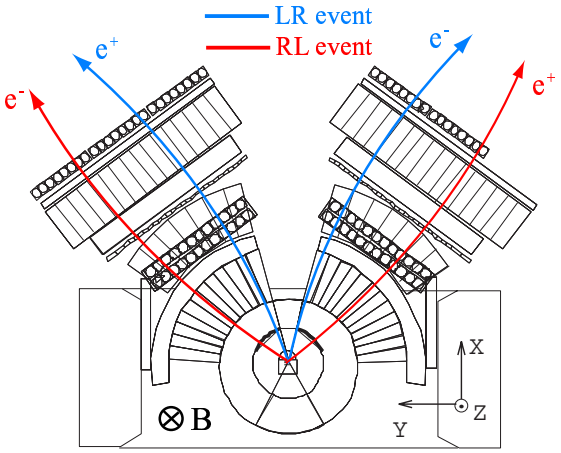

Figure 3.31: The definition of LR (blue) and RL (red) event.

The invariant mass spectra of the final e^+e^- sample are shown in Fig. 3.32. The figure contains the LR and RL events and the 2001 and 2002 data. The invariant mass spectra divided into the LR and RL events are shown in Fig. 3.33, and the spectra in the mass region from 0.85 to 1.2 GeV/c^2 are shown in Fig. 3.34. For reference, Fig. 3.35 shows the invariant mass spectra divided into each target disk, and Fig. 3.36 shows their close up views for the ϕ meson peak. Because e^+e^- events were requested to be a double-arm event by the trigger logic, the low-mass regions of the spectra are largely suppressed. The suppressions of the low-mass regions in the RL events are larger than those in the LR events, whereas differences in mass spectra are small in each target.

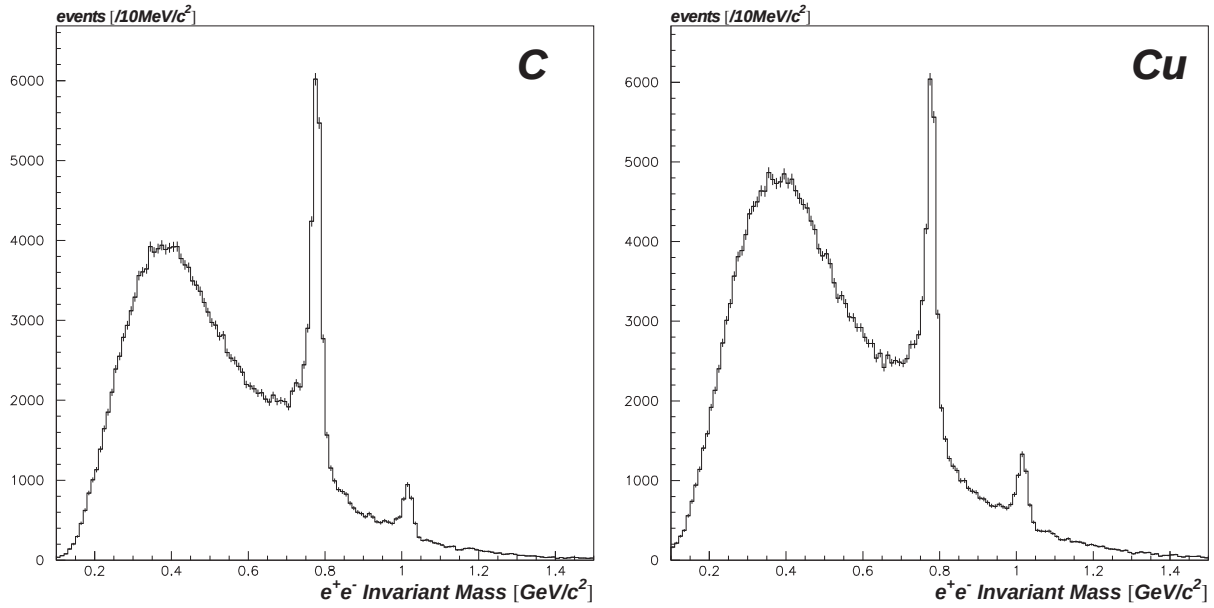

Figure 3.32: The e^+e^- invariant mass spectra of the final data sample for the carbon targets (left) and for the copper targets (right).

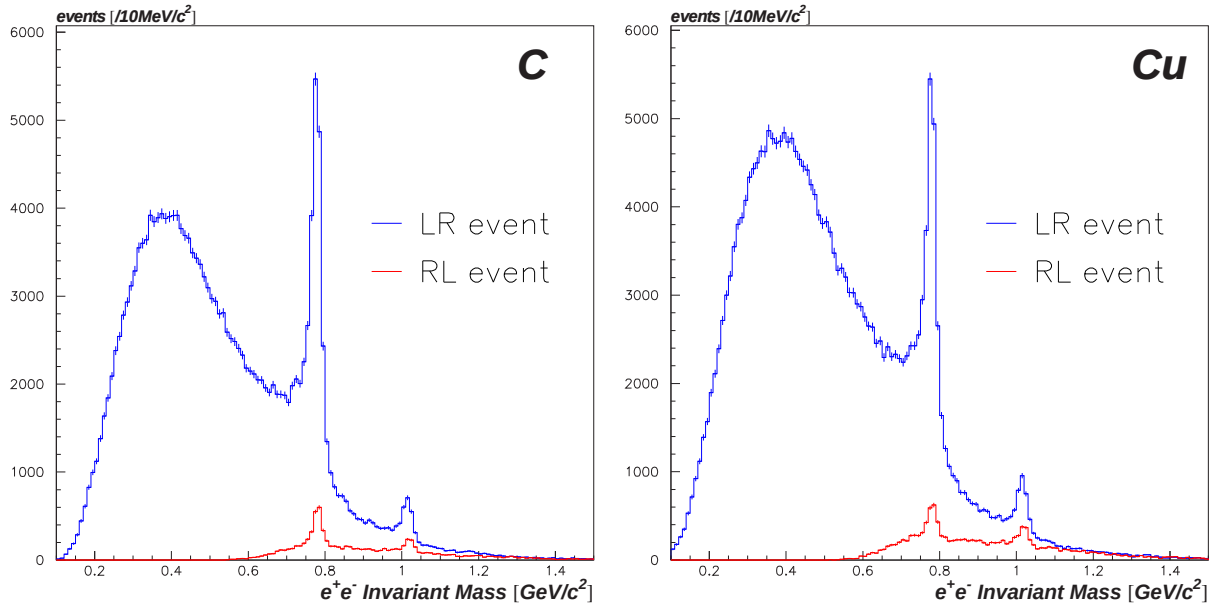

Figure 3.33: The e^+e^- invariant mass spectra. The spectra of the LR events and the RL events are shown separately.

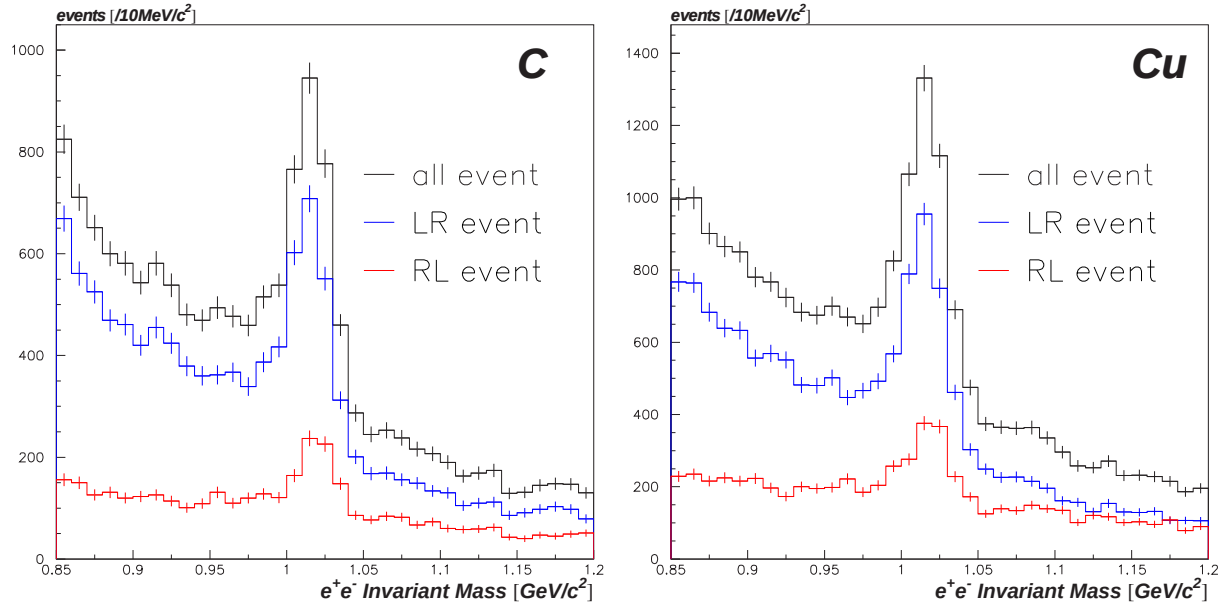

Figure 3.34: The e^+e^- invariant mass spectra, close up views of Fig. 3.32 and 3.33 to the ϕ meson peak.

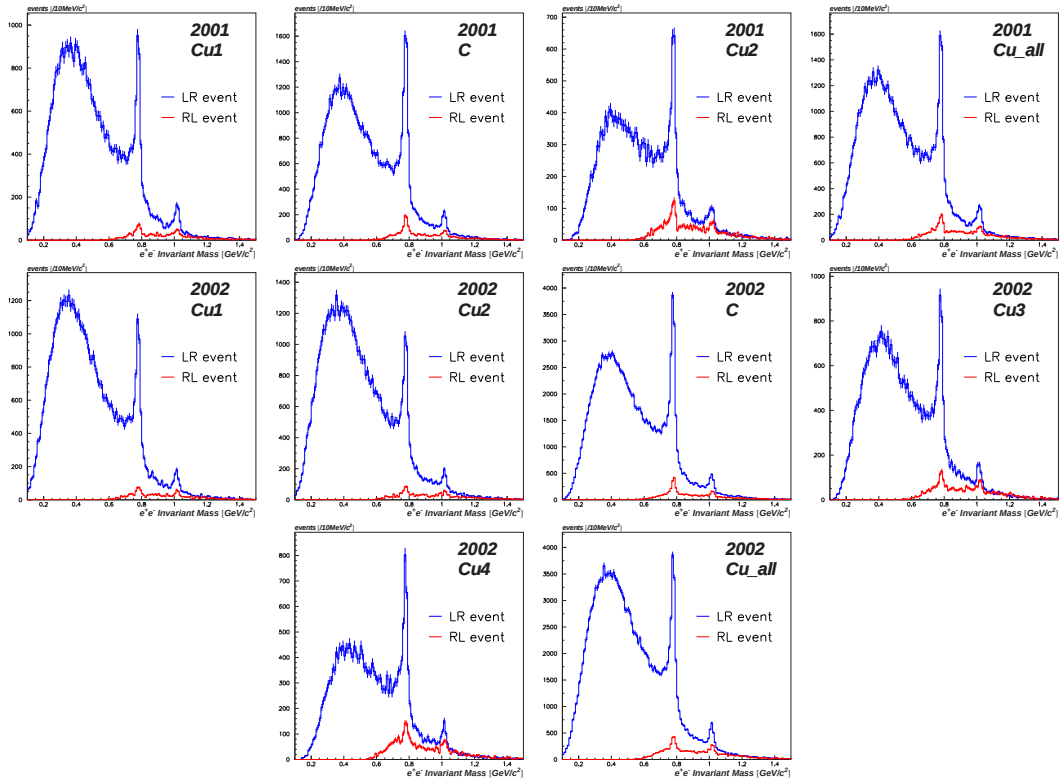

Figure 3.35: The e^+e^- invariant mass spectra divided into each target disk.

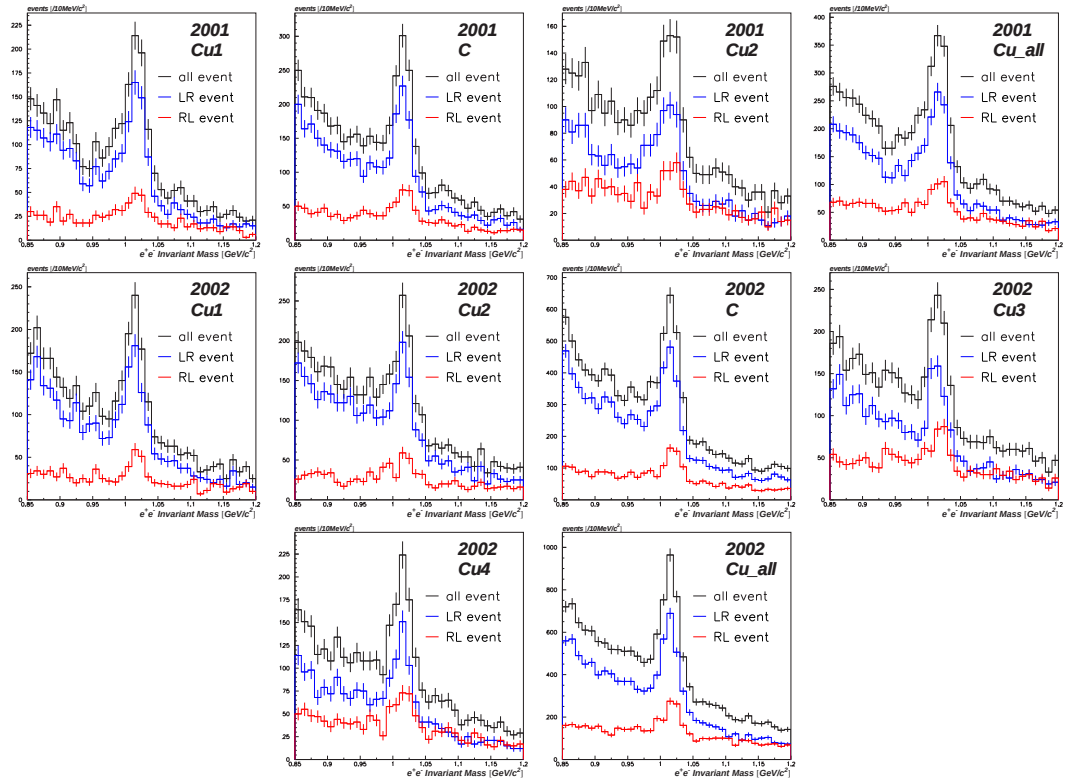

Figure 3.36: The e^+e^- invariant mass spectra, close up views of Fig. 3.35 to the ϕ meson peak.

3.4.2 K^+K^- Invariant Mass Spectra

In the K^+K^- channel, the events were required to have K^+ and K^- tracks in a same arm because of the small Q value in the $\phi \to K^+K^-$ decays. The invariant mass spectra of the final K^+K^- sample are shown in Fig. 3.37 for the carbon and copper targets. The spectra divided into each target disk are shown in Fig. 3.38, and Fig. 3.39 shows the spectra divided into the L and R arm events. Differences in mass spectra are small in each target and arm.

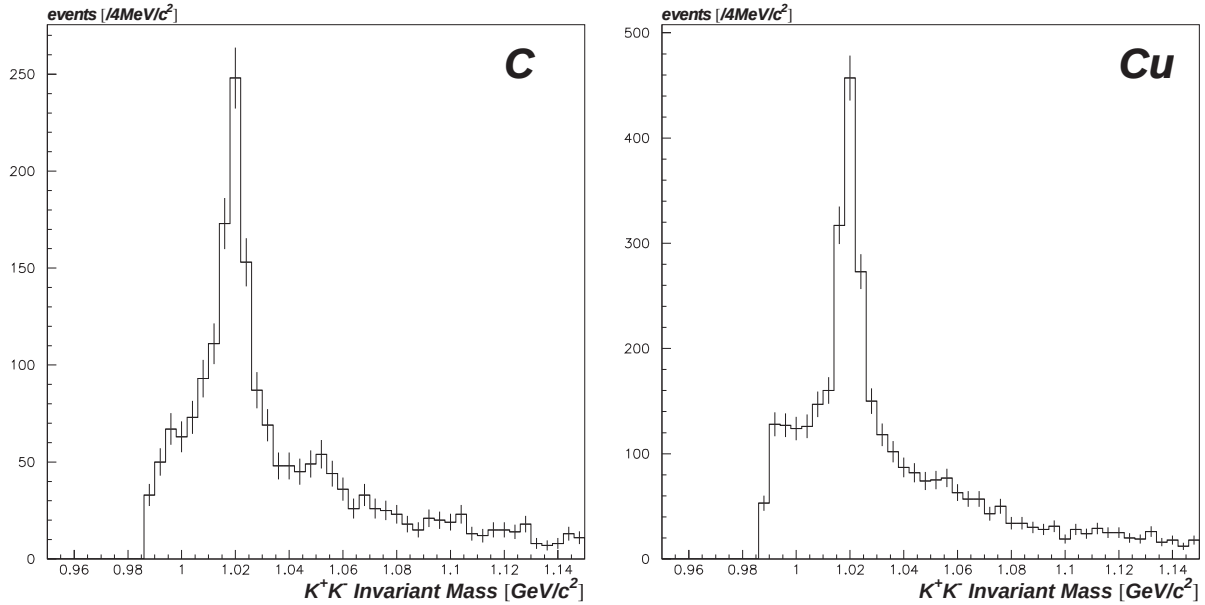

Figure 3.37: The K^+K^- invariant mass spectra for C (left) and Cu (right) targets.

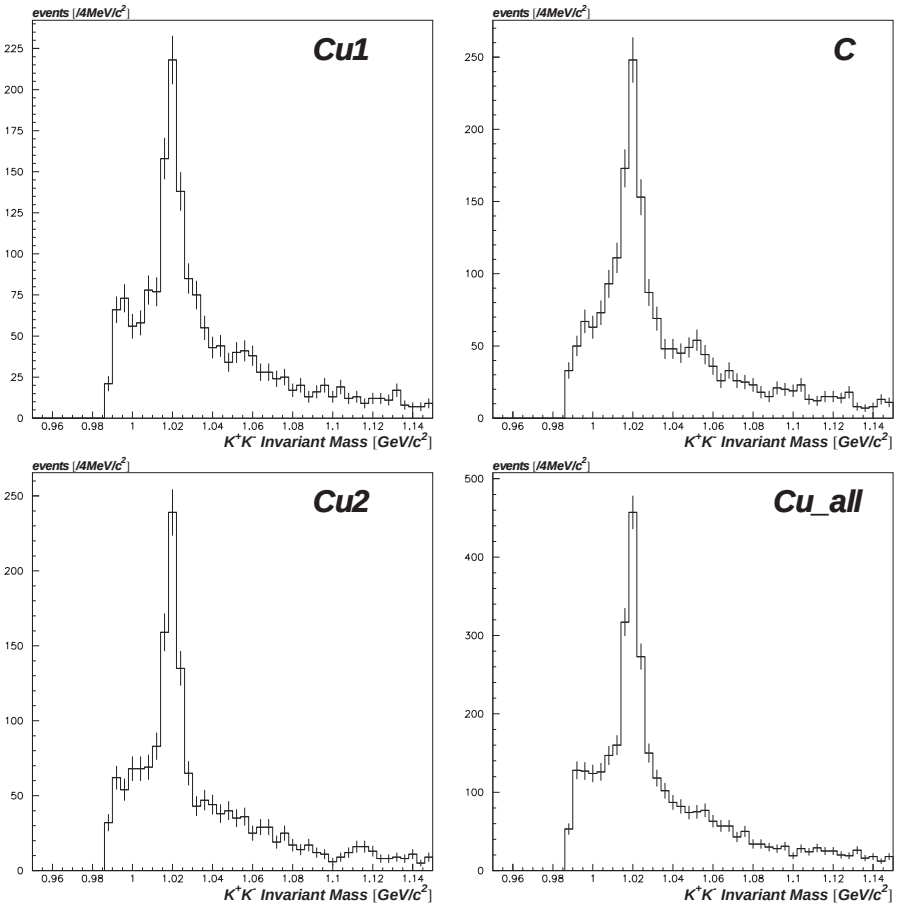

Figure 3.38: The K^+K^- invariant mass spectra divided into each target disk.

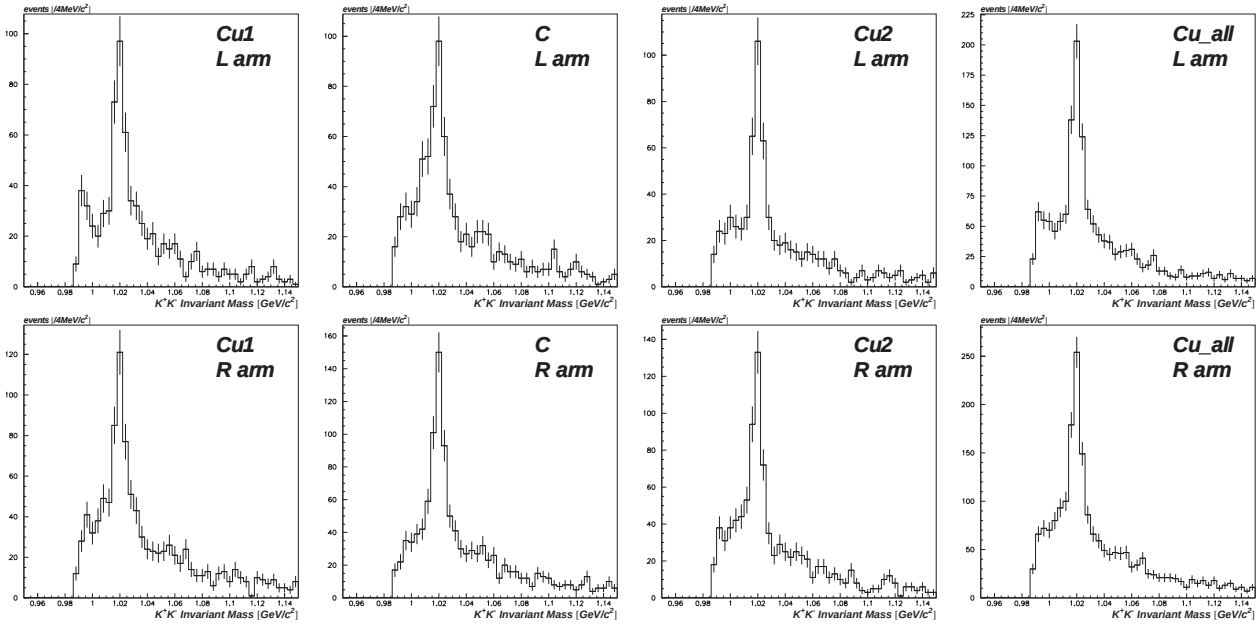

Figure 3.39: The K^+K^- invariant mass spectra divided into the L and R arm events.

3.5 Detector Simulation for ϕ

The detailed detector simulation was performed using Geant4.5.1.p01 toolkit [62] to evaluate all the detector effects, such as energy loss of particles, external bremsstrahlung, multiple scattering, detector acceptance, and the tracking performance with the chamber position resolution. To reproduce precisely those effects on a passage of particles through the detector materials, we implemented the all detector components from the targets to BDC's with the materials listed in Table 2.2. It should be noted that all chamber wires, which included sense, potential, and guard wires, were implemented as they were in the simulation. However, materials behind BDC's were neglected in the simulation, since the determination of the track momentum was performed with CDC and BDC's.

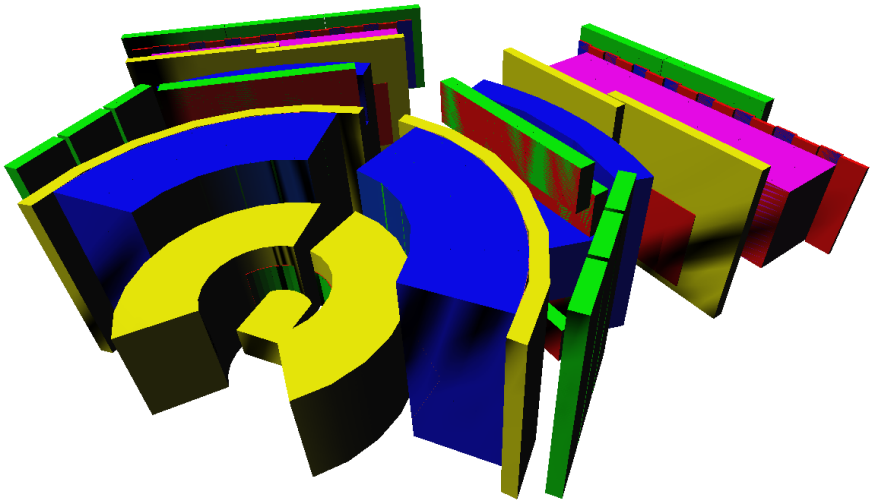

Figure 3.40: The E325 spectrometer implemented in the detector simulation using Geant4 toolkit.

Charged particles were traced in the magnetic field, and chamber and counter hits were generated according to the measured efficiencies. The chamber hits were smeared with the position resolution as described in Sec. 3.3.2. For e^+e^- pairs, the functions of counter efficiency were applied to each track as described in Sec. 3.3.5. For K^+K^- pairs, $(T_{\mathrm{FTOF}} - T_{\mathrm{STC}})$ were smeared with the overall TOF resolution as described in Sec. 3.2.5. The tracks were reconstructed and the cuts were applied to the reconstructed tracks as same as the real-data analysis.

3.5.1 $\phi \rightarrow e^+e^-$ Simulation

Spectral Shape of $\phi \rightarrow e^+e^-$

The spectral shape of $\phi \rightarrow e^+e^-$ was generated using the non-relativistic Breit-Wigner distribution

$$BW\left(m\right) = \frac{\Gamma_{\mathrm{tot}}^2/4}{\left(m - m_0\right)^2 + \Gamma_{\mathrm{tot}}^2/4} \ , \tag{3.12}$$

with the pole mass m_0 of 1019.456 MeV/c^2 and the total decay width Γ_{tot} of 4.26 MeV/c^2 [7].

We compared the non-relativistic Breit-Wigner distribution with the relativistic Breit-Wigner distribution which is given by

$$\frac{d\sigma}{dm} = \frac{m m_0 \Gamma_{\mathrm{ee}}\left(m\right)}{\left(m^2 - m_0^2\right)^2 + \left(m_0 \Gamma_{\mathrm{tot}}\left(m\right)\right)^2} \ , \tag{3.13}$$

where

$$\Gamma_{\rm tot}\left(m\right) = \Gamma_{\rm tot}\left(q^{\rm tot}\Big/q_0^{\rm tot}\right)^3\left(m_0/m\right), \tag{3.14}$$

$$q^{\rm tot} = \sqrt{m^2\Big/4 - m_K^2}\ , \tag{3.15}$$

$$q_0^{\rm tot} = \sqrt{m_0^2\Big/4 - m_K^2}\ , \tag{3.16}$$

$$\Gamma_{\rm ee}\left(m\right) = \Gamma_{\rm ee}\left(q^{\rm ee}/q_0^{\rm ee}\right)^3\left(m_0/m\right), \tag{3.17}$$

$$q^{\rm ee} = \sqrt{m^2\Big/4 - m_e^2}\ , \tag{3.18}$$

$$q_0^{\rm ee} = \sqrt{m_0^2\Big/4 - m_e^2}\ , \tag{3.19}$$

with the partial decay width of $\phi \to e^+e^-$, $\Gamma_{\rm ee}$ [66]. Since a difference between the non-relativistic and the relativistic Breit-Wigner distribution in $\phi \to e^+e^-$ is negligible as shown in Fig. 3.41, we used the non-relativistic Breit-Wigner distribution in the $\phi \to e^+e^-$ simulation.

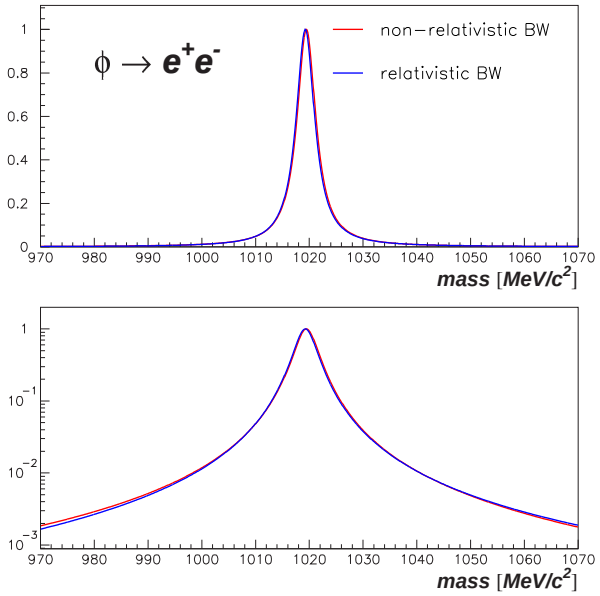

Figure 3.41: The non-relativistic (red) and the relativistic (blue) Breit-Wigner distributions for the $\phi \to e^+e^-$ decays. The distributions are normalized by their peak count to unity.

Kinematical Distribution

In the simulation, ϕ mesons were generated using the nuclear cascade code JAM 1.011.00 [63]. Only three momenta of generated mesons were obtained by JAM and the mass distribution was forced to have the Breit-Wigner. The kinematical distributions of the generated ϕ's are shown in Fig. 3.42 together with those in detector acceptance, and the differences between the C and Cu target are compared in Fig. 3.43.

The generated ϕ mesons were forced to decay into e^+e^-, and the daughter particles were traced in the detector simulation using Geant4. The angular distribution of vector-meson decay into e^+e^- was considered to be isotropic, i.e. no alignment exists in produced mesons. This assumption was supported by the fact that the observed decay angular distribution was well reproduced with the simulation as shown in Fig. 3.44. The momentum distributions of electrons and positrons are also shown in Fig. 3.45.

The observed and simulated distributions of ϕ mesons are compared in Fig. 3.46 and 3.47. The observed distributions were obtained by subtracting the background distribution from that of the signal region from 0.99 to 1.04 GeV/c^2 as shown in Fig. 3.48. The background distributions were obtained as an average of the region from 0.94 to 0.99 GeV/c^2 (left side) and the region from 1.04 to 1.09 GeV/c^2 (right side). The observed kinematical distributions are again well reproduced with the simulated ones.

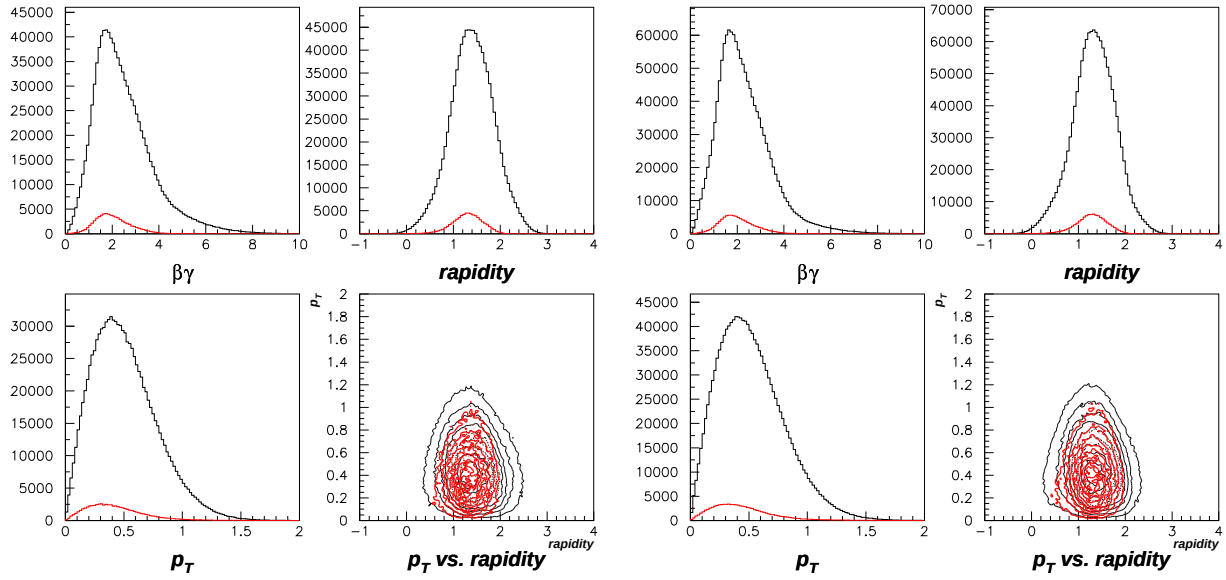

(a) C (b) Cu

Figure 3.42: The kinematical distributions of the generated ϕ mesons using JAM (black lines) and for the accepted $\phi \to e^+e^-$ in the detector (red lines).

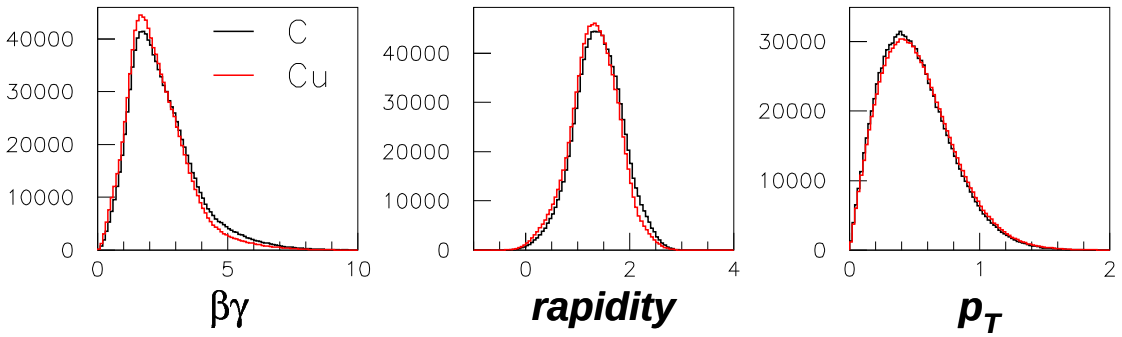

Figure 3.43: The kinematical distributions of the generated ϕ mesons for C (black lines) and Cu (red lines), normalized with the number of entries.

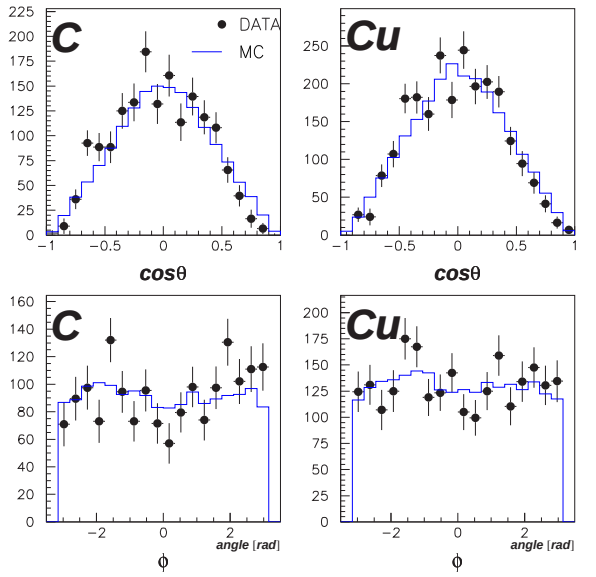

(a) the Gottfried-Jackson frame

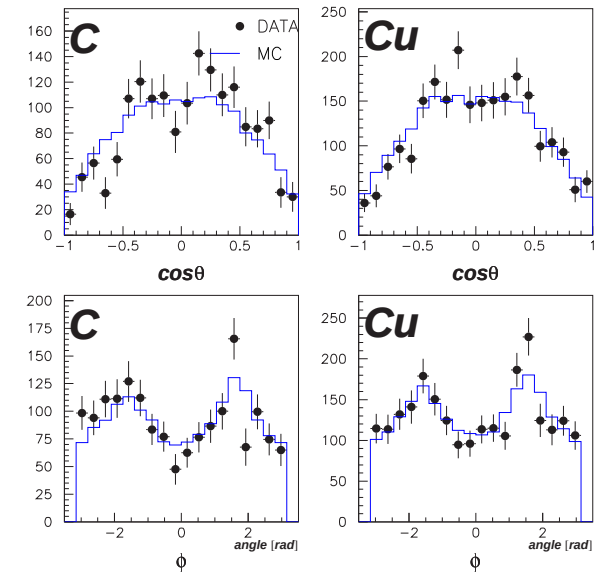

(b) the helicity frame

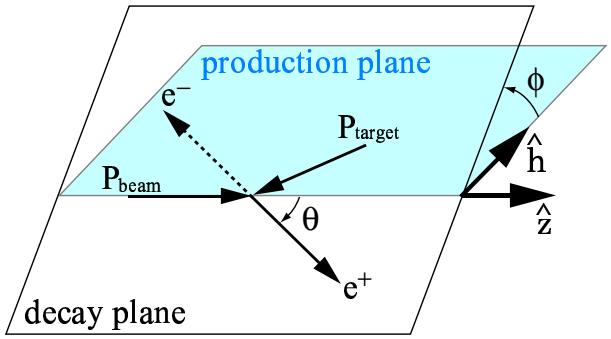

(c) the Gottfried-Jackson frame

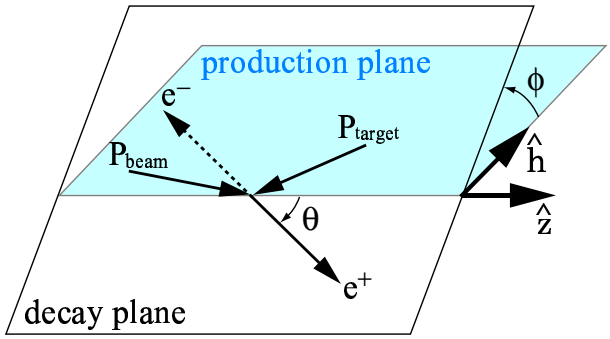

(d) the helicity frame

Figure 3.44: The decay angular distributions for the data (closed circles) and the simulation (lines), (a) in the Gottfried-Jackson frame and (b) in the helicity frame. The LR and RL events are summed. The scaling is determined arbitrarily. (c) In the Gottfried-Jackson frame, z-axis parallel to the beam direction in the ϕ rest frame. (d) In the helicity frame, z-axis parallel to the ϕ direction in the center-of-mass frame.

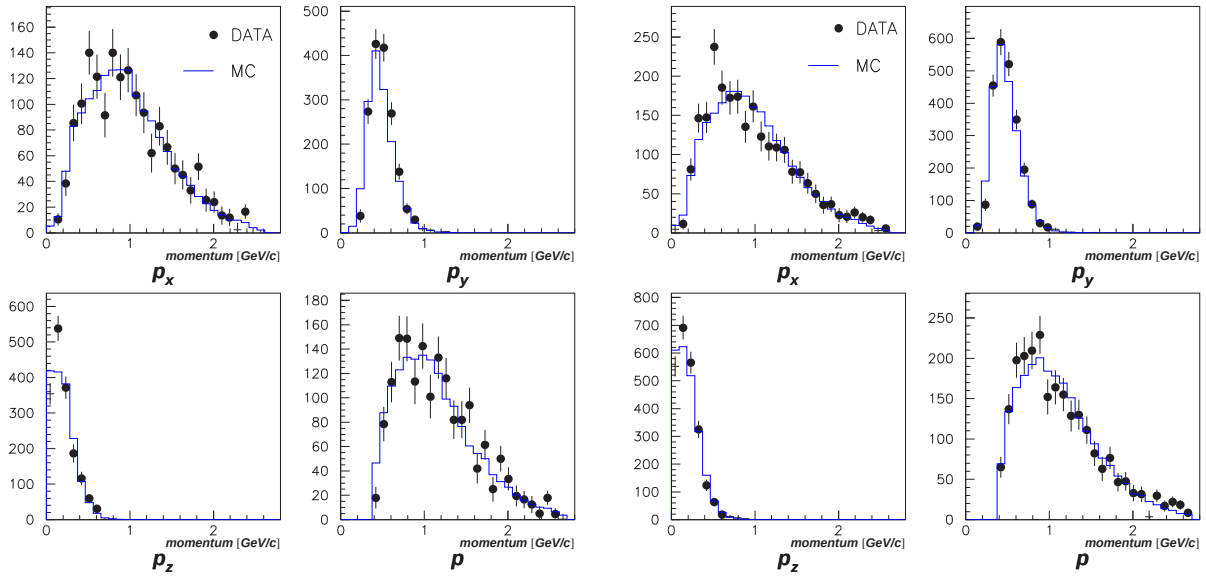

(a) e^+ in $\phi \to e^+e^-$ for C

(b) e^+ in $\phi \to e^+e^-$ for Cu

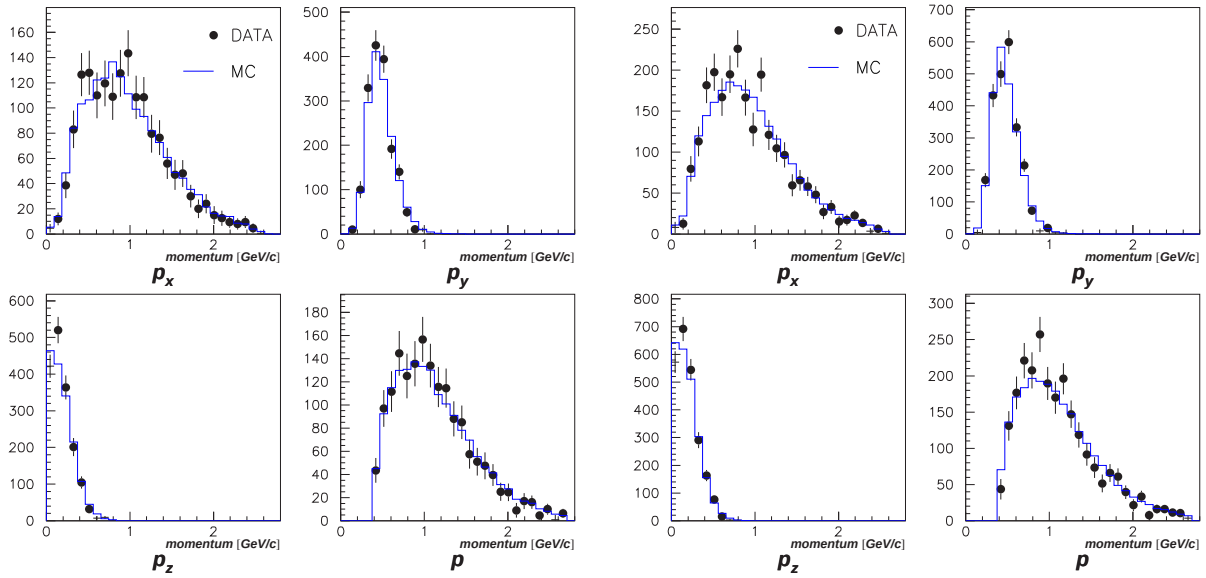

(c) e^- in $\phi \to e^+e^-$ for C

(d) e^- in $\phi \to e^+e^-$ for Cu

Figure 3.45: The momentum distributions of the observed (closed circles) and simulated (lines) daughter e^+ (upper panels) and e^- (bottom panels) in the $\phi \to e^+e^-$ decays, for C (left panels) and for Cu (right panels). The LR and RL events are summed. The scaling is determined arbitrarily.

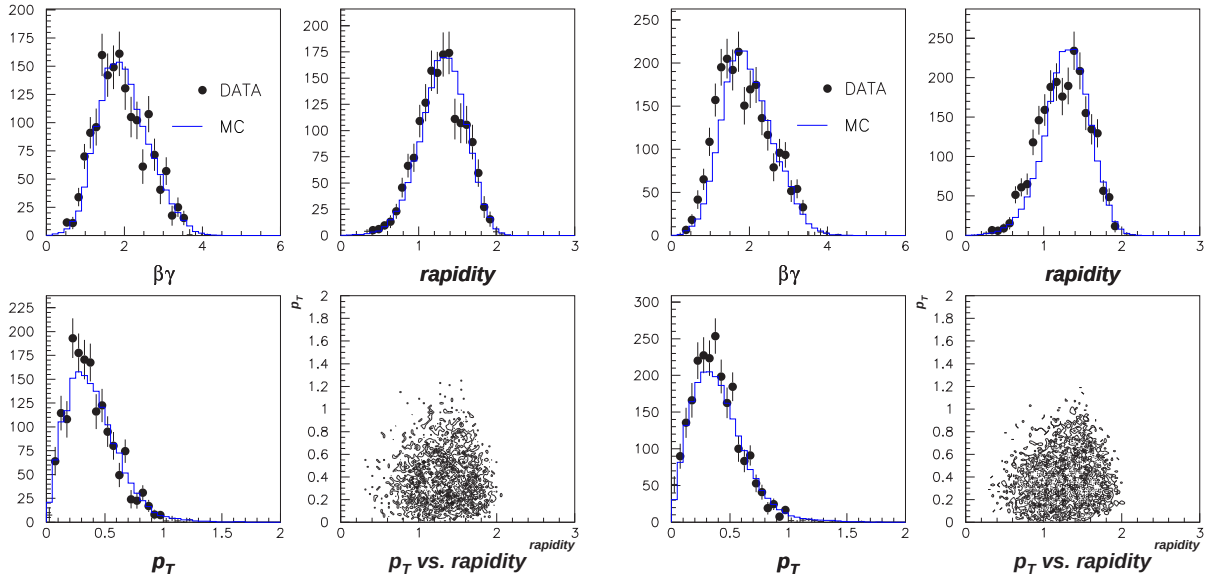

(a) $\phi \to e^+e^-$ for C (b) $\phi \to e^+e^-$ for Cu

Figure 3.46: The kinematical distributions of the observed (closed circles) and simulated (lines) $\phi \to e^+e^-$ pairs, for C (left four panels) and for Cu (right four panels). In the scatter plots of p_T versus rapidity, only the observed events are shown. The LR and RL events are summed. The scaling is determined arbitrarily.

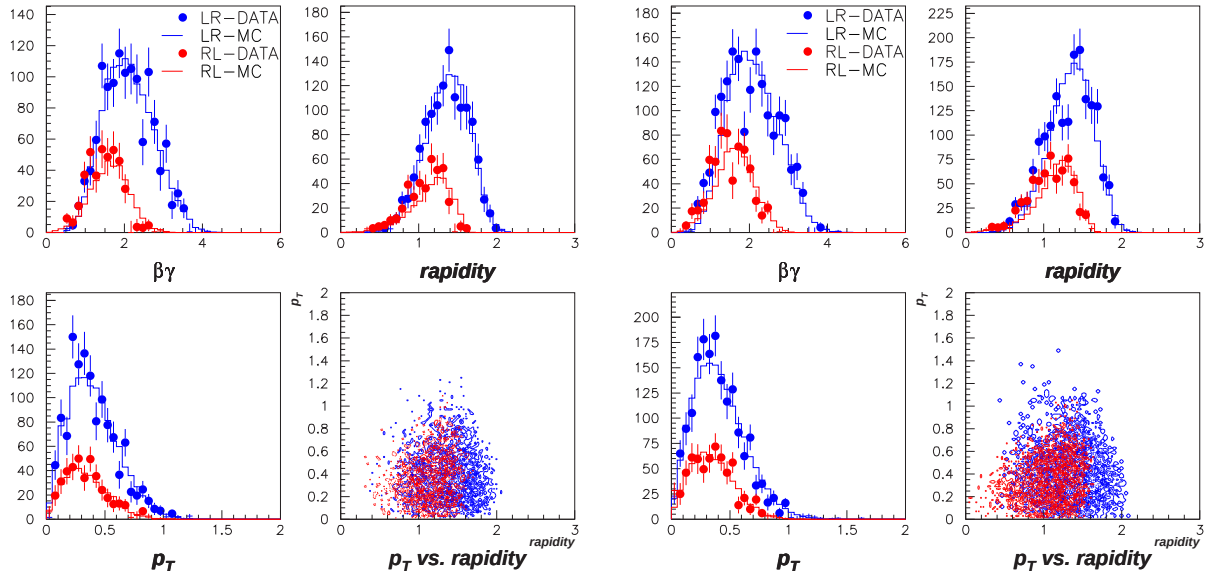

(a) $\phi \to e^+e^-$ for C (b) $\phi \to e^+e^-$ for Cu

Figure 3.47: The kinematical distributions of the observed (closed circles) and simulated (lines) $\phi \to e^+e^-$ as Fig. 3.46. Here the LR and RL events are represented in red and blue, respectively. The scaling is determined arbitrarily, but the ratio of the number of LR events to RL events is not changed in the data and the simulation.

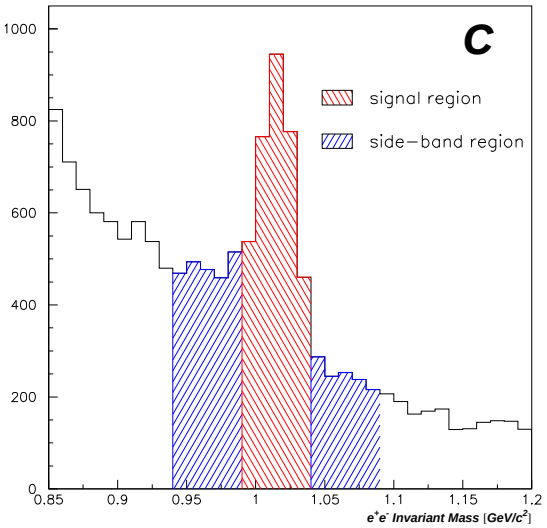

Figure 3.48: The separation of the signal region and the side-band (background) regions.

Internal Radiative Effects and Expected Mass Shape

The mass spectrum of $\phi \to e^+e^-$ is deformed by the internal radiative effects like internal bremsstrahlung, vertex correction, vacuum polarization, etc. As a result, only the effect of the "internal bremsstrahlung" is only significant and other effects discussed as follows are neglected to evaluate the mass shape of $\phi \to e^+e^-$. Here, the "internal bremsstrahlung" is including the cancellation by the vertex correction, of course.

- Internal Bremsstrahlung

The internal bremsstrahlung is expressed by the Feynman diagram in Fig. 3.49, which is a process in next to the leading order. It has an infrared divergence, but the divergence cancels with the vertex correction term as described later.

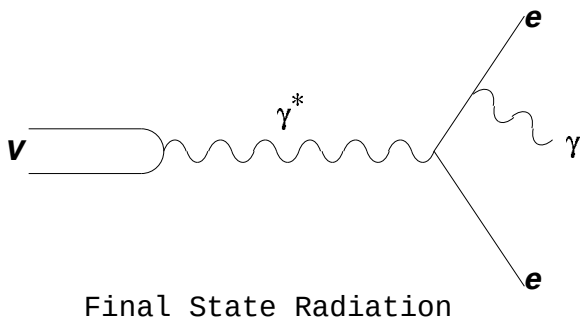

Figure 3.49: Internal bremsstrahlung in $V \to e^+e^-$ decays.

According to Ref. [67], the invariant mass shape of $V \to e^+e^-$ are deformed as shown in Fig. 3.50, which was calculated by using the Eq. (14) in Ref. [67];

$$\frac{1}{\Gamma_0}\frac{d\Gamma\left(V \to l^+l^-\gamma\right)}{dm} = \frac{\alpha}{\pi}\frac{2m}{\left(M^2-m^2\right)}\left(1+\frac{m^4}{M^4}\right)\left(\ln\frac{1+\tau}{1-\tau}-\tau\right), \tag{3.20}$$

where V is the vector meson, Γ_0 is the partial decay width of $V \to l^+l^-$, m is the invariant mass of lepton pair l^+l^-, α is the fine structure constant, M is the mass of V, and $\tau = \sqrt{1 - 4m_l^2/m^2}$ with the lepton mass m_l. The effect is small but visible as shown in Fig. 3.50(a). In Fig. 3.50(b), we include all the material effects in the detectors and the chamber resolution, and the blue curve was used to reproduce the measured spectra.

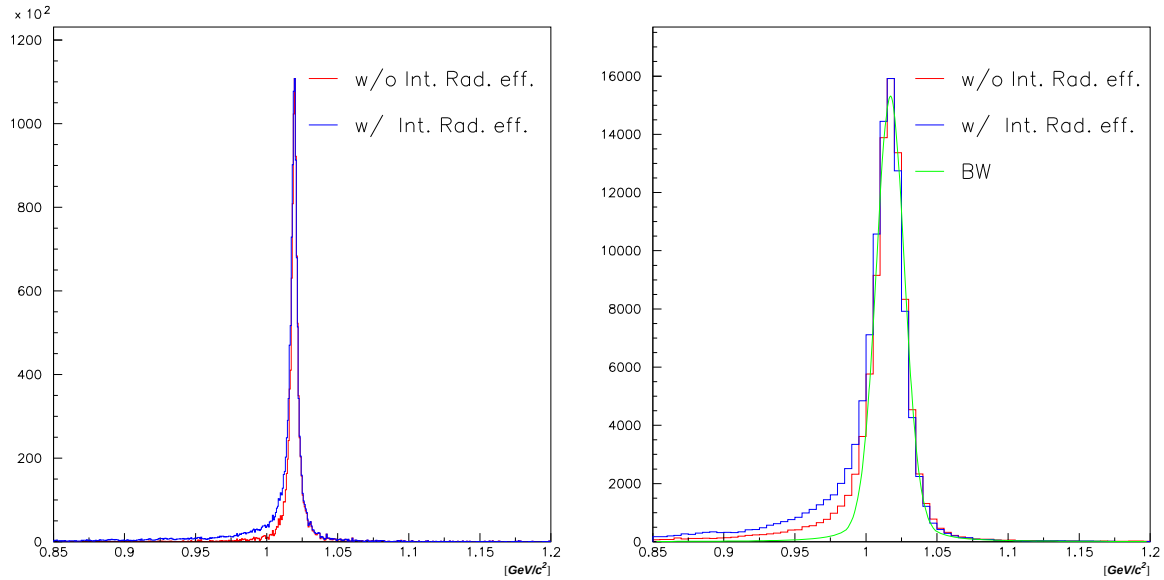

(a) w/o exp. eff. (b) w/ exp. eff.

Figure 3.50: The internal radiative effects in $\phi \to e^+e^-$ decays. The red spectra are with internal radiative effects, and the blue are without. (a)The detector effects are not considered. (b)The detector effects are considered. The green line is the fit result to the blue spectrum with the Breit-Wigner function folded with a Gaussian.

- Other Internal Radiative Corrections

Possible other smearing effects in the decay $V \to e^+e^-$ are vertex correction, vacuum polarization, and box diagrams of propagating gauge bosons. Although those are all negligible in the present experiment, we describe them briefly below.

According to Ref. [68], the magnitude of quantum electrodynamics (QED) radiative correction $\left(\delta \dfrac{d\sigma}{d\Omega}\right)$ up to order α^3 can be written as

$$\delta \frac{d\sigma}{d\Omega} = \left(\delta_{\rm VC} + \delta_{\rm VP} + \delta^{\rm Q}_{\gamma\gamma}\right) \frac{d\sigma^{\rm Q}_0}{d\Omega}, \tag{3.21}$$

where $\delta_{\rm VC}$ is the vertex correction term, $\delta_{\rm VP}$ is the vacuum polarization term, $\delta^{\rm Q}_{\gamma\gamma}$ is two photon box diagram correction term, and $\dfrac{d\sigma^{\rm Q}_0}{d\Omega}$ is the pure QED cross section in tree level. From the parity conservation, a vector meson does not decay into two photons, thus the contribution of the box diagram $\delta^{\rm Q}_{\gamma\gamma}$ is zero.

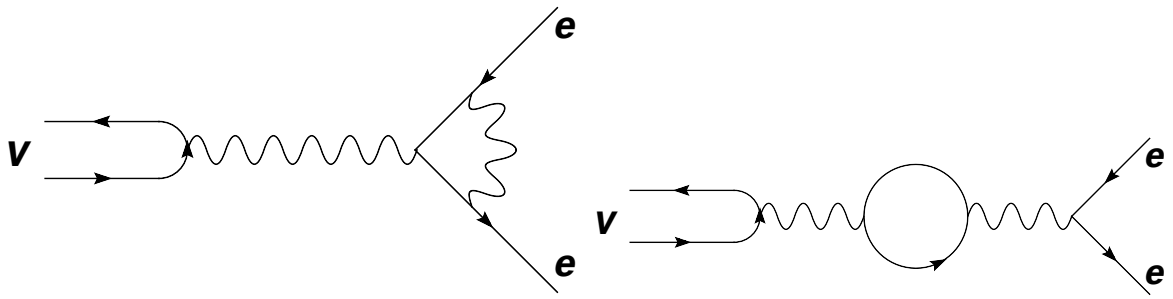

Figure 3.51: Feynman diagrams of the vertex correction term (left) and the vacuum polarization term (right).

The left panel of Fig. 3.51 shows the Feynman diagram of the vertex correction term $\delta_{\rm VC}$, which is expressed as Eq. (2.11) in Ref. [68],

$$\delta_{\rm VC}\left(m_e^2\right) = \frac{2\alpha}{\pi}\left[-1+\frac{1}{3}\pi^2+\frac{3}{4}\ln\frac{s}{m_e^2}-\frac{1}{4}\ln^2\frac{s}{m_e^2}+\left(1-\ln\frac{s}{m_e^2}\right)\ln\frac{m_e}{\lambda}\right], \tag{3.22}$$

where m_e is the electron mass, s is the meson mass square, and λ is a fictitious photon mass regularizing the infrared divergence. This infrared divergence cancels an infrared divergence in the internal bremsstrahlung. The Feynman diagram of the vacuum polarization term $\delta_{\rm VP}$ is shown in the right panel of Fig. 3.51. This term is expressed as Eq. (2.12) in Ref. [68],

$$\delta_{\rm VP} = \delta_{\rm VP}\left(m_e^2\right)+\delta_{\rm VP}\left(m_\mu^2\right)+\delta_{\rm VP}\left(m_\tau^2\right)+\delta_{\rm had}, \tag{3.23}$$

with the various contributions originating from lepton loops and hadron loops. Both diagrams change the partial decay width of $\phi \to e^+e^-$. The former diagram changes Γ_{ee} by factor of about 15% and the latter diagram by factor of about 2% at $\sqrt{s} = 1.2$ GeV. These are negligible in the observed line shapes since $\Gamma_{ee} \ll \Gamma_{\rm total}$.

Coulomb Potential of Target Nucleus

The effect of the Coulomb potential of target nuclei was small enough to be ignored in the simulation. The magnitude of this effect was estimated with a toy model, in which only Coulomb field of the target nucleus was considered. The potential $V(r)$ is given as

$$V(r) = \begin{cases} \dfrac{Ze^2}{2R_{\rm C}}\left(3-\left(\dfrac{r}{R_{\rm C}}\right)^2\right) & r \le R_{\rm C} \\ \dfrac{Ze^2}{r} & R_{\rm C} \le r \end{cases} \tag{3.24}$$

where Ze is the charge of a target nucleus, e is the charge of an electron, $R_{\rm C}$ is the radius of a target nucleus, and r is the radial distance from the centre of a target nucleus. We checked two cases, one is that vector mesons are generated uniformly on the incident surface of a nucleus and the other is that they are generated uniformly in a nucleus. We considered ^{12}C and ^{63}Cu as target nuclei, whose radii ($R_{\rm C}$ in Eq. (3.24)) are 2.4 fm and 4.2 fm, respectively. The momenta of vector mesons were distributed as those produced by JAM. The mesons were considered to fly without any interaction and decay into e^+e^- with their natural total width. We have chased e^+e^- and bent them with the Coulomb potential $V(r)$ until they reached 10 nm away from the target nucleus. The results of $\omega \to e^+e^-$ decays are shown in Fig. 3.52. The changes of invariant mass shapes are found to be negligible (below a half MeV/c^2) in the present experiment.

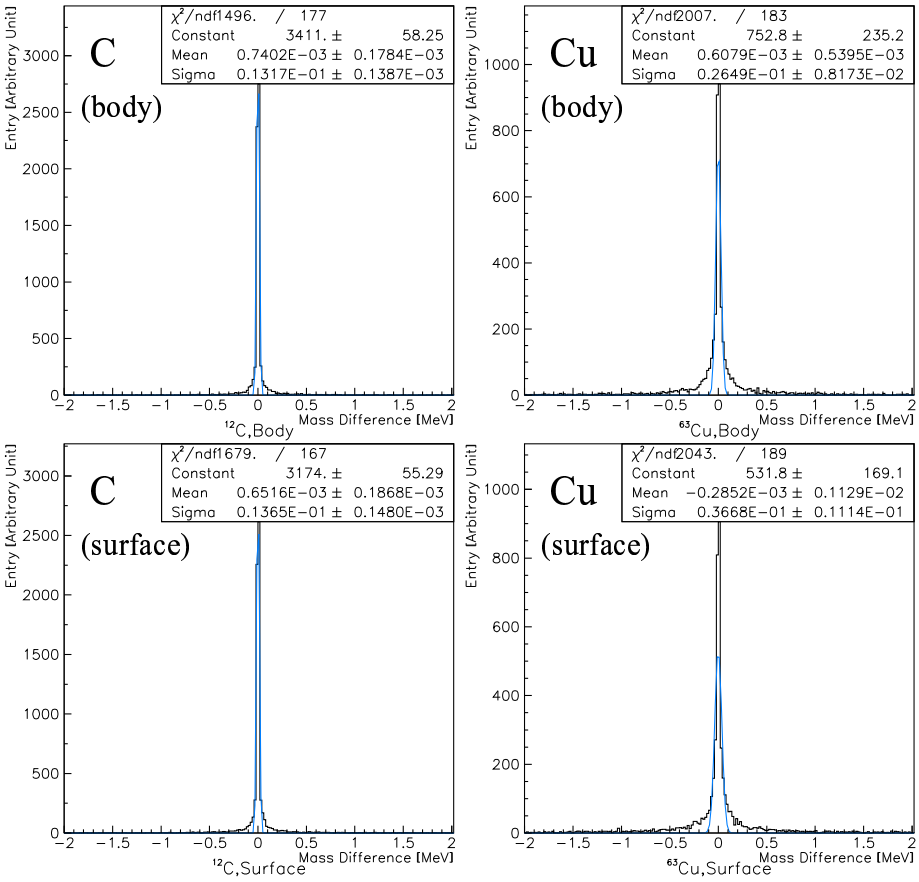

Figure 3.52: The effect of electromagnetic field of target nuclei, for carbon (left) and copper (right). In the upper two panels, mesons were generated uniformly in a nucleus. In the lowers, mesons were generated uniformly on a nuclear surface of the half hemisphere where the beam protons enter.

Mass Acceptance for e^+e^- Decays

The effect of the acceptance on the invariant mass spectrum was examined in the same detector simulation. In the 2001(2002) run, we used the 3(5) targets simultaneously and they were placed 46(23) mm apart from each other, so the acceptance of the spectrometer for each target is different from each other. The arrangement of the target disks (Cu-C-Cu or Cu-Cu-C-Cu-Cu) assumed that the average of the Cu-target acceptances is equivalent to the C-target acceptance. We examined this assumption as follows.

We evaluated the mass acceptance for each target using artificial mesons with the flat mass distribution from 0.85 to 1.2 GeV/c^2, with the momentum distribution of ϕ-mesons obtained by JAM. We used the same momentum distribution for the C and Cu targets to compare directly the experimental acceptance among the targets. We estimated the mass acceptance as the ratio of the accepted mesons to the generated mesons. It should be noted that the acceptance included not only the geometrical acceptance but the detector efficiencies and all other cut conditions which were used in the present analysis.

The obtained mass acceptances for each target in the 2001 run are shown in Fig. 3.53. The averaged acceptance for the two Cu targets is compared with the C target in Fig. 3.54 showing good agreements. In the future discussions in Sec. 4.1, we divide the data into four bins in $\beta\gamma$, rapidity, and p_T. With these divisions, we obtained the mass acceptances as shown in Fig. 3.55. The acceptance at the ϕ-meson peak (1.02 GeV/c^2) was about 1.5%, 1.2%, and 0.3% for the all, LR, and RL event respectively.

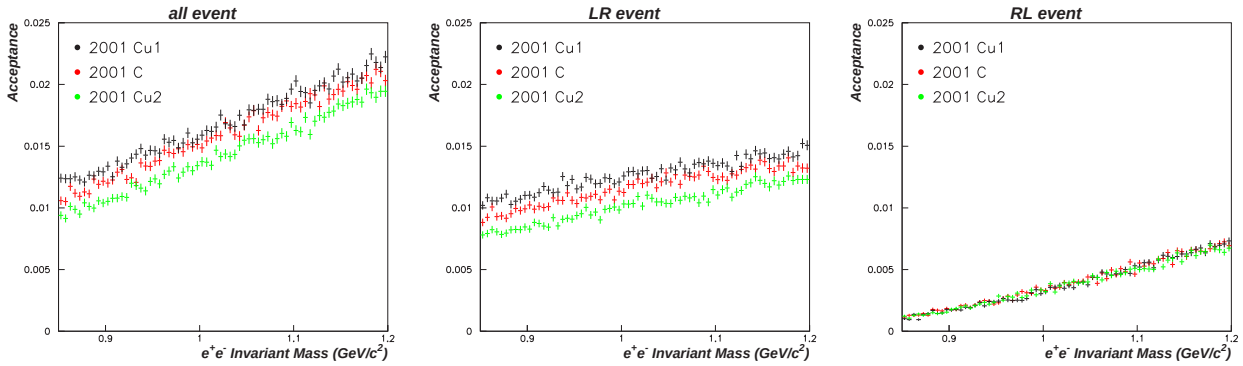

Figure 3.53: The mass acceptances for e^+e^- decays in the 2001 run. The acceptances of each target disk for the all events (left), LR events (center), and RL events (right) are shown.

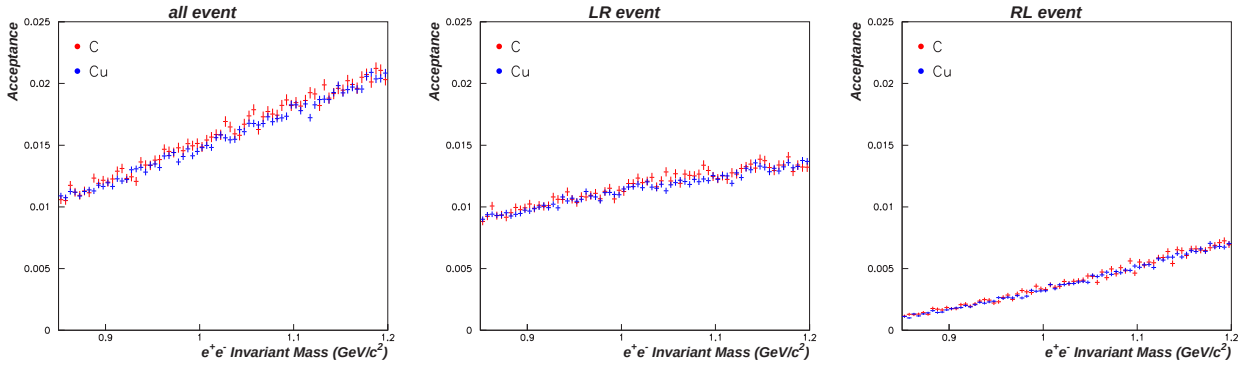

Figure 3.54: The mass acceptances for e^+e^- decays for the C and the averaged Cu targets, for the all events (left), LR events (center), and RL events (right).

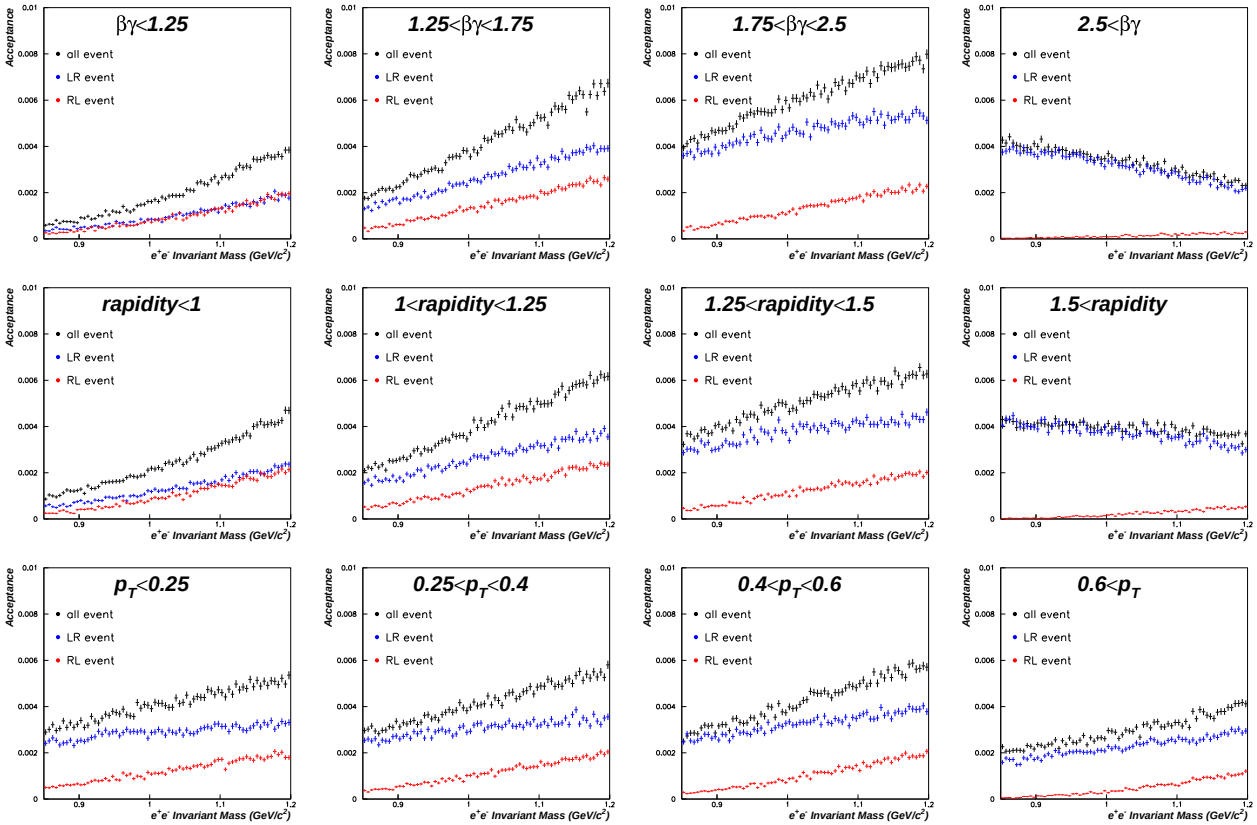

Figure 3.55: The mass acceptances for e^+e^- decays divided into four bins in $\beta\gamma$ (top), rapidity (middle), and p_T (bottom). The acceptances for the averaged Cu targets for the all events, LR events, and RL events are shown.

3.5.2 $\phi \to K^+K^-$ Simulation

Spectral Shape of $\phi \to K^+K^-$

The spectral shape of $\phi \to K^+K^-$ was generated using the relativistic Breit-Wigner distribution which is given by Ref. [66];

$$\frac{d\sigma}{dm} = \frac{m m_0 \Gamma(m)}{\left(m^2 - m_0^2\right)^2 + \left(m_0 \Gamma(m)\right)^2} , \tag{3.25}$$

where

$$\Gamma(m) = \Gamma_0 \left(q/q_0\right)^3 (m_0/m) , \tag{3.26}$$

$$q = \sqrt{m^2/4 - m_K^2} , \tag{3.27}$$

$$q_0 = \sqrt{m_0^2/4 - m_K^2} , \tag{3.28}$$

with K^+K^- invariant mass (m), the pole mass of the ϕ (m_0), and kaon mass (m_K). The distribution is compared with the non-relativistic one in Fig. 3.56, in which visible changes exist. In addition, the K^+K^- threshold should be included in the mass shape. Thus we used relativistic Breit-Wigner form unlike the the $\phi \to e^+e^-$ case.

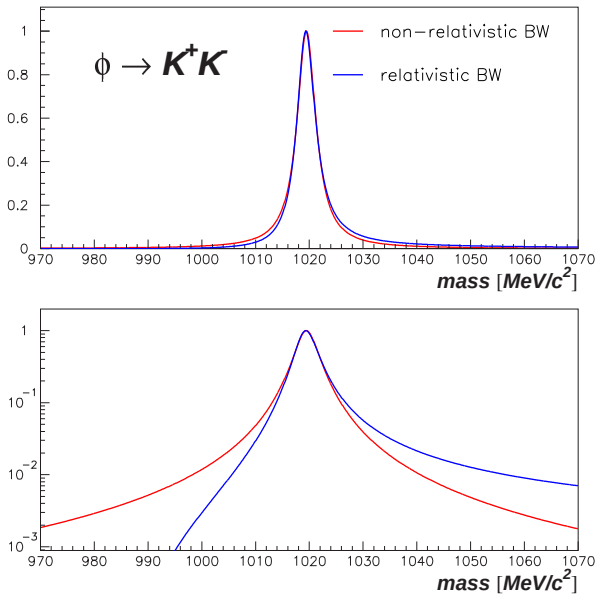

Figure 3.56: The non-relativistic (red) and the relativistic (blue) Breit-Wigner distribution for $\phi \to K^+K^-$ decays. The distributions are normalized by their peak count to unity.

Kinematical Distribution

The kinematical distribution of $\phi \to K^+K^-$ decays was obtained as same as e^+e^- decays as described before, and the results are shown in Fig. 3.57. The observed and simulated distributions are compared in Fig. 3.58, 3.59, and 3.60. The agreements are quite good again. The observed distributions were obtained again with the side-band subtracting method, as $\phi \to e^+e^-$ decays. The signal region was chosen from 1.01 to 1.03 GeV/c^2 and the side-bands were from 1.00 to 1.01 and from 1.03 to 1.04 GeV/c^2, as shown in Fig. 3.61.

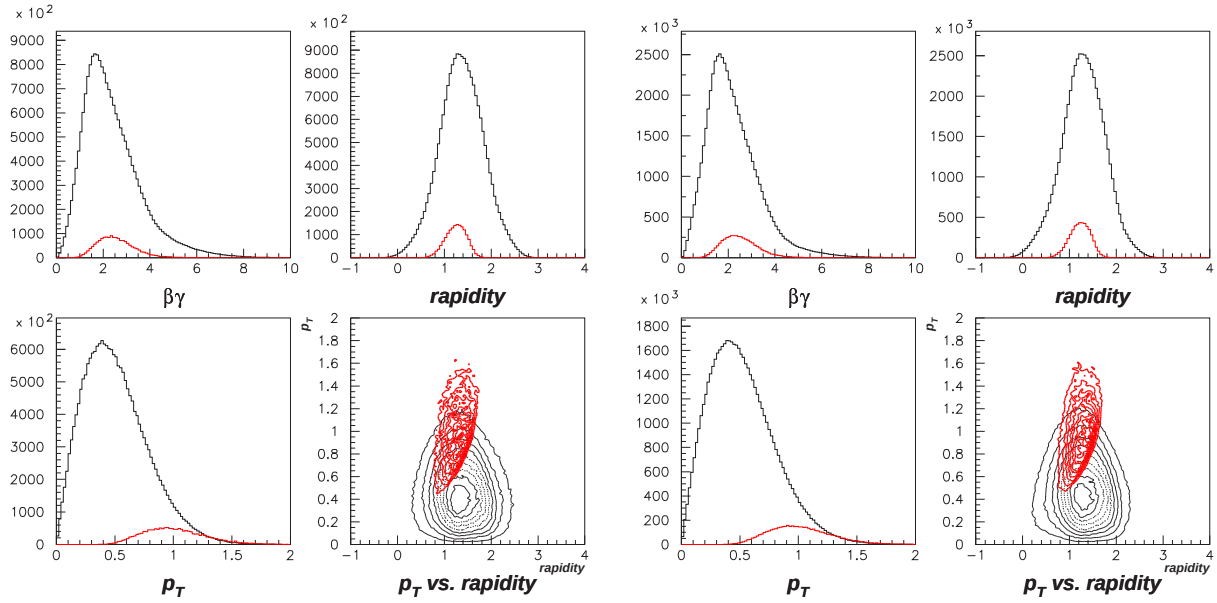

(a) C (b) Cu

Figure 3.57: The kinematical distributions of the generated ϕ mesons using JAM (black lines) and of the accepted $\phi \to K^+K^-$ in the detector (red lines). The accepted $\phi \to K^+K^-$ are scaled up by a factor of 50.

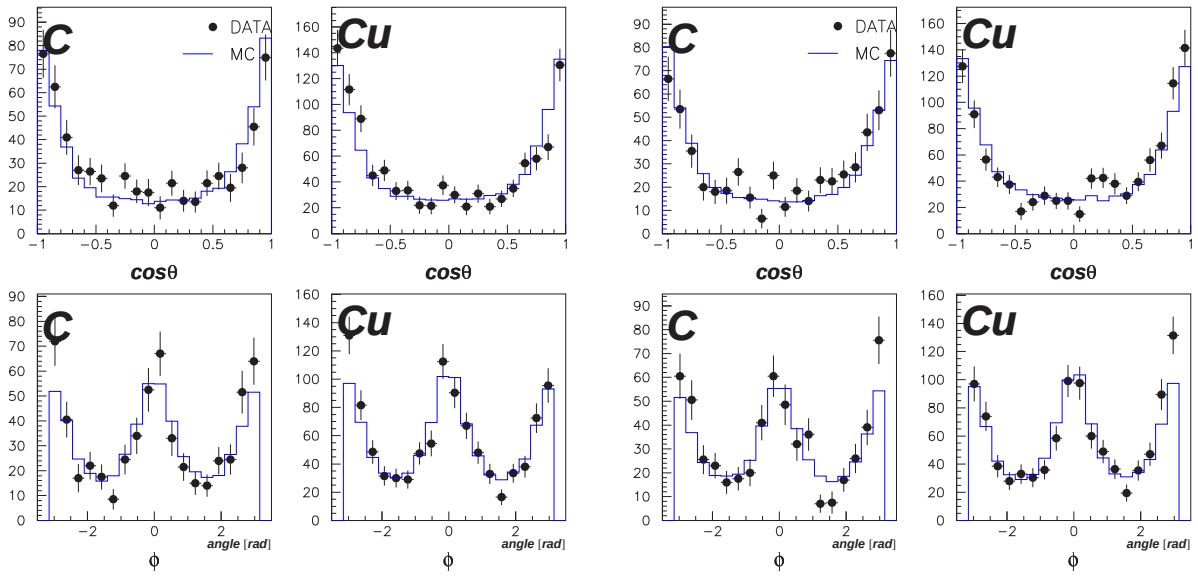

(a) the Gottfried-Jackson frame (b) the helicity frame

Figure 3.58: The decay angular distributions for the data (closed circles) and the simulation (lines), (a) in the Gottfried-Jackson frame and (b) in the helicity frame. The scaling is determined arbitrarily.

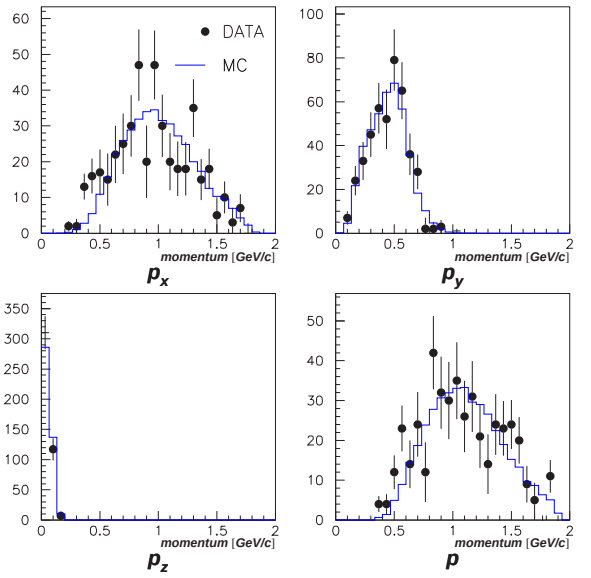

(a) K^+ in $\phi \to K^+K^-$ for C

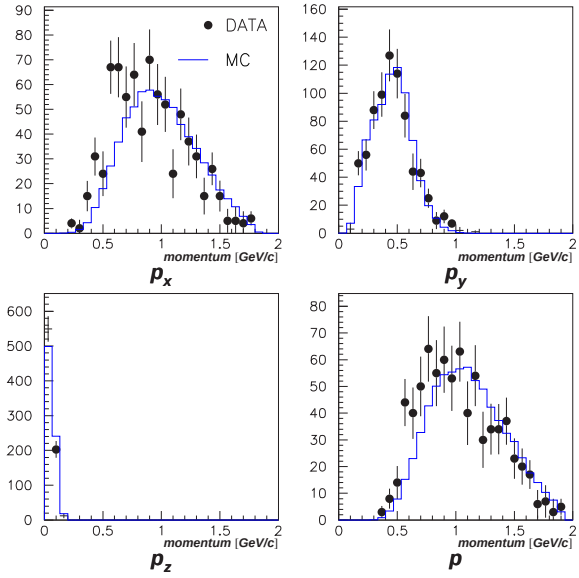

(b) K^+ in $\phi \to K^+K^-$ for Cu

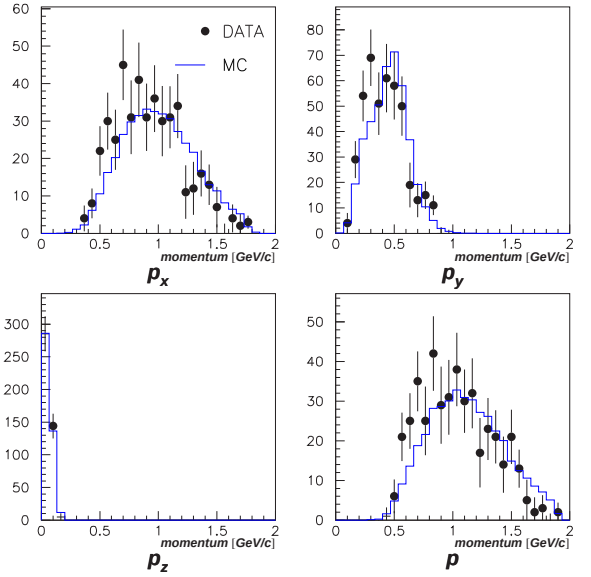

(c) K^- in $\phi \to K^+K^-$ for C

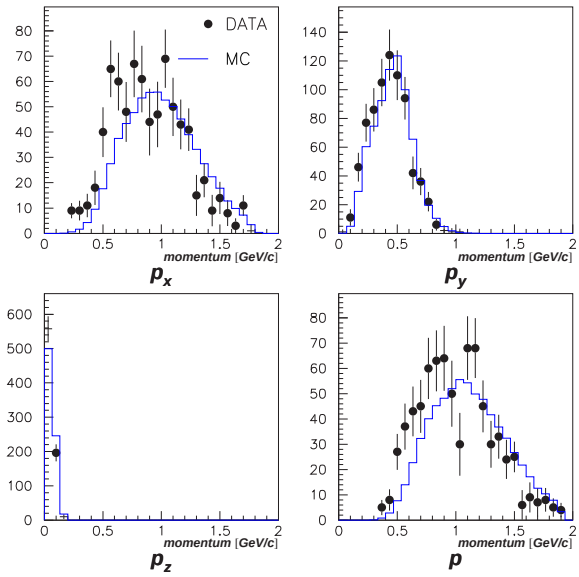

(d) K^- in $\phi \to K^+K^-$ for Cu

Figure 3.59: The momentum distributions of the observed (closed circles) and simulated (lines) daughter K^+ (top panels) and K^- (bottom panels) in the $\phi \to K^+K^-$ decays, for C (left panels) and for Cu (right panels). The scaling is determined arbitrarily.

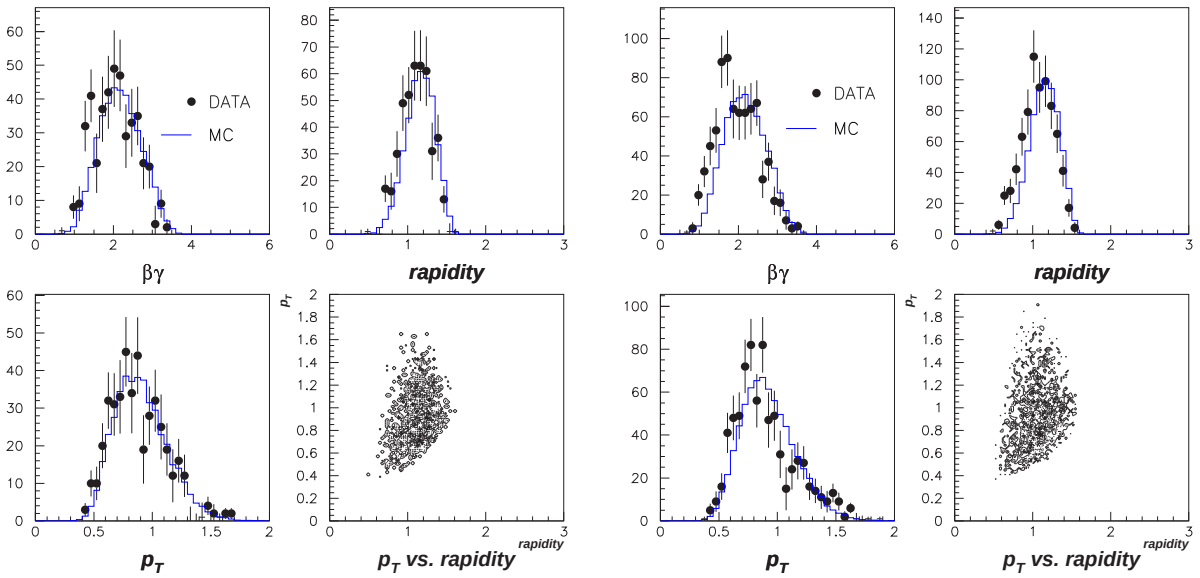

(a) $\phi \to K^+K^-$ for C (b) $\phi \to K^+K^-$ for Cu

Figure 3.60: The kinematical distributions of the observed (closed circles) and simulated (lines) $\phi \to K^+K^-$ pairs, for C (left four panels) and for Cu (right four panels). In the scatter plots of p_T versus rapidity, only the observed events are shown. The scaling is determined arbitrarily.

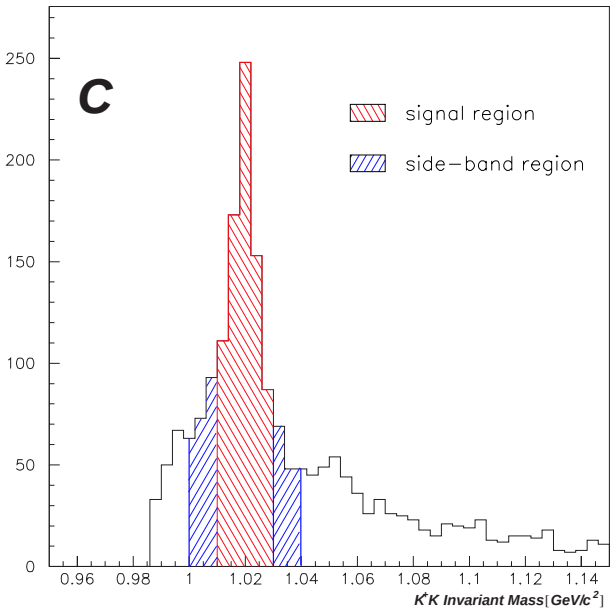

Figure 3.61: The separation of the signal region and the side-band (background) regions.

Rescattering of Kaons in Nucleus

When a ϕ meson decays inside a nucleus, daughter K and $\bar{K}$ are considered to be absorbed or rescattered in the nucleus. The K and $\bar{K}$ absorptions decrease the observed cross section while do not change the invariant mass spectrum. However, the KN and $\bar{K}N$ rescatterings affect both the cross section and the invariant mass spectrum. The effects of KN and $\bar{K}N$ rescattering were studied using JAM.

We chased $\phi \to K^+K^-$ decays in JAM, and then the daughters were flagged when they were absrobed or rescattered in the nucleus. The obtained yields of these events are summarized in Table 3.8, and the invariant mass distributions are shown in Fig. 3.62. It can be concluded that the probability of the rescattering is small, less than 3% even in the Cu nucleus, and that the rescattered events cannot be identified as ϕ mesons. We neglect such a rescattering effect in the later analysis, which at the same time implies that the experiment is not sensitive to a few % level of the mass shape modification.

When we define the ϕ-meson which decays inside the half-density radius of the Woods-Saxon distribution as the inside decay in the nucleus, as described in Sec. 4.4, probabilities of the inside decay are estimated to be 1.3% and 3.3% in the carbon and copper nucleus respectively. So the daughters of $\phi \to K^+K^-$ decays which decays inside in the nucleus are almost absorbed or rescatterd [3].

	^{12}C		^{63}Cu	
generated $\phi \to K^+K^-$	52.2k	100.0%	72.4k	100.0%
w/o kaon absorption	51.5k	98.6%	69.3k	95.8%
w/o kaon absorption and rescattering	50.8k	97.3%	67.9k	93.8%

Table 3.8: The numbers of generated $\phi \to K^+K^-$ decays and kaon absroptions and rescatterings.

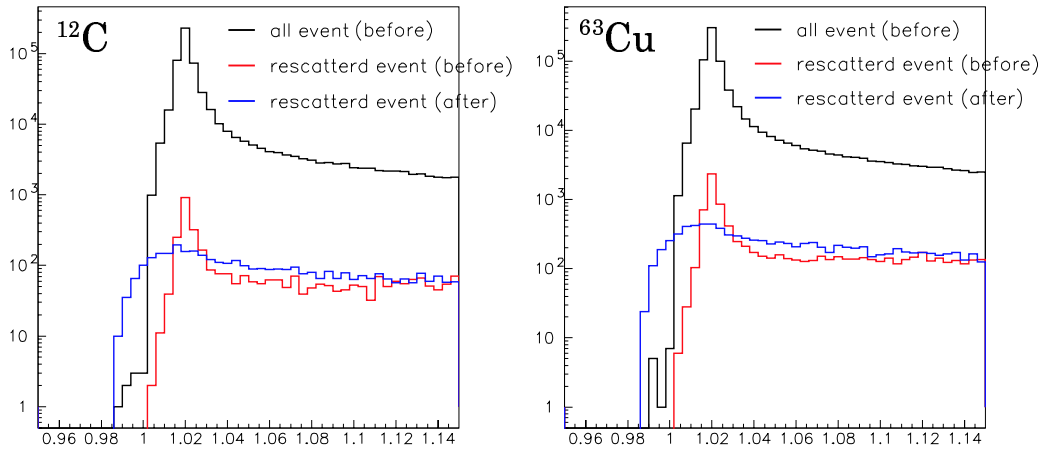

Figure 3.62: The $\phi \to K^+K^-$ invariant mass distributions obtained by JAM. The black lines represent all the $\phi \to K^+K^-$ events before the rescattering. The red and blue lines represent the events with the rescattering before and after the rescattering, respectively.

[3] When we define the ϕ-meson which decays inside the 1/10-density radius as the inside decay, probabilities of the inside decay are estimated to be 3.1% and 5.1% in the carbon and copper nucleus respectively.

Mass Acceptance for K^+K^- Decays

The acceptance of the K^+K^- invariant mass spectrum was studied through the detector simulation, as same as the e^+e^- pair case as explained before. This time a flat mass distribution from $2m_{K^\pm}(0.987)$ to 1.15 GeV/c^2 was used.

The obtained mass acceptances for each target disk are shown in Fig. 3.63(a). Because of the small opening angle of $\phi \to K^+K^-$ decays, there is a high probability that K^+ and K^- tracks cross each other in a chamber drift cell. In such case, the chamber hit information in the cell is correct for one track and lost from other track, and a pair reconstruction efficiency for such event becomes worse. Therefor the mass acceptance decreases kinematically on the low mass side of the ϕ-meson peak. The obtained acceptances are almost equivalent between the C target and the average of the Cu targets, as shown in Fig. 3.63(b). The small but visible difference in Fig. 3.63(b) will be considered later in Sec.4.3.2. In the later discussions in Sec. 4.2, we divide the data into three bins in $\beta\gamma$, rapidity, and p_T. With these divisions, we obtained the mass acceptances as shown in Fig. 3.64. The acceptance at the ϕ-meson peak (1.02 GeV/c^2) was about 0.12%.

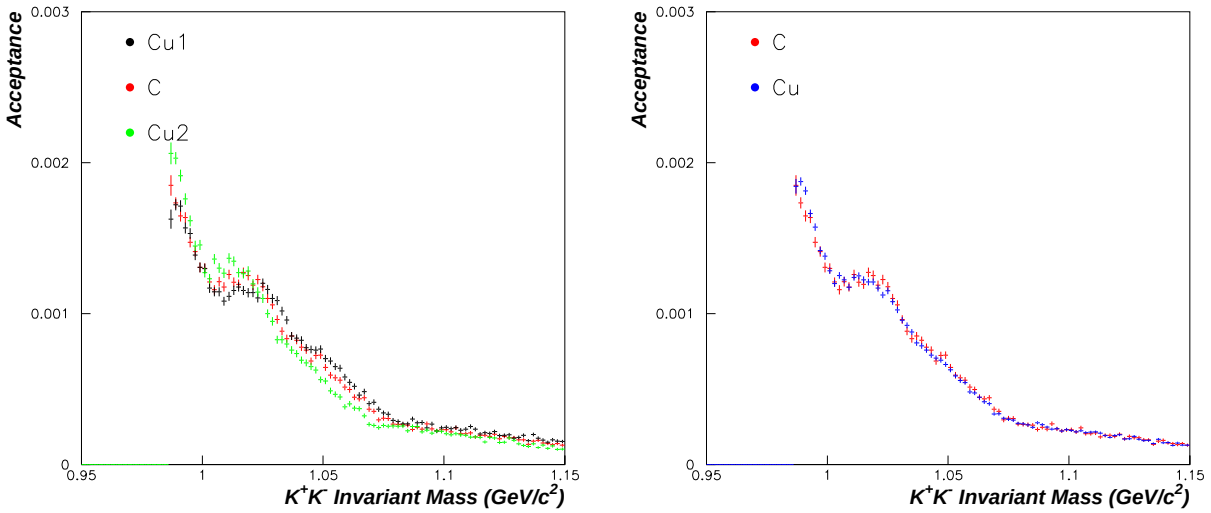

(a) (b)

Figure 3.63: (a)The mass acceptances for each target disk in K^+K^- decays. (b)The mass acceptances for the C target and the averaged one for the Cu targets.

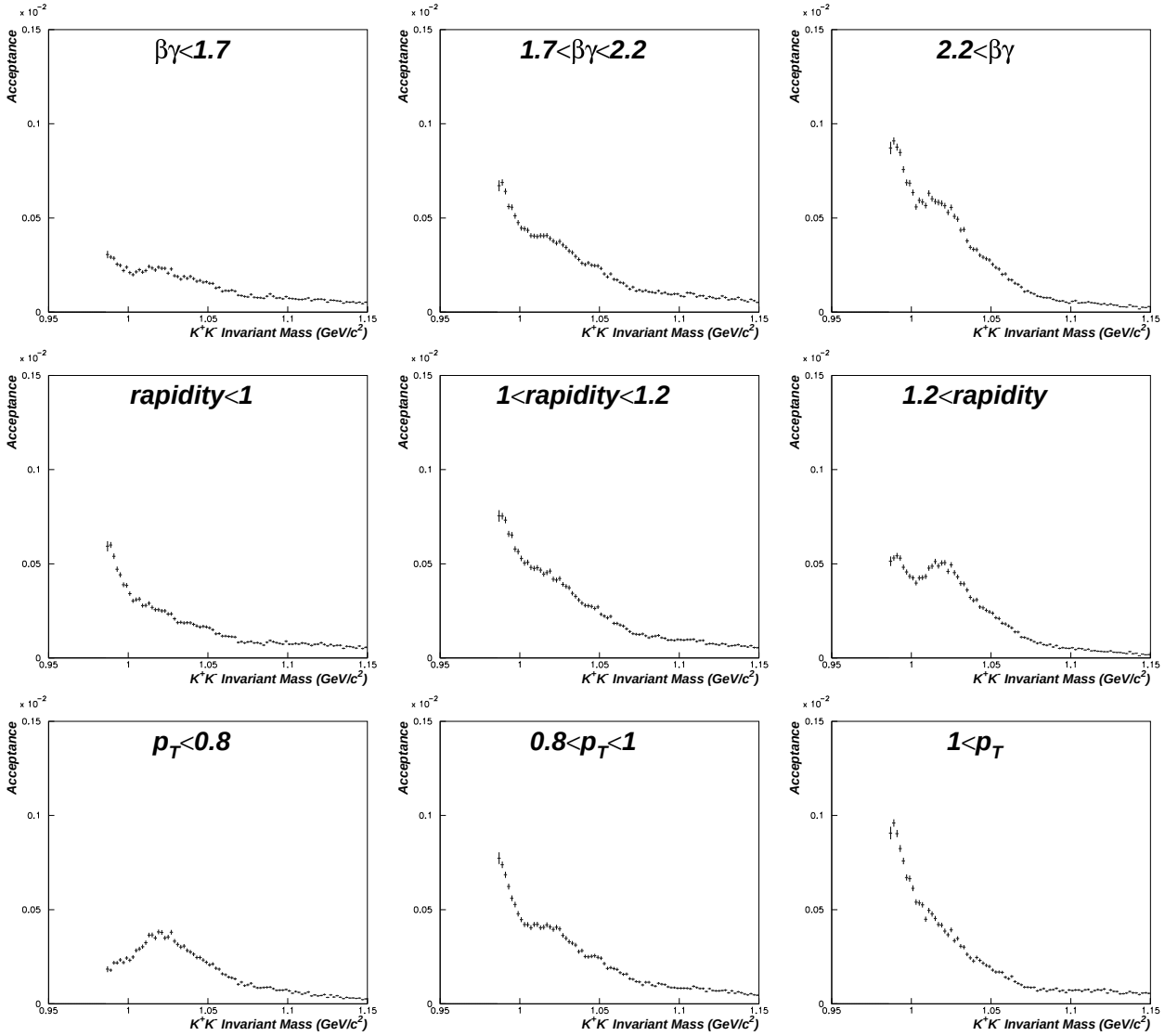

Figure 3.64: The mass acceptances for Cu targets in K^+K^- decays divided into three bins in $\beta\gamma$ (top), rapidity (middle), and p_T (bottom).

3.5.3 Momentum Resolution

Single Track Resolution

The effects of the detector materials and the chamber resolution were studied with use of the detector simulation. We evaluated the momentum resolution for e, π, K, and p as shown in Fig. 3.65(a), and the differences of the obtained momenta from the original value are shown in Fig. 3.65(b). The sources of the momentum resolution are from the chamber resolution, coulomb multiple scattering, and the energy losses as shown in Fig. 3.66. The energy losses here include external bremsstrahlung, ionization, and δ-ray processes. It should be noted that in the electron curves in Fig. 3.66(a), the amount of an energy-loss tail from the external bremsstrahlung is not taken into account in the evaluation since we used the values of the Gaussian-fitting width.

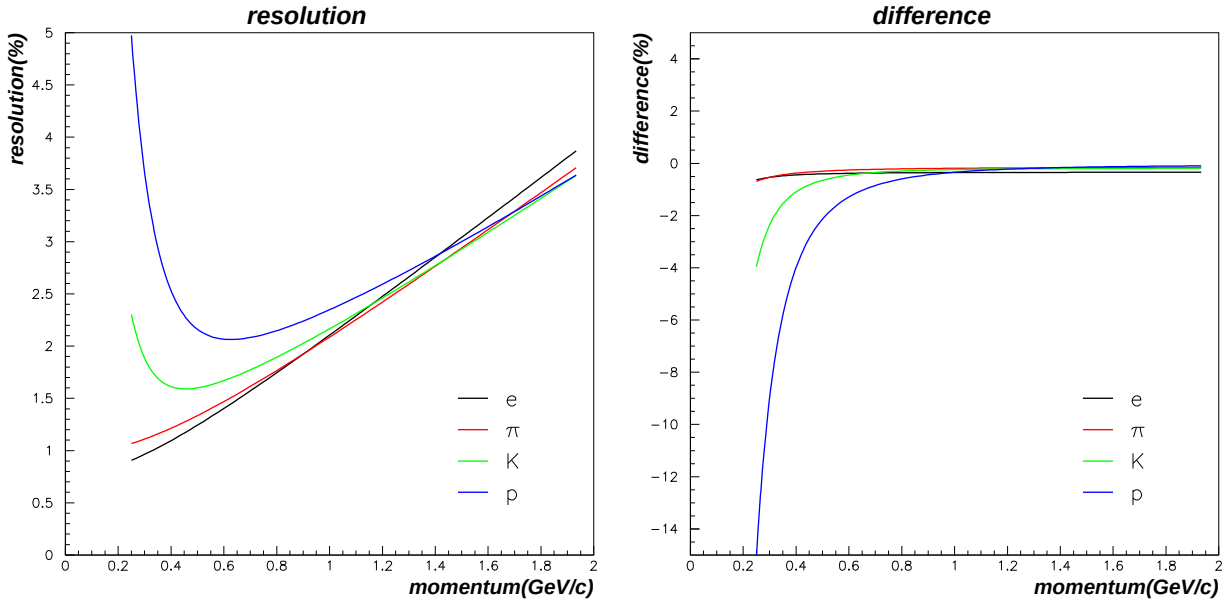

(a) momentum resolution (b) difference of momentum

Figure 3.65: (a)The momentum resolution for e, π, K, and p. (b)The difference of the obtained momenta from the original values.

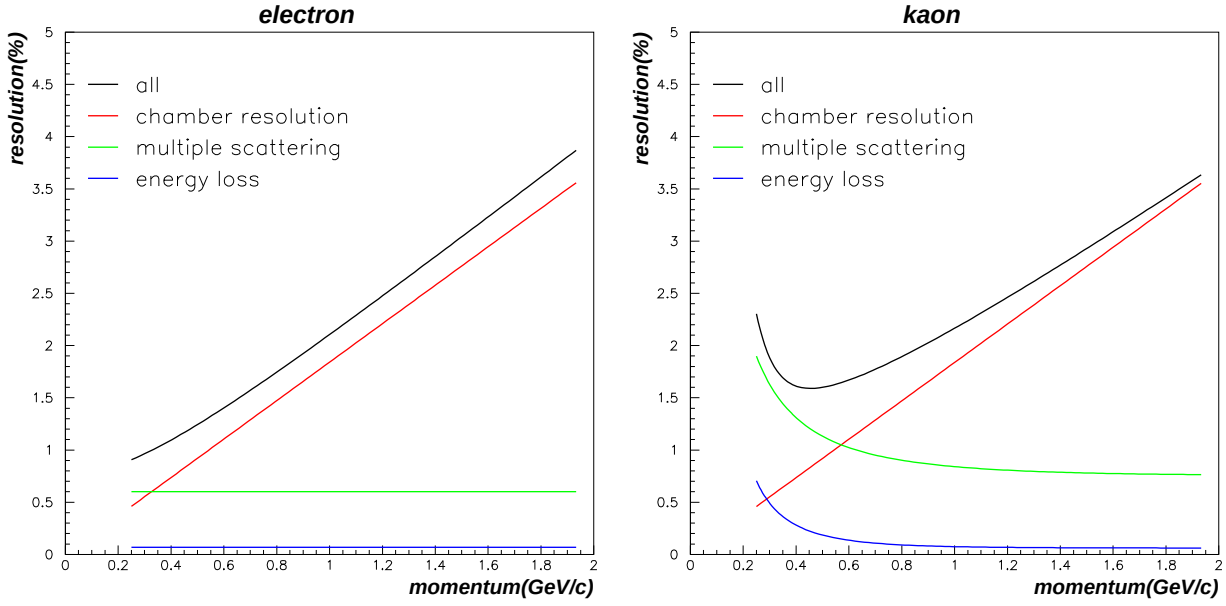

(a) electron (b) kaon

Figure 3.66: Breakdown of the sources in the momentum resolution, (a) for e and (b) for K.

Momentum Resolution with Common-Vertex Track Fitting

In the analysis of e^+e^- and K^+K^- pairs, we constrained the vertex position onto the target position (see Sec. 3.3.4). This "Common Vertex Track Fitting" (CVTF) improved the momentum resolution as shown in Fig. 3.67.

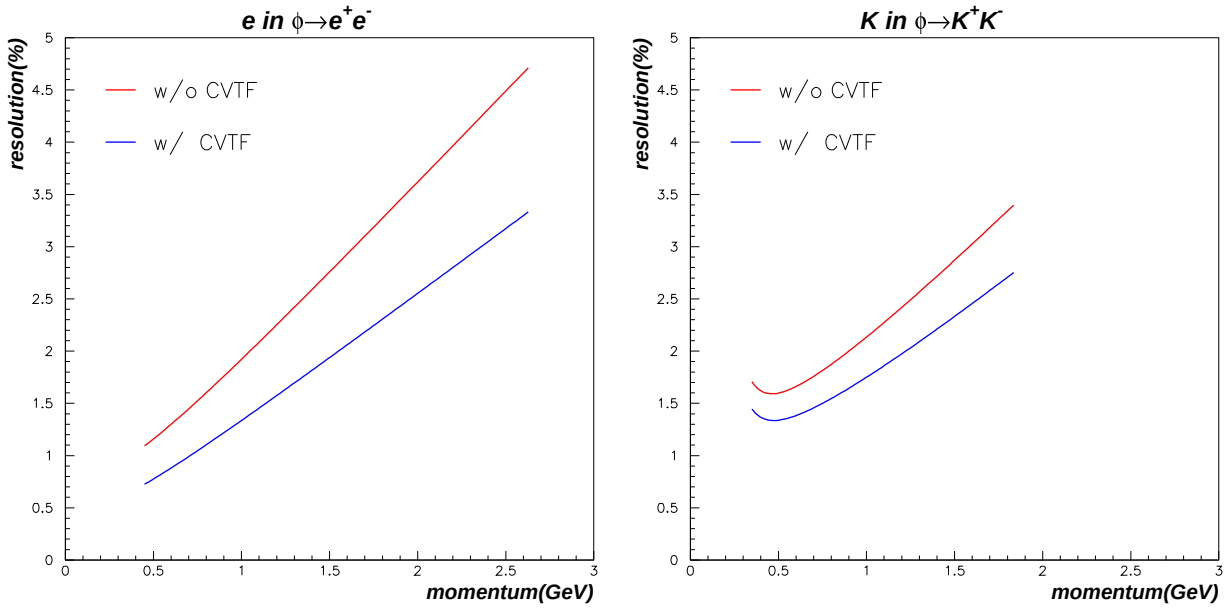

(a) e in $\phi \to e^+e^-$ (b) K in $\phi \to K^+K^-$

Figure 3.67: The momentum resolution (a) for e in $\phi \to e^+e^-$ and (b) for K in $\phi \to K^+K^-$. The resolution "without CVTF" and "with CVTF" are plotted.

3.6 Background Estimation

3.6.1 Background in the $\phi \to e^+e^-$ Channel

The sources of the background were uncorrelated pairs of e^+ and e^-, which mainly come from π^0 Dalitz decays, γ-conversions in the targets and the detector materials, and miss-identified pions. Because all the correlated background from Dalitz decays and γ-conversions fall in below the π^0 and η mass, all the e^+e^- pairs around the ϕ mass region must be originated from uncorrelated pairs of π^0 or η which decay into $e^+e^-\gamma$ or $\gamma\gamma$ followed by eventual conversions. In order to evaluate the amount of $e^+\pi^-$, $e^-\pi^+$, or $\pi^+\pi^-$ pairs originated from the miss-identified pions in the background, we examined the signal to noise ratio S/N in the ϕ mass region.

The invariant mass spectra were fitted with the simulated ϕ resonance shape and a quadratic background curve. The fit region was from 0.85 GeV/c^2 to 1.2 GeV/c^2 except that the mass region from 0.95 to 1.00 GeV/c^2, where the excess signal was observed [31], was excluded from the fit. The amount of the signal was defined by subtracting the background from the data in the mass region from 0.99 to 1.04 GeV/c^2. Although S does not contain the miss-identified pion, N contains the pion contamination. Thus, we consider $N = e + c$, where e is from pure e^+e^- pairs and c is from contamination. When the electron selections are tightened enough to reject miss-identified pions completely, the ratio S/N should become better and saturate. So we obtained the S/N by varying the electron identification condition to strict ones (ID=1 to 14 in Fig. 3.68). The fitted spectra for ID = 1 and 9 are shown in Fig. 3.69. The maximum $(S/N)_{\max} = S/e$ was obtained to be 2.01 ± 0.06 when ID is greater than 8.

The S/N in the present analysis (ID=1) was obtained to be 1.21 ± 0.03. Since $(S/N)_{\max}$ is independent of the electron purity, the contaminations can be obtained as

$$c = N - \frac{S}{(S/N)_{\max}}. \tag{3.29}$$

We conclude that the ϕ mass region from 0.99 to 1.04 GeV/c^2 contains 54.7 ± 1.0 % of the

signal ($\phi \to e^+e^-$), 27.2 ± 0.9 % of combinatorial e^+e^- background, and 18.1 ± 0.8 % of particle miss-identifications ($e^+\pi^-$, $e^-\pi^+$, and $\pi^+\pi^-$).

With a separate study described later in Sec. 3.6.2 and also in Ref. [35], we found the $\pi^+\pi^-$ invariant mass distribution is well reproduced by the event-mixing method except for a small peak from $K^0_s \to \pi^+\pi^-$ decays. Thus we can safely assume that the background shape of the e^+e^- mass spectra is reproducible also by the event-mixing. Nevertheless we used a quadratic function for the background shape in the later analysis to leave a room to take a possible tail from the ρ/ω region into account.

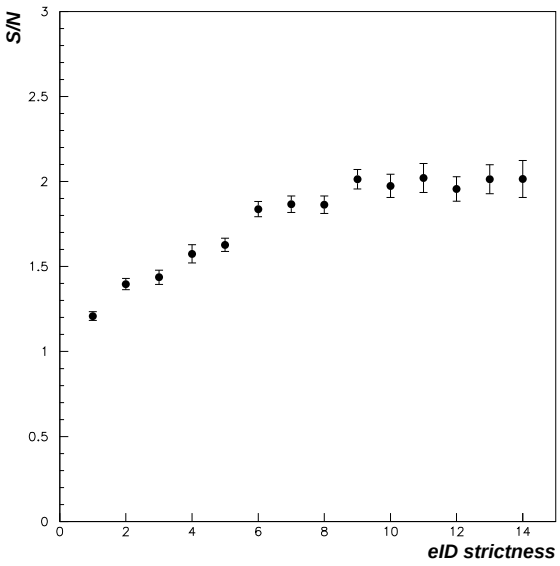

ID	threshold above pedestal (ADC counts)		
	FGC ADC	RGC ADC	lead-glass E/p
1	200	50	0.5
2	400	50	0.5
3	600	50	0.5
4	800	50	0.5
5	400	50	0.6
6	400	50	0.7
7	400	100	0.7
8	400	150	0.7
9	400	100	0.8
10	600	100	0.8
11	800	100	0.8
12	600	150	0.8
13	600	100	0.9
14	800	150	0.9

Figure 3.68: The S/N with a various electron identification conditions. The condition is severe with larger IDs. The conditions are listed in the right panel.

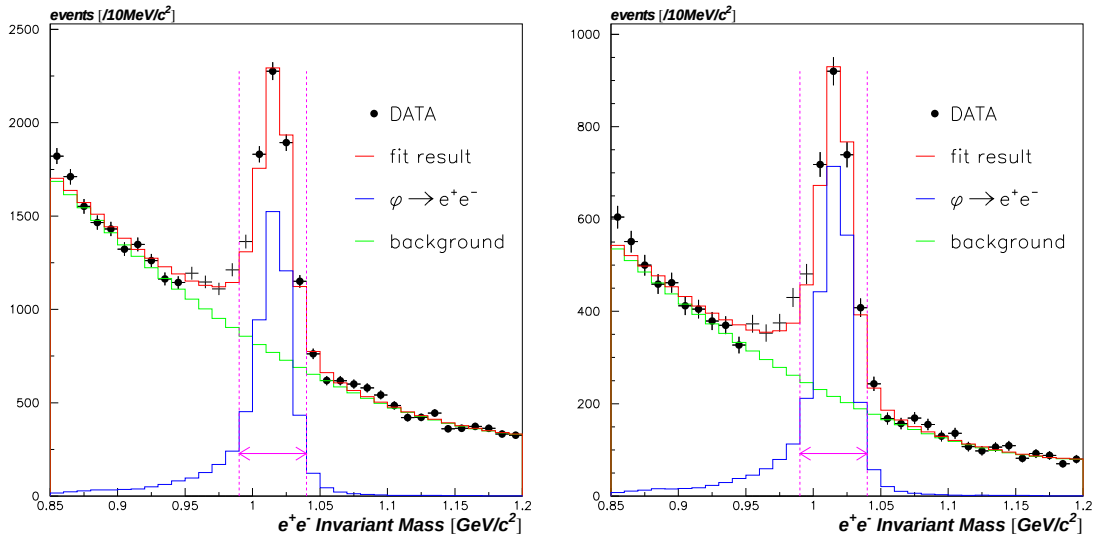

(a) ID = 1 (b) ID = 9

Figure 3.69: The e^+e^- mass distributions with the fit results for (a) ID = 1 and (b) ID = 9 in Fig. 3.68. The data for all the targets are summed. The closed circles represent the data and the thin crosses represent the excluded region from the fit. The red, green and blue lines represent the fit results, the quadratic backgrounds and the expected $\phi \to e^+e^-$ shapes, respectively. The arrows indicate the region to examine the S/N.

3.6.2 Background in the $\phi \to K^+K^-$ Channel

The sources of the background in $\phi \to K^+K^-$ decays are non-resonant K^+K^- pairs like $K^+K^{*-} \to K^+K^-\pi^0$, $K^{*0}\bar{K^{*0}} \to K^+\pi^-K^-\pi^+$, and so on, and pairs due to miss-identified pions and protons. The purity of the K^+K^- pair samples was estimated to be 85.6 $\pm$ 4.7(stat) $\pm$ 0.7(syst) % as described in Sec. 3.3.6, so that the miss-identification is not a major issue. The correlation in non-resonant K^+K^- pairs, however, are not well known. If the non-resonant K^+K^- pairs have no correlation, it is reasonable to use the event-mixing method for the K^+K^- background estimation in which a K^+-track from one event is combined with a K^--track from other event which comes from the same target as K^+-track. We need to impose the track-crossing effect described in Sec. 3.5.2 in the event mixing. So we reconstructed the tracks of the mixed event as same as the real-data analysis, i.e., the track finding, the fitting by the Runge-Kutta method, and Common Vertex Track Fitting. In the following sections, we examine;

- whether it is reasonable to use the mixed event for the combinatorial background or not,
- whether the non-resonant K^+K^- pairs have correlation or not.

Study of $\pi^+\pi^-$ Data

First, we checked usability of the event-mixing method to reproduce the shape of the combinatorial background. In this study, we used $\pi^+\pi^-$ pairs which were assumed to be uncorrelated [4]. Figure 3.70(a) and (b) show the invariant mass spectra of $\pi^+\pi^-$ pairs with CVTF for the single-arm events and the double-arm events, respectively, compared to the mixed-event spectra. It can be concluded that the invariant mass spectra of $\pi^+\pi^-$ pairs are well reproduced with the mixed event.

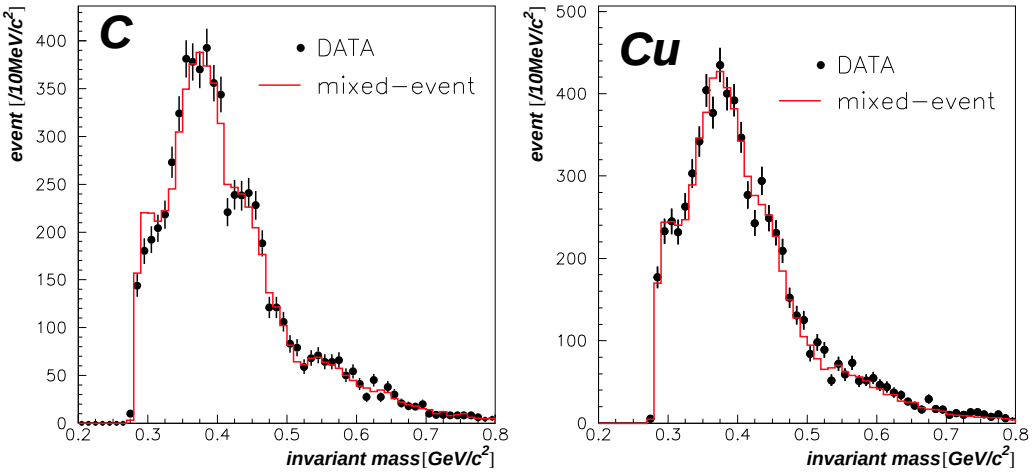

(a) single-arm events

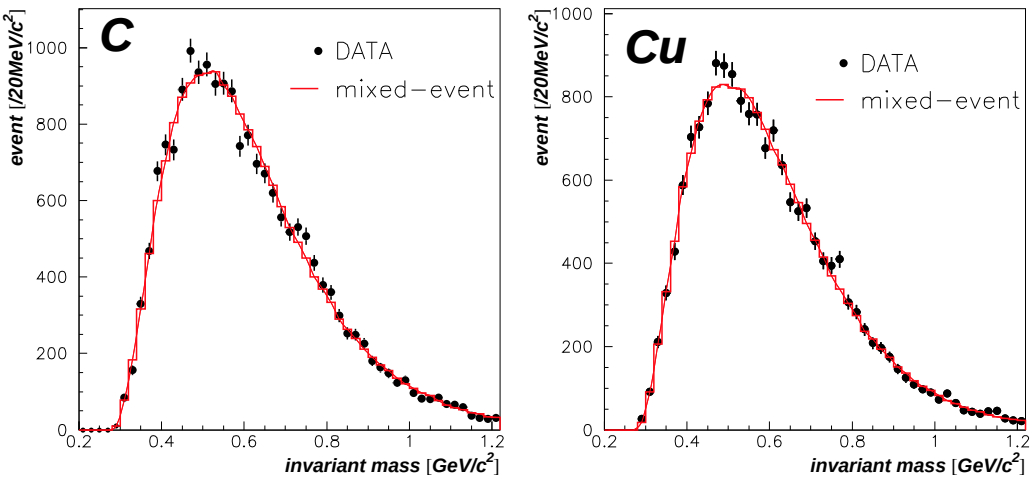

(b) double-arm events

Figure 3.70: The invariant mass spectra of $\pi^+\pi^-$ pairs with CVTF for (a) the single-arm events and (b) the double-arm events (LR events only). The closed circles and lines represent the data and the mixed event, respectively.

[4] This assumption is safe since the $\rho \to \pi^+\pi^-$ mass distribution is wide and we have a small acceptance for those. A peak of $K^0_s \to \pi^+\pi^-$ is negligible as long as we do not apply a delayed-decay condition.

Study of Non-Resonant K^+K^- by JAM

Next, we examined whether the non-resonant K^+K^- pairs have a correlation or not. The mass and kinematical distributions of non-resonant K^+K^- pairs were obtained by JAM, and experimental effects were taken into account using the detector simulation. Figure 3.71(a) and (b) show the invariant mass spectra of non-resonant K^+K^- pairs with CVTF for the single-arm events and the double-arm events, respectively, which are well reproduced with the mixed event. So the non-resonant K^+K^- pairs in JAM can be considered to have no correlation.

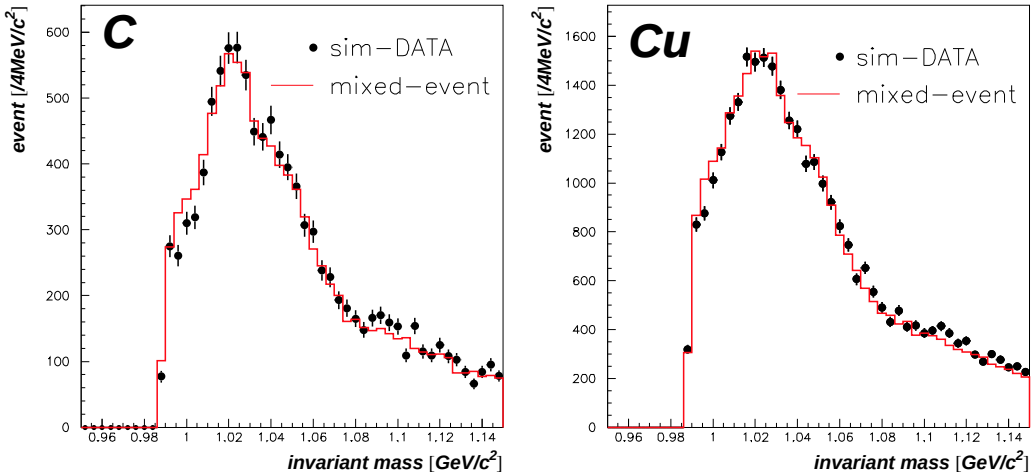

(a) single-arm events

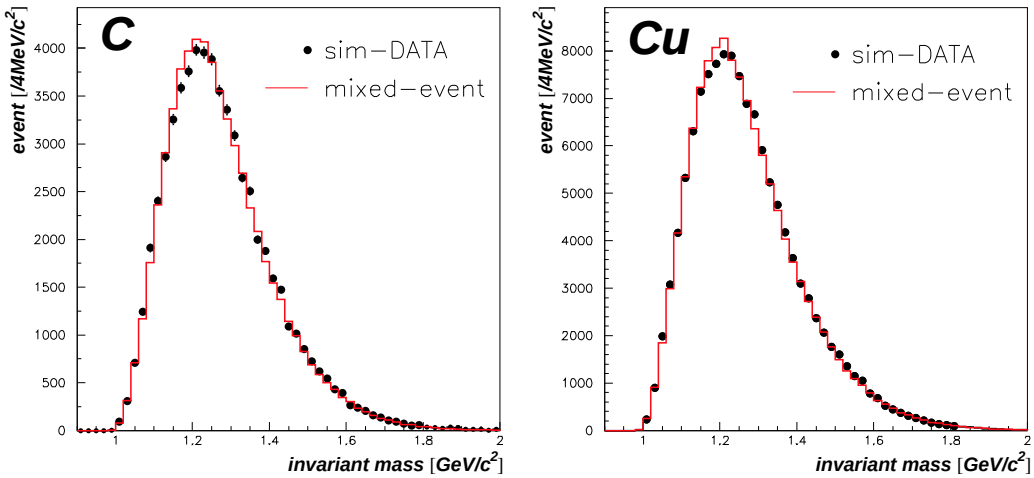

(b) double-arm events

Figure 3.71: The invariant mass spectra of non-resonant K^+K^- pairs with CVTF for (a) the single-arm events and (b) the double-arm events (LR events only) obtained by JAM. The closed circles and lines represent the simulated data and those after the event-mixing, respectively.

Study of Double-Arm K^+K^- Data

In addition to the results using JAM described above, we studied the non-resonant K^+K^- pairs using the double-arm K^+K^- event data. Because of the small Q value in $\phi \to K^+K^-$ decays, the $\phi \to K^+K^-$ events were negligible in the double-arm K^+K^- events (see Appendix B). So the double-arm K^+K^- events should consist of the non-resonant K^+K^- pairs and contaminations from miss-identified pions and protons. As same as Sec. 3.3.6, we evaluated the purity of the kaon in the double-arm data as listed in Table 3.9 for reference. Figure 3.72 show the invariant mass spectra of K^+K^- pairs with CVTF for the double-arm events. The invariant mass spectra of K^+K^- pairs are well reproduced with the mixed event, so that the double-arm K^+K^- pairs can be considered to contain only uncorrelated pairs.

	purity(%)
K^+	$84.7 \pm 5.4(\text{stat}) \pm 0.3(\text{syst})$
K^-	$81.8 \pm 7.3(\text{stat}) \pm 0.1(\text{syst})$
K^+K^-	$69.3 \pm 7.6(\text{stat}) \pm 0.3(\text{syst})$

Table 3.9: The purity of the kaon in the double-arm data (LR events only).

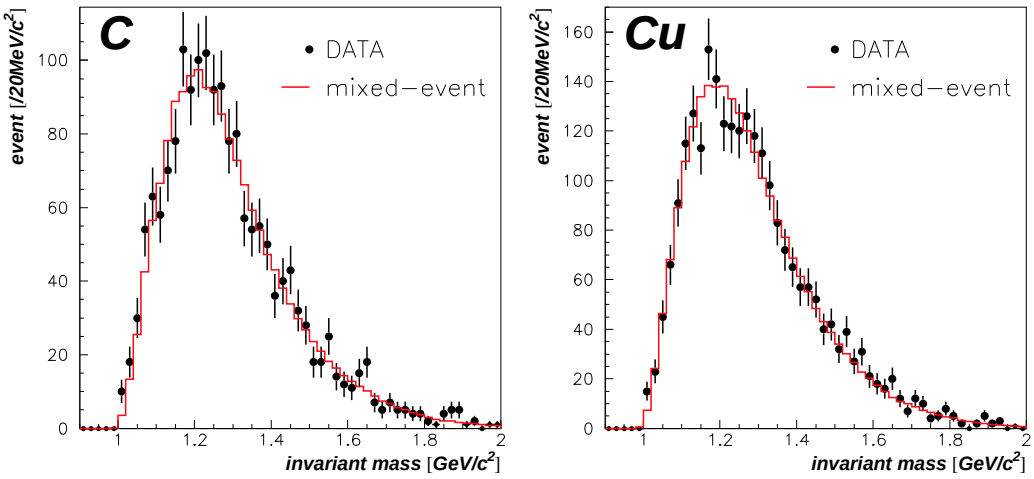

Figure 3.72: The invariant mass spectra of K^+K^- pairs with CVTF for the double-arm events (LR events only). The closed circles and lines represent the data and the mixed events, respectively.

Combinatorial Background for the Final K^+K^- Sample

Considering the confirmations described above, it is reasonable to use the event-mixing method to estimate the K^+K^- background shape. Below we describe the method in detail.

The event-mixing method is usually used in heavy-ion experiments by simply taking K^+ and K^- from different events. In our experiment, the signal to noise ratio (S/N) is much better, S/N is about unity at the $\phi \to K^+K^-$ resonances, compared with heavy-ion experiments. Thus we considered the distortion of the background shape due to the K^- or K^+ originated from the resonance itself. To eliminate such a distortion, the weights to the pairs in the resonance regions (correlated pairs) were reduced according to the S/N in the mass region from 1.002 to 1.038 GeV/c^2 which was determined by the fit. At the first step, we chose arbitrary values as the input weights for the correlated pairs in the event-mixing, and obtained the tentative background shape. Next, we fitted the spectra with this background shape and the simulated ϕ resonance shape to obtain the S/N. The obtained S/N was used as the input weights in making the new combinatorial background shape. We repeated this procedure until the background shape got stabilized (converged).

To study a systematic uncertainty in the background estimation, we made the different background shape by setting the weights to 1 or 0 to the tracks belonging to the resonance region. In other words, we considered three types of backgrounds;

Type 1: including all tracks belong the resonance mass-region ("all-in" in Fig. 3.73),

Type 2: using the tracks in the resonance mass-region with the weights determined by S/N ("S/N" in Fig. 3.73), and

Type 3: excluding all tracks belong the resonance mass-region ("all-ex" in Fig. 3.73).

Figure. 3.73 shows the shapes of those backgrounds normalized with the number of entries. In the following analysis, we used the Type 2 (S/N) background for the fit, and used the Type 3 (all-ex) background for the study of systematic errors [5].

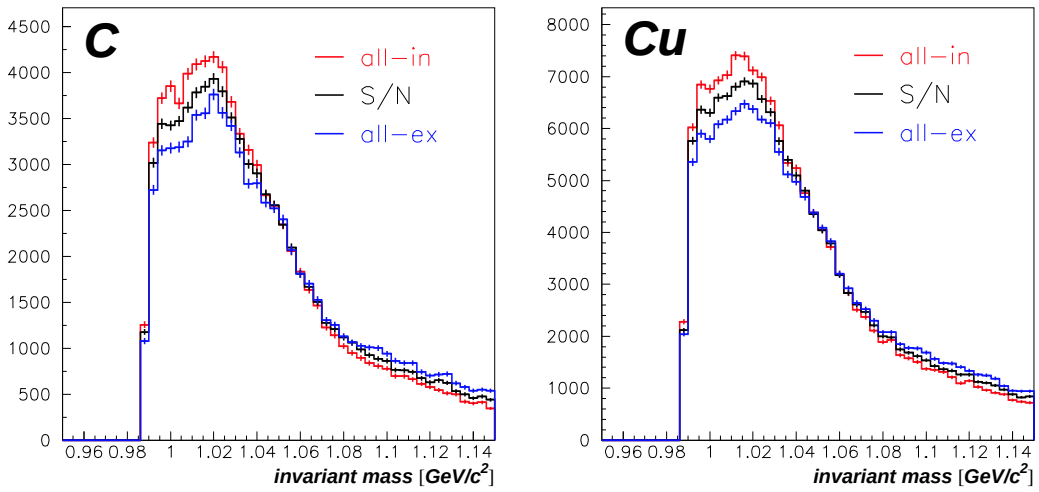

Figure 3.73: Three types of the combinatorial background shape obtained by the event-mixing and normalized by the number of the mixed events. The red, black, and blue lines represent Type 1, 2, and 3, respectively (see text).

[5] The obtained yields of the ϕ mesons used the Type 1 and Type 3 background are almost symmetric about the yields used the Type 2 background. So we used only the Type 3 background for the systematic-error study.

3.7 Mass Scale and Resolution for ϕ

3.7.1 $\phi \to e^+e^-$ Decays

We examined the reproducibility of the detector simulation using $K^0_s \to \pi^+\pi^-$ and $\Lambda \to p\pi^-$ decays as described in Sec. 3.3.3. The observed resolution and centroids of the resonances were well reproduced by the simulation.

For $\phi \to e^+e^-$ decays, we estimated the mass resolution to be 10.7 MeV/c^2 in the data, and to be 10.1 MeV/c^2 in the detector simulation. Since $\phi \to e^+e^-$ events were required to be "double-arm event", the uncertainty of the mass scale and the resolution emerged from the remaining errors due to the alignment of the chambers as described in Sec. 3.2.3. In other words, the BDC alignment was not precise enough in this mass scale and the resolution (a few MeV/c^2). It should be noted that such a problem due to the chamber miss-alignment was negligible in "single-arm event", i.e. for $\phi \to K^+K^-$, $\mathrm{K}^0_s \to \pi^+\pi^-$, and $\Lambda \to \mathrm{p}\pi^-$.

Thus we examined the amount of changes in the mass scale and the resolution by fitting the mass spectra with the detector simulation. First, we shifted the simulated $\phi \to e^+e^-$ shape step by step using parameter δm with an interval of 0.1 MeV/c^2, and we also smeared the shape step by step with a Gaussian of a width $\delta\sigma$ with an interval of 0.1 MeV/c^2. Next, in the high $\beta\gamma$ region ($\beta\gamma > 1.5$), we fitted the data with these modified $\phi \to e^+e^-$ shapes and a quadratic background. The obtained best values and the associated errors of δm and $\delta\sigma$ are summarized in Table 3.10. The systematic errors contain contributions from the uncertainty due to the background shape, the binning of histograms, and the fit region. We used these modified shapes with the mass resolution of 10.7 MeV/c^2 to fit the e^+e^- spectra in the analysis presented in Sec. 4.1. Please note that, although this treatment is somewhat arbitrarily, the values applied for δm and $\delta\sigma$ are consistently understood within one σ error of the uncertainty in the BDC alignment (see Table 3.2 in Sec. 3.2.3). Detailed analysis is described in Sec. 3.3.2 in Ref. [36].

	LR		RL	
	2001	2002	2001	2002
additional mass scale δm	$0.7 \pm 0.9^{+0.0}_{-0.6}$	$-0.7 \pm 0.6^{+0.0}_{-0.4}$	$0.6 \pm 2.8^{+0.5}_{-0.6}$	$4.2 \pm 1.3^{+0.1}_{-0.2}$
additional resolution $\delta\sigma$	$3.6 \pm 1.3^{+1.2}_{-0.0}$			

Table 3.10: The obtained best values in the additional mass scale δm and the resolution $\delta\sigma$, in a unit of [MeV/c^2]. The values are obtained separately for the LR and RL events and the year 2001 and 2002, due to the expected nature of the BDC alignments. The first errors are statistical and the seconds are systematic.

3.7.2 $\phi \to K^+K^-$ Decays

For $\phi \to K^+K^-$ decays, we evaluated the mass centroid and the resolution in the data by fitting the spectra with the combinatorial background and the relativistic Breit-Wigner shape with the natural width of 4.26 MeV/c^2 after folded with a Gaussian. The combinatorial background was obtained by the event-mixing method as described in Sec. 3.6.2, and the relativistic Breit-Wigner was modified by using the mass acceptance as described in Sec. 3.5.2. For the detector simulation spectra, we evaluated the values as same as the data but without a background. The obtained values are summarized in Table. 3.11, and the fitting results for the data are shown in Fig. 3.74. The systematic errors contain contributions from the uncertainties in the background estimation as described in Sec. 3.6.2 and the binning of histograms. The agreements are quite remarkable, and we used the simulated mass shape in the fit described in Sec. 4.2.

		mass centroid	mass resolution
C	DATA	$1019.38 \pm 0.31 \pm 0.13$	$2.19 \pm 0.42 \pm 0.30$
	MC	1019.53	2.35
Cu	DATA	$1019.43 \pm 0.21 \pm 0.04$	$1.91 \pm 0.29 \pm 0.23$
	MC	1019.49	2.24

Table 3.11: The obtained values of the mass centroid and the resolution for the data (DATA) and the detector simulation (MC) in a unit of [MeV/c^2]. The first errors are statistical and the seconds are systematic.

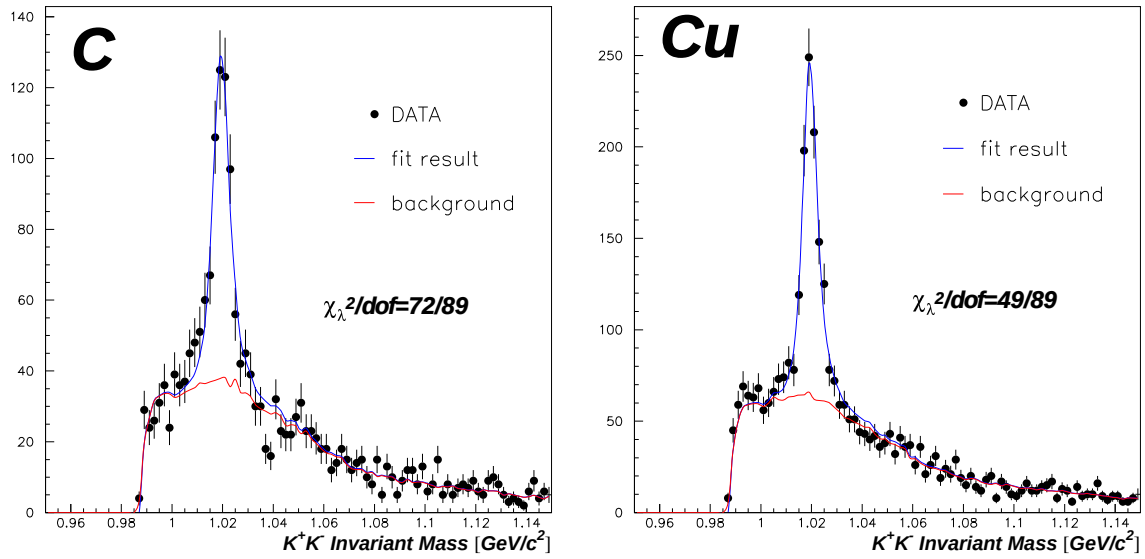

Figure 3.74: The invariant mass spectra of the final K^+K^- sample. The closed circles represent the data. The blue and red lines represent the fit results and the combinatorial backgrounds respectively.

Chapter 4

Results and Discussions

4.1 Spectral Shape and Yield of ϕ Meson in the e^+e^- Channel

The invariant mass spectra of the final e^+e^- sample in the mass region from 0.85 to 1.2 GeV/c^2 are shown in Fig. 4.1 for C and Cu targets. We fitted each mass spectrum with a resonance shape of $\phi \to e^+e^-$ and a quadratic background curve. For the ϕ meson resonance shape, we used the simulated shape as described in Sec. 3.5.1. The fit region was from 0.85 to 1.2 GeV/c^2 excluding the region from 0.95 to 1.00 GeV/c^2, where the excess attributed to the ϕ meson modification was observed. Detailed studies on the modification of the ϕ meson are made in Ref [31, 36]. In this manuscript, we just set a focus to evaluate the ϕ-meson yields to compare the nuclear mass-number dependences of $\phi \to e^+e^-$ with $\phi \to K^+K^-$.

Figures 4.2, 4.3, and 4.4 show the invariant mass spectra in the four kinematical regions of $\beta\gamma$ (=p/m), rapidity (y), and transverse momentum (p_T) of observed e^+e^- pairs, respectively. It should be noted that an excess visible on the low-mass side of the ϕ meson peak in $\beta\gamma < 1.25$ of the Cu target data (Fig. 4.2) looks somewhat different from the one in Ref. [31, 36]. This is because the analysis cuts applied in the present work are different from the cuts in Ref. [31, 36], where the S/N for the ϕ peak is optimized while the yield statistics are optimized in the present work.

The relative abundances of the ϕ mesons and the parameters of the quadratic background were obtained from the fit. The yields of ϕ mesons are listed later in Table 4.5(a). They were obtained by integrating the mass region from 0.9 and 1.1 GeV/c^2 after subtracting the background. Thus the excess observed in Ref. [31, 36] is in principle included in the ϕ meson yields here. As listed as χ^2/dof in Fig. 4.2, 4.3, and 4.4, all the fits were satisfactory performed.

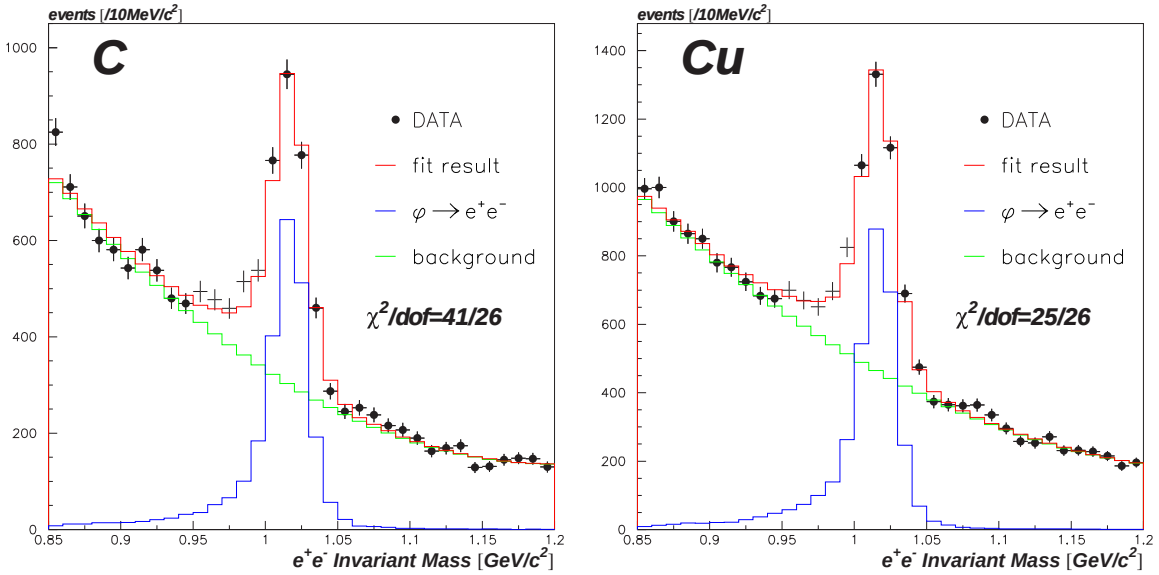

Figure 4.1: The invariant mass spectra of the final e^+e^- sample. The closed circles represent the data and the thin crosses represent the excluded region from the fit. The red, green and blue lines represent the fit results, the quadratic backgrounds and the expected $\phi \rightarrow e^+e^-$ shapes, respectively.

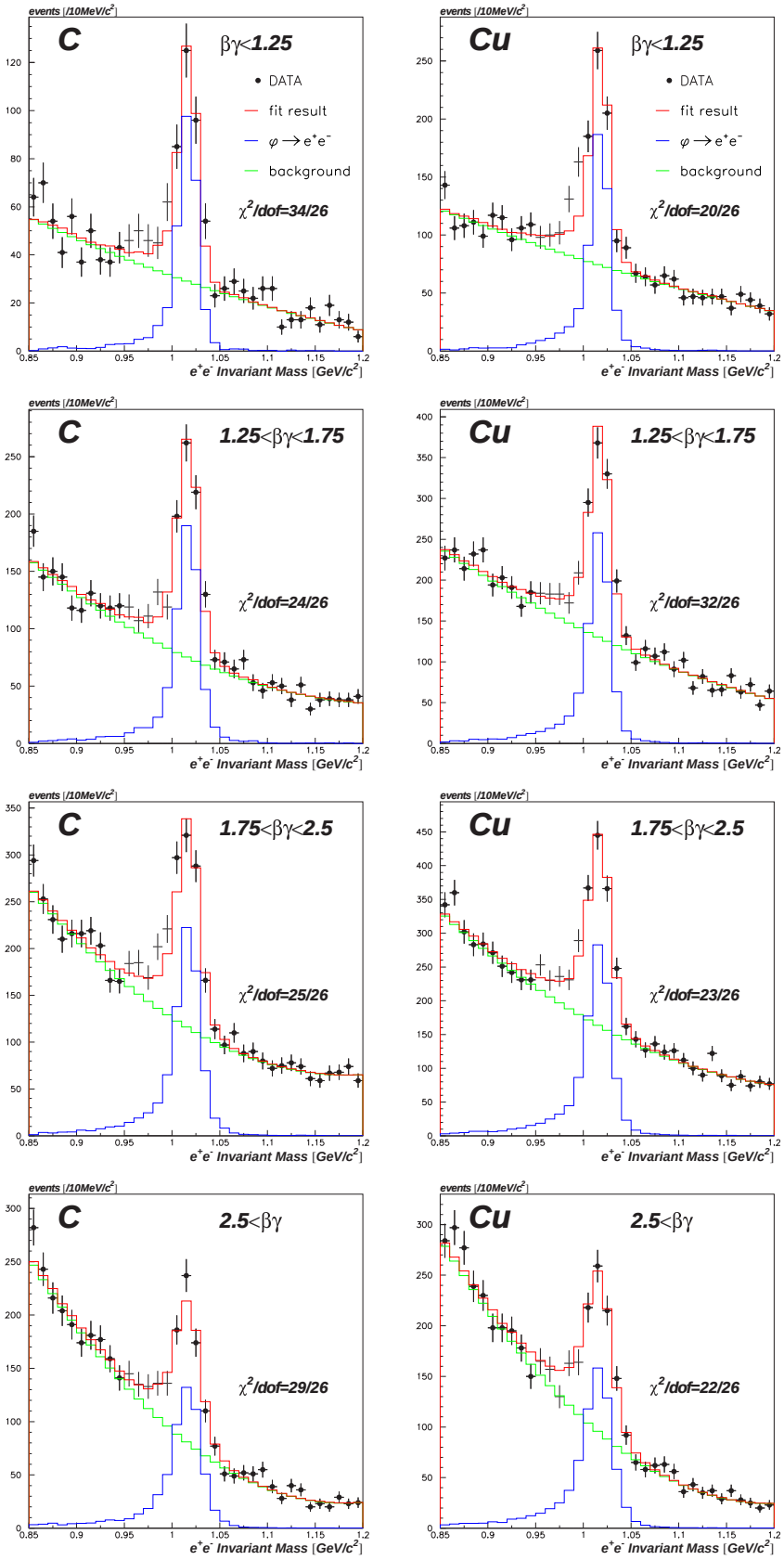

Figure 4.2: The invariant mass spectra of the final e^+e^- sample divided into four $\beta\gamma$ bins. The closed circles represent the data and the thin crosses represent the excluded region from the fit. The red, green and blue lines represent the fit results, the quadratic backgrounds and the expected $\phi \to e^+e^-$ shapes, respectively.

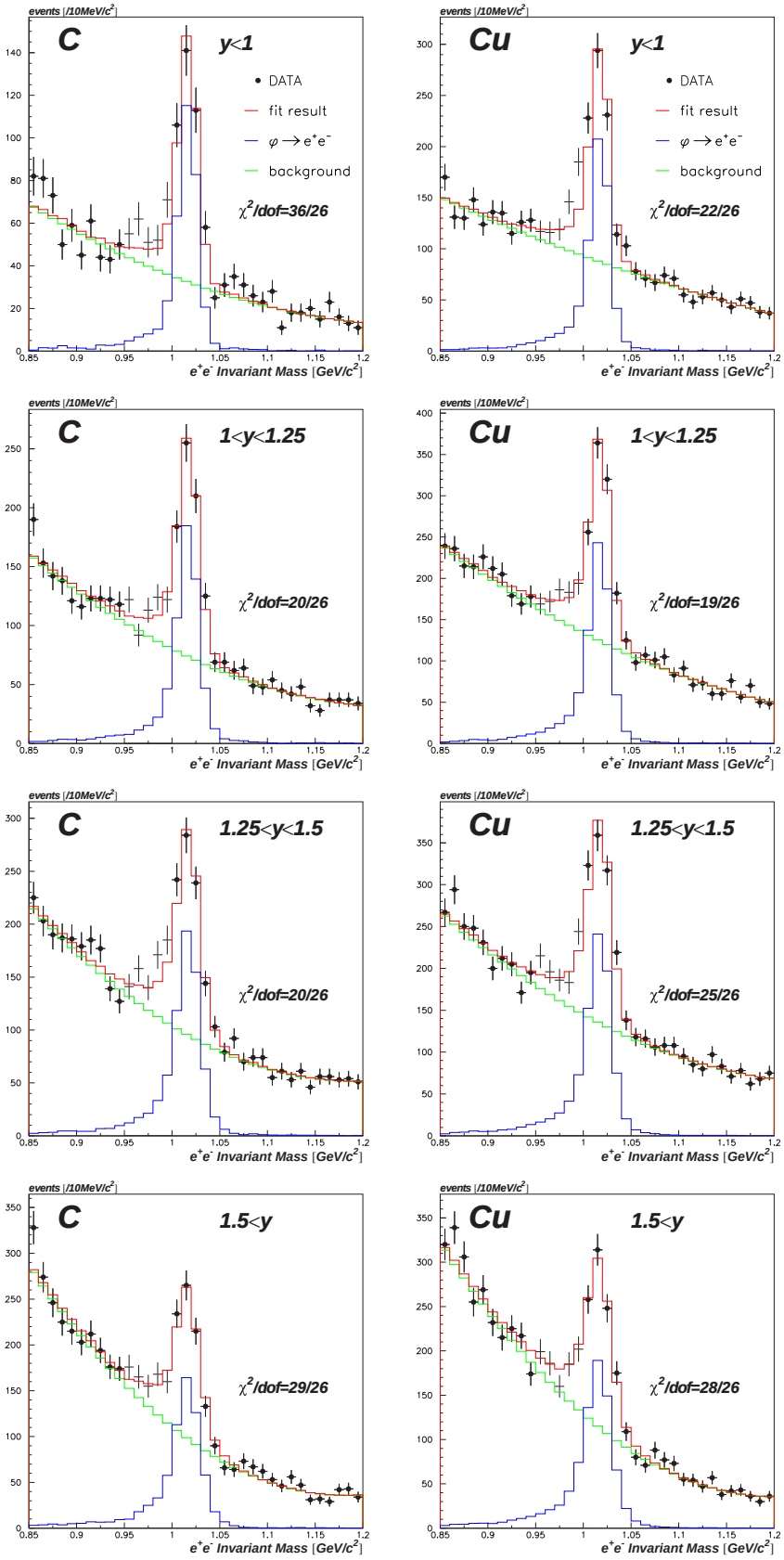

Figure 4.3: The invariant mass spectra of the final e^+e^- sample divided into four rapidity bins. The closed circles represent the data and the thin crosses represent the excluded region from the fit. The red, green and blue lines represent the fit results, the quadratic backgrounds and the expected $\phi \to e^+e^-$ shapes, respectively.

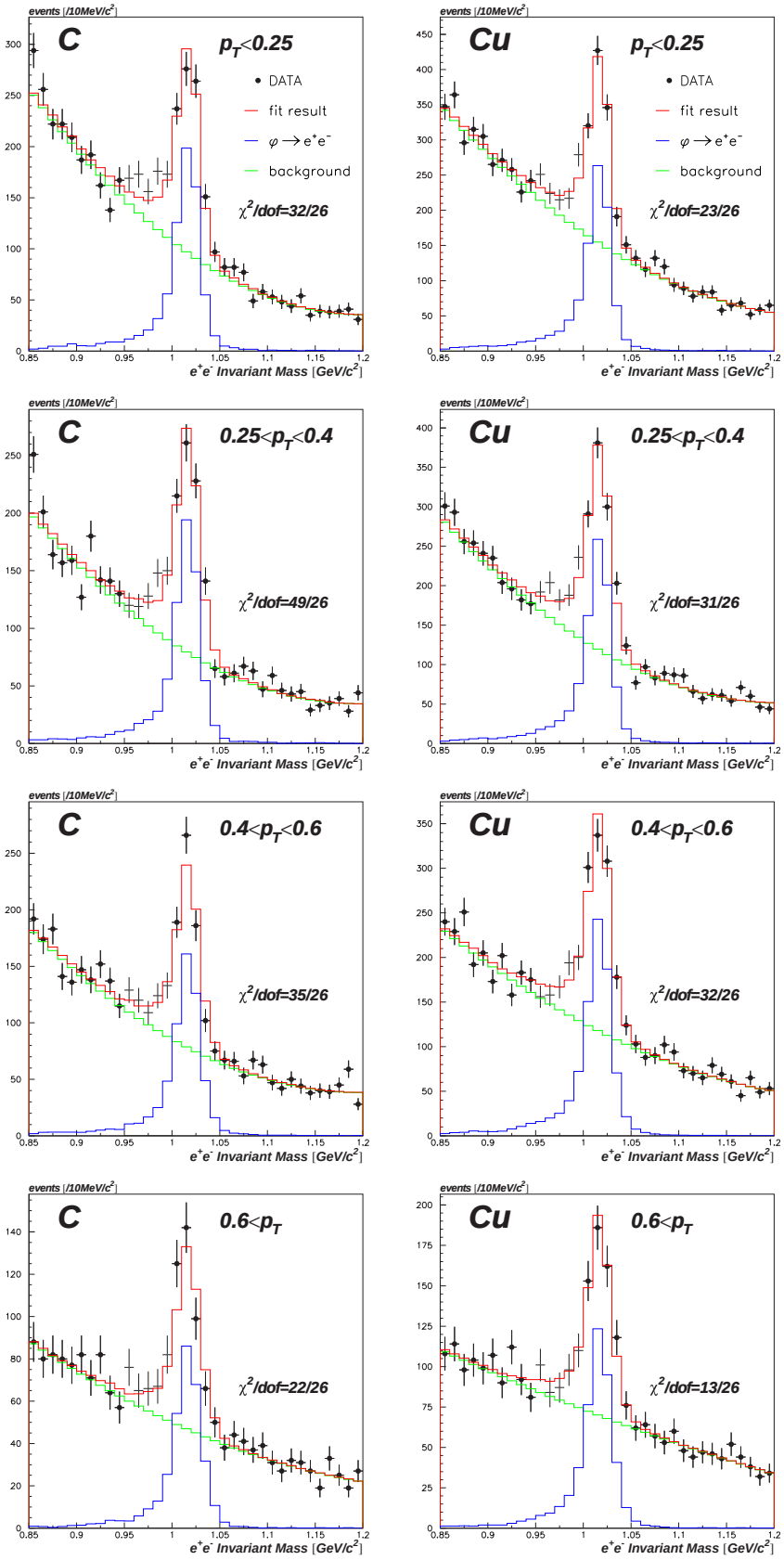

Figure 4.4: The invariant mass spectra of the final e^+e^- sample divided into four p_T bins. The closed circles represent the data and the thin crosses represent the excluded region from the fit. The red, green and blue lines represent the fit results, the quadratic backgrounds and the expected $\phi \rightarrow e^+e^-$ shapes, respectively.

4.2 Spectral Shape and Yield of ϕ Meson in the K^+K^- Channel

The invariant mass spectra of the final K^+K^- sample are shown in Fig. 4.5. We fitted each mass spectrum with the resonance shape of $\phi \rightarrow K^+K^-$ and the combinatorial background shape described in Sec. 3.5.2 and 3.6.2 respectively, in the mass region from $2m_{K^\pm}(0.987)$ to 1.15 GeV/c^2. The fits were performed by using the maximum likelihood method. To examine the quality of the fit, the "likelihood chi-square χ^2_λ", which is defined in Ref. [69] as

$$\chi^2_\lambda = 2\sum_i [y_i - n_i + n_i \ln(n_i/y_i)], \tag{4.1}$$

where n_i is the number of events in the i-th bin and y_i is the number of events predicted by the fit, is calculated and shown in each figure. The likelihood chi-square χ^2_λ asymptotically obeys a chi-square distribution.

Figure 4.6, 4.7, and 4.8 show the invariant mass spectra in the three kinematical regions of $\beta\gamma$, rapidity, and p_T of the observed K^+K^- pairs, respectively.

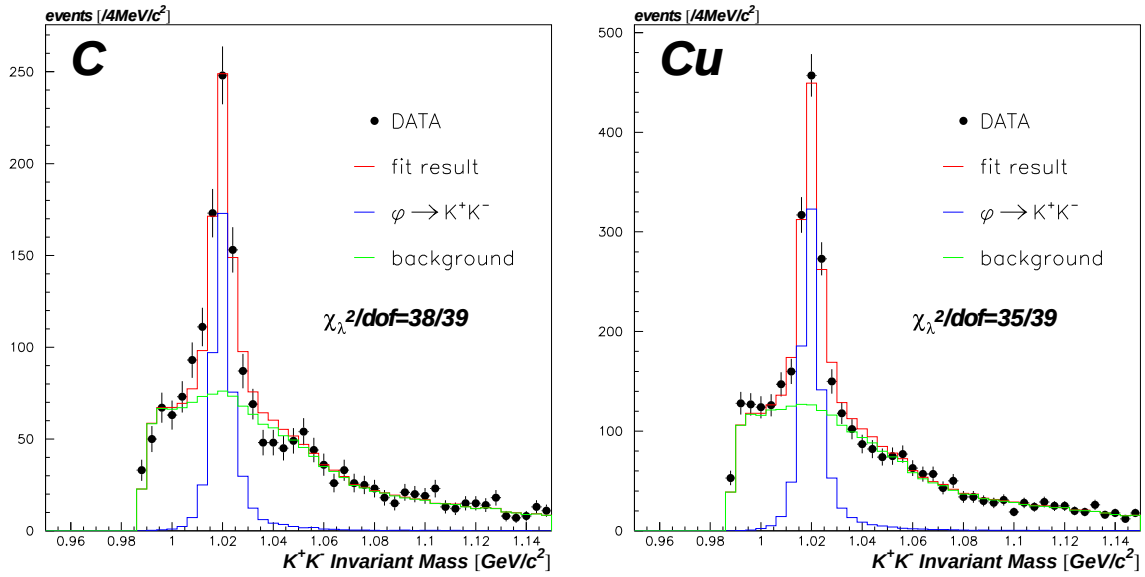

Figure 4.5: The invariant mass spectra of the final K^+K^- sample. The closed circles represent the data. The red, green and blue lines represent the fit results, the combinatorial backgrounds and the expected $\phi \rightarrow K^+K^-$ shapes, respectively.

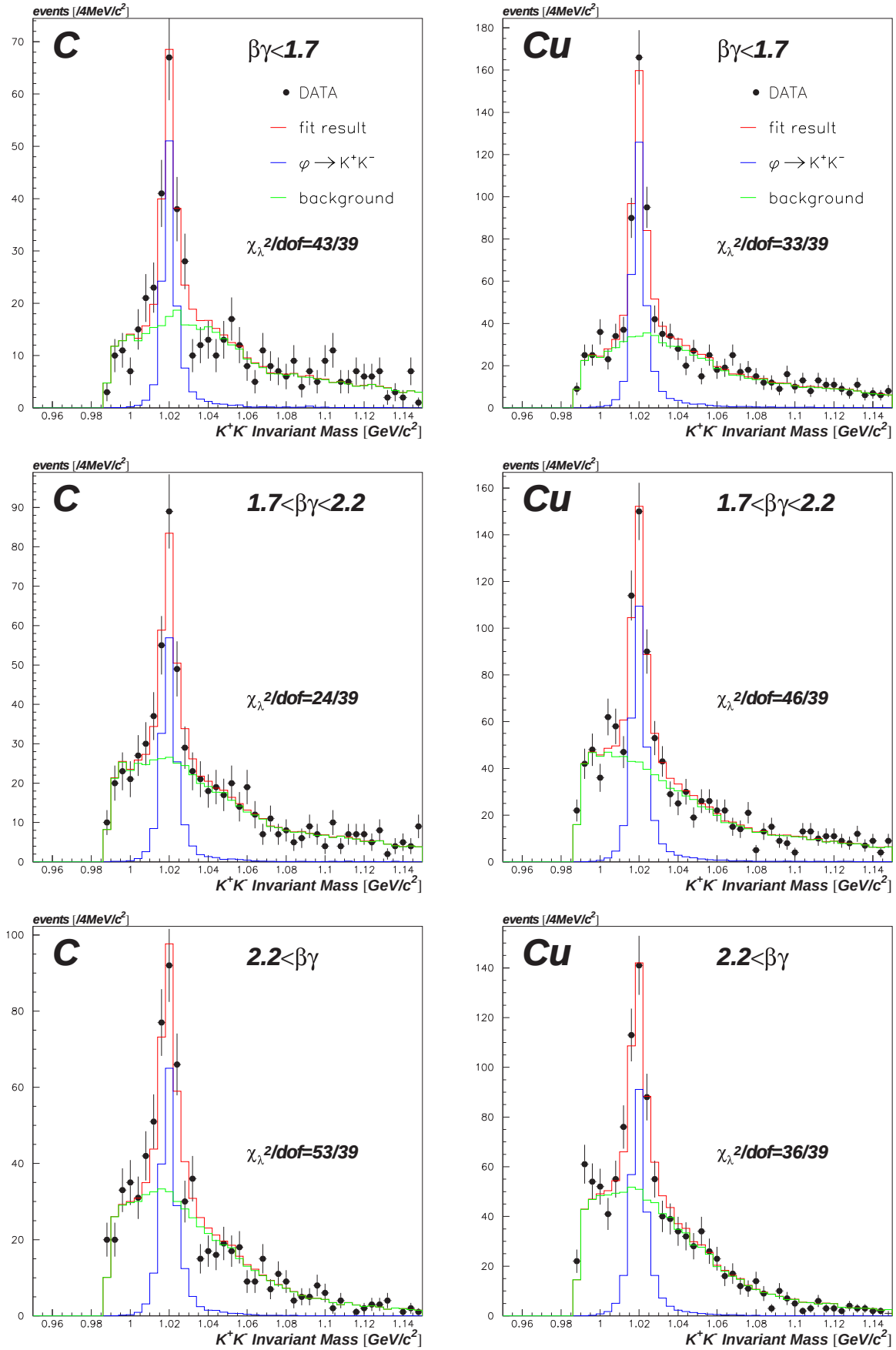

Figure 4.6: The invariant mass spectra of the final K^+K^- sample divided into three $\beta\gamma$ bins. The closed circles represent the data. The red, green and blue lines represent the fit results, the combinatorial backgrounds and the expected $\phi \to K^+K^-$ shapes, respectively.

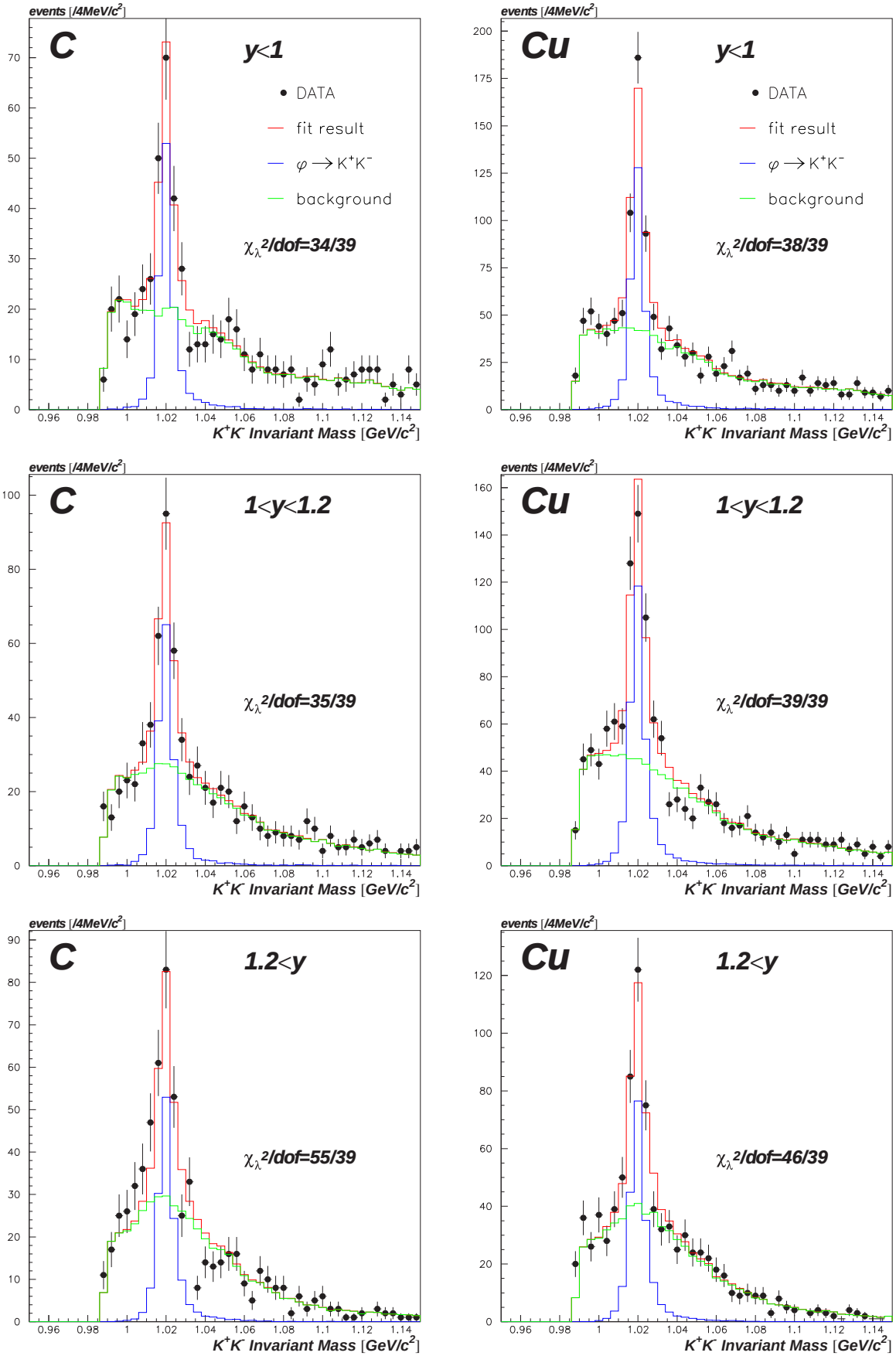

Figure 4.7: The invariant mass spectra of the final K^+K^- sample divided into three rapidity bins. The closed circles represent the data. The red, green and blue lines represent the fit results, the combinatorial backgrounds and the expected $\phi \to K^+K^-$ shapes, respectively.

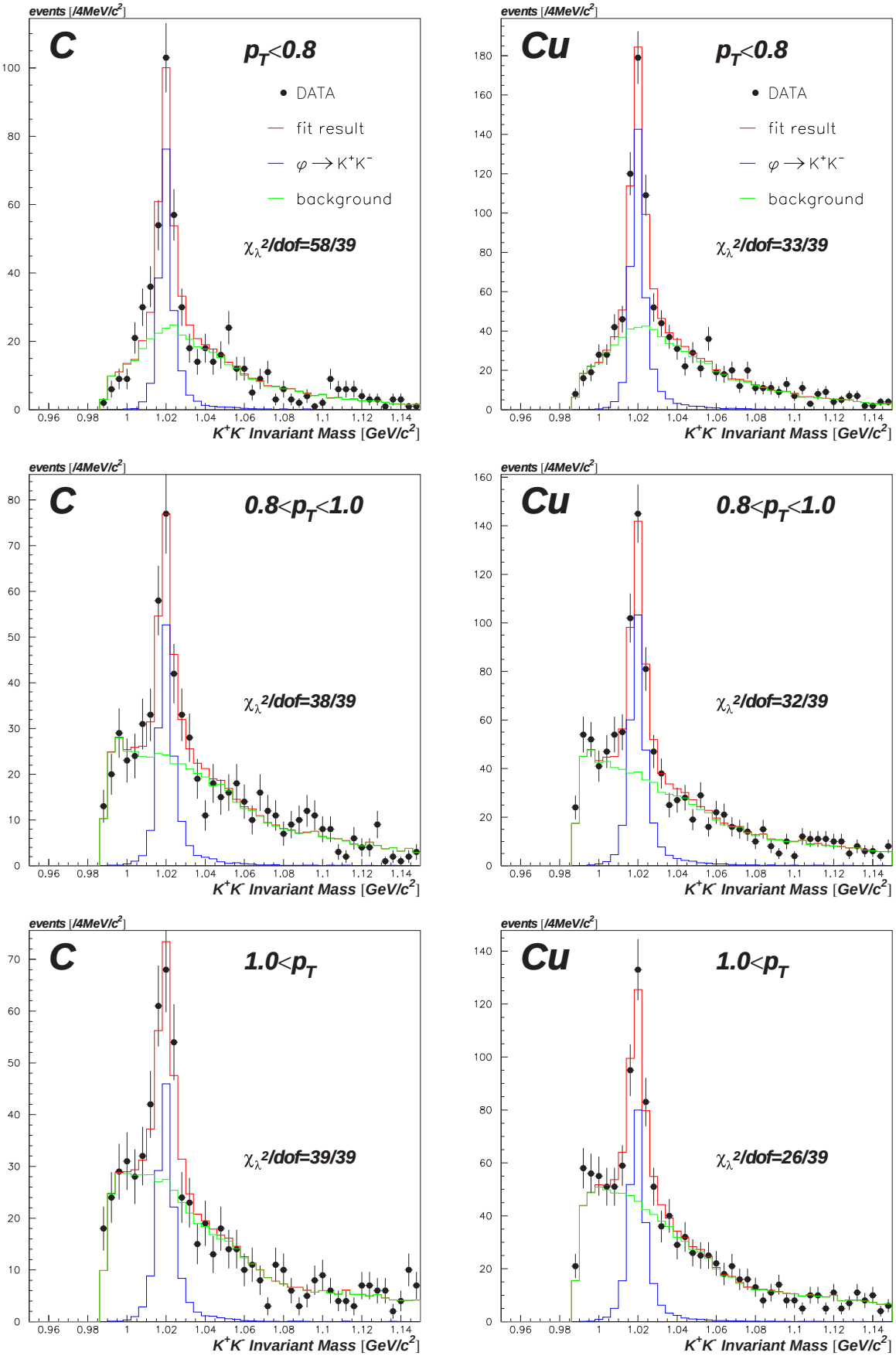

Figure 4.8: The invariant mass spectra of the final K^+K^- sample divided into three p_T bins. The closed circles represent the data. The red, green and blue lines represent the fit results, the combinatorial backgrounds and the expected $\phi \rightarrow K^+K^-$ shapes, respectively.

The observed K^+K^- spectra are well reproduced by the fit in all the $\beta\gamma$ bins (and all others). Therefore, the changes in mass spectra are not statistically significant in the $\phi \rightarrow K^+K^-$ channel. Indeed, we have observed mass-shape modification in the $\phi \rightarrow e^+e^-$ channel in the very low $\beta\gamma$ region ($\beta\gamma < 1.25$) for the copper target data [31, 36]. In Fig. 4.9, we compare the acceptances of the K^+K^- and e^+e^- channels. In the region of $\beta\gamma < 1.25$, we have very limited statistics for $\phi \rightarrow K^+K^-$, and we cannot obtain a reasonable fit for the K^+K^- data when $\beta\gamma < 1.25$ is selected. Thus, it is impossible to compare the $\phi \rightarrow K^+K^-$ shape directly with the modified shape observed in the e^+e^- channel. It can be concluded that in the region $\beta\gamma > 1.25$, both $\phi \rightarrow K^+K^-$ and $\phi \rightarrow e^+e^-$ do not show any signs of shape modification.

The relative abundances of the ϕ mesons and the background were obtained from the fit. The yields of ϕ mesons are listed later in Table 4.5(b). They were obtained by integrating the mass region from $2m_{K^\pm}$ to 1.07 GeV/c^2 after subtracting the background.

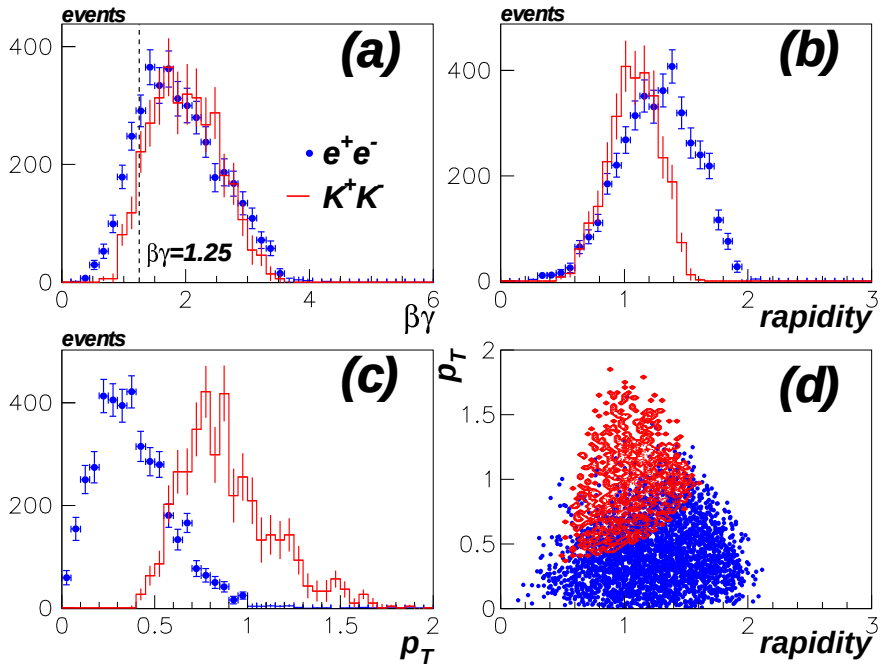

Figure 4.9: The observed kinematical distributions of $\phi \rightarrow e^+e^-$ and $\phi \rightarrow K^+K^-$, as functions of (a) $\beta\gamma$, (b) rapidity, (c) p_T, and (d) p_T and rapidity. The points blue represent $\phi \rightarrow e^+e^-$ and the red histograms and contours represent $\phi \rightarrow K^+K^-$. The dotted lines in (a) represent $\beta\gamma = 1.25$. The histograms for $\phi \rightarrow K^+K^-$ are scaled up by a factor of about 3.

4.3 Nuclear Mass Number Dependences α in the $\phi \to e^+e^-$ and $\phi \to K^+K^-$ Channels

The cross section for a nuclear target of mass number A is parameterized as $\sigma(A) = \sigma_0 \times A^\alpha$. When the ϕ meson and/or kaon is modified in a medium and $\Gamma_{\phi\to K^+K^-}/\Gamma_{\phi\to e^+e^-}$ changes, the ratio of the ϕ-meson yield $R = N_{\phi\to K^+K^-}/N_{\phi\to e^+e^-}$ becomes dependent on the mass number since a larger number of ϕ mesons are to be modified in a larger nucleus. Consequently, by using two different nuclear targets A_1 and A_2, the difference in the α parameter between $\phi \to e^+e^-$ ($\alpha_{\phi\to e^+e^-}$) and $\phi \to K^+K^-$ ($\alpha_{\phi\to K^+K^-}$) can be related to R as follows:

$$\begin{aligned}
\Delta\alpha &= \alpha_{\phi\to K^+K^-} - \alpha_{\phi\to e^+e^-} \\
&= \left\{ \ln\left[\frac{N_{\phi\to K^+K^-}(A_1)}{N_{\phi\to K^+K^-}(A_2)}\right] - \ln\left[\frac{N_{\phi\to e^+e^-}(A_1)}{N_{\phi\to e^+e^-}(A_2)}\right] \right\} \Big/ \ln(A_1/A_2) \\
&= \ln[R(A_1)/R(A_2)]/\ln(A_1/A_2). \qquad (4.2)
\end{aligned}$$

It is important that most of the experimental efficiencies are canceled in obtaining α as described in Sec. 4.3.2. The major effects are present in geometrical acceptance, trigger efficiency, and tracking and analysis efficiencies.

4.3.1 Determination of α Parameters in the $\phi \to e^+e^-$ and $\phi \to K^+K^-$ Channels

The production cross section of ϕ meson, σ_ϕ, is written as $\sigma_\phi = N_\phi/(N_p \cdot N_t \cdot \eta)$, where N_ϕ is the number of the observed ϕ mesons, N_p is the number of beam protons, N_t is the number density of nucleus per unit area of the target, and η is the correction factor which includes geometrical acceptance, trigger efficiency, and tracking and analysis efficiencies. Since N_p was common for C and Cu targets in the present experiment, we can extract the α parameter as

$$\begin{aligned}
\alpha &= \ln\left[\frac{N_\phi(Cu)}{N_\phi(C)} \cdot \frac{N_t(C)}{N_t(Cu)} \cdot \frac{\eta_C}{\eta_{Cu}}\right] \Big/ \ln\left(\frac{A_{Cu}}{A_C}\right) \\
&= \ln\left[\frac{N_\phi(Cu)}{N_\phi(C)} \cdot \frac{N_t(C)}{N_t(Cu)}\right] \Big/ \ln\left(\frac{A_{Cu}}{A_C}\right) + \ln\left(\frac{\eta_C}{\eta_{Cu}}\right) \Big/ \ln\left(\frac{A_{Cu}}{A_C}\right) \\
&= \ln\left[\frac{N_\phi(Cu)}{N_\phi(C)} \cdot \frac{N_t(C)}{N_t(Cu)}\right] \Big/ \ln\left(\frac{A_{Cu}}{A_C}\right) + \delta\alpha. \qquad (4.3)
\end{aligned}$$

Although most of the experimental effects are canceled in obtaining α, small experimental effects remain as the second term in Eq. 4.3, i.e., $\delta\alpha \neq 0$ if η_C is different from η_{Cu}.

The values of $N_t(C)$ and $N_t(Cu)$ were determined by measuring the dimensions and the weights of the target materials used for the experiment. These information is summarized in Appendix C. We obtained $N_t(C)/N_t(Cu) = 3.354 \pm 0.016$ and 3.348 ± 0.028 for 2001 and 2002 respectively. Since the ratios are almost identical between the two data taking periods, we considered the ratios were the same, and treated the measurement errors as a systematic error in α. The values used in the analysis are listed in Table 4.1. For the e^+e^- channels we used the average ratio of 2001 and 2002, and for the K^+K^- channel we used the ratio of 2001.

	$N_t(C)/N_t(Cu)$	systematic error in α
for $\phi \to e^+e^-$	3.351 ± 0.031	0.006
for $\phi \to K^+K^-$	3.354 ± 0.016	0.003

Table 4.1: The values of $N_t(C)/N_t(Cu)$ for $\phi \to e^+e^-$ (average of 2001 and 2002) and for $\phi \to K^+K^-$ (2001 only). The systematic errors in α from the errors in $N_t(C)/N_t(Cu)$ are also listed.

In the rest of this section, we describe how to estimate η_C/η_{Cu} and its error. As a result, the most significant correction was obtained from the geometrical acceptance, and we corrected the values of α. Next, there was a correction from the trigger efficiency, which we included in the systematic error. The corrections from the other efficiencies were negligibly small.

Difference in Geometrical Acceptance

The targets were aligned in-line, like Cu-C-Cu or Cu-Cu-C-Cu-Cu depending on the data taking year. Since these configurations were symmetric about the C target, we considered that the average of the Cu targets is equivalent to that of the C target. However this assumption was not perfect, particularly in the $\phi \to K^+K^-$ channel as described in Sec. 3.5.2. Table 4.2 shows the geometrical acceptance effects on $\eta_C/\eta_{Cu}(\phi \to K^+K^-)$ and $\delta\alpha_{\phi\to K^+K^-}$ obtained with the nuclear cascade code JAM as described in Sec. 3.5.2. We estimated the systematic errors in them to be 0.006 and 0.004 for $\eta_C/\eta_{Cu}(\phi \to K^+K^-)$ and $\delta\alpha_{\phi\to K^+K^-}$, respectively, mainly due to the Monte Carlo statistics. Apparently this correction is significant at low p_T and low rapidity, i.e., in the small-angle region. The reason is that the center of the kinematical distribution of the ϕ-meson is on the edge of the detector acceptance for K^+K^- pairs as shown in Fig. 4.10(b), and consequently the number of accepted mesons is very sensitive to the target position.

On the other hand, in the $\phi \to e^+e^-$ channel in which e^+ and e^- are widely separated, $\eta_C/\eta_{Cu}(\phi \to e^+e^-)$ is consistent with unity within a systematic error of 0.011 which corresponds to 0.006 in $\alpha_{\phi\to e^+e^-}$. This is because the center of the kinematical distribution of the ϕ-meson is on the center of the detector acceptance unlike $\phi \to K^+K^-$, as shown in Fig. 4.10(a).

Table 4.2 was used to correct $\alpha_{\phi\to K^+K^-}$, and the above-mentioned systematic errors (both $\phi \to K^+K^-$ and $\phi \to e^+e^-$) were included as the error of $\delta\alpha$.

		$\eta_C/\eta_{Cu}(\phi \to K^+K^-)$	$\delta\alpha_{\phi\to K^+K^-}$
all		1.021	0.012
$\beta\gamma$	1 – 1.7	1.009	0.005
	1.7 – 2.2	1.010	0.006
	2.2 – 3.5	1.040	0.024
rapidity	0.5 – 1	1.063	0.037
	1 – 1.2	1.011	0.007
	1.2 – 1.5	0.992	−0.005
p_T	0.4 – 0.8	1.030	0.018
	0.8 – 1	1.016	0.010
	1 – 1.5	1.020	0.012

Table 4.2: The geometrical acceptance effects in $\eta_C/\eta_{Cu}(\phi \to K^+K^-)$ and $\delta\alpha_{\phi\to K^+K^-}$ obtained with the nuclear cascade code JAM and the detector simulation.

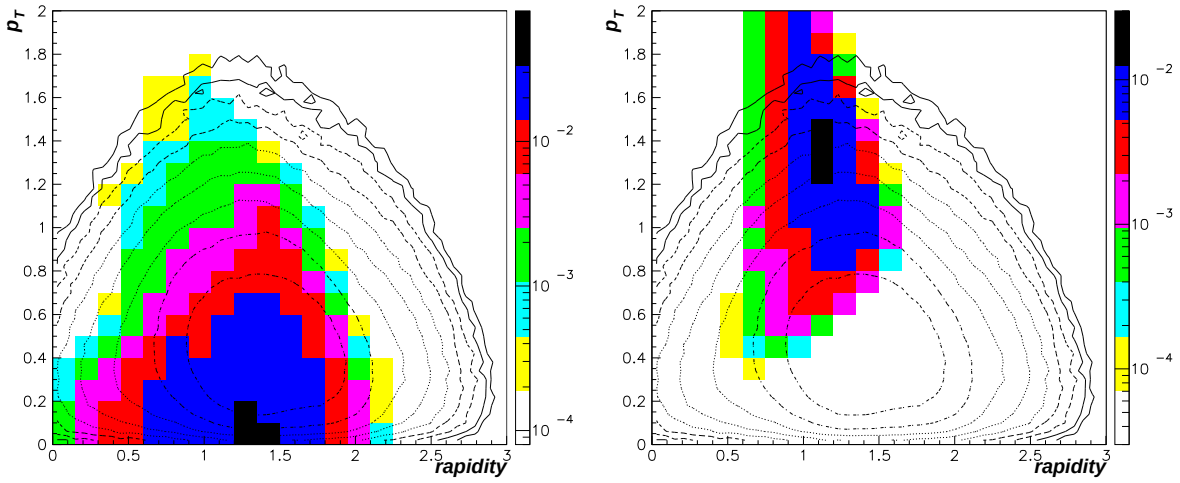

(a) $\phi \to e^+e^-$ (b) $\phi \to K^+K^-$

Figure 4.10: The simulated detector acceptances for (a) $\phi \to e^+e^-$ decays and (b) $\phi \to K^+K^-$ decays are plotted as the color maps. The acceptances are calculated using a flat kinematical distribution in the region of $0 < y < 3$ and $0 < p_T < 2$, and include not only the geometrical acceptance but also the detector efficiencies and all other conditions used in the present analysis. The kinematical distribution of the generated ϕ-meson yield obtained by JAM is also plotted as the contour plot in each panel.

Difference in Experimental Efficiencies

The ratio η_C/η_{Cu} can differ from unity due to the particle multiplicity difference between the C and Cu targets.

We first discuss the particle identification efficiencies. In the case of $\phi \to e^+e^-$ decays, η_C/η_{Cu} can be considered to be multiplicity independent, because the two tracks are well separated and there is no veto logic neither in the trigger nor in the analysis. In the case of $\phi \to K^+K^-$ decays, the situation is different because the two tracks are close to each other and the veto logic exists in the particle identification. The following two situations are worth considered.

1. If a fast pion overlaps with a kaon within the same trigger segment in AC (consists of three physical AC segments), the kaon is overkilled.

2. If a fast pion overlaps with a kaon within the same TOF counter, the kaon is miss-identified and overkilled.

These two possibilities can be multiplicity dependent. We denote these overkilling probabilities as $P_{\rm AC}(arm, target)$ and $P_{\rm TOF}(arm, target)$, where arm is L (the left arm) or R (right) and $target$ is C (the carbon target) or Cu (copper). We evaluated these two cases using the final K^+K^- sample as follows.

We obtained a probability that an event has one or more AC hits in the arm in which a K^+K^- pair was detected. By scaling the AC hit multiplicity to the entire AC segments including the ones used for the veto logic, we evaluated the overkilling probabilities for K^+K^- pairs in AC to be $P_{\rm AC}$(L,C)=0.138±0.006, $P_{\rm AC}$(R,C)=0.101±0.005, $P_{\rm AC}$(L,Cu)=0.123±0.006, and $P_{\rm AC}$(R,Cu)=0.105±0.004. For TOF, we obtained the FTOF hit multiplicity in the arm in which a K^+K^- pair was detected and then we calculated a probability that one FTOF segment contained a kaon and other particles which change the TOF value to outside the

kaon identification window. The overkilling rates thus obtained in TOF for K^+K^- pairs were $P_{\rm TOF}$(L,C)=0.013, $P_{\rm TOF}$(R,C)=0.017, $P_{\rm TOF}$(L,Cu)=0.010, and $P_{\rm TOF}$(R,Cu)=0.014.

To check the estimations above, we also introduced the event-mixing technique. We combined the AC hits from one event with the kaon tracks from an other event, and we evaluated the overkilling probability in AC to be $P_{\rm AC}$(L,C)=0.146±0.004, $P_{\rm AC}$(R,C)=0.097±0.002, $P_{\rm AC}$(L,Cu)=0.124±0.006, and $P_{\rm AC}$(R,Cu)=0.099±0.004. For TOF, we combined the kaon tracks and the associated FTOF hits from one event with the FTOF hits which are not associated with the kaon tracks from another event. Considering the timing window for the kaon used for the kaon identification, we evaluated the overkilling probability in TOF to be $P_{\rm TOF}$(L,C)=0.010, $P_{\rm TOF}$(R,C)=0.007, $P_{\rm TOF}$(L,Cu)=0.009, and $P_{\rm TOF}$(R,Cu)=0.008.

The overkilling probabilities in the AC and TOF are summarized in Table 4.3. We took the averages of above two estimations and the differences as the errors. It should be noted that only the difference of the overkilling probabilities between C and Cu affects the α parameters. The overkilling in the TOF changes $\alpha_{\phi\to K^+K^-}$ by a maximum value of 0.002, which is negligible, whereas the overkilling in AC changes $\alpha_{\phi\to K^+K^-}$ by a maximum value of 0.016. The latter value was included in the systematic error.

(a) AC

AC	L-arm	R-arm
C	0.142 ± 0.005	0.099 ± 0.003
Cu	0.123 ± 0.006	0.102 ± 0.004

(b) TOF

TOF	L-arm	R-arm
C	0.011 ± 0.002	0.012 ± 0.005
Cu	0.009 ± 0.000	0.011 ± 0.003

Table 4.3: The overkilling probabilities in (a) AC and (b) TOF.

Second, we consider $\delta\alpha$ caused by the track multiplicity difference between the C and Cu targets. Using the relations between the tracking efficiency and the track multiplicity described in Sec. 3.4.2 in Ref. [38], we compare it with the multiplicity difference between the C and Cu targets. Table 4.4 lists the track multiplicities in the final data sample. We estimated the differences in the average tracking efficiency between the C and Cu targets to be 0.3% at most, which corresponds to the correction on α of 0.002 and is negligibly small.

(a) e^+e^-

e^+e^-	L-arm	R-arm
C	1.194 ± 0.001	1.166 ± 0.001
Cu	1.230 ± 0.001	1.206 ± 0.001

(b) K^+K^-

K^+K^-	L-arm	R-arm
C	2.10 ± 0.01	2.05 ± 0.01
Cu	2.16 ± 0.01	2.11 ± 0.01

Table 4.4: Track multiplicity in the final data sample, (a) for e^+e^- and (b) for K^+K^-.

4.3.2 Obtained ϕ-meson Yields and α Parameters

We obtained the ϕ-meson yields for the K^+K^- and e^+e^- decay channels as functions of $\beta\gamma$, rapidity, and p_T. In the K^+K^- decay channel, the ϕ-meson yields were obtained by integrating the data from $2m_{K^\pm}$ to 1.07 GeV/c^2 after subtracting the background. In the e^+e^- decay channel, the yields were obtained by integrating the data from 0.9 to 1.1 GeV/c^2 after subtracting the background.

Table 4.5(a) and (b) summarize the yields for both decay channels with the systematic errors mainly from the uncertainties in the background estimation described in Sec.3.6.2. Additionally, we change the excluded region from the fit, and check the stability of the fit in the $\phi \to e^+e^-$ decays.

In the tables, the α parameters are corrected for the target dependence of the experimental efficiencies, i.e., η_C/η_{Cu}. The most significant correction was from the difference in the geometrical acceptance for each target position. The other corrections were estimated to be small and were included in the systematic errors together with those from the background estimations and the target thicknesses. In the analysis thereafter, the errors in α are the quadratic sums of the statistical and systematic errors.

The observed α parameters are plotted as functions of $\beta\gamma$ in Fig. 4.11(a) and as functions of the rapidity and p_T in (b) and (c), respectively. The e^+e^- and K^+K^- decay channels cannot be compared directly because of the difference in the detector acceptance between the e^+e^- and K^+K^- decay channels, as shown in Fig. 4.9. Table 4.6 shows how the acceptances were different in each bin of $\beta\gamma$, rapidity, and p_T. In the table, we list the mean value and RMS of each bin for $\phi \to e^+e^-$ and $\phi \to K^+K^-$ decays. Here the target dependence is neglected and the C and Cu target data are summed. Figure 4.12 demonstrates how they look in the y-p_T plane.

(a) $\phi \to e^+e^-$

	$N_{\phi\to e^+e^-}(C)$	$N_{\phi\to e^+e^-}(Cu)$	$\alpha_{\phi\to e^+e^-}$
all	2528 ± 101 ± 6	3302 ± 121 ± 25	0.89 ± 0.03 ± 0.01
$\beta\gamma < 1.25$	331 ± 32 ± 6	703 ± 50 ± 26	1.18 ± 0.07 ± 0.02
$1.25 < \beta\gamma < 1.75$	702 ± 51 ± 9	899 ± 63 ± 4	0.87 ± 0.06 ± 0.02
$1.75 < \beta\gamma < 2.5$	945 ± 62 ± 14	1096 ± 71 ± 12	0.81 ± 0.06 ± 0.01
$2.5 < \beta\gamma$	579 ± 52 ± 4	626 ± 56 ± 5	0.77 ± 0.08 ± 0.01
$y < 1$	397 ± 35 ± 6	774 ± 54 ± 26	1.13 ± 0.07 ± 0.02
$1 < y < 1.25$	649 ± 50 ± 5	854 ± 62 ± 3	0.89 ± 0.06 ± 0.01
$1.25 < y < 1.5$	828 ± 57 ± 11	937 ± 65 ± 12	0.80 ± 0.06 ± 0.01
$1.5 < y$	687 ± 57 ± 6	758 ± 61 ± 2	0.79 ± 0.07 ± 0.01
$p\_T < 0.25$	794 ± 57 ± 3	987 ± 70 ± 18	0.86 ± 0.06 ± 0.02
$0.25 < p\_T < 0.4$	748 ± 53 ± 2	993 ± 63 ± 12	0.90 ± 0.06 ± 0.01
$0.4 < p\_T < 0.6$	646 ± 51 ± 2	899 ± 61 ± 1	0.92 ± 0.06 ± 0.01
$0.6 < p\_T$	370 ± 39 ± 3	474 ± 46 ± 1	0.87 ± 0.09 ± 0.01

(b) $\phi \to K^+K^-$

	$N_{\phi\to K^+K^-}(C)$	$N_{\phi\to K^+K^-}(Cu)$	$\alpha_{\phi\to K^+K^-}$
all	426 ± 41 ± 49	849 ± 54 ± 79	1.15 ± 0.07 ± 0.03
$\beta\gamma < 1.7$	99 ± 20 ± 18	285 ± 29 ± 27	1.38 ± 0.13 ± 0.07
$1.7 < \beta\gamma < 2.2$	142 ± 24 ± 18	279 ± 32 ± 30	1.14 ± 0.12 ± 0.03
$2.2 < \beta\gamma$	177 ± 26 ± 11	269 ± 33 ± 21	0.99 ± 0.12 ± 0.03
$y < 1$	113 ± 22 ± 17	318 ± 32 ± 31	1.35 ± 0.13 ± 0.05
$1 < y < 1.2$	162 ± 25 ± 19	301 ± 33 ± 24	1.10 ± 0.11 ± 0.04
$1.2 < y$	139 ± 24 ± 10	217 ± 29 ± 22	1.02 0.13 ± 0.04
$p\_T < 0.8$	175 ± 23 ± 16	329 ± 31 ± 29	1.14 ± 0.10 ± 0.02
$0.8 < p\_T < 1$	132 ± 24 ± 19	283 ± 31 ± 27	1.19 ± 0.13 ± 0.05
$1 < p\_T$	122 ± 24 ± 12	237 ± 32 ± 21	1.12 ± 0.14 ± 0.03

Table 4.5: The yields and the α parameters for (a) $\phi \to e^+e^-$ and (b) $\phi \to K^+K^-$. The first errors are statistical and the second are systematic.

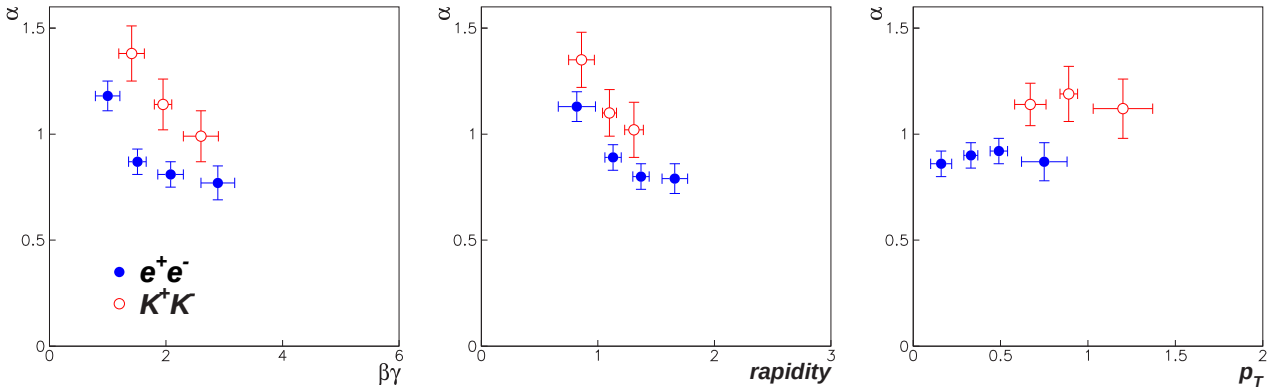

(a) $\beta\gamma$ (b) rapidity (c) p_T

Figure 4.11: α parameters of $\phi \to e^+e^-$ (closed circle) and $\phi \to K^+K^-$ (open circle) as functions of (a) $\beta\gamma$, (b) rapidity, and (c) p_T. The horizontal error bars are the RMS values of the horizontal bins.

(a) $\phi \to e^+e^-$

	$\beta\gamma$ value		rapidity value		p_T value	
	mean	RMS	mean	RMS	mean	RMS
all	1.89	0.67	1.26	0.31	0.38	0.21
$\beta\gamma < 1.25$	1.00	0.21	0.81	0.16	0.28	0.15
$1.25 < \beta\gamma < 1.75$	1.51	0.15	1.12	0.11	0.35	0.17
$1.75 < \beta\gamma < 2.5$	2.08	0.22	1.38	0.12	0.40	0.20
$2.5 < \beta\gamma$	2.89	0.29	1.66	0.14	0.49	0.26
$y < 1$	1.06	0.24	0.82	0.16	0.34	0.18
$1 < y < 1.25$	1.56	0.21	1.13	0.07	0.38	0.21
$1.25 < y < 1.5$	2.07	0.28	1.37	0.07	0.41	0.22
$1.5 < y$	2.78	0.36	1.66	0.11	0.40	0.21
$p_T < 0.25$	1.65	0.64	1.22	0.33	0.16	0.06
$0.25 < p_T < 0.4$	1.85	0.65	1.27	0.32	0.33	0.04
$0.4 < p_T < 0.6$	1.96	0.63	1.27	0.30	0.49	0.05
$0.6 < p_T$	2.37	0.61	1.33	0.26	0.75	0.13

(b) $\phi \to K^+K^-$

	$\beta\gamma$ value		rapidity value		p_T value	
	mean	RMS	mean	RMS	mean	RMS
all	2.02	0.54	1.08	0.20	0.90	0.25
$\beta\gamma < 1.7$	1.41	0.22	0.88	0.13	0.70	0.15
$1.7 < \beta\gamma < 2.2$	1.95	0.15	1.09	0.11	0.88	0.17
$2.2 < \beta\gamma$	2.60	0.30	1.25	0.14	1.09	0.22
$y < 1$	1.52	0.36	0.86	0.11	0.83	0.27
$1 < y < 1.2$	2.03	0.34	1.10	0.06	0.92	0.25
$1.2 < y$	2.56	0.36	1.31	0.08	0.96	0.19
$p_T < 0.8$	1.60	0.36	1.01	0.18	0.67	0.09
$0.8 < p_T < 1$	2.11	0.42	1.14	0.20	0.89	0.05
$1 < p_T$	2.46	0.44	1.12	0.18	1.20	0.17

Table 4.6: The mean and RMS values of each kinematical bin for (a) $\phi \to e^+e^-$ and (b) $\phi \to K^+K^-$.

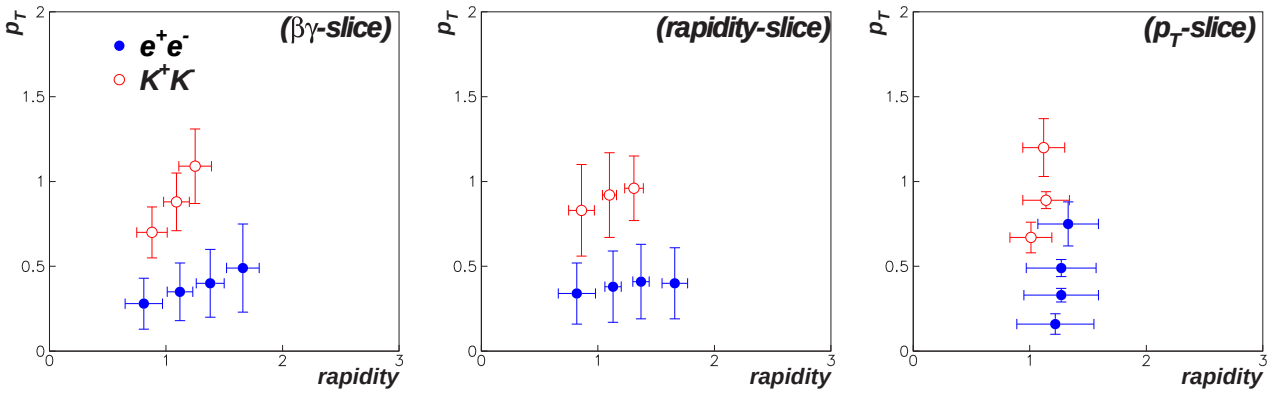

(a) $\beta\gamma$-slice (b) rapidity-slice (c) p_T-slice

Figure 4.12: The mean and RMS values of each bin of $\phi \to e^+e^-$ (closed circle) and $\phi \to K^+K^-$ (open circle) in the y-p_T plane for (a) $\beta\gamma$-slice, (b) rapidity-slice, and (c) p_T-slice. The error bars are the RMS values in each kinematical bin.

α Parameters in the Overlapped Acceptance

The detector acceptance is different between the e^+e^- and K^+K^- decay channels, however, there is overlapped region as shown in Fig. 4.13(d); which is enclosed by the lines connecting the four points in the (y,pT) plane, (0.7,0.5), (1.1,0.5), (1.6,1.0), and (1.2,1.0). So we evaluated the values of α in the overlapped region to check the consistency with $\alpha_{\phi\to e^+e^-}$ and $\alpha_{\phi\to K^+K^-}$. The mean and RMS values of $\beta\gamma$, rapidity, and p_T for $\phi \to e^+e^-$ and $\phi \to K^+K^-$ in the overlapped acceptance are listed in Table 4.7. Figure 4.14(a) and (b) show the invariant mass spectra of the e^+e^- and K^+K^- pairs with the fit result in the overlapped acceptance, respectively. Table 4.8 summarizes the yields for both decay channels with the systematic errors. In the table, the α parameters are corrected for the target dependence of the experimental efficiencies. The ratio $\eta_C/\eta_{Cu}(\phi \to K^+K^-)$ and $\delta\alpha_{\phi\to K^+K^-}$ are obtained to be 1.028 and 0.017, respectively. As listed in Table 4.8, we obtained $\Delta\alpha = 0.18 \pm 0.14$. Although the center value has a finite value, $\Delta\alpha$ is statistically consistent with zero within the large error.

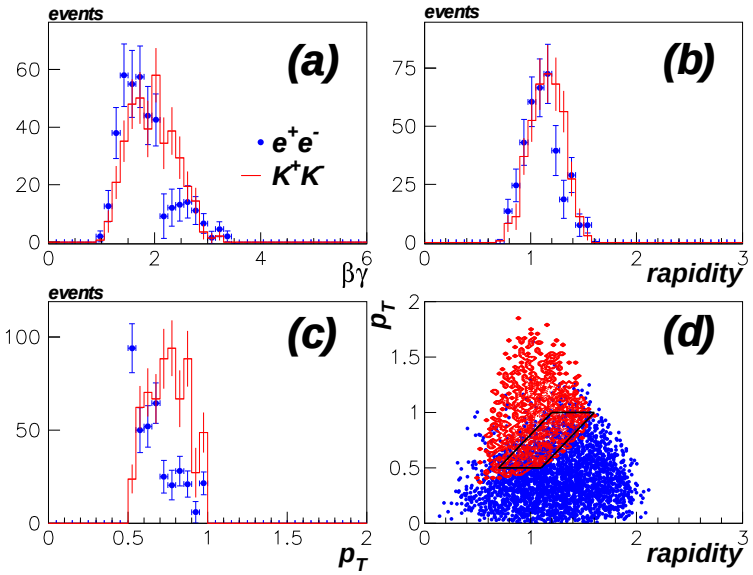

Figure 4.13: The kinematical distributions of $\phi \to e^+e^-$ and $\phi \to K^+K^-$ in the overlapped region shown with the rectangle in (d), as functions of (a) $\beta\gamma$, (b) rapidity, (c) p_T. The closed circles represent $\phi \to e^+e^-$ and the lines represent $\phi \to K^+K^-$.

	$\beta\gamma$ value		rapidity value		p_T value	
	mean	RMS	mean	RMS	mean	RMS
$\phi \to e^+e^-$	1.81	0.48	1.11	0.17	0.67	0.13
$\phi \to K^+K^-$	1.96	0.44	1.15	0.16	0.75	0.12

Table 4.7: The mean and RMS of kinematic variables for $\phi \to e^+e^-$ and $\phi \to K^+K^-$ decays in the overlapped acceptance.

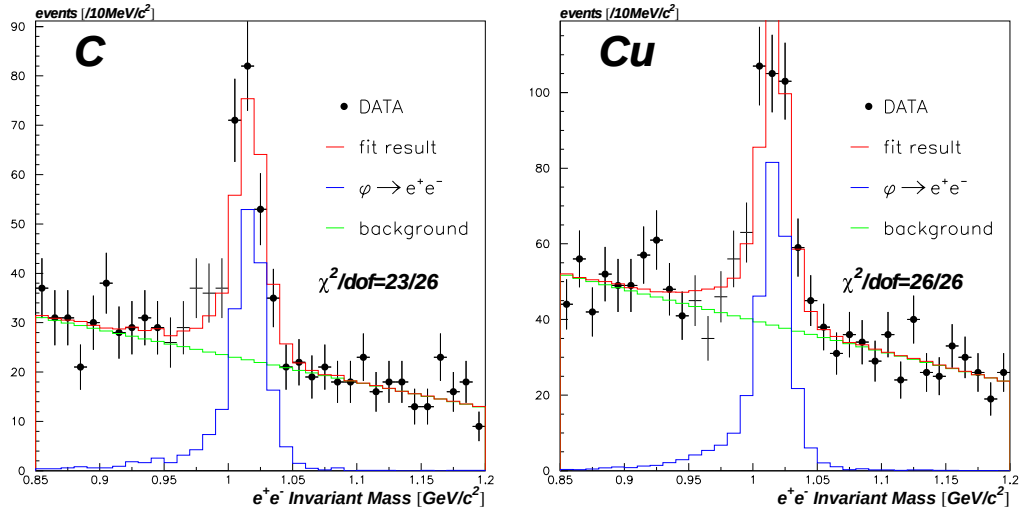

(a) $\phi \to e^+e^-$

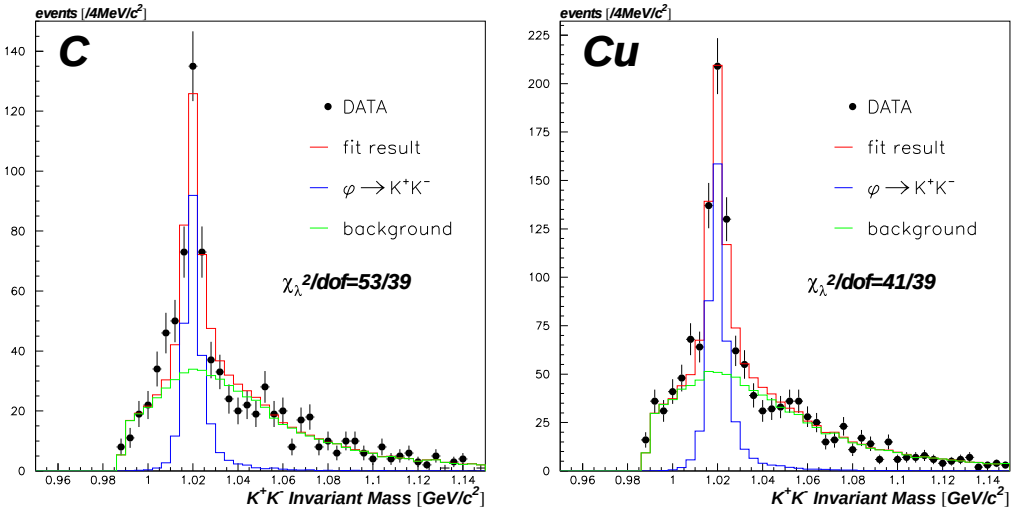

(b) $\phi \to K^+K^-$

Figure 4.14: (a) The invariant mass spectra of the e^+e^- sample in the overlapped acceptance. The closed circles represent the data and the thin crosses represent the excluded region from the fit. The red, green and blue lines represent the fit results, the quadratic backgrounds and the expected $\phi \to e^+e^-$ shapes, respectively. (b) The invariant mass spectra of the K^+K^- sample in the overlapped acceptance. The closed circles represent the data. The red, green and blue lines represent the fit results, the combinatorial backgrounds and the expected $\phi \to K^+K^-$ shapes, respectively.

	$N_\phi(C)$	$N_\phi(Cu)$	α
$\phi \to e^+e^-$	$214 \pm 27 \pm 0$	$293 \pm 34 \pm 1$	$0.91 \pm 0.10 \pm 0.01$
$\phi \to K^+K^-$	$226 \pm 27 \pm 20$	$408 \pm 35 \pm 35$	$1.10 \pm 0.09 \pm 0.02$

Table 4.8: The yields and the α parameters for $\phi \to e^+e^-$ and $\phi \to K^+K^-$ in the overlapped acceptance. The first errors are statistical and the second are systematic.

4.3.3 Comparison of $\alpha_{\phi\to e^+e^-}$ and $\alpha_{\phi\to K^+K^-}$

The e^+e^- and K^+K^- decay channels cannot be compared directly because of the difference in the detector acceptance. Therefore, we determined $\alpha_{\phi\to e^+e^-}$ two-dimensionally on the y-p_T plane under the assumption that $\alpha_{\phi\to e^+e^-}$ is linearly dependent on y and p_T, and estimated the values corresponding to the kaon acceptance windows (see Appendix D for the detail).

The y-p_T dependence of $\alpha_{\phi\to e^+e^-}$ is parameterized as $\alpha(y, p_T) = a \times y + b \times p_T + c$, and we determined the parameters as follows:

1. The e^+e^- data was divided into 3×3 bins in the y-p_T plane as shown in Fig. 4.15.
2. The value of $\alpha_{\phi\to e^+e^-}$ in each bin was obtained as listed in Table 4.9.
3. The values were fitted with the above function.

We obtained a $= -0.32 \pm 0.11$, b $= 0.13 \pm 0.17$, c $= 1.24 \pm 0.15$, and $\chi^2/\mathrm{dof} = 4.2/6$, indicating that the above assumption is statistically acceptable. Since the fit was statistically reasonable, we estimated $\alpha(y, p_T)$ of each K^+K^- data point according to its kinematical coverage and we used the estimated values for the comparison of $\alpha_{\phi\to e^+e^-}$ and $\alpha_{\phi\to K^+K^-}$.

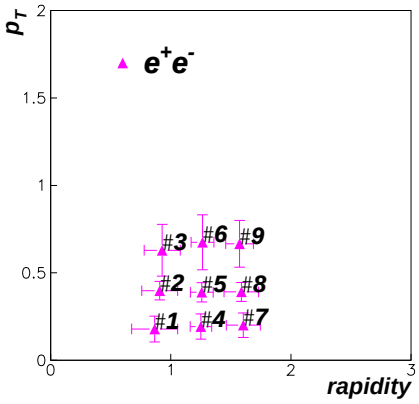

			rapidity value		p_T value	
			mean	RMS	mean	RMS
#1	$y < 1.1$	$p_T < 0.3$	0.87	0.19	0.18	0.07
#2	$y < 1.1$	$0.3 < p_T < 0.5$	0.91	0.15	0.40	0.05
#3	$y < 1.1$	$0.5 < p_T$	0.93	0.15	0.63	0.15
#4	$1.1 < y < 1.4$	$p_T < 0.3$	1.25	0.09	0.19	0.07
#5	$1.1 < y < 1.4$	$0.3 < p_T < 0.5$	1.26	0.09	0.39	0.06
#6	$1.1 < y < 1.4$	$0.5 < p_T$	1.26	0.10	0.67	0.16
#7	$1.4 < y$	$p_T < 0.3$	1.60	0.14	0.20	0.07
#8	$1.4 < y$	$0.3 < p_T < 0.5$	1.59	0.14	0.39	0.05
#9	$1.4 < y$	$0.5 < p_T$	1.57	0.11	0.67	0.13

Figure 4.15: The mean and RMS values of each bin of $\phi \to e^+e^-$ decays divided into 3×3 in the y-p_T plane. The error bars are the RMS values. The ID number ($\#x$) in the figure for each data point corresponds to the number in the table showing the actual values.

	$N_{\phi\to e^+e^-}(C)$	$N_{\phi\to e^+e^-}(Cu)$	$\alpha_{\phi\to e^+e^-}$
#1	$280 \pm 30 \pm 4$	$495 \pm 43 \pm 15$	$1.07 \pm 0.08 \pm 0.02$
#2	$243 \pm 27 \pm 1$	$377 \pm 38 \pm 12$	$0.99 \pm 0.09 \pm 0.03$
#3	$137 \pm 20 \pm 1$	$223 \pm 28 \pm 1$	$1.02 \pm 0.11 \pm 0.01$
#4	$407 \pm 39 \pm 3$	$454 \pm 47 \pm 4$	$0.79 \pm 0.08 \pm 0.01$
#5	$359 \pm 34 \pm 5$	$426 \pm 41 \pm 5$	$0.83 \pm 0.08 \pm 0.01$
#6	$257 \pm 30 \pm 2$	$319 \pm 37 \pm 1$	$0.86 \pm 0.10 \pm 0.01$
#7	$388 \pm 42 \pm 2$	$391 \pm 46 \pm 2$	$0.73 \pm 0.10 \pm 0.01$
#8	$306 \pm 38 \pm 8$	$389 \pm 42 \pm 1$	$0.87 \pm 0.10 \pm 0.02$
#9	$296 \pm 36 \pm 2$	$386 \pm 39 \pm 1$	$0.89 \pm 0.10 \pm 0.01$

Table 4.9: The yields and the α parameters for the $\phi \to e^+e^-$ decays divided into 3×3 bins in the y-p_T plane. The first errors are statistical and the second are systematic.

In Fig. 4.16, we show the estimated values of $\alpha_{\phi\to e^+e^-}$ in the kaon acceptance windows as hatched bands; these can be compared to the measured values of $\alpha_{\phi\to K^+K^-}$. The difference $\Delta\alpha$'s in the kaon acceptance are plotted in Fig. 4.17, and listed in Table 4.10. We expect that $\Delta\alpha$ should be zero when $\Gamma_{\phi\to K^+K^-}/\Gamma_{\phi\to e^+e^-}$ does not change in a nuclear media. Although it is interesting to observe that $\Delta\alpha$ increases when $\beta\gamma$ decreases, $\Delta\alpha$ at the lowest $\beta\gamma$ bin is 0.33 $\pm$ 0.17. The averaged value, which is obtained by using all kinematical region for the K^+K^- channel, is 0.14 $\pm$ 0.12. It seems that these values have discrepancies from zero, however, $\alpha_{\phi\to e^+e^-}$ and $\alpha_{\phi\to K^+K^-}$ are consistent with each other within errors in the measured kinematic region.

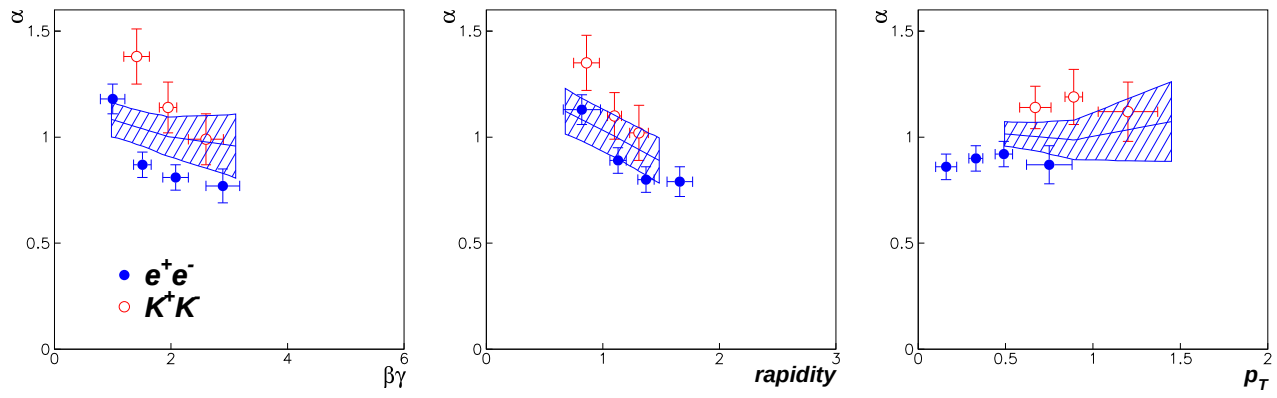

(a) $\beta\gamma$ (b) rapidity (c) p_T

Figure 4.16: The α parameters of $\phi \to e^+e^-$ (closed circle) and $\phi \to K^+K^-$ (open circle) as functions of (a) $\beta\gamma$, (b) rapidity, and (c) p_T, before the acceptance correction. The corrected $\alpha_{\phi\to e^+e^-}$ with the errors for the K^+K^- acceptance are shown as the hatched bands.

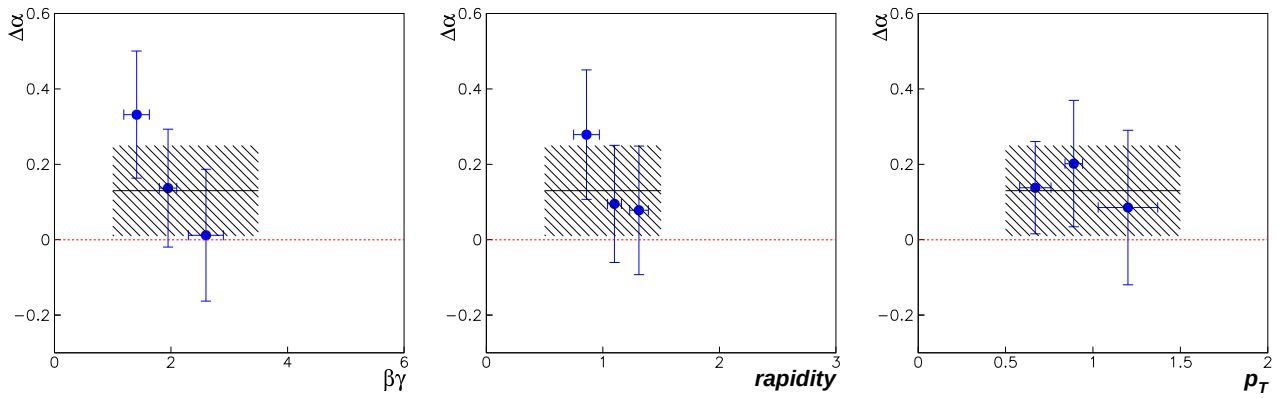

(a) $\beta\gamma$ (b) rapidity (c) p_T

Figure 4.17: The differences between $\alpha_{\phi\to K^+K^-}$ and $\alpha_{\phi\to e^+e^-}$, $\Delta\alpha$, in the kaon acceptance as functions of (a) $\beta\gamma$, (b) rapidity, and (c) p_T. The average value and error are also plotted as the hatched bands.

	rapidity value		p_T value		$\alpha_{\phi\to K^+K^-}$	estimated $\alpha_{\phi\to e^+e^-}$	$\Delta\alpha$
	mean	RMS	mean	RMS			
all	1.08	0.20	0.90	0.25	1.15 ± 0.07 ± 0.03	1.01 ± 0.10	0.14 ± 0.12
$\beta\gamma < 1.7$	0.88	0.13	0.70	0.15	1.38 ± 0.13 ± 0.07	1.05 ± 0.08	0.33 ± 0.17
$1.7 < \beta\gamma < 2.2$	1.09	0.11	0.88	0.17	1.14 ± 0.12 ± 0.03	1.00 ± 0.10	0.14 ± 0.16
$2.2 < \beta\gamma$	1.25	0.14	1.09	0.22	0.99 ± 0.12 ± 0.03	0.98 ± 0.12	0.01 ± 0.17
$y < 1$	0.86	0.11	0.83	0.27	1.35 ± 0.13 ± 0.05	1.07 ± 0.10	0.28 ± 0.17
$1 < y < 1.2$	1.10	0.06	0.92	0.25	1.10 ± 0.11 ± 0.04	1.01 ± 0.10	0.09 ± 0.16
$1.2 < y$	1.31	0.08	0.96	0.19	1.02 ± 0.13 ± 0.04	0.94 ± 0.10	0.08 ± 0.17
$p_T < 0.8$	1.01	0.18	0.67	0.09	1.14 ± 0.10 ± 0.02	1.00 ± 0.07	0.14 ± 0.12
$0.8 < p_T < 1$	1.14	0.20	0.89	0.05	1.19 ± 0.13 ± 0.05	0.99 ± 0.09	0.20 ± 0.17
$1 < p_T$	1.12	0.18	1.20	0.17	1.12 ± 0.14 ± 0.03	1.03 ± 0.15	0.09 ± 0.20

Table 4.10: $\alpha_{\phi\to K^+K^-}$ and estimated $\alpha_{\phi\to e^+e^-}$ in the kaon acceptance window. The first errors are statistical and the second are systematic. For "estimated $\alpha_{\phi\to e^+e^-}$" and "$\Delta\alpha$", the errors are the quadratic sums of the statistical and systematic errors.

4.4 Discussion on the Possible Modification of $\Gamma_{\phi\to K^+K^-}$ and $\Gamma_{\phi\to e^+e^-}$

On the basis of the obtained results, the possible modification of the decay widths is discussed below. In medium, we suppose the total and partial decay widths Γ to change to Γ^* according to the relation

$$\begin{aligned} \Gamma^*_{\phi}\Big/\Gamma^0_{\phi} &= 1 + k_{\rm tot}\,(\rho/\rho_0)\,, \\ \Gamma^*_{\phi\to K^+K^-}\Big/\Gamma^0_{\phi\to K^+K^-} &= 1 + k_K\,(\rho/\rho_0)\,, \\ \Gamma^*_{\phi\to e^+e^-}\Big/\Gamma^0_{\phi\to e^+e^-} &= 1 + k_e\,(\rho/\rho_0)\,, \end{aligned} \tag{4.4}$$

where Γ^0 is the value in vacuum, ρ_0 is the normal nuclear density, and $k_{\rm tot}$, k_K, and k_e are width broadening parameters (see Appendix E). We expect $k_{\rm tot} \simeq k_K$ since the ϕ meson mainly decays into $K\bar{K}$ as long as such decays are kinematically allowed.

To estimate the relation between $\Delta\alpha$, k_K, and k_e, we performed the Monte Carlo calculation. We considered that ϕ mesons were uniformly generated in the target nucleus according to the nuclear density. This is because the mass-number dependence of the ϕ meson production cross section α is obtained to be about unity as described in Sec. 4.3. Generated ϕ mesons were traced until the decay point with the modified decay width according to the nuclear density distribution. The decay probability increases in the medium due to the width broadening. We used the Woods-Saxon form as shown in Fig. 4.18 for the nuclear density distribution;

$$\rho/\rho_0 \propto (1 + \exp((r - R)/\tau))^{-1}, \tag{4.5}$$

where $R = 4.1(2.3)$ fm, and $\tau = 0.50(0.57)$ fm for the Cu(C) target. In the plane of k_K and k_e, the expected values of $\Delta\alpha$ were obtained. The results are shown in Fig. 4.19, in which the measured $\Delta\alpha$ provides constraints for k_K and k_e.

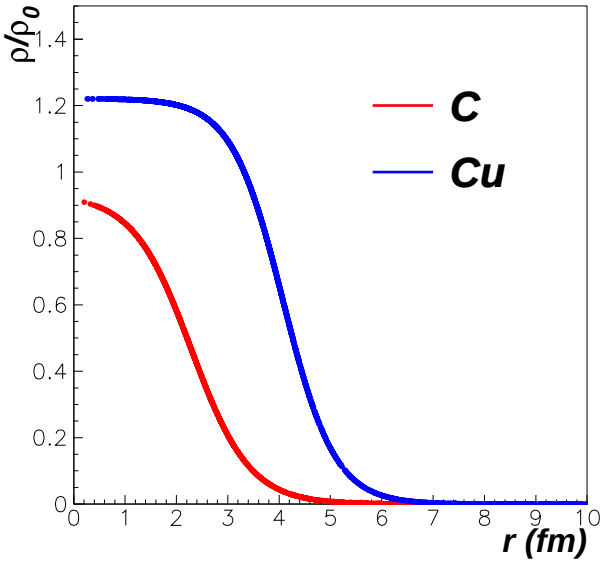

Figure 4.18: The Woods-Saxon distribution for C and Cu nuclei.

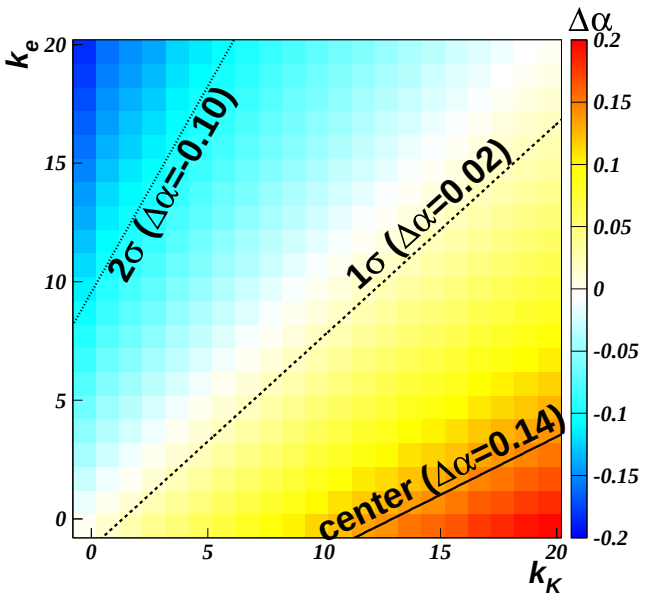

Figure 4.19: The values of expected $\Delta\alpha$ shown in color, which are obtained by the Monte Carlo calculation. The measured $\Delta\alpha$ and its error band are shown with the lines.

Next, we considered how the K^+K^- spectra could provide constraints on k_K. Since we observed a significant excess on the low-mass side of the ϕ-meson peak in the $\phi \to e^+e^-$ channel [31, 36], we consider that a similar excess can exist in the $\phi \to K^+K^-$ spectra. We thus reanalyzed the $\phi \to K^+K^-$ spectra with the same fitting procedure as described earlier, except that the mass range from $2m_{K^\pm}(0.987)$ to 1.01 GeV/c^2 (0.01 GeV/c^2 below the ϕ peak) was excluded from the fit, as shown in Fig. 4.20. Due to the statistical limitation, we combined all the kinematical bins into one.

This procedure gives the amount of excess $N_{\rm ex}$ as a surplus over the natural ϕ-meson peak and the background. Since the K^+K^- acceptance is a function of the invariant mass as described in Sec. 3.5.2 (Fig. 3.63(b)), we corrected obtained values as listed in Table 4.11. In this

table, the systematic errors contain the uncertainty in the background estimation. Although these surpluses $N_{\rm ex}$ are close to zero, they statistically limit the number of modified ϕ mesons in the K^+K^- spectra. The ratio $N_{\rm ex}/N_\phi$ can be considered as the ratio of the number of ϕ mesons decayed inside the nucleus to that outside it, i.e., $N_{\rm ex}/N_\phi = N_\phi^{\rm in}/N_\phi^{\rm out}$.

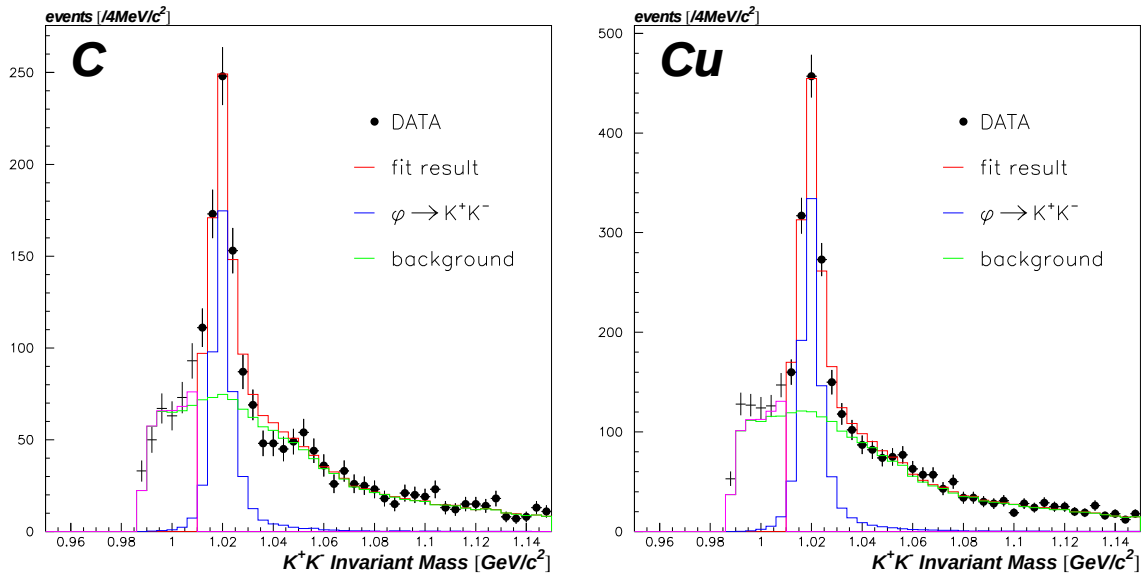

Figure 4.20: The invariant mass spectra of the final K^+K^- sample. The closed circles represent the data and the thin crosses represent the excluded region, from $2m_{K^\pm}(0.987)$ to 1.01 GeV/c^2, for the fit. The red, green and blue lines represent the fit results, the combinatorial backgrounds and the expected $\phi \to K^+K^-$ shapes, respectively.

	before the mass acceptance correction		after the mass acceptance correction	
	C	Cu	C	Cu
N_ϕ	$454 \pm 33 \pm 29$	$880 \pm 44 \pm 50$	$356\text{k} \pm 12\text{k} \pm 23\text{k}$	$697\text{k} \pm 16\text{k} \pm 40\text{k}$
$N_{\rm ex}$	$23 \pm 20 \pm 37$	$90 \pm 28 \pm 54$	$16\text{k} \pm 13\text{k} \pm 23\text{k}$	$53\text{k} \pm 18\text{k} \pm 34\text{k}$
$N_{\rm ex}/N_\phi$	$0.051 \pm 0.045 \pm 0.073$	$0.103 \pm 0.032 \pm 0.053$	$0.044 \pm 0.037 \pm 0.058$	$0.076 \pm 0.025 \pm 0.043$

Table 4.11: The number of ϕ meson N_ϕ, the excess $N_{\rm ex}$, and $N_{\rm ex}/N_\phi$ before and after the mass acceptance correction. The first errors are statistical and the second are systematic.

The relation between $N_\phi^{\rm in}/N_\phi^{\rm out}$ and k_K was also obtained by the Monte Carlo calculation. We assumed that the decays inside the half-density radius of the Woods-Saxon distribution contribute to $N_\phi^{\rm in}$. Figure 4.21 shows the relation between $N_\phi^{\rm in}/N_\phi^{\rm out}$ and k_K for C and Cu nuclei obtained by the Monte Carlo calculation. Using the relation in Fig. 4.21, we obtained the allowed region of k_K with a constraint by the observed $N_{\rm ex}/N_\phi$ as listed in Table 4.12. By averaging the k_K for C and Cu, we obtained $k_K = 1.4 \pm 1.1$ (stat) $\pm$ 2.1 (syst), and plotted in Fig. 4.22.

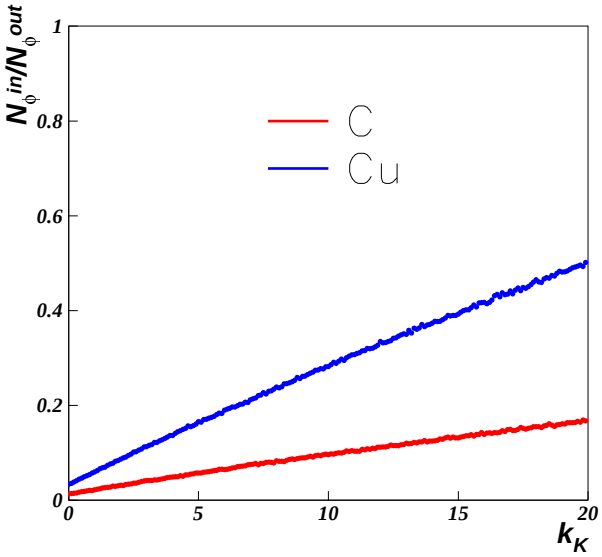

Figure 4.21: The relation $N_\phi^{\rm in}/N_\phi^{\rm out}$ and k_K for C and Cu nuclei obtained by the Monte Carlo calculation.

	k_K
C	$3.4 \pm 4.8 \pm 7.6$
Cu	$1.3 \pm 1.1 \pm 1.8$
weighted mean	$1.4 \pm 1.1 \pm 2.1$

Table 4.12: The obtained k_K from the observed $N_{\rm ex}/N_\phi$ in Table 4.11 and the calculated $N_\phi^{\rm in}/N_\phi^{\rm out}$-$k_K$ relation in Fig. 4.21. The first errors are statistical and the second are systematic.

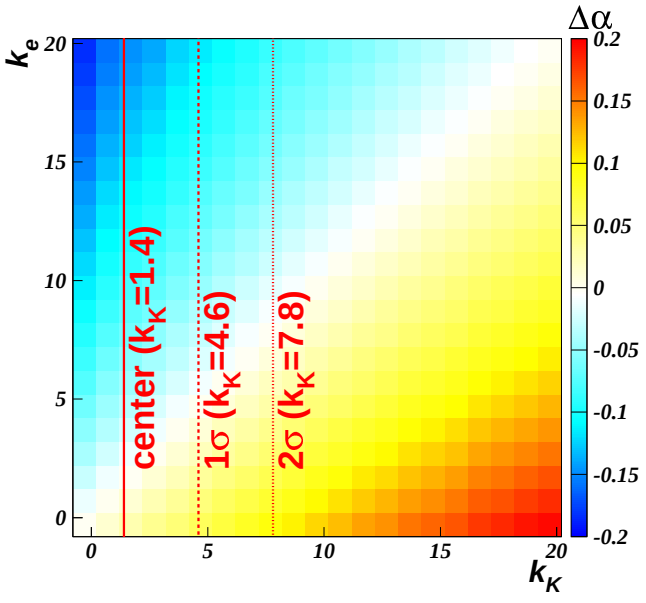

Figure 4.22: The constraint given by the $N_{\rm ex}/N_\phi$ ratio in the plane of k_K and k_e.

Using the above two constraints in the plane of k_K and k_e, the 90% confidence limits are obtained and shown in Fig. 4.23. We have renormalized the probability distribution functions eliminating an unphysical region corresponding to $\Gamma^*/\Gamma^0 < 0$. These are the first experimental limits assigned to the in-media broadening of the partial decay widths.

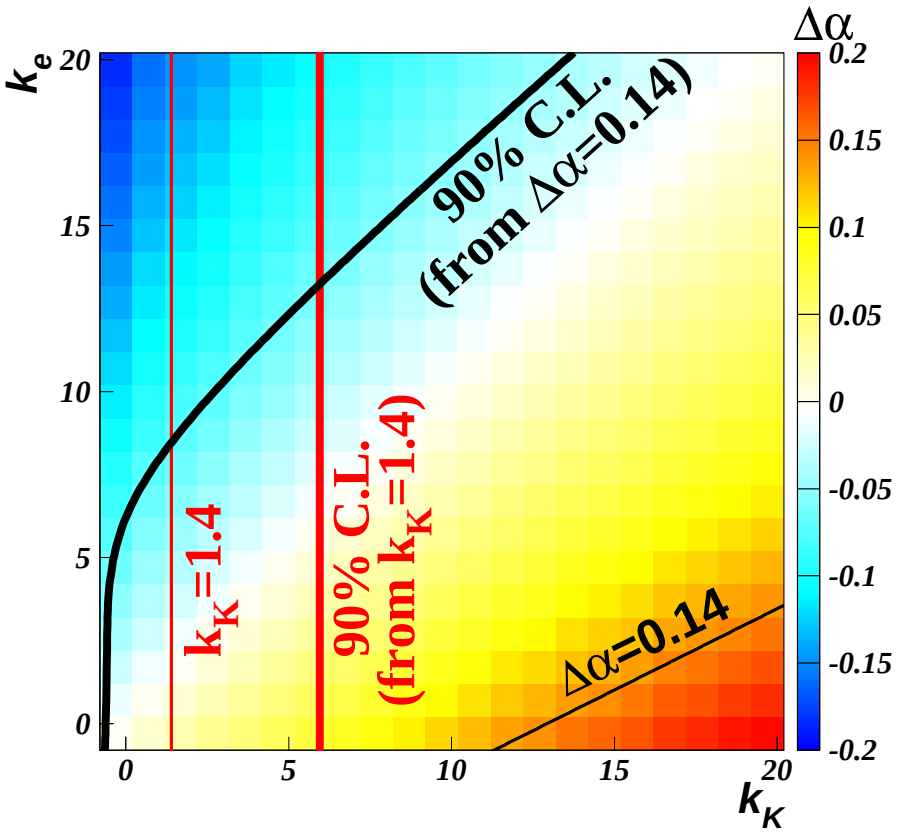

Figure 4.23: The obtained constraints on the in-medium modification of the partial decay widths of $\phi \to K^+K^-$ and $\phi \to e^+e^-$. The 90% confidence limits, which are renormalized for the probability distribution functions by eliminating an unphysical region corresponding to $\Gamma^*/\Gamma^0 < 0$, are plotted.

With our previous result of the $\phi \to e^+e^-$ decay channel, the constraints on the in-medium modification of the partial decay widths of $\phi \to K^+K^-$ and $\phi \to e^+e^-$, and the constraint obtained in Ref. [31], parameter $k_2^{\rm tot}$, are plotted in Fig. 4.24. Here the parameter of $k_2^{\rm tot}$ in Ref. [31] is defined as $\Gamma^*_\phi/\Gamma^0_\phi = 1 + k_2^{\rm tot}\,(\rho/\rho_0)$ with an assumption that $\Gamma_\phi/\Gamma_{\phi\to e^+e^-}$ are not changed in a medium, and obtained to be $k_2^{\rm tot} = 2.6^{+1.8}_{-1.2}$. In the figure, our two works are consistent with each other.

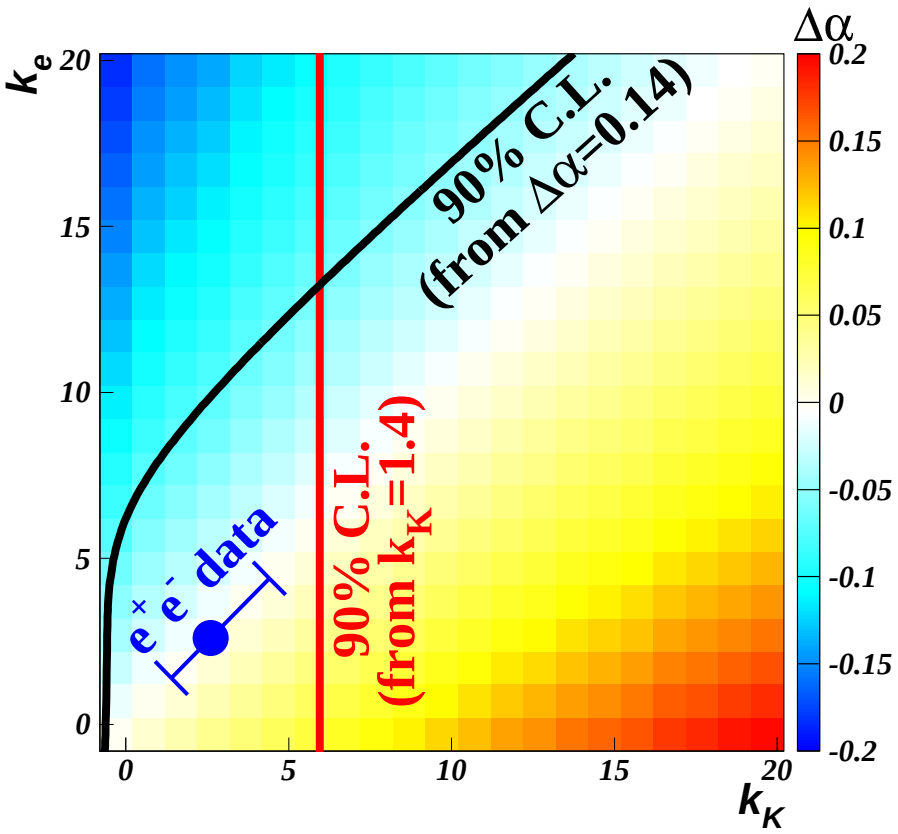

Figure 4.24: The obtained constraints on the in-medium modification of the partial decay widths of $\phi \to K^+K^-$ and $\phi \to e^+e^-$, and the constraint obtained in Ref. [31].

Although the present analysis gave "null" results on the decay width modification of $\Gamma_{\phi\to e^+e^-}$ and $\Gamma_{\phi\to K^+K^-}$ as well as on the mass shape modification in the $\phi \to K^+K^-$ decay channel, the data can set limits on the in-media broadening using a simple model calculation with a minimal assumption that the modified ϕ appears in the low mass side of the ϕ peak as experimentally shown by our previous work [31, 36]. It should be noted that the remarkable S/N ratio (compared to the high-energy $A+A$ reactions) of the present experiment enabled us to perform this analysis. Such an analysis was impossible by the past experiments. Therefore, it is very meaningful to set those experimental limits to be compared with various theoretical models for the width broadening as described in Sec. 1.2.

Chapter 5

Conclusion

The experiment KEK-PS E325 has measured the invariant mass spectra of e^+e^- and K^+K^- pairs in 12 GeV $p+A$ reactions. The goal of the experiment is to detect a possible signature of the partially-restored chiral-symmetry at normal nuclear density to appear as modification of the spectral shape of vector mesons. We have searched for a possible change of the branching ratio $\Gamma_{\phi\to K\bar{K}}/\Gamma_{\phi\to e^+e^-}$, which is theoretically predicted as a consequence of a change in the spectral functions of ϕ and/or kaon in medium, using the nuclear mass-number dependences of the $\phi \to e^+e^-$ and $\phi \to K^+K^-$ yields.

The spectrometer was newly constructed at the high-intensity primary beam-line in KEK to detect slowly moving vector mesons in the $\rho \to e^+e^-$, $\omega \to e^+e^-$, $\phi \to e^+e^-$, and $\phi \to K^+K^-$ decay modes simultaneously. The e^+e^- data described in this manuscript was taken in the year 2001 and 2002, and the K^+K^- data was taken in 2001.

The clear peaks of the $\phi \to e^+e^-$ and $\phi \to K^+K^-$ decays were obtained both in the carbon and copper targets data, and we have observed a mass shape modification in the $\phi \to e^+e^-$ channel in the very low $\beta\gamma$ region ($\beta\gamma < 1.25$) for the copper target data [Phys. Rev. Lett. **98**, 042501 (2007)]. The observed K^+K^- spectra are well reproduced by the relativistic Breit-Wigner distribution with a combinatorial background shape. Because of the difference in the detector acceptances between $\phi \to e^+e^-$ and $\phi \to K^+K^-$, we have very limited statistics for $\phi \to K^+K^-$ in the region $\beta\gamma < 1.25$. Thus, it is impossible to compare the $\phi \to K^+K^-$ shape directly with the modified shape observed in the e^+e^- channel, and it can be concluded that in the region $\beta\gamma > 1.25$, both $\phi \to K^+K^-$ and $\phi \to e^+e^-$ do not show any shape modification.

The nuclear mass number dependences of ϕ meson production are compared between the e^+e^- and K^+K^- channels, using the parametrization of $\sigma(A) = \sigma_0 \times A^\alpha$. Because of the difference in the detector acceptances, we extrapolated $\alpha_{\phi\to e^+e^-}$ two-dimensionally on the rapidity (y) and transverse momentum (p_T) plane to the kaon arm acceptance under the assumption, which is verified with the data, that $\alpha_{\phi\to e^+e^-}$ changes linearly on both rapidity and p_T. We obtain $\Delta\alpha = \alpha_{\phi\to K^+K^-} - \alpha_{\phi\to e^+e^-}$ to be 0.33 ± 0.17 at the lowest $\beta\gamma$ region, $\beta\gamma < 1.7$. The averaged value of $\Delta\alpha$ is obtained to be 0.14 ± 0.12 in the full $\beta\gamma$ region, $1 < \beta\gamma < 3.5$. It seems that these values have discrepancies from zero, however, $\alpha_{\phi\to e^+e^-}$ and $\alpha_{\phi\to K^+K^-}$ are consistent with each other within errors in the measured kinematic region. This is the first measurement of the branching ratio $\Gamma_{\phi\to K^+K^-}/\Gamma_{\phi\to e^+e^-}$ in a nuclear medium.

Using a simple Monte Carlo calculation, we related $\Delta\alpha$ to the in-media broadening parameters k_K for $\Gamma_{\phi\to K^+K^-}$ and k_e for $\Gamma_{\phi\to e^+e^-}$, and the observed $\Delta\alpha$ set the limit on k_K and k_e. Here k_x is defined as $\Gamma^*_{\phi\to x^+x^-}\Big/\Gamma^0_{\phi\to x^+x^-} = 1 + k_x\,(\rho/\rho_0)$. We also searched for possible mass-modification signals on the low mass side of the $\phi \to K^+K^-$ peak. We found zero-consistent signal which set the limit on k_K. Using the above two constraints in the plane of k_K and k_e, the 90% confidence limits are obtained in the k_K-k_e plane for the first time.

Acknowledgments

First of all, I would like to express my gratitude for Professor Hideto En'yo who has been the spokesman of the present experiment. He has continuously encouraged, advised, and supported me at every stage of this work. I gratefully acknowledge Prof. K. Imai and Prof. N. Saito for their guidance, discussions, and support for myself to accomplish the present works.

I wish to acknowledge all the collaborators of the E325 experiment. I express my thanks to Prof. J. Chiba, Dr. M. Sekimoto, Prof. H. Funahashi, Dr. T. Murakami, and Prof. H. Hamagaki for their helpful advice at every stage of the experiment, including the design, construction, data-taking, and analysis. I greatly acknowledge Prof. M. Ieiri, Prof. K.H. Tanaka, and Prof. M. Takasaki who constructed and maintained the EP1B beam line, for their helpful support. I would like to thank Dr. S. Yokkaichi, Dr. T. Tabaru, Dr. M. Naruki, Dr. R. Muto, Dr. K. Ozawa, Dr. M. Ishino, and Dr. S. Mihara. They are the major players who carried out this experiment. They have also provided clear and helpful advice. I would also like to say thanks to Mr. T. Miyashita and Mr. Y. Yoshimura for the construction and the maintenance of the spectrometer. Thanks are also delivered to Dr. M. Kitaguchi, Dr. S. Yamada, Mr. Y. Fukao, Dr. K. Miwa, Mr. T. Nakura, and Mr. M. Togawa for their tireless efforts during the data-taking period. I also thank Dr. H. Kanda and for assistance during the beam time.

The experiment was fully supported by the staffs of KEK, including the PS beam channel group, the PS floor staff, the on-line group, the electronics division, and the accelerator division.

This work was partly supported by the Japan Society for the Promotion of Science and a Grant-in-Aid for Scientific Research from the Japan Ministry of Education, Culture, Sports, Science and Technology (MEXT). Finally, we also thank the staff members of RIKEN Super Combined Cluster system and RIKEN-CCJ.

Finally, I express my appreciation to my wife Karen and my parents for their lasting assistance and encouragements.

Appendix A

Squared-Mass Distribution in Kaon Sample

As described in Sec. 3.3.6, we obtained the momentum-sliced M^2 distributions from Fig. 3.25, and each M^2 distribution was fitted by three peaks, pion, kaon and proton using a double Gaussian distribution. All the results are shown in Fig. A.1 and A.2, and Fig. A.3 shows the sum of the sliced M^2 distributions.

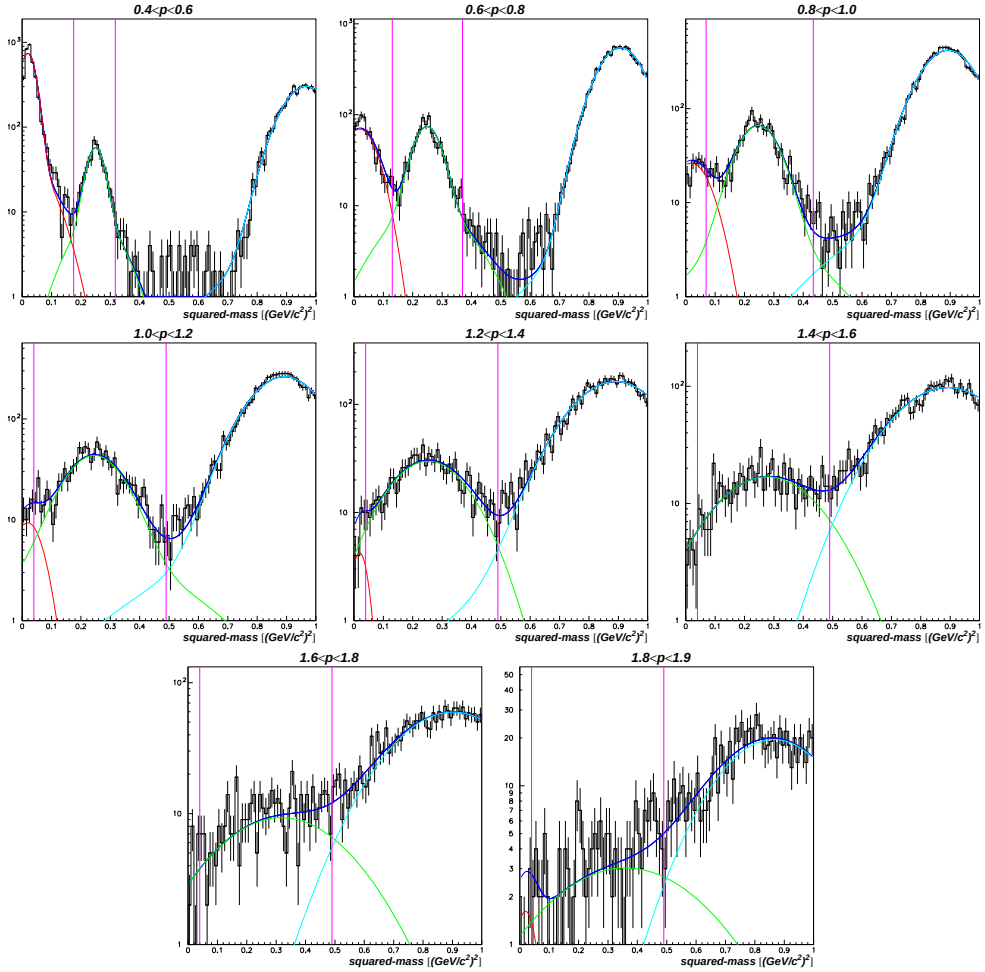

Figure A.1: The distributions of the squared-mass for positive particles with momentum slices of every 0.2 GeV/c step. The distributions were fitted using a double Gaussian distribution. The vertical magenta lines indicate the regions for the kaon selection.

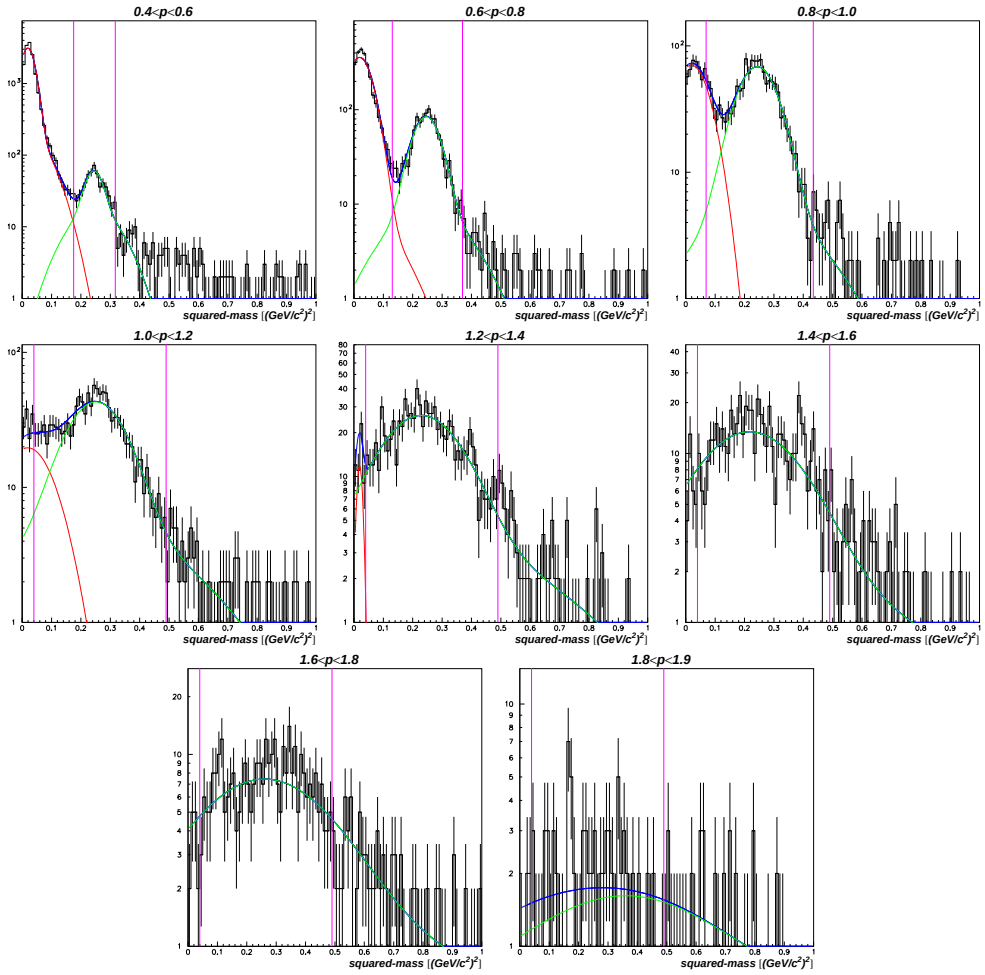

Figure A.2: The distributions of the squared-mass for negative particles with momentum slices of every 0.2 GeV/c step. The distributions were fitted using a double Gaussian distribution. The vertical magenta lines indicate the regions for the kaon selection.

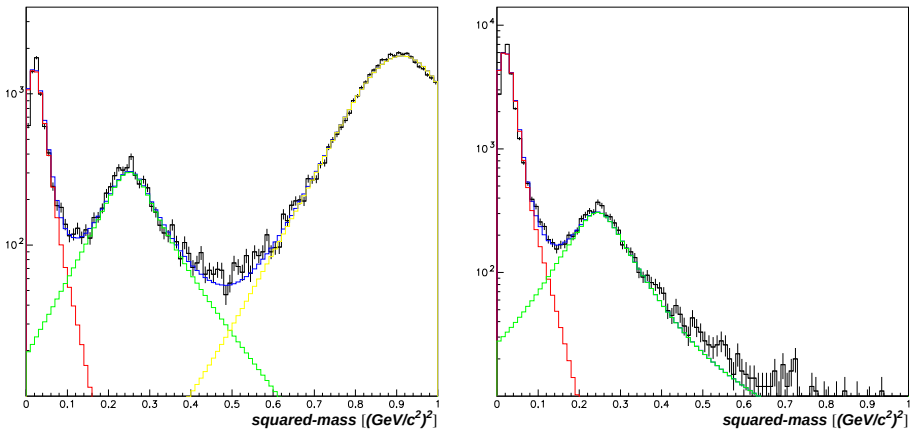

(a) + charge (b) – charge

Figure A.3: The distributions of the squared-mass for (a) positive and (b) negative particles. The fit results, which were the sum of the fits on the momentum-sliced M^2 distributions as shown in Fig. A.1 and A.2, was also plotted.

Appendix B

Double-Arm $\phi \to K^+K^-$ Event

Because of the small Q value in $\phi \to K^+K^-$ decays, the number of $\phi \to K^+K^-$ events were negligible in the double-arm K^+K^- event, which has larger opening angle than that of the single-arm event. Here, "double-arm event" means that K^+ is detected in the left arm and other is detected in the right arm of the spectrometer (LR event), and vice versa (RL event). Since the mass acceptance of RL events is largely suppressed in the mass region near threshold, as same as e^+e^- events, we used LR events for the analysis. Table 3.9 in Sec. 3.6.2 listed the purity of the kaon in the double-arm data (LR events).

Figure B.1 shows the invariant mass spectra of K^+K^- pairs in the double-arm events (LR events) in the mass range from 0.95 to 1.15 GeV/c^2. Small peaks of double-arm $\phi \to K^+K^-$ decays are seen. We fitted each mass spectrum with a resonance shape of $\phi \to K^+K^-$ and a combinatorial background shape in the mass region from $2m_{K^\pm}(0.987)$ to 1.15 GeV/c^2, and the fits were performed by using the maximum likelihood method. For the ϕ meson resonance shape, we used the simulated shape as described in Sec. 3.5.2, but the double-arm events were required. And for the combinatorial background shape, we used the mixed event as described in Sec. 3.6.2. The relative abundance of the ϕ mesons and the background were obtained from the fit.

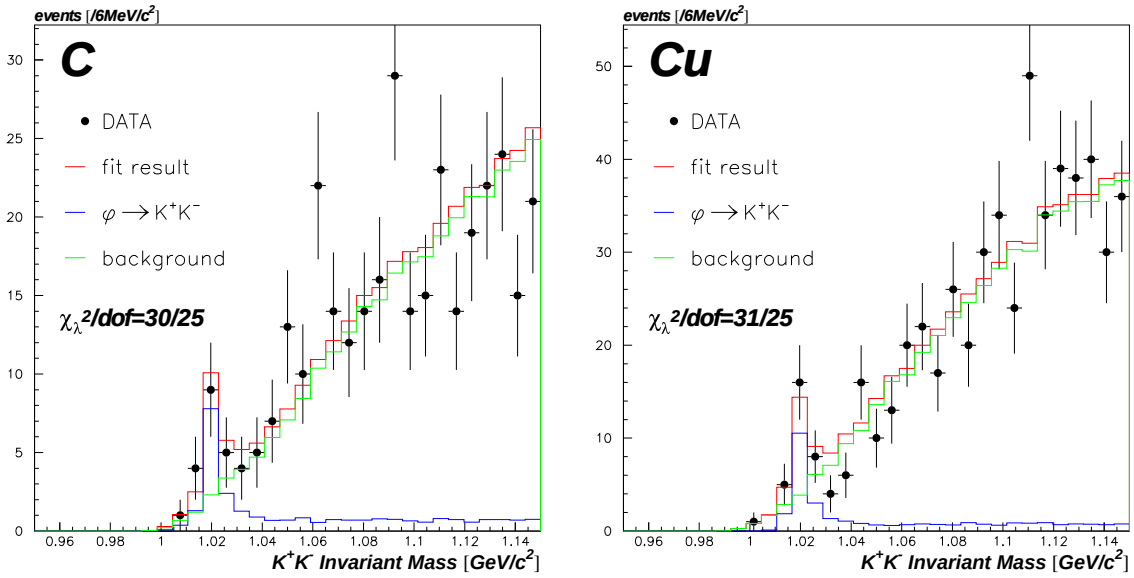

Figure B.1: The invariant mass spectra of the double-arm K^+K^- sample. The closed circles represent the data. The red, green and blue lines represent the fit results, the combinatorial backgrounds and the expected $\phi \to K^+K^-$ shapes, respectively.

Table B.1 summarizes the ϕ-meson yields. The yields were obtained by integrating the mass region from 1.01 to 1.03 GeV/c^2 after subtracting the background. In the table, the α parameter is corrected for the target dependence of the experimental efficiencies as described in Sec. 4.3.2. For this correction, the overall efficiency ratio $\eta_C/\eta_{Cu}(\phi \to K^+K^-)$ and the correction value $\delta\alpha_{\phi\to K^+K^-}$ were obtained to be 0.859 and -0.092, respectively. Figure B.2 shows the detector acceptance for the double-arm K^+K^- pairs (LR event only). In Fig. B.3, we compare the acceptances of double-arm $\phi \to e^+e^-$, single-arm $\phi \to K^+K^-$, and double-arm $\phi \to K^+K^-$. The observed α parameters are plotted as a function of $\beta\gamma$ in Fig. B.4(a) and as functions of the rapidity and p_T in (b) and (c), with the single-arm $\phi \to K^+K^-$ data and the double-arm $\phi \to e^+e^-$ data.

$N_\phi(C)$	$N_\phi(Cu)$	α
11.2 ± 4.3 ± 0.1	15.9 ± 5.4 ± 0.3	0.85 ± 0.31 ± 0.04

Table B.1: The yields and the α parameters for double-arm $\phi \to K^+K^-$ decays. The first errors are statistical and the second are systematic.

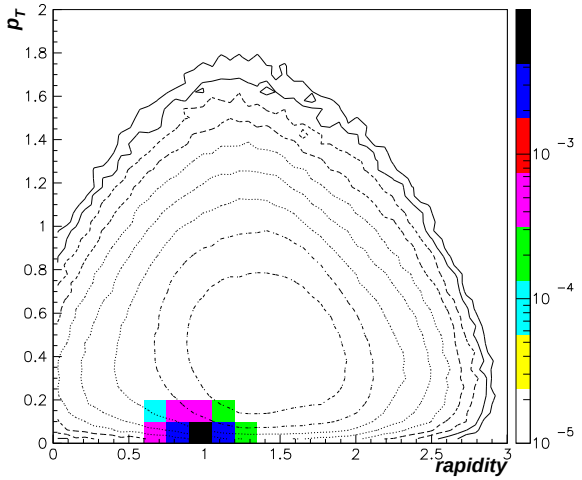

Figure B.2: The simulated detector acceptance for double-arm $\phi \to K^+K^-$ decays (LR event only) is plotted as the color map. The acceptance is calculated using a flat kinematical distribution in the region of $0 < y < 3$ and $0 < p_T < 2$, and includes not only the geometrical acceptance but also the detector efficiencies and all other conditions used in the present analysis. The kinematical distribution of the generated ϕ-meson yield obtained by JAM is also plotted as the contour plot.

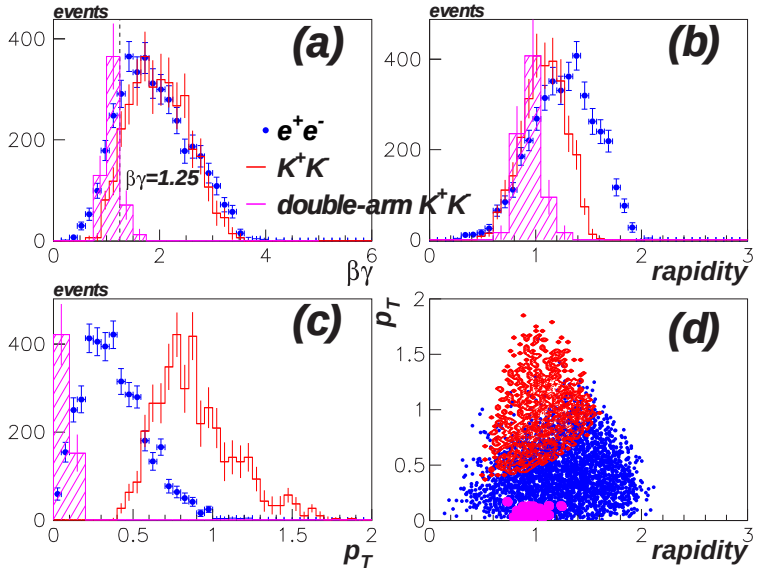

Figure B.3: The observed kinematical distributions of double-arm $\phi \to e^+e^-$, single-arm $\phi \to K^+K^-$, and double-arm $\phi \to K^+K^-$(LR event only), as functions of (a) $\beta\gamma$, (b) rapidity, (c) p_T, and (d) p_T and rapidity. The points represent $\phi \to e^+e^-$, the red lines represent single-arm $\phi \to K^+K^-$, and the pink lines represent double-arm $\phi \to K^+K^-$. The histograms for single-arm and double-arm $\phi \to K^+K^-$ are scaled by a factor of about 3 and 13, respectively.

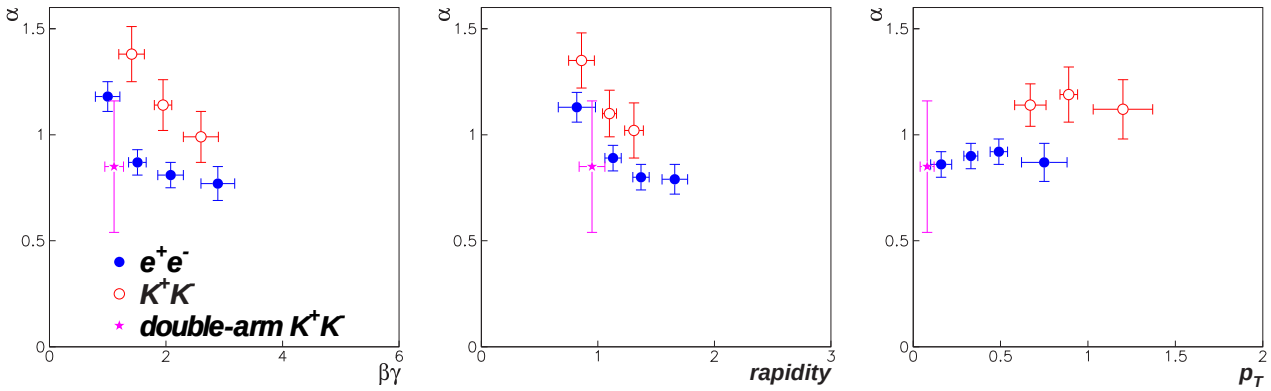

(a) $\beta\gamma$ (b) rapidity (c) p_T

Figure B.4: α parameters of $\phi \to e^+e^-$ (closed circle), $\phi \to K^+K^-$ (open circle), and the double-arm $\phi \to K^+K^-$ (star) as functions of (a) $\beta\gamma$, (b) rapidity, and (c) p_T. The horizontal error bars are the RMS values of the horizontal bins.

Appendix C

Target Thickness

Table C.1 and C.2 list the detailed description of the targets used in 2001 and 2002, respectively. The errors in the tables are the precision in the measurements of the sizes and weights of the targets. The target dimensions in the tables are the values we received those materials from companies. Actual target disks used in the experiment were cut away from those, into the dimensions summarized in Table 2.4 in Sec. 2.4.1. The ratio of the target number densities $N_t(C)/N_t(Cu)$ were almost equivalent between 2001 and 2002, i.e. $N_t(C)/N_t(Cu) = 3.354 \pm 0.016$ and 3.348 ± 0.028 for 2001 and 2002 respectively.

	C	Cu1	Cu2	Cu (sum)
total weight [g]	2.30230	0.45663	0.45980	0.91643
	± 0.00001	± 0.00001	± 0.00001	± 0.00001
paper weight [g]				
target weight [g]	2.30230	0.45663	0.45980	0.91643
	± 0.00001	± 0.00001	± 0.00001	± 0.00001
L1 [mm]	50.00	25.00	25.30	
	± 0.05	± 0.05	± 0.05	
L2 [mm]	50.05	25.05	25.05	
	± 0.05	± 0.05	± 0.05	
L5 [mm]	70.70	35.25	35.50	
	± 0.05	± 0.05	± 0.05	
L3 [mm]	50.00	25.25	25.25	
	± 0.05	± 0.05	± 0.05	
L4 [mm]	50.05	25.00	25.15	
	± 0.05	± 0.05	± 0.05	
target area [cm^2]	25.025	6.287	6.344	12.631
	± 0.071	± 0.035	± 0.035	± 0.050
target density [g· cm^{-2}]	0.09200	0.07263	0.07248	0.07255
	± 0.00026	± 0.00041	± 0.00040	± 0.00029
$N_t/10^{20}$ [cm^{-2}]	46.126	6.883	6.869	13.752
	± 0.130	± 0.038	± 0.038	± 0.054

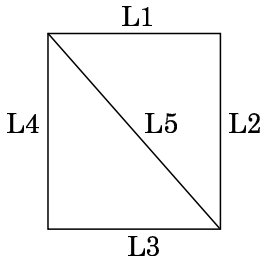

Table C.1: The detailed description of the targets used in 2001, and the measured dimensions, L1 $\sim$ L5.

	C	Cu1	Cu2	Cu3	Cu4	Cu (sum)
total weight [g]	4.81935	0.17911	0.39197	0.17841	0.39199	1.14148
	± 0.00001	± 0.00001	± 0.00001	± 0.00001	± 0.00001	± 0.00002
paper weight [g]	0.21277		0.21277		0.21277	0.42554
	± 0.00001		± 0.00001		± 0.00001	± 0.00001
target weight [g]	4.60658	0.17911	0.17920	0.17841	0.17922	0.71594
	± 0.00001	± 0.00001	± 0.00001	± 0.00001	± 0.00001	± 0.00002
L1 [mm]	50.05	9.80	9.85	9.90	9.90	
	± 0.05	± 0.05	± 0.05	± 0.05	± 0.05	
L2 [mm]	50.00	25.10	24.80	25.25	25.00	
	± 0.05	± 0.05	± 0.05	± 0.05	± 0.05	
L5 [mm]	70.65	27.00	26.60	26.60	26.75	
	± 0.05	± 0.05	± 0.05	± 0.05	± 0.05	
L3 [mm]	50.05	9.90	9.90	9.80	9.80	
	± 0.05	± 0.05	± 0.05	± 0.05	± 0.05	
L4 [mm]	50.05	24.90	25.10	24.80	25.00	
	± 0.05	± 0.05	± 0.05	± 0.05	± 0.05	
target area [cm^2]	25.037	2.462	2.463	2.463	2.462	9.850
	± 0.071	± 0.040	± 0.039	± 0.039	± 0.039	± 0.078
target density [$g\cdot cm^{-2}$]	0.18399	0.07275	0.07276	0.07243	0.07279	0.07268
	± 0.00052	± 0.00117	± 0.00114	± 0.00114	± 0.00116	± 0.00058
$N_t/10^{20}$ [cm^{-2}]	92.247	6.894	6.895	6.864	6.898	27.551
	± 0.260	± 0.111	± 0.108	± 0.108	± 0.110	± 0.219

Table C.2: The detailed description of the targets used in 2002.

Appendix D

Linear Assumption on α Parameter

We assumed $\alpha(y, p_T)$ is linearly dependent on y and p_T. Indeed, the pair acceptance depends quadratically on the rapidity interval, but the α parameter does not show such a dependence because the acceptance term is almost canceled out by taking the ratio in calculating of α. We found that the linear assumption is statistically valid for the present data, and we also examined the assumption for a result of the intra-nuclear cascade calculation, as follows.

For the real data, as described in Sec. 4.3.3, the two-dimensional linear fit for the e^+e^- data, which were divided into 3×3 bins in the y-p_T plane, was successful with $\chi^2/\mathrm{dof} = 4.2/6$. This supports the fact that the "linear" assumption is valid within the e^+e^- acceptance. Using the fit result, we estimated the values corresponding to the kinematical coverage of the K^+K^- data points. The comparison between $\alpha_{\phi\to K^+K^-}$ and $\alpha_{\phi\to e^+e^-}$ (in the K^+K^- acceptance) yielded Fig. 4.17, which shows that the value of $\Delta\alpha = \alpha_{\phi\to K^+K^-} - \alpha_{\phi\to e^+e^-}$ is consistent with zero within the present statistics. If we assume that there are no differences between $\alpha_{\phi\to e^+e^-}$ and $\alpha_{\phi\to K^+K^-}$ the "linear" assumption can be tested using both with the e^+e^- and K^+K^- data together. We performed the fit for the e^+e^- data of 3×3 bins and the K^+K^- data of 3 bins in the $\beta\gamma$ regions simultaneously, and obtained $\chi^2/\mathrm{dof} = 8.7/9$, which is quite reasonable.

To test the assumption for the case of the intra-nuclear cascade calculation, we generated the events by JAM, 10 times as large statistics as the real data, as listed in Table D.1 and D.2. The obtained $\alpha(y, p_T)$ are different from the data but the "linear" fit was successful. Table D.3 summarizes the fit qualities for both the data and the cascade calculations. Therefore, the assumption that α is linearly dependent on y and p_T in the detector acceptance is considered to be reasonable.

	$N_{\phi\to e^+e^-}(C)$	$N_{\phi\to e^+e^-}(Cu)$	$\alpha_{\phi\to e^+e^-}$
#1	1184 ± 30	4825 ± 43	1.150 ± 0.016
#2	1041 ± 27	4501 ± 38	1.185 ± 0.016
#3	679 ± 20	3023 ± 28	1.203 ± 0.018
#4	1906 ± 39	7761 ± 47	1.149 ± 0.013
#5	1719 ± 34	7298 ± 41	1.175 ± 0.012
#6	1509 ± 30	6517 ± 37	1.185 ± 0.013
#7	2163 ± 42	7891 ± 46	1.084 ± 0.012
#8	1952 ± 38	7553 ± 42	1.119 ± 0.012
#9	1545 ± 36	6359 ± 39	1.156 ± 0.015

Table D.1: The simulated yields and the α parameters for the $\phi \to e^+e^-$ decays divided into 3×3 bins in the y-p_T plane. The errors are statistical. The ID numbers ($\#x$) in the table correpond to the number in Fig. 4.15.

	$N_{\phi\to K^+K^-}(C)$	$N_{\phi\to K^+K^-}(Cu)$	$\alpha_{\phi\to K^+K^-}$
$\beta\gamma < 1.7$	666 ± 26	2163 ± 47	1.263 ± 0.027
$1.7 < \beta\gamma < 2.2$	1110 ± 33	3605 ± 60	1.263 ± 0.021
$2.2 < \beta\gamma$	1673 ± 41	5124 ± 72	1.228 ± 0.017

Table D.2: The simulated yields and the α parameters for the $\phi \to K^+K^-$ decays divided into three $\beta\gamma$ bins. The errors are statistical.

		χ^2/dof	a	b	c
DATA	3x3(e^+e^-)	4.2/6	-0.32 ± 0.11	0.13 ± 0.17	1.24 ± 0.15
	3x3(e^+e^-)+3(K^+K^-)	8.6/9	-0.39 ± 0.11	0.22 ± 0.11	1.31 ± 0.14
MC	3x3(e^+e^-)	8.5/6	-0.09 ± 0.02	0.11 ± 0.02	1.23 ± 0.03
	3x3(e^+e^-)+3(K^+K^-)	13.8/9	-0.10 ± 0.02	0.12 ± 0.02	1.24 ± 0.02

Table D.3: The results of the fit with $\alpha(y, p_T) = a \times y + b \times p_T + c$, using values of α in Table 4.5, 4.9, D.1, and D.2.

Appendix E

Linear Assumption on Width Broadening

The assumption that the width broadening is linearly dependent on the nuclear density as Eq. 4.4 is not based on a particular theoretical prediction. However, this assumption is considered to be reasonable by referring to E.Oset and A.Ramos [9], for example, who gave theoretical predictions on Γ^* as functions of density and the ϕ meson mass. From Fig.4 of Ref. [9] (=Fig. E.1), the values of Γ^* at 1020 MeV/c^2 as a function of the density are read off by the eye as listed in Table E.1. When we fit the values with a linear function $\Gamma^*/\Gamma^0 = 1 + k(\rho/\rho_0)$ as Eq. 4.4, the fit reproduces their prediction reasonably well and generates $k = 4.4 \pm 0.2$ as shown in Fig. E.2.

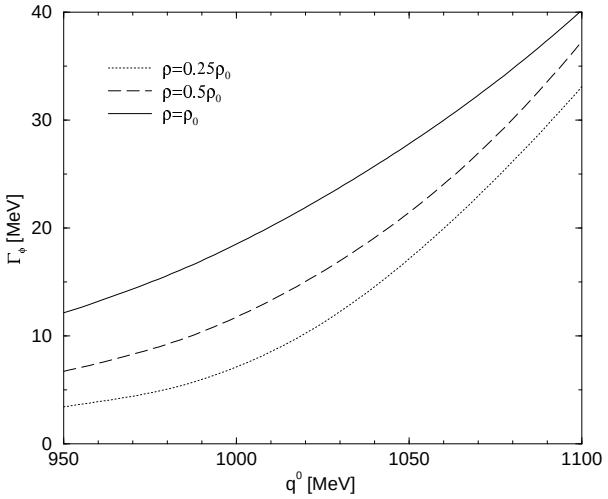

Figure E.1: Width of the ϕ meson in nuclear matter at three densities ($\rho = 0.25\rho_0, 0.5\rho_0, \rho_0$) as a function of the ϕ energy (Fig. 4 of Ref. [9]).

ρ/ρ_0	0	0.25	0.5	1
Γ (MeV/c^2)	4.26	5 ± 1	10 ± 1	22 ± 1

Table E.1: The values of Γ^* at 1020 MeV/c^2 as a function of density read from Fig E.1 (Fig. 4 of Ref. [9]) by the eye.

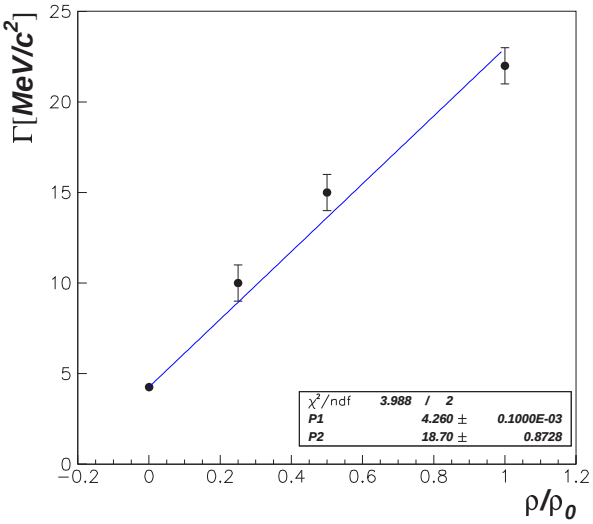

Figure E.2: The fit result of the values in Table E.1.

Appendix F

Effects of Target Thickness on Invariant Mass Spectrum

One of the key points in the E325 experiment is to use thin targets in order to suppress the background from γ-conversions in the e^+e^- channel. Moreover, thick targets increase a radiative tail on the invariant mass peaks, caused mainly by the energy loss of the electrons by bremsstrahlung. So we evaluated the effects of the target thickness on the e^+e^- invariant mass spectrum using Geant4 simulation. We used the non-relativistic Breit-Wigner distribution as the ϕ-meson mass shape with the internal radiative corrections described in Sec. 3.5.1. Their kinematical distribution was generated by JAM. We compared 8 kinds of targets:

- C-target, thickness = 1.0mm = 0.227g/cm^2 (E325 in 2002) [1],
- C-target, thickness = 10mm = 2.27g/cm^2,
- C-target, thickness = 20mm = 4.54g/cm^2,
- C-target, thickness = 4.42mm = 1.0g/cm^2,
- Cu-target, thickness = 0.08mm = 0.072g/cm^2 (E325 in 2001/2002),
- Cu-target, thickness = 0.8mm = 0.72g/cm^2,
- Cu-target, thickness = 1.6mm = 1.44g/cm^2, and
- Cu-target, thickness = 1.12mm = 1.0g/cm^2.

The ϕ mesons were decayed into the e^+e^- pairs at the center of the target thickness. When e^+e^- pairs escaped out the target, we calculated the invariant mass from their momenta. Figure F.1 shows the distortion of the mass spectrum caused by the target material. The targets used in the E325 experiment hardly change the mass spectrum as shown in the two figures (top-center and top-right).

In addition to the target material effect, we show the decomposition of various effects in the simulated ϕ-meson spectrum by the detector simulation in Fig. F.2. The figure shows how the mass spectra of (1) the non-relativistic Breit-Wigner distribution get distorted with (2) internal radiative effects, (3) the target material, (4) the detector materials, and (5) the chamber position resolution as described in Sec. 3.3.2, for the C and Cu targets.

[1] The measured target thickness of C-target in the 2002 run was 0.184g/cm^2, so we overestimated the target thickness of about 20% in the detector simulation. However the following results show that the effect is negligibly small.

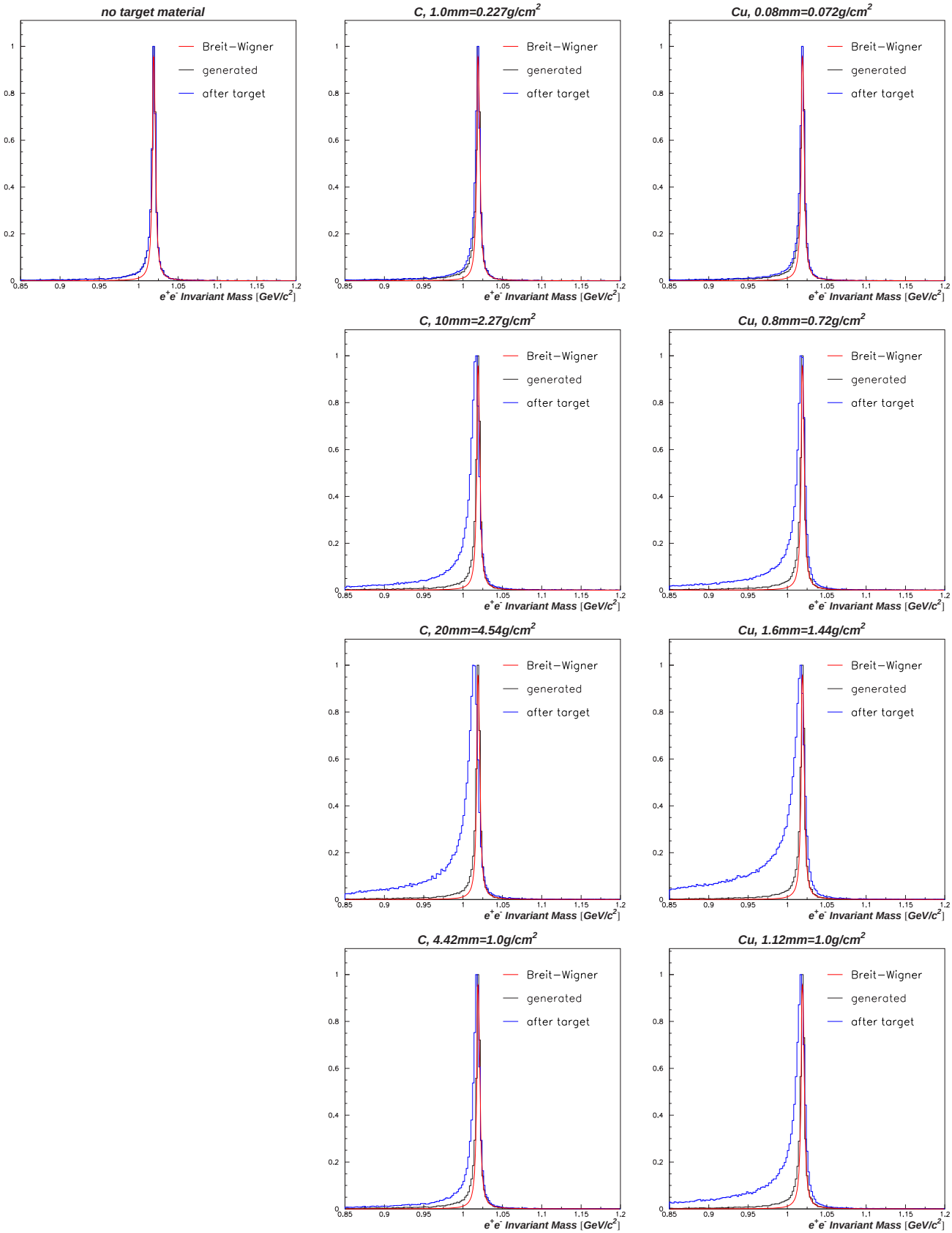

Figure F.1: The invariant mass spectra of $\phi \to e^+e^-$ decays for different target thickness of C and Cu. The red, black, and blue lines represent the Breit-Wigner distribution, the spectrum with the internal radiative effects, and the distorted mass spectrum by the target material, respectively. The mass spectra are normalized by their peak count to unity.

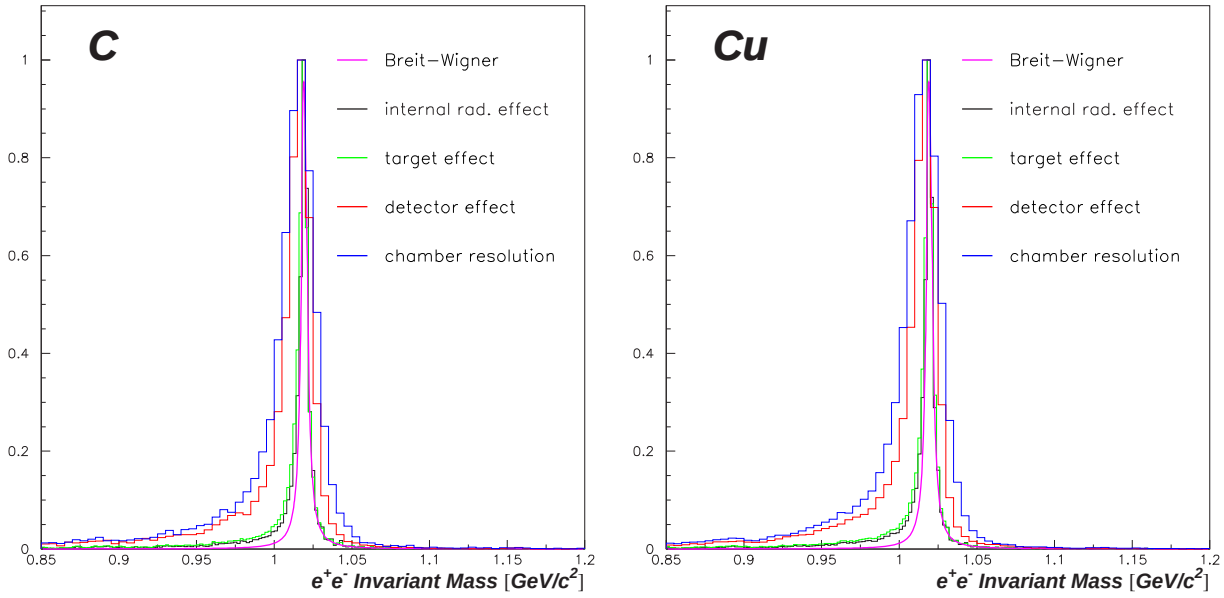

(a) C (b) Cu

Figure F.2: The expected invariant mass spectra of $\phi \to e^+e^-$ obtained by the detector simulation. The pink, black, green, red, and blue lines correspond to the contribution from (1) to (5) described in the text. Both LR and RL events are included. The mass spectra are normalized by their peak count to unity.

Appendix G

Run List used for the Present Analysis

Table G.1(a) and (b) list the run shows used for the present analysis for the year 2001 and 2002, respectively. The list for 2001 is common to the e^+e^- and K^+K^- data.

(a) the year 2001

	1	2	3	4	5	6	7	8	9	10
1	6010	6022	6023	6025	6026	6027	6029	6036	6038	6040
2	6042	6044	6051	6053	6054	6056	6058	6060	6062	6064
3	6068	6069	6072	6077	6078	6079	6083	6086	6088	6089
4	6091	6092	6094	6098	6100	6101	6103	6107	6108	6109
5	6112	6113	6114	6116	6117	6121	6122	6123	6126	6127
6	6131	6133	6134	6137	6138	6139	6140	6142	6143	6145
7	6148	6153	6155	6157	6159	6235	6242	6247	6248	6254
8	6261	6266	6272	6274	6281	6285	6289	6290	6293	6296
9	6300	6306	6308	6313	6314	6317	6320	6323	6327	6330
10	6337	6344	6347	6350	6353	6357	6360	6363	6372	6373
11	6377	6382	6383	6386	6389	6395	6398	6401	6404	6407
12	6412	6415	6418	6424	6427	6430	6433	6436	6442	6444
13	6447	6451	6454	6455	6456	6462	6464	6469	6472	6476
14	6479	6482	6487	6490	6493	6501				

(b) the year 2002

	1	2	3	4	5	6	7	8	9	10
1	7017	7022	7024	7027	7029	7031	7036	7038	7040	7046
2	7051	7053	7055	7056	7060	7062	7064	7067	7069	7070
3	7072	7074	7081	7086	7088	7091	7096	7098	7100	7102
4	7106	7109	7111	7115	7118	7120	7121	7123	7127	7128
5	7130	7134	7140	7142	7144	7148	7150	7152	7154	7156
6	7158	7160	7162	7164	7166	7168	7170	7172	7174	7176
7	7178	7180	7182	7183	7185	7187	7190	7193	7195	7197
8	7199	7202	7204	7206	7208	7210	7212	7214	7216	7218
9	7220	7222	7224	7226	7231	7233	7235	7242	7243	7245
10	7251	7253	7257	7259	7261	7263	7265	7267	7269	7272
11	7273	7277	7281	7283	7285	7287	7290	7292	7294	7296
12	7322	7324	7326	7328	7330	7332	7334	7338	7345	7347
13	7352	7355	7357	7359	7362	7365				

Table G.1: The run lists used for the present analysis, (a) for the year 2001 [136 runs] and (b) for 2002 [126 runs].

Appendix H

Search for J/ψ Production in 12 GeV $p + A$ Reactions

Understanding the production mechanism of J/ψ in high-energy hadronic collisions is an important topic in QCD. Although the structures of $c\bar{c}$ mesons are well understood in terms of quark model, the production mechanism of them is not clear yet. Understanding of such mechanism is particularly important to give the basement both in the search for quark-gluon plasma and the study of the spin structure of nucleon. There are some theoretical models to investigate the J/ψ production mechanism which assumes a different theoretical assumption and treatment; the color-evaporation model (CEM) [70, 71], the color-singlet model (CSM) [72, 73], and the color-octet model (COM) [74] for example. These theoretical models are successful to explain experimental results of J/ψ production in various energy ranges to some extent, but not complete yet.

Experimentally, there are many experiments of J/ψ production in $p + p$, $p + A$, and $A + A$ collisions. Figure H.1 shows the proton-induced J/ψ total cross-sections in energy ranges from $\sqrt{s_{NN}} = 6.8$ to 200 GeV [75]. Theoretical models predict that J/ψ production through quark-antiquark annihilation gives the largest contribution at large x_F, while gluon-gluon fusion dominates the production at small x_F [76]. The present experiment, KEK-PS E325, is performed at $\sqrt{s_{NN}} = 5.1$ GeV, so that searching for J/ψ production in the present energy is attractive for the investigation of the production mechanism of J/ψ near threshold (threshold energy is $\sqrt{s_{NN}} = 4.9$ GeV at $p + p \rightarrow J/\psi + p + p$), which is not well studied theoretically and experimentally yet.

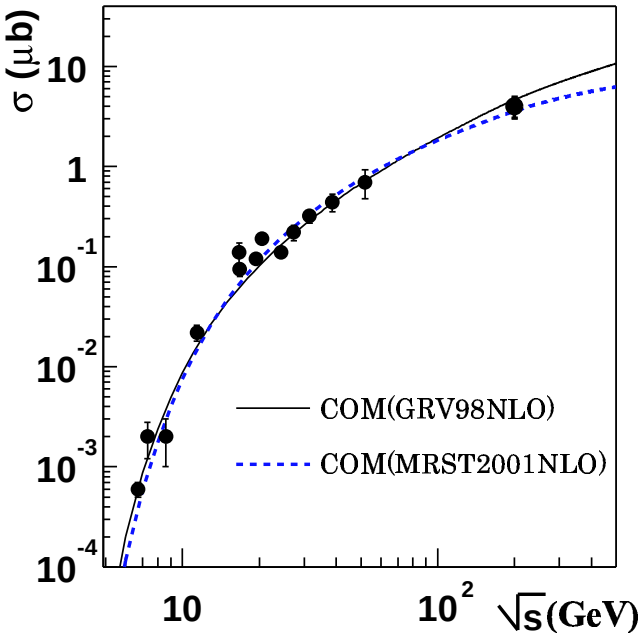

Figure H.1: The J/ψ total cross-sections at various $\sqrt{s}$ [73, 77, 78, 79]. The curves are the calculations of the color-octet model using different parton distribution functions.

In the present $J/\psi \to e^+e^-$ analysis, the electron identification was performed as follows. Tracks were required to have position-matched hits in both the first and the second stage electron counters, particle momentum $p_{\rm track} > 0.4$ GeV/c (shown in Fig. H.2), counter position matching (within $\pm$ 1.0 counter size), ADC of the gas-Čerenkov counters $ADC_{\rm FGC} > 200$ and $ADC_{\rm RGC} > 50$ channels (shown in Fig. H.3), the time difference between the measured TOF value ($T_{\rm FGC} - T_{\rm STC}$) and the expected TOF value ($T_{\rm exp}$) to be within $\pm$ 10 ns, and energy deposit of the EM calorimeters $E > 0.3$ GeV and $E/p > 0.2$ (shown in Fig. H.4). Note that pions with momentum larger than 2.7 GeV/c produce Čerenkov light in GC's, as visible in Fig. H.2 $\sim$ H.4.

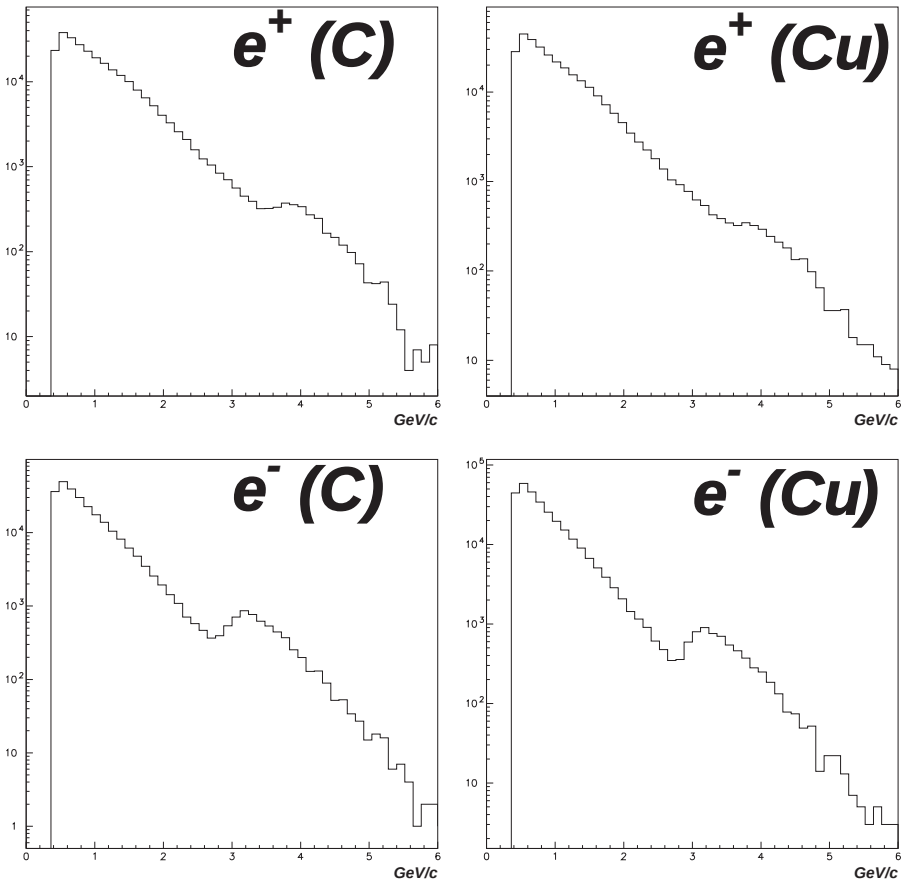

Figure H.2: The momentum distributions of electrons candidates. Pion contamination is visible above 2.7 GeV/c. The upper figures are for e^+ and the lower figures are for e^-, for the targets C and Cu as indicated in the figures.

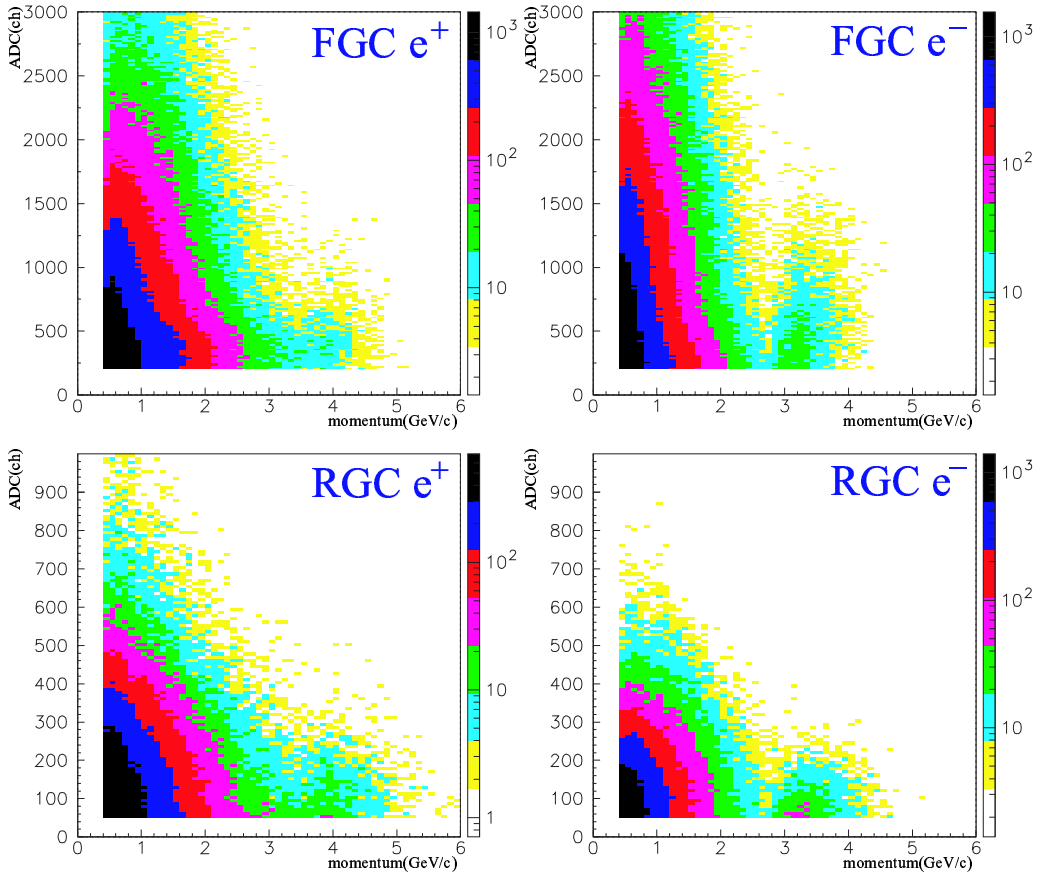

Figure H.3: The correlations between ADC pulse-hight and track momentum in FGC (upper) and in RGC (lower). The left figures are for e^+ and the right figures are for e^-. Events from the C and Cu targets are summed.

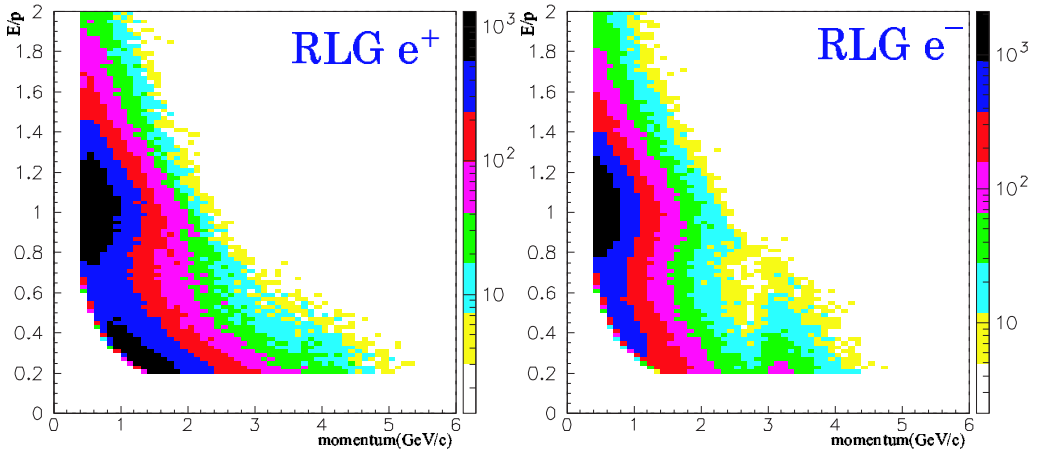

(a) RLG

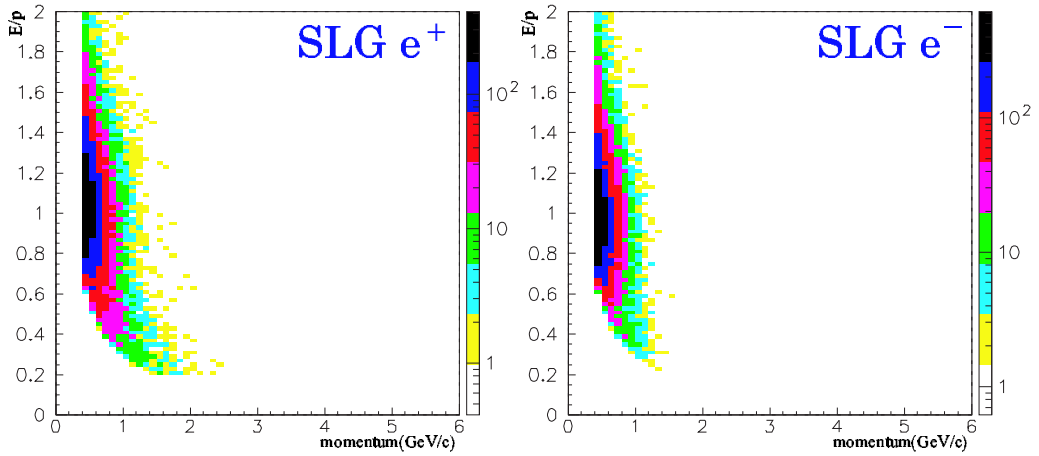

(b) SLG

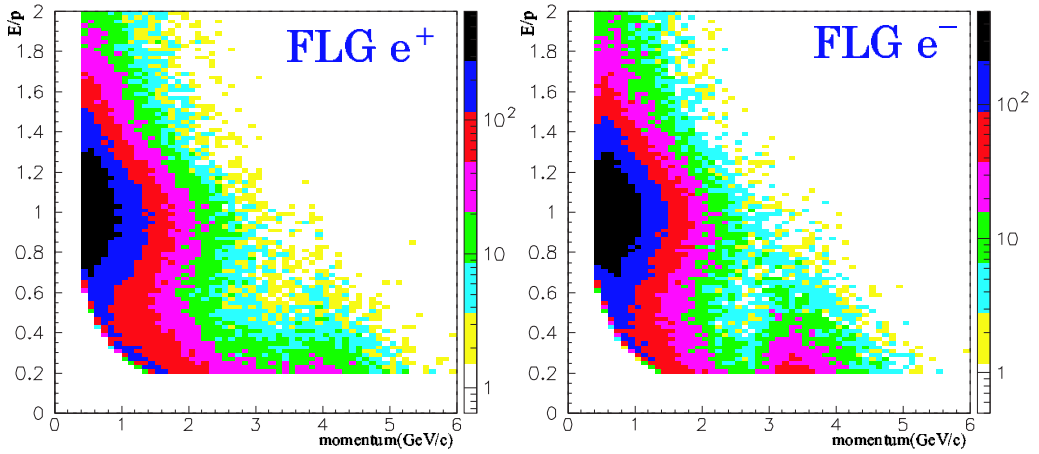

(c) FLG

Figure H.4: The correlations between E/p and track momentum in (a) RLG, (b) SLG, and (c) FLG. The left figures are for e^+ and the right figures are for e^-. Events from the C and Cu targets are summed.

We also calculated expected detector responses to e, μ, and π using Geant4, as shown in Fig. H.5 and H.6. The E/p of electrons, the ratio of energy deposit to momentum, decreases as momentum increases, since the back-end leakage of 7.5 λ_0 radiator is increases.

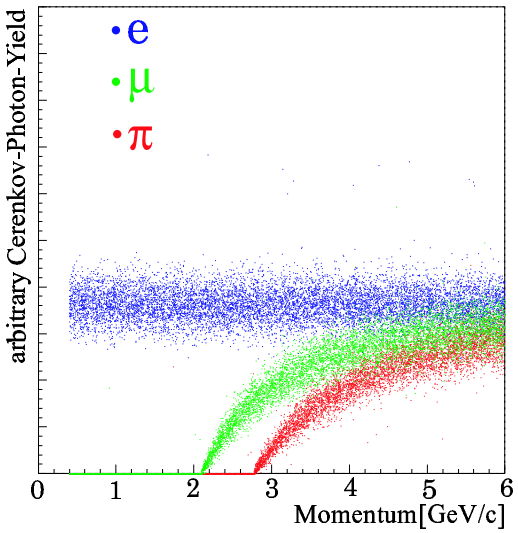

Figure H.5: The simulated correlations between Čerenkov-photon-yields and track momentum when particles pass through 600 mm iso-butane gas. The blue, green, red points represent photon-yields by e, μ, and π, respectively.

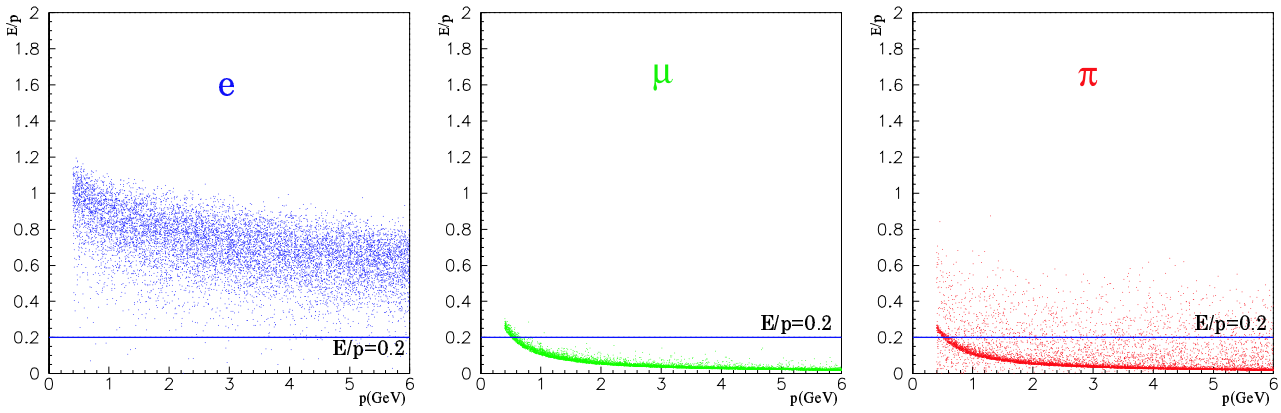

(a) e (b) μ (c) π

Figure H.6: The simulated correlations between E/p and track momentum when particles pass through 126 mm lead-glass block, for (a) e, (b) μ, and (c) π.

The obtained invariant mass spectra are shown in Fig. H.7, which contain the LR and RL events and the 2001 and 2002 data. A small peak is seen around 3 GeV/c^2 in the C-target data, although there is no peak in the Cu-target data. When the mass spectrum for the C-targets was fitted with a Gaussian shape and a combinatorial background shape in the mass region from 2.4 to 3.4 GeV/c^2 as shown in Fig. H.8, we obtained the peak position to be 3.073 $\pm$ 0.014 GeV/c^2, the Gaussian σ to be 43 $\pm$ 14 MeV/c^2, and the entry of the peak to be 25.9 $\pm$ 8.0 events. Where the combinatorial background shape was evaluated by the event-mixing method. Using the detector simulation described in Sec. 3.5, the simulated J/ψ shape gave the peak position to be 3.079 GeV/c^2 and the Gaussian σ to be 55 MeV/c^2. The agreements are quite remarkable. We obtained the entry of the peak for the Cu-targets to be 4.7 $\pm$ 6.9 events using the above fitting procedure, except that the Gaussian peak and σ were fixed to the values of the C-targets data.

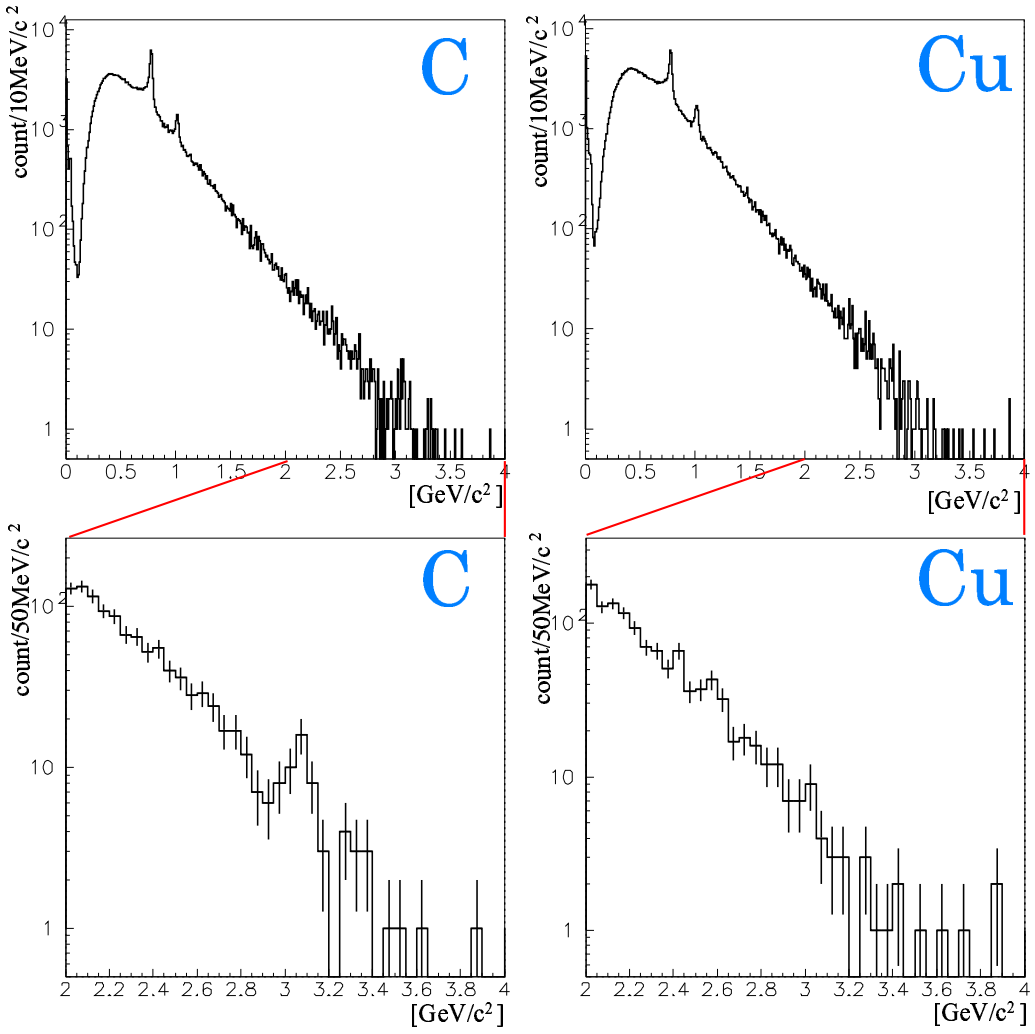

Figure H.7: The e^+e^- invariant mass spectra for the C-targets (left) and for the Cu-targets (right).

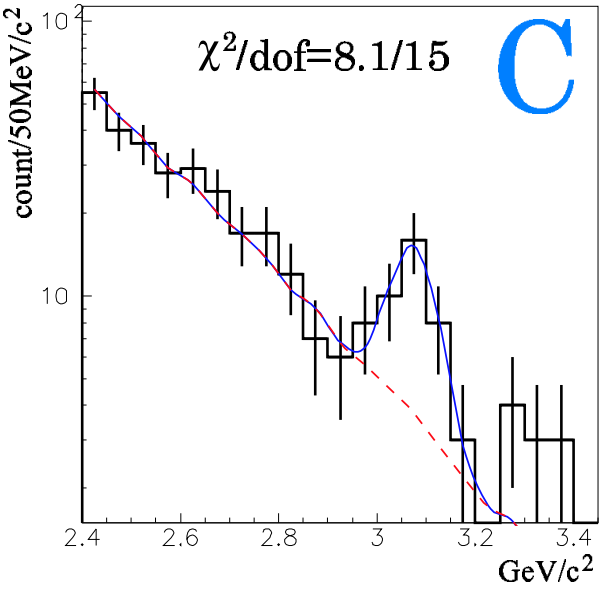

Figure H.8: The e^+e^- invariant mass spectrum for the C-targets. The solid and dotted lines represent the fit result and the combinatorial background, respectively.

However when the E/p cuts in the EM calorimeters were tightened from $E/p > 0.2$ to $E/p > 0.3$, the peak structure around 3 GeV/c^2 in the C-target data vanished, as shown in Fig. H.9. In the present experiment, the dynamic-range of ADC modules used for the EM calorimeters was limited (typically up to about 2 GeV/c^2 as the energy deposit), so that the energy deposit from the high momentum electron should saturate around 2 GeV/c^2. In other words, the values of E/p at the higher momentum region should be flatten against the saturation values; $E/p \simeq 0.4$ at $p = 5$ GeV/c for example. Although these saturations were expected in the J/ψ mass region, there were no such tendencies observed as shown in Fig. H.11.

Therefore we cannot conclude that the J/ψ peak is observed in the present experiment ($\sqrt{s_{NN}} = 5.1$), because the electron identifications in the higher momentum region have less reliability. Nevertheless, we plot the data in Fig. H.7 as the acceptance-corrected cross section of $p + C \to J/\psi + X$ and the 90% onfidence limit of the cross section of $p + Cu \to J/\psi + X$ in Fig. H.12, as a record.

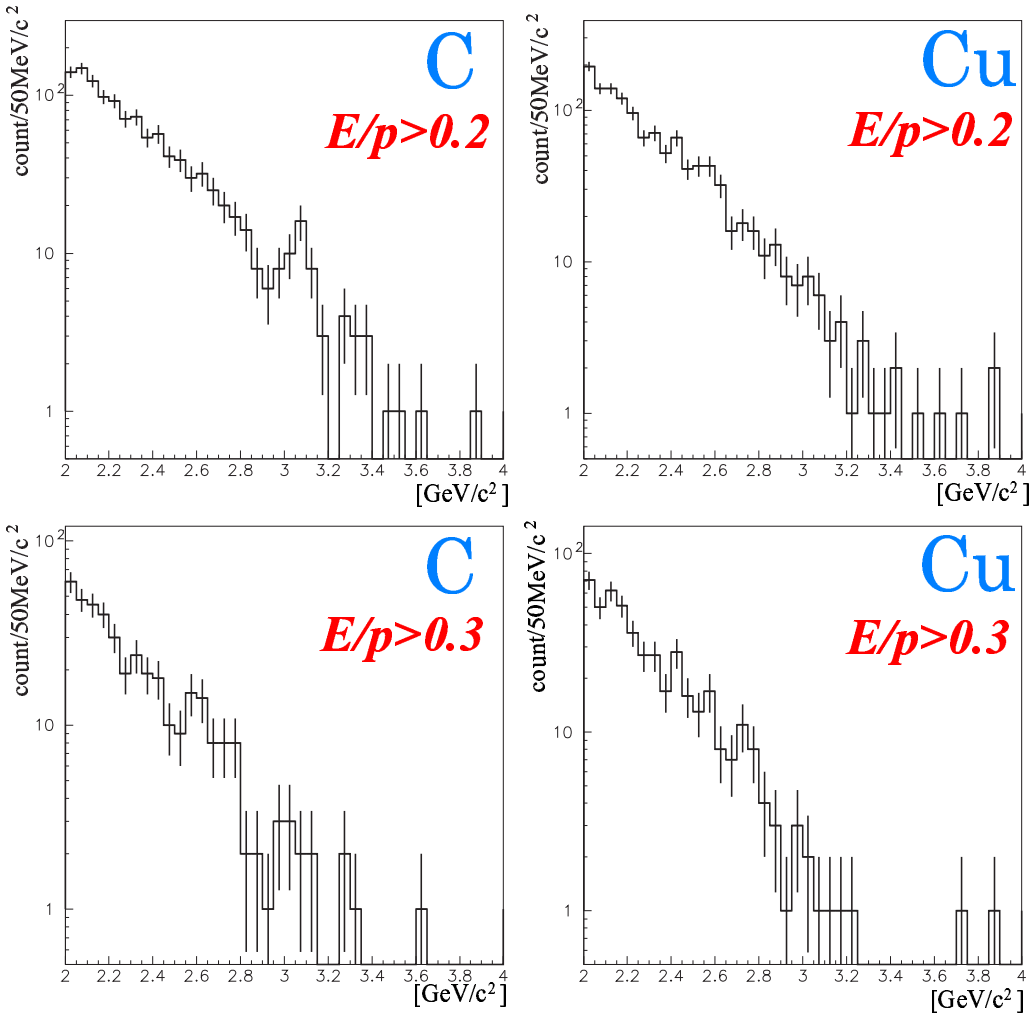

Figure H.9: The e^+e^- invariant mass spectra for the C-targets (left) and for the copper targets (right). The upper figures are $E/p > 0.2$ in the EM calorimeters, and the lower figures are $E/p > 0.3$.

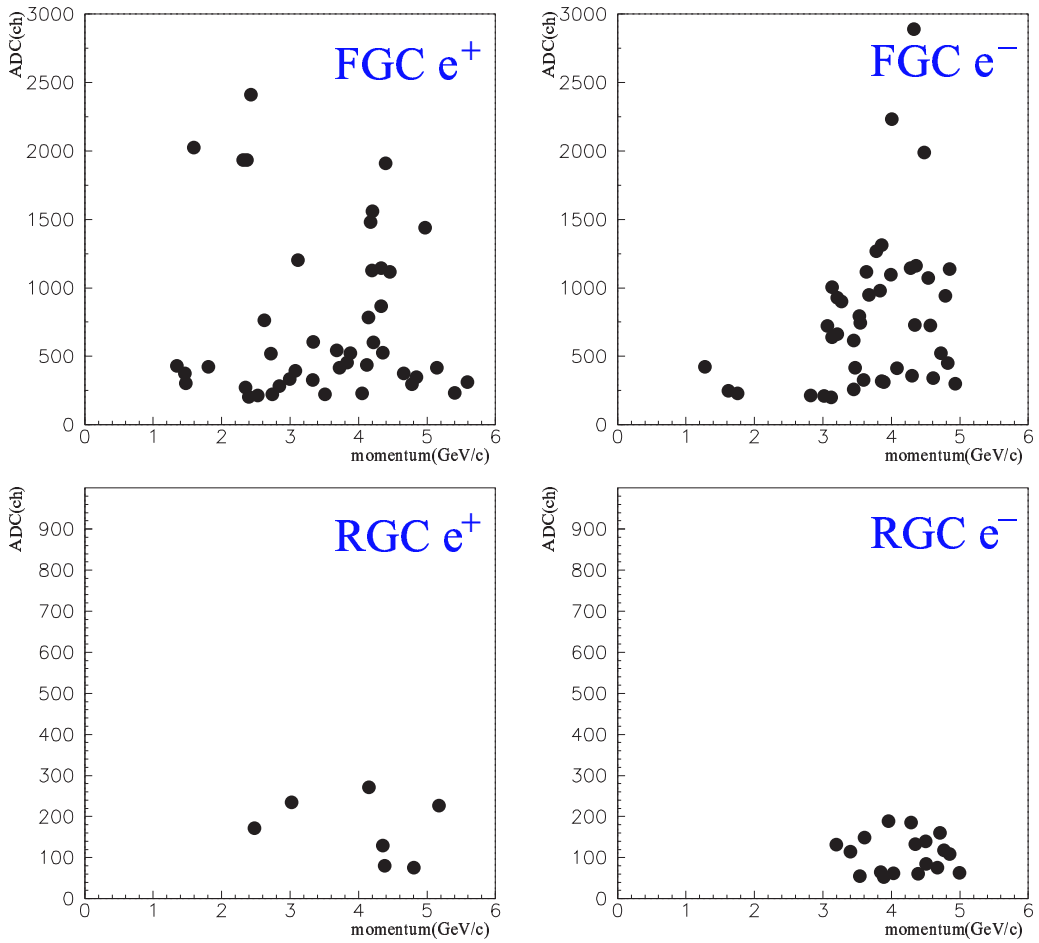

Figure H.10: The correlations between ADC pulse-hight and track momentum in the mass region from 2.95 to 3.2 GeV/c^2 in the C-target data, for FGC (upper) and RGC (lower) . The left figures are for e^+ and the right figures are for e^-.

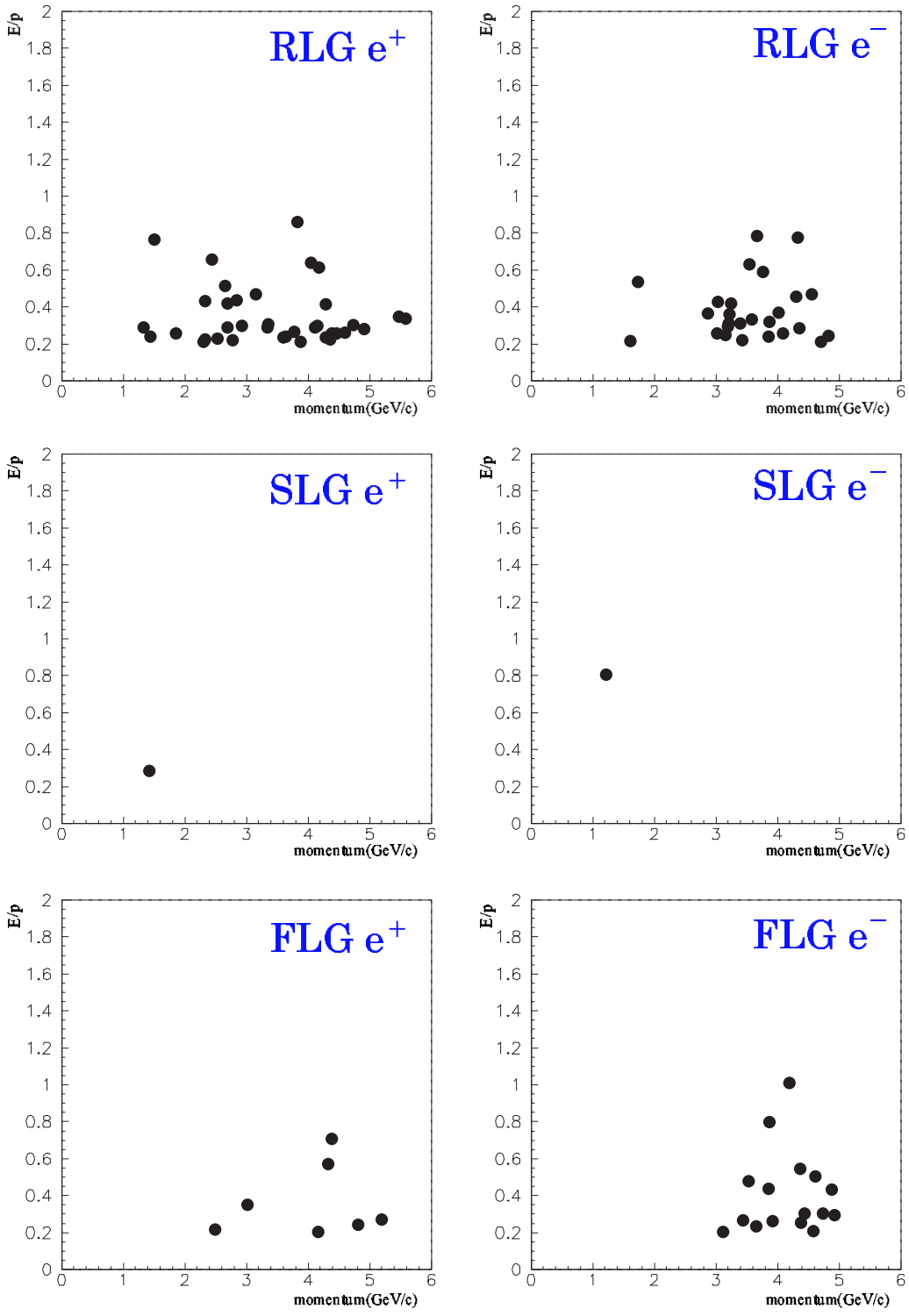

Figure H.11: The correlations between E/p and track momentum in the mass region from 2.95 to 3.2 GeV/c^2 in the C-target data, for RLG (upper), SLG (middle), and FLG (lower). The left figures are for e^+ and the right figures are for e^-.

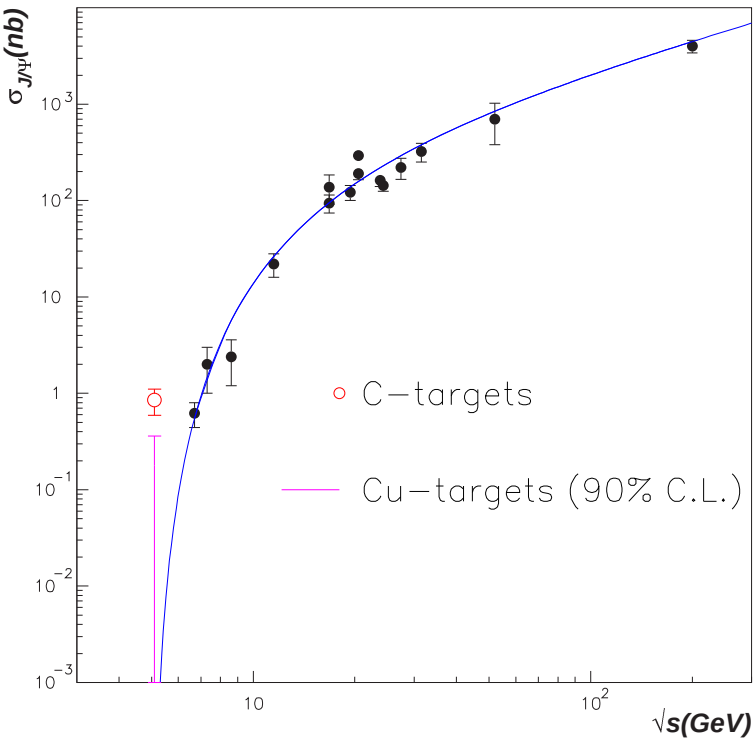

Figure H.12: The J/ψ total cross-sections, added the E325 data for the C-targets (open circle) and Cu-targets (line for 90% confidence level). The curve is the fit result with a empirical equation, $\sigma = \alpha \times \left(\frac{\Gamma_{J/\Psi}}{\left(m_{J/\Psi}+2m_p\right)^3} \right) \times \left\{ \left(\frac{\sqrt{s}}{\left(m_{J/\Psi}+2m_p\right)} \right) \times \left(1 - \frac{\left(m_{J/\Psi}+2m_p\right)}{\sqrt{s}} \right)^{\beta} \right\}$, where α and β are fit parameters.

Bibliography

[1] Yoichiro Nambu and G. Jona-Lasinio. Dynamical model of elementary particles based on an analogy with superconductivity. I. *Phys. Rev.*, 122:345–358, 1961.

[2] Yoichiro Nambu and G. Jona-Lasinio. Dynamical model of elementary particles based on an analogy with superconductivity. II. *Phys. Rev.*, 124:246–254, 1961.

[3] W. Weise. Nuclear aspects of chiral symmetry. *Nucl. Phys.*, A553:59c–72c, 1993.

[4] G. E. Brown and Mannque Rho. Scaling effective Lagrangians in a dense medium. *Phys. Rev. Lett.*, 66:2720–2723, 1991.

[5] Tetsuo Hatsuda and Su Houng Lee. QCD sum rules for vector mesons in nuclear medium. *Phys. Rev.*, C46:34–38, 1992.

[6] T. Hatsuda, H. Shiomi, and H. Kuwabara. Light Vector Mesons in Nuclear Matter. *Prog. Theor. Phys.*, 95:1009–1028, 1996.

[7] S. Eidelman et al. Review of particle physics. *Phys. Lett.*, B592:1, 2004.

[8] F. Klingl, T. Waas, and W. Weise. Modification of the ϕ-meson spectrum in nuclear matter. *Phys. Lett.*, B431:254–262, 1998.

[9] E. Oset and A. Ramos. ϕ decay in nuclei. *Nucl. Phys.*, A679:616–628, 2001.

[10] D. Cabrera and M. J. Vicente Vacas. ϕ meson mass and decay width in nuclear matter. *Phys. Rev.*, C67:045203, 2003.

[11] Subrata Pal, C. M. Ko, and Zi-wei Lin. Phi meson production in relativistic heavy ion collisions. *Nucl. Phys.*, A707:525–539, 2002.

[12] P. M. Ivanov et al. Measurement of the charged kaon form factor in the energy range 1.0 to 1.4 GeV. *Phys. Lett.*, B107:297–300, 1981.

[13] Pin-Zhen Bi and Johann Rafelski. Decay of phi in hot matter. *Phys. Lett.*, B262:485–491, 1991.

[14] Jean Paul Blaizot and Ramon Mendez Galain. ϕ and K mesons in hot dense matter. *Phys. Lett.*, B271:32–36, 1991.

[15] Wade Smith and Kevin L. Haglin. Collision broadening of the ϕ meson in baryon rich hadronic matter. *Phys. Rev.*, C57:1449–1453, 1998.

[16] D. Lissauer and Edward V. Shuryak. K meson modification in hot hadronic matter may be detected via ϕ meson decays. *Phys. Lett.*, B253:15–18, 1991.

[17] G. J. Lolos et al. Evidence for ρ^0 Mass Modification in the ^{3}He(γ,ρ^0)ppn Reaction. *Phys. Rev. Lett.*, 80:241–244, 1998.

[18] M. A. Kagarlis et al. Subthreshold ρ^0 photoproduction on ^{3}He. *Phys. Rev.*, C60:025203, 1999.

[19] G. J. Lolos et al. Helicity signatures in subthreshold ρ^0 production on nuclei. *Phys. Lett.*, B528:65–72, 2002.

[20] G. M. Huber et al. In-medium ρ^0 spectral function study via the ^{2}H, ^{3}He, ^{12}C(γ,$\pi^+\pi^-$) reaction. *Phys. Rev.*, C68:065202, 2003.

[21] K. Suzuki et al. Precision Spectroscopy of Pionic 1s States of Sn Nuclei and Evidence for Partial Restoration of Chiral Symmetry in the Nuclear Medium. *Phys. Rev. Lett.*, 92:072302, 2004.

[22] D. Trnka et al. Observation of In-Medium Modifications of the ω Meson. *Phys. Rev. Lett.*, 94:192303, 2005.

[23] G. Agakishiev et al. Enhanced Production of Low-Mass Electron Pairs in 200 GeV/Nucleon S-Au Collisions at the CERN Super Proton Synchrotron. *Phys. Rev. Lett.*, 75:1272–1275, 1995.

[24] J. Adams et al. ρ^0 Production and Possible Modification in Au + Au and $p + p$ Collisions at $\sqrt{s_{NN}} = 200$ GeV. *Phys. Rev. Lett.*, 92:092301, 2004.

[25] R. Arnaldi et al. First Measurement of the ρ Spectral Function in High-Energy Nuclear Collisions. *Phys. Rev. Lett.*, 96:162302, 2006.

[26] G. Agakichiev et al. e^+ e^--pair production in Pb-Au collisions at 158 GeV per nucleon. *Eur. Phys. J.*, C41:475–513, 2005.

[27] S. V. Afanasev et al. Production of ϕ-mesons in p+p, p+Pb and central Pb+Pb collisions at E_{beam}=158 A GeV. *Phys. Lett.*, B491:59–66, 2000.

[28] B. Alessandro et al. ϕ production in Pb–Pb collisions at 158 GeV/c per nucleon incident momentum. *Phys. Lett.*, B555:147–155, 2003.

[29] D. Rohrich. Review of SPS experimental results on strangeness. *J. Phys.*, G27:355–366, 2001.

[30] D. Adamova et al. Leptonic and Charged Kaon Decay Modes of the ϕ Meson Measured in Heavy-Ion Collisions at the CERN Super Proton Synchrotron. *Phys. Rev. Lett.*, 96:152301, 2006.

[31] R. Muto et al. Evidence for in-medium modification of ϕ meson at normal nuclear density. *Phys. Rev. Lett.*, 98:042501, 2007.

[32] K. Ozawa et al. Observation of ρ/ω Meson Modification in Nuclear Matter. *Phys. Rev. Lett.*, 86:5019–5022, 2001.

[33] K. Ozawa. *STUDY OF ρ/ω MESON MASS MODIFICATION IN NUCLEAR MATTER.* PhD thesis, Department of Physics, Faculty of Science, Kyoto University, 2001.

[34] M. Naruki et al. Experimental Signature of Medium Modifications for ρ and ω Mesons in the 12 GeV p+A Reactions. *Phys. Rev. Lett.*, 96:092301, 2006.

[35] M. Naruki. *Experimental signature of medium modifications for ρ and ω mesons in 12 GeV p + A reactions.* PhD thesis, Department of Physics, Faculty of Science, Kyoto University, 2006.

[36] R. Muto. PhD thesis, Department of Physics, Faculty of Science, Kyoto University, 2006. in preparation.

[37] T. Tabaru et al. Nuclear mass number dependence of inclusive production of ω and ϕ mesons in 12 GeV p+A collisions. *Phys. Rev.*, C74:025201, 2006.

[38] T. Tabaru. *Production of ω and ϕ Mesons in 12 GeV p + A Interaction Measured in e^+e^- Decay Mode*. PhD thesis, Department of Physics, Faculty of Science, Kyoto University, 2006.

[39] S. Yokkaichi. *Study of Nuclear Dependence of Production and Decay of ϕ meson in 12-GeV p + A Interaction*. PhD thesis, Department of Physics, Faculty of Science, Kyoto University, 2000.

[40] M. Ishino. *Study of nuclear-matter effect on K^+K^- invariant mass measured in 12-GeV p + A reactions*. PhD thesis, Department of Physics, Faculty of Science, Kyoto University, 2000.

[41] M. Takasaki et al. Design for the Radiation Protection of the EP1-B Beam Line in the KEK-PS North Counter Hall. *KEK Internal*, 1, 1995.

[42] M. Sekimoto et al. Spectrometer for measurements of phi mesons in nuclear matter produced through 12-gev p + a reactions. *Nucl. Instrum. Meth.*, A516:390–405, 2004.

[43] I. Adachi et al. Study of a threshold Cherenkov counter based on silica aerogels with low refractive indices. *Nucl. Instrum. Meth.*, A355:390–398, 1995.

[44] M. Ishino et al. Mass production of hydrophobic silica aerogel and readout optics of Cherenkov light. *Nucl. Instrum. Meth.*, A457:581–587, 2001.

[45] Y. Sugaya et al. Ionization chamber as p, d and α beam intensity monitor. *Nucl. Instrum. Meth.*, A368:635–639, 1996.

[46] TOSCA. *Vector Fields Limited (UK)*. http://www.vectorfields.co.uk/.

[47] Garfield. *developed in CERN*. http://consult.cern.ch/writeup/garfield/.

[48] O. Sasaki. ATLAS Thin Gap Chamber, Amplifier-Shaper-Discriminator ICs and ASD Boards. Technical report, 1999. http://www-online.kek.jp/~sosamu/.

[49] M. Kollefrath et al. Ageing studies for the ATLAS-monitored drift tubes. *Nucl. Instrum. Meth.*, A419:351–356, 1998.

[50] H. Hinterberger and R. Winston. Efficient Light Coupler for Threshold Čerenkov Counters. *Rev. Sci. Instrum.*, 37:1094–1095, 1966.

[51] S. Kawabata et al. TOPAZ barrel electromagnetic calorimeter at TRISTAN, KEK. *Nucl. Instrum. Meth.*, A270:11–20, 1988.

[52] *VMEbus architecture*. IEEE 1014/D1.0.

[53] T. K. Ohsuka et al. Tko specification. kek data acquisition development working group. Tsukuba Kek - KEK-85-10 (85,REC.JAN.86) 40p.

[54] CAMAC, A MODULAR SYSTEM OF INSTRUMENTATION IN DATA PROCESSING. REVISED DESCRIPTION AND SPECIFICATION. (IN GERMAN). Euratom Ispra - EUR 4100 D (72,REC.AUG 75) 64p.

[55] Superconducting Super Collider Laboratory. *Unidaq Documentation Set*, SDC-93-487, 1993.

[56] Rene Brun, Olivier Couet, Carlo E. Vandoni, and Pietro Zanarini. PAW, a general-purpose portable software tool for data analysis and presentation. *Comput. Phys. Commun.*, 57:432–437, 1989.

[57] R. Brun and D. Lienart. Hbook User Guide: Cern Computer Center Program Library Long Writeup: Version 4. CERN-Y250.

[58] X.org foundation. *X Windows system.* http://wiki.x.org/wiki/Home.

[59] CCJ. http://ccjsun.riken.go.jp/ccj/.

[60] Andy Hanushevsky. *man page of bbcp.* SLAC, 2002. http://www.slac.stanford.edu/~abh/bbcp/.

[61] HPSS. http://www.hpss-collaboration.org/hpss/index.jsp.

[62] S. Agostinelli et al. GEANT4 - a simulation toolkit. *Nucl. Instrum. Meth.*, A506:250–303, 2003.

[63] Y. Nara, N. Otuka, A. Ohnishi, K. Niita, and S. Chiba. Relativistic nuclear collisions at $10A$ GeV energies from p+Be to Au+Au with the hadronic cascade model. *Phys. Rev.*, C61:024901, 2000.

[64] REPIC Corporation. Kita-otsuka 1-28-3, Toshima-ku, Tokyo 170-0004, Japan.

[65] F. James and M. Roos. Minuit - a system for function minimization and analysis of the parameter errors and correlations. *Comput. Phys. Commun.*, 10:343–367, 1975. http://wwwasdoc.web.cern.ch/wwwasdoc/minuit/minmain.html.

[66] J. D. Jackson. Remarks on the phenomenological analysis of resonances. *Nuovo Cim.*, 34:1644–1666, 1964.

[67] Alexander Spiridonov. Bremsstrahlung in leptonic onia decays: Effects on mass spectra. 2004. hep-ex/0510076.

[68] Frits A. Berends, R. Kleiss, and S. Jadach. Radiative corrections to muon pair and quark pair production in electron-positron collisions in the Z_0 region. *Nucl. Phys.*, B202:63, 1982.

[69] Steve Baker and Robert D. Cousins. Clarification of the use of CHI-square and likelihood functions in fits to histograms. *Nucl. Instrum. Meth.*, 221:437–442, 1984.

[70] F. Halzen. CVC FOR GLUONS AND HADROPRODUCTION OF QUARK FLAVORS. *Phys. Lett.*, B69:105, 1977.

[71] Harald Fritzsch. PRODUCING HEAVY QUARK FLAVORS IN HADRONIC COLLISIONS: A TEST OF QUANTUM CHROMODYNAMICS. *Phys. Lett.*, B67:217, 1977.

[72] R. Baier and R. Ruckl. HADRONIC COLLISIONS: A QUARKONIUM FACTORY. *Z. Phys.*, C19:251, 1983.

[73] Gerhard A. Schuler. Quarkonium production and decays. 1994. hep-ph/9403387.

[74] Geoffrey T. Bodwin, Eric Braaten, and G. Peter Lepage. Rigorous QCD analysis of inclusive annihilation and production of heavy quarkonium. *Phys. Rev.*, D51:1125–1171, 1995.

[75] S. S. Adler et al. J/ψ Production from Proton-Proton Collisions at $\sqrt{s}$=200 GeV. *Phys. Rev. Lett.*, 92:051802, 2004.

[76] Charles J. Benesh, Jian-wei Qiu, and James P. Vary. J/ψ suppression in hadron - nucleus collisions. *Phys. Rev.*, C50:1015–1023, 1994.

[77] R. Vogt. J/ψ production and suppression. *Phys. Rept.*, 310:197–260, 1999.

[78] A. Gribushin et al. Production of J/ψ mesons in pBe collisions at 530 and 800 GeV/c. *Phys. Rev.*, D62:012001, 2000.

[79] and references in [73, 77, 78].

List of Figures

List of Tables